THE UNIVERSITY OF CHICAGO

QUANTUM MANY-BODY DYNAMICS WITH DRIVEN BOSE CONDENSATES: KIBBLE-ZUREK MECHANISM AND BOSE FIREWORKS

A DISSERTATION SUBMITTED TO
THE FACULTY OF THE DIVISION OF THE PHYSICAL SCIENCES
IN CANDIDACY FOR THE DEGREE OF
DOCTOR OF PHILOSOPHY

DEPARTMENT OF PHYSICS

BY
LOGAN WILLIAM CLARK

CHICAGO, ILLINOIS
DECEMBER 2017

To my loving family

TABLE OF CONTENTS

LIST OF FIGURES

LIST OF TABLES

ACKNOWLEDGMENTS

First of all, I would like to sincerely thank my adviser, Prof. Cheng Chin, without whom none of this work would have been possible. Naturally, Cheng is an impressive scientist. He has great knowledge and interests spanning many subjects, an infectious enthusiasm for discovery, and a keen eye for fruitful research directions. But, he is also an excellent *adviser*. Cheng makes his students' development into independent, well-rounded scientists a genuine priority. He gives students the invaluable opportunity to pursue their own interests and ideas in the lab, and he encourages them to take ownership of every piece of a project. On top of all this, Cheng makes a research group into a warm and supportive team, frequently bringing the lab together for fun outings and activities (not to mention the creative group videos). I will always treasure my friendship with Cheng and the many fond memories of my time in his lab.

Over these past five years, I have had many wonderful teammates in the Cesium lab. I am particularly grateful to my good friend and original partner in crime Harry Li-Chung Ha, who was the elder graduate student in Cesium lab for my first few years. Harry is an incredibly kind and genuine person, and he exhibited great patience with me when I was a new and inexperienced graduate student. I used to "joke" that Harry taught me everything I knew, and even if I may have learned a few other things since then, Harry's guidance will always remain with me. We shared many great moments together, from discovering rotons in our BEC to board game nights and the National Day parade. Wherever Harry goes in the future, they will be extremely lucky to have him. As Harry's time in lab was winding down, we were very lucky to have Lei Feng cross the aisle and join us from the lithium-cesium lab. As soon as he joined, Lei injected fresh enthuasism and excitement into our team. He is extremely hard-working and a quick learner, and I am very proud of the work that we have done together. More importantly we've had a lot of fun, from hunting snakes in the dipole trap, to water frisbee, to Lei teaching me to ski so that he could capture embarrassing

video of my wipeouts. Lei has a very bright future, and I'm excited to see where he goes. Furthermore, I am very grateful to Chen-Lung Hung and Xibo Zhang, whose hard work laid the foundation for everything we do in cesium lab. Finally, I would like to thank my good friend Klaus Hueck, who brightened the lab in his few months with us, and made many valuable contributions including the fantastic code which is still the basis for our data analysis.

I have also had the pleasure of working with many sage postdocs in the cesium lab. From the first day that I arrived, Colin Parker was like a second adviser for the entire lab; he was always quick to provide excellent suggestions for what to do and how to do it. Thank you to Eric Hazlett and Ulrich Eismann, who patiently worked with me when I was new in the lab. I enjoyed the fun times that we shared assembling the new imaging and projection system. Thank you to Chen-Yu Xu for the fun conversations that we shared and all of your excellent advice. I am also very grateful to my friend Anita Gaj, who brought great knowledge and insight, along with some fun new games, to the team over the course of my last year in the lab.

I am grateful to the many other members of the Chin lab who have made it a pleasure to work here over the years. From the Lithium-Cesium experiment, I want to thank Jacob Johansen, for helping me to build my first diode laser and for always having five movie quotes suitable for any occasion. Thank you to Shih-Kuang Tung and Karina Jiménez Garcia for your helpful advice and warm company during my early years in the lab. Thank you also to Krutik Patel and Brian DeSalvo, who have recently, very impressively taken over the experiment and who will no doubt produce fantastic and exciting results in the coming years. I also had the pleasure of seeing the birth of Quantum Matter Synthesizer experiment, pioneered by Gustaf Downs and now led by Mickey McDonald and Jonathan Trisnadi. Thank you all for your friendship and your inspirational hard work. Thank you especially to Mickey for sharing with me both countless Patriots games and your boundless

enthusiasm for new and exotic science. I am also very grateful to Professor Kathy Levin and Brandon Anderson, with whom I had the great pleasure of collaborating on the theoretical side of our projects in recent years, and who reliably provide both valuable insights and very efficient simulations.

My time in the lab would not have been the same without our many wonderful and enthusiastic undergraduate students. I would like to thank Francisco Fonta, Kate Schreiber, Chung-Kuan Lin, Dylan Sabulsky, Yu-Ting Chen, Tyler Smart, Junbo Zhu, Paloma Ocola, Nicholas Kowalski, Tyler Johnson, Misha Usatyuk, Frankie Fung, Kuan-Wen Chen, Tongtong Liu, Yunpeng Ji, Marissa Montoya, Ben Foster, and Connor Fieweger for all of your contributions both to the science and fellowship in the lab.

I am very grateful to my thesis committee members, Professors Jonathan Simon, Thomas A. Witten, and Paolo Privitera, for their valuable advice over the years and their hard work reviewing my thesis. Thank you especially to Jon, on whom I could always rely for friendly greetings, sarcastic comments, insightful questions and excellent advice.

Thank you to the staff of the James Franck Institute, whose hard work enables a wonderful research environment. I am particularly grateful to the kind and caring Maria Jimenez, who kept us organized, orchestrated countless group events, and demonstrated great patience for our collective flakiness. I would also like to thank John Phillips, who tirelessly ensures that the building runs smoothly while we hunker down in the sub-basement. Even with all that on his plate, I appreciate that John can always be counted on for a big smile and a friendly greeting.

Thank you also to the many members of the University of Chicago Physics Department who helped to create such a comfortable and stimulating learning environment for my graduate studies. Thank you to Nobuko McNeill, whose warm and welcoming attitude helped me to feel at home here. Thank you also to Amy Schulz and Prof. David Reid, whom it is always a pleasure to visit in the department office, for your crucial work to keep us graduate

students afloat.

I am grateful for the fellowship support that I have received throughout my years in graduate school, which gave me the time and flexibility to freely explore my interests. In particular, I appreciate my support from the Department of Defense through the National Defense Science and Engineering Graduate Fellowship. I would also like to thank the University of Chicago and the donors for supporting me through the Eugene and Niesje Parker fellowship, the Sachs Fellowship, the Yoichiro Nambu Fellowship, the Grainger graduate Fellowship and the Harper Dissertation Fellowship.

I am deeply grateful for the constant love and support I have received from my family and friends. Thank you to Seth and Matt, who are always excited to hear about the crazy new science that I am working on. Thank you to the Walwemas, for welcoming me into your family. Thank you to my mom, for always thinking that I am the best, no matter what I actually do, and for always answering the phone on my way home from the lab. Thank you to my dad, for teaching me to be curious, always asking the right questions, and putting me in front of a computer earlier than I can actually remember. Thank you to Tanen, for being the best sister in the world, for sharing treasure troves of fantastic books that help me wind down, and for always pointing out that science is hilarious. Finally, thank you to my wife Marianne for your patient listening, great questions, and faithful support; I am so proud of you, and I look forward to sharing my new discoveries with you for many years to come.

ABSTRACT

In recent years there has been an explosion of interest in the field of quantum many-body physics. Understanding the complex and often unintuitive behavior of systems containing interacting quantum constituents is not only fascinating but also crucial for developing the next generation of quantum technology, including better materials, sensors, and computers. Yet understanding such systems remains a challenge, particularly when considering the dynamics which occur when they are excited far from equilibrium. Ultracold atomic gases provide an ideal system with which to study dynamics by enabling clean, well-controlled experiments at length- and time-scales which allow us to observe the dynamics directly.

This thesis describes experiments on the many-body dynamics of ultracold, bosonic cesium atoms. Our apparatus epitomizes the versatility of ultracold atoms by providing extensive control over the quantum gas. In particular, we will discuss our use of a digital micromirror device to project arbitrary, dynamic external potentials onto the gas; our development of a powerful new scheme for optically controlling Feshbach resonances to enable spatiotemporal control of the interactions between atoms; and our use of near-resonant shaking lattices to modify the kinetic energy of atoms.

Taking advantage of this flexible apparatus, we have been able to test a longstanding conjecture based on the Kibble-Zurek mechanism, which says that the dynamics of a system crossing a quantum phase transition should obey a universal scaling symmetry of space and time. After accounting for this scaling symmetry, critical dynamics would be essentially independent of the rate at which a system crossed a phase transition. We tested the universal scaling of critical dynamics by using near-resonant shaking to drive Bose-Einstein condensates across an effectively ferromagnetic quantum phase transition. After crossing the phase transition, condensates divide themselves spatially into domains with finite quasimomentum. We measured the growth of these domains over time and the correlation functions describing their spatial distribution by directly reconstructing the quasimomentum distribution. We

observed the expected scaling laws across more than an order of magnitude in the crossing rate, aside from which the observed critical dynamics were indeed independent of the crossing rate. These experiments provide strong support for the universal scaling symmetry of space and time and the extension of the Kibble-Zurek mechanism to quantum phase transitions.

We also present the first observation of Bose Fireworks: the sudden emission of many bright, narrow jets of atoms from condensates with oscillating interaction strength. Even though the underlying inelastic s-wave collisions induced by oscillating interactions are isotropic, the collective nature of collisions in the condensate causes the outgoing bosonic atoms to bunch into narrow jets in the horizontal plane. This bunching results from runaway stimulated collisions, which we find can only occur above a threshold oscillation amplitude. The observed atom number in the jets suggests that they are seeded by quantum fluctuations. Moreover, in azimuthal correlation functions we observe forward correlations consistent with theory, which saturate the limit from the uncertainty principle. We also observe partial correlation between counterpropagating jets. Bose Fireworks provide a well-controlled platform for understanding the diverse class of systems in which a coherent source rapidly emits pairs of counterpropagating bosons.

CHAPTER 1

INTRODUCTION

1.1 Quantum many-body dynamics with ultracold atoms

There is a lot going on near absolute zero. For much of history, scientists would have expected absolute zero to be where fluctuation stopped and any matter became frozen. Yet modern physics labs find that, instead of stopping, ultra-cold systems simply enter the realm of quantum mechanics. A striking example of this is the Bose-Einstein condensation of ultracold atoms [9, 49, 122]. Bose-Einstein condensates (BECs) are formed by using lasers to cool atoms to the lowest temperatures of any objects in the known universe. In fact, NASA will soon launch BECs into space and likely push those record low temperatures even farther down[1]. BECs manifest the quantum mechanical wave behavior of matter in spectacular ways, forming interference patterns and diffracting off of gratings like light or water waves. All the while BECs act as superfluids, flowing around obstacles without friction. Yet they contain a macroscopic number of atoms and have a size comparable to the thickness of human hair. With all of these features it is no wonder that, in the past 22 years since the first BECs were formed, they have captured the imaginations of physicists, and an enormous and active field of research has formed around them.

Exotic and sometimes unintuitive features of quantum mechanics frequently manifest in the study of ultracold atoms. Even when the atoms reach ultracold temperatures and technical noise is carefully controlled, one sees dynamics driven by the ever-present quantum fluctuations. In our experiments, the wave-particle duality is made obvious when the same object exhibits the wave phenomena of interference and diffraction while also undergoing phase transitions due to strong two-particle interactions or having pairs of atoms form into molecules near Feshbach resonances. Key features, such as the increasing momentum spread

1. https://coldatomlab.jpl.nasa.gov/

when a condensate shrinks, result from the fundamental limit at which parameters of a system can be simultaneously characterized, set by the Heisenberg uncertainty principle. Under the right conditions, the atoms can even develop a high degree of quantum entanglement, in which the state of one atom is fundamentally dependent on those of the other atoms.

Developing a fundamental understanding of the many-body behavior which emerges in the presence of these exotic quantum features is an important and challenging goal for modern physicists. In particular situations, such as weakly interacting systems near equilibrium, the many-body problem becomes tractable and one can develop a relatively simple description of the system. Yet it has long been understood that quantum many-body problems are fundamentally difficult to solve. In general, specifying and time-evolving the state of a quantum many-body system requires exponentially greater resources than doing the same for the corresponding classical system [63]. This difficulty often manifests in two situations. The first is strongly correlated equilibrium phases such as superconductors, Mott insulators, or fractional quantum hall systems. The second situation, which is the focus of this thesis, arises when a quantum many-body system is brought far away from equilibrium.

Historically, a great deal of attention has been paid to systems at or near equilibrium. Such systems are generally understood by the powerful apparatus of statistical mechanics. To oversimplify things a bit, the power of statistical mechanics lies in the variety of systems which it links and makes amenable to the same basic analysis. Indeed, statistical mechanics has been extremely successful in predicting the emergent behavior of complex, interacting many-body systems, as long as they are near equilibrium.

However, a variety of factors often prevent systems from reaching thermal equilibrium. For example, the presence of a strong driving field or a large influx of energy or particles will often keep a system away from equilibrium. Yet other systems may be brought out of equilibrium by a sudden quench of their parameters, or by bringing them across phase transitions. Even fundamental structural properties, such as strong disorder or topological

defects, may prevent normal equilibration.

As a result, much of the universe around us is far from equilibrium. Indeed, starting at the largest scales, the complex distributions of matter and energy at the scale of star systems, galaxies, and clusters throughout the universe are certainly not in equilibrium. The influx of solar energy holds the Earth itself away from equilibrium, resulting in the complex patterns of weather and even in life itself. For practical purposes, a variety of important materials are either formed by rapid quenches, such as strong alloys and plastics, or stuck in far-from-equilibrium states, such as glasses, powders or foams [86]. At yet smaller scales, quantum computing or simulation devices must be isolated and their interactions carefully controlled in order to maintain their delicate quantum information. Of course, these are just a small set of intriguing examples which hardly do justice to the multitude of fascinating far-from-equilibrium systems around us.

No general paradigm exists for understanding the behavior of far-from-equilibrium systems. At least from our current perspective, these systems appear to exhibit a fantastic variety of behaviors, which are not obviously connected. While their richness makes these systems appealing, it poses a clear challenge to scientists: can we find universal principles and classifications which link these seemingly disparate systems together? Just as the tools of statistical mechanics provide a generic approach to understanding equilibrium systems, we wish to develop general principles describing far-from-equilibrium systems. To that end, it is invaluable to have clean and controllable platforms for performing experiments on far-from-equilibrium dynamics. Such platforms enable us to develop the paradigmatic examples from which we can infer (and later test) more general principles.

Ultracold atoms provide an ideal platform for studying quantum many-body physics far from equilibrium. First of all, the laser cooling and evaporation techniques required to remove entropy and access the quantum realm are extremely effective and well established [111]. Second, atoms are extremely well understood at the level of individual properties and

few-body collisions [36, 71]. This knowledge often enables us to derive simple models which describe the many-body system dynamics and are microscopically justified [122, 24]. Third, since the atoms are held in magnetic or laser traps under extremely high vacuum, they are naturally very well isolated from their room-temperature environment. Not only does this protect the delicate quantum state of the system, but it affords us the opportunity to bring the system out of equilibrium in a controlled way. Fourth, the interesting features of these quantum gases are large, typically at least hundreds of nanometers, and most dynamics are slow, occurring at least on microsecond timescales. The length scale makes it possible to measure density distributions or correlation functions with simple optical probes. The timescale is amenable to the capture of movies which directly reveal interesting far-from-equilibrium dynamical processes. The slow dynamics also makes cold atoms convenient for Floquet engineering, in which one can generate effective Hamiltonians with desirable properties by periodically driving the system on timescales much faster than the typical dynamics.

On top of all of these desirable features, we have a spectacular array of capabilities for controlling the many-body Hamiltonian. We generally think of this Hamiltonian,

$$H = H_{\mathrm{K}} + H_{\mathrm{P}} + H_{\mathrm{I}}, \tag{1.1}$$

as the sum of three parts: the term H_{K} for the kinetic energy, the term H_{P} for the potential of individual atoms, and the term H_{I} describing interactions between atoms. In the ultracold atom community there are well-established techniques for controlling each of these terms. The kinetic term can be dramatically modified by the presence of an optical lattice. The lattice replaces the free-space kinetic energy of $p^2/2m$ per atom with the band structure familiar from condensed matter systems. With optical lattices, formed from the interference between laser beams, one can choose the geometry and depth of the lattice to create the desired band structure. The potential energy term can be controlled using the geometry

and strength of dipole and magnetic traps. It is possible to achieve both homogeneous and harmonic trapping, with aspect ratios from fully symmetric spherical traps to flattened "pancakes" or even the highly elongated "cigar". In the extreme of these aspect ratios, one can achieve effectively two-dimensional or one-dimensional samples, in which the spacing of energy levels in the other dimensions is much greater than any energy scale of the atoms, preventing dynamics along that direction. Finally, we can control the interaction strength for pairs of atoms by using Feshbach resonances [36]. Adjusting the magnetic field near a Feshbach resonance can make the interaction strength between atoms strongly repulsive, strongly attractive, or even nonexistent. The interaction energy can also be enhanced by the high local density at the minima of an optical lattice. Together, all of these capabilities position ultracold atoms as an ideal platform for studying quantum many-body dynamics far from equilibrium.

1.2 Developments in this thesis

This thesis describes experimental studies of far-from-equilibrium quantum many-body dynamics using ultracold cesium atoms. We primarily explore two important situations: the Kibble-Zurek mechanism for a quantum phase transition and Bose Fireworks in a system which collectively emits identical boson pairs. We also discuss a variety of technological developments which expand the cold-atom toolbox. In particular, we have developed a new scheme for optical control of Feshbach resonances in order to spatiotemporally modulate the interaction strength between atoms. We have also implemented a digital micromirror device to generate arbitrary, dynamic potential energy surfaces.

The Kibble-Zurek mechanism (KZM) is uniquely fascinating for suggesting a universal approach to the critical dynamics across a continuous, symmetry-breaking phase transition [91, 168]. The KZM compares the time remaining for a system to cross equilibrium to the relaxation time at the corresponding distance from the critical point. When the relaxation

time becomes longer than the time remaining, the system becomes effectively frozen, and its correlation length stops growing. It is well established that both the relaxation time and the correlation length of the *equilibrium* system should take a universal form, with a simple power-law scaling in terms of the distance from the critical point. After the system crosses the phase transition, the density of topological defects is directly related to the maximum length of correlations established in the system. By this simple argument one can derive scaling exponents for the spatial and temporal structures characterizing the dynamics from the well established, universal scaling laws for the equilibrium state of the system.

We explore this space-time scaling symmetry of the critical dynamics using the effectively ferromagnetic quantum phase transition for bosons in a shaken optical lattice. This phase transition is enormously advantageous for studying the KZM. Because of the convenient dynamical timescales, we can directly watch the critical dynamics rather than merely testing the structure of topological defects after dynamics have ceased. Moreover, it is straightforward to adjust the rate at which we cross the transition over orders of magnitude, since the lattice shaking amplitude is directly controlled electronically. Finally, we are able to carefully characterize the dynamics by reconstructing the domain structure of the gas and even directly identifying individual topological defects.

This system enables us to experimentally test the applicability of the Kibble-Zurek mechanism to a much broader set of systems than has been previously explored. In particular, we present one of the first comprehensive tests of the Kibble-Zurek scaling in a quantum phase transition, a scenario which had not previously been explored experimentally (see also [11]). We also provide new insights into the breakdown (or lack thereof) of the Kibble-Zurek scaling in certain inhomogeneous systems. Furthermore, we demonstrate that the expected scaling can still hold when the phase transition occurs in a Floquet engineered system with periodic driving, in spite of the many ways in which Floquet systems challenge the typical predictions of statistical mechanics [58]; for example, the long-time equilibrium state of most interacting

Floquet systems is expected to be equivalent to an infinite temperature state [99, 47].

Our second major study began with the discovery of "Bose fireworks," in which a BEC with an oscillating scattering length suddenly emits many bright, narrow jets of atoms. The oscillating scattering length enables inelastic, s-wave collisions in which pairs of atoms absorb one quantum of energy from the oscillating field and are ejected in opposite directions. Even though the underlying inelastic collisions are isotropic, the collective nature of collisions in the condensate causes the outgoing bosonic atoms to bunch into narrow jets in the horizontal plane. Moreover, by tuning the emission rate we have observed the threshold rate above which Bose stimulation leads to runaway emission and the appearance of jets. We also see that each jet is correlated (though not perfectly) with a counter-propagating partner. We explain the typical width of the jets with a careful theoretical calculation, which indicates that the jet width saturates the limit set by the Heisenberg uncertainty principle due to the finite size of the BEC.

The behavior of Bose fireworks is closely related to the dynamics of a large class of systems in which a cooperative source emits excited pairs of identical bosons. The nature of such systems can vary widely: for example, it may be a laser in a nonlinear medium, a decaying molecular BEC, or two colliding BECs. In many respects, because of their common features these systems and many others are expected to exhibit similar dynamics. The major advantage of studying Bose fireworks is the wide tunability of nearly every parameter relevant to the emission process. We can control the size and shape of the BEC, the rate of emission, and the energy of each emitted particle. Moreover, we can turn the emission process on and off at will to carefully probe the state of the system at every stage of the dynamical process. On top of all of these features, the technical noise is sufficiently small that the emission is only seeded by quantum fluctuation. Thus, Bose fireworks are well positioned for future studies which dive deeper into its many interesting features and develop a comprehensive picture of dynamics in this large class of closely related systems.

We have also made a variety of technological advancements to expand the toolbox of ultracold atoms. Most notably, we have developed and demonstrated a new scheme for fine spatial and temporal control of the interaction strength using optical control of Feshbach resonances (OFR). Unlike previous demonstrations of OFR [60, 144, 160, 59, 17, 158, 23, 159, 66], we achieve lifetimes of hundreds of milliseconds for a reasonable change in the scattering length in a degenerate quantum gas, which is long compared to the typical dynamical timescales. Moreover, by using a laser at a tune-out wavelength we eliminate the parasitic dipole forces which typically accompany the local change in scattering length and would often swamp out the interesting effects of spatially modulated interactions. We have used OFR to study the response of the system to a rapidly oscillating effective magnetic field, as well as the local collapse dynamics of a condensate with repulsive interactions at its edge and attractive interactions at its center.

Almost every experiment we perform now takes advantage of our ability to create arbitrary, dynamic potentials with a blue-detuned laser modulated by a digital micromirror device. This fantastic device consists of an array of mirrors, each a few microns across, which can be independently turned on or off thousands of times per second. We image the intensity pattern reflected from the on-state mirrors onto the atoms using our high-resolution objective, thus creating a finely-structured repulsive potential landscape which we can control at will. We will particularly focus on our applications of this technology to performing bragg spectroscopy to measure the roton-maxon dispersion relation in the shaken lattice, as well as to dynamically forming homogeneous BECs with arbitrary shapes in two dimensions.

Finally, our studies of bosons in shaken lattices required a careful theoretical treatment as well as a clean, well controlled experimental setup. We first explain the nature of the effectively ferromagnetic quantum phase transition, explored originally in Ref. [119, 75]. We continue by providing new insights into the influence of micromotion on interactions. We further demonstrate a different kind of phase transition which occurs when the shaking

frequency is slightly red-detuned from the ground to first excited band gap. Throughout, we describe a number of key technical improvements for obtaining the best performance of the shaken lattice setup.

This thesis is organized as follows: First, in Ch. 2 we describe the essential features of the apparatus with which we perform experiments on ultracold cesium atoms. Our primary focus is on new developments or improvements made for this thesis. Next, in Ch. 3 we provide a theoretical overview of bosons in shaken optical lattices using Floquet theory. The three subsequent chapters present the core results of this thesis on quantum many-body dynamics far from equilibrium: In Ch. 4 we present our study of the space-time scaling symmetry of critical dynamics, closely associated with the Kibble-Zurek mechanism, using the phase transition in the shaken optical lattice. Then, in Ch. 5 we present the first observation of Bose Fireworks, the collective emission of matter wave jets from BECs with oscillating interaction strength. Next, in Ch. 6 we explain our new approach to optically controlling Feshbach resonances while maintaining a long-lived quantum gas and without parasitic dipole forces. This thesis concludes in Ch. 7 with a discussion of many interesting future directions for each of our projects, including a variety of preliminary results.

CHAPTER 2

VERSATILE ULTRACOLD CESIUM APPARATUS

Our apparatus for performing experiments with ultracold cesium atoms is extremely versatile. We can create gases in one, two, or three dimensions. We have a high resolution objective lens for detecting fine structure in absorption images and also for projecting arbitrary, dynamic potentials created using a digital micromirror device. We can engineer exotic band structures by forming and shaking optical lattices. We can even create complex spatiotemporal patterns of the interaction strength between atoms, using a combination of magnetic and optical control of Feshbach resonances. While some features of the ultracold cesium apparatus on which these experiments are performed have been discussed in great detail in previous theses from the lab [81, 162, 75], the purpose of this chapter is to explain the key features required for understanding the experiments in this thesis and to describe the exciting new features and technical improvements made for this thesis work.

In Sec. 2.1 we will review the features of the apparatus which are most important for understanding the experiments discussed in later chapters. The three subsequent sections focus on extensions of pre-existing features of the experiment, specifically the saturated absorption imaging in Sec. 2.2, the use of magnetic Feshbach resonances to induce oscillating interaction strength in Sec. 2.3, and the use of phase-modulated RF to drive the acousto-optic modulators which shake the lattice in Sec. 2.4. In Sec. 2.5 we discuss our implementation of a digital micromirror device in order to project arbitrary potentials for the atoms. This versatile technology serves a valuable role in many of our experiments, particularly for performing Bragg spectroscopy and creating homogeneous gases of arbitrary shapes and sizes. Many other technical improvements are best explained in the context of particular science goals, and we defer those discussions to Secs. 4.3 and 5.3. Finally, the development and demonstration of a new technique for optically controlling Feshbach resonances is discuss in Ch. 6.

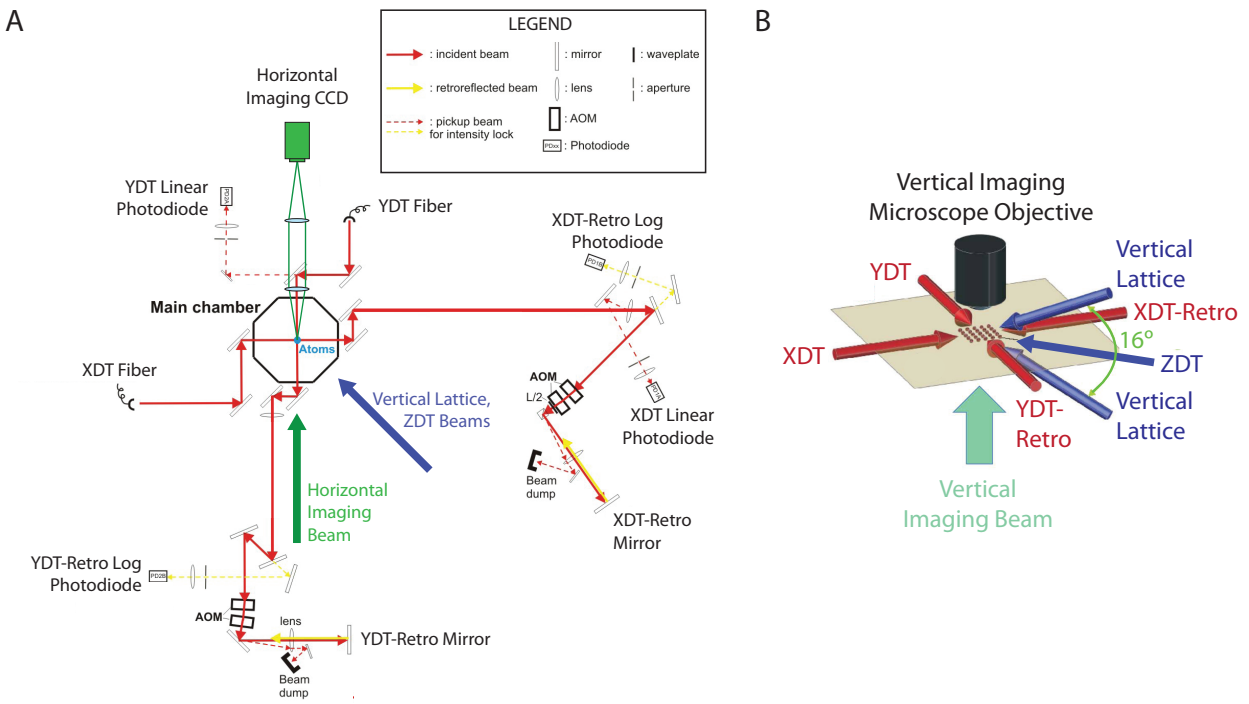

Figure 2.1: A schematic overview of the apparatus. A) A top-down view emphasizing the arrangement of the dipole trap (DT) beams, the corresponding retro-reflection mirrors for forming horizontal lattices, and the horizontal imaging path. B) An isometric view focusing on the arrangement of dipole trapping beams near the atoms. Note that the two beams which form the vertical lattice are separated by 16°. These figures are a modified version of those which originally appeared in Ref. [162].

2.1 General Setup

Almost all of our experiments begin with a standard procedure for laser cooling and evaporating a gas of ^{133}Cs atoms to generate a Bose-Einstein condensate of $30,000 \sim 100,000$ atoms in an elliptical trap [81, 162, 75]. For approximately two seconds we load atoms into a Magneto-Optical trap (MOT), followed by relatively brief periods of compressed MOT, molasses, and degenerate Raman Sideband Cooling (dRSC). Unlike in the original experiment setup [81, 162], the tight lattice in which we perform dRSC is now formed by a laser near-detuned to the D1 transition of Cs. This adjustment was made so that these lattice beams could remain on during imaging (as the beam incident on the vertical camera can be spectrally filtered). However, we have not yet implemented an imaging scheme which in-

volves the presence of the dRSC lattice. After dRSC we employ a roughly six second period of forced evaporation [82], by the end of which the atoms are Bose condensed. Depending on the needs of particular experiments, the evaporation period can be made faster by one or two seconds at the expense of the atom number in the condensate. For example, in general fewer atoms are necessary for experiments in lower dimensions.

There are three primary dipole traps formed from 1064 nm lasers in our experiment, see Fig. 2.1A. The so-called z-axis dipole trap (ZDT) or "light sheet" is a beam with an elliptical intensity profile which provides the primary vertical confinement during the initial loading and evaporation stages of the experiment. Due to its high intensity, ZDT also provides the primary horizontal trapping perpendicular to its propagation direction, causing the density profile of the BEC to be highly elliptical. At 45° on either side of the ZDT beam are the x-axis dipole trap (XDT) and y-axis dipole trap (YDT). These play an important role in capturing atoms for evaporation during the early stages of the experiment and provide (primarily) horizontal trapping to the BEC.

After passing through the main chamber, the XDT and YDT beams can be retro-reflected to form optical lattices. The intensity of each retro-reflected beam is controlled by a pair of acousto-optic modulators, see Fig. 2.1A. When the AOMs are off (that is, the radio-frequency (RF) wave which drives an AOM is not present), there is no retroreflection, but by turning on the AOMs we can turn on the YDT- or XDT-retro beams, which interfere with the main dipole traps to form optical lattices. In this way we can form one-dimensional (1D) or two-dimensional (2D) horizontal optical lattices of spacing $d = 532$ nm whose depth we control by modulating the driving power of the AOMs. See Sec. 2.4 for a discussion of using the RF phase to shift the lattice position. Note that we typically report the depth of the lattice in terms of the recoil energy $E_{\mathrm{R}} = \frac{\hbar^2 k_{\mathrm{L}}^2}{2m} = h \times 1.325$ kHz, where $k_{\mathrm{L}} \equiv 2\pi/\lambda$ is the wavenumber of the laser with wavelength $\lambda = 2d = 1064$ nm, $m = 133$ amu is the mass of a cesium atom and h is Planck's constant.

When we are interested in studying three-dimensional (3D) gases and the elliptical density profile is not an issue, the XDT, YDT, and ZDT beams provide adequate trapping for the BEC; for example, see the experiments described in Ch. 4. These three beams typically form a trap with frequencies $(\omega_{x'}, \omega_{y'}, \omega_z) = 2\pi \times (12, 30, 70)$ Hz, where the axis x' is the propagation axis of ZDT and y' is the perpendicular axis in the horizontal plane. By tuning the power in each beam after evaporation, one can typically tune these values by roughly $\pm 50\%$. However, when adjusting dipole trap powers after the BEC has already formed one must take care not to excite motion of the gas, because collective motion of the superfluid will persist for a very long time and can cause deleterious systematic effects.

If we wish to form effectively two-dimensional gases by using extremely tight vertical confinement, or if we wish to remove ZDT and form circular gases with symmetric horizontal trapping, then we take advantage of the vertical lattice beams, see Fig. 2.1B. These two beams are split vertically from the same source and meet each other in the center of the chamber at a 16° angle to form an optical lattice with a spacing of roughly 3.8 μm along the vertical axis. The vertical confinement from ZDT makes the gas thin enough to fit into a single site of the vertical lattice. By loading the entire gas into a single site of the lattice we form a single "pancake" of atoms. At the maximum intensity of the vertical lattice beams, the vertical trapping frequency is $\omega_z = 2$ kHz, much larger than the typical chemical potentials or temperatures of our gases. Thus, all of the atoms occupy the vertical ground state and the gas is effectively limited to two-dimensions. If we wish to form circular gases without limiting the gas to 2D, we can reduce the intensity of the vertical lattice and compensate by turning on a vertical magnetic field gradient which prevents the atoms from falling out of the trap under the influence of gravity. In this way we can trap the atoms vertically with frequencies as low as $\omega_z = 200$ Hz while avoiding the elliptical horizontal trapping from the ZDT beam.

Another crucial control parameter for our ultracold Bose gases is the magnetic field. The

primary set of magnetic field coils (the "MOT" or "main" field coils) are embedded close to the vacuum chamber, underneath the vertical objective lens. The main coils produce approximately homogeneous fields pointing along the vertical z-axis, as well as the vertical gradients which are often used to levitate the atoms against gravity. Note that a vertical levitation field gradient which cancels gravity is accompanied by weak horizontal magnetic anti-trapping of frequency $2\pi\times 3$ Hz. The offset field is essential for controlling the interaction strength between pairs of atoms, see Sec. 2.3. Because of a carefully tuned pre-emphasis circuit, the main coil magnetic field can be jumped to a new value with a time-constant of roughly 100 μs [81]. Pairs of bias coils are also available along all three axes. The bias coils play a crucial role in setting an appropriate field magnitude and direction for dRSC as well as in positioning the horizontal center of the magnetic antitrapping when a vertical gradient is present.

2.2 Absorption imaging

Essentially all of our experiments conclude with a measurement of the atomic density distribution via absorption imaging. We primarily use the vertical imaging path (Fig. 2.1B), along which we can achieve a large numerical aperture NA=0.5 because the objective lens is only one inch away from the atoms [75]. With perfect elimination of aberrations we could achieve imaging resolution of 1 μm; in reality, aberrations typically limit us to 1.4 μm. The magnification of the vertical imaging is 21.5×, such that each 13 μm pixel on the camera corresponds to 0.605 μm at the atom plane. We use a high intensity imaging beam which saturates the atomic transition so that we can obtain large signals in a short amount of time (before atoms fly out of focus) and faithfully image high density samples. We also have a low resolution horizontal imaging path (Fig. 2.1A) which we use primarily for characterizing the cooling stages of the experiment or for experiments involving very large distances due to a long time-of-flight (TOF). The horizontal imaging has a magnification of 1.2× and a

resolution of 10.8 μm, which is limited by the CCD pixel size.

It is useful to take a brief detour and consider the behavior of a simple, coherent imaging system with a single ideal lens [70]. In an idealized case which neglects diffraction effects (geometric optics) there would be a perfect correspondence between the field distribution of $U_o(\boldsymbol{\xi})$ of the object and that of the image $U_i(\boldsymbol{u})$, satisfying

$$U_i(\boldsymbol{u}) = \frac{1}{|M|} U_o\left(\frac{\boldsymbol{u}}{M}\right)$$

where the magnification of the system $M = -d_i/d_o$ is determined by the distances d_i (d_o) of the image (object) from the lens. In reality, diffraction effects limit the fidelity of the correspondence between the object and image field distributions. Specifically, the image field satisfies,

$$U_i(\boldsymbol{u}) = \int d^2\boldsymbol{\xi} h(\boldsymbol{u} - M\boldsymbol{\xi}) U_o(\boldsymbol{\xi}), \tag{2.1}$$

corresponding to the convolution of the object field with the amplitude spread function $h(\boldsymbol{r})$, which encodes the field distribution on the image plane corresponding to a single point from the object plane. Note that h is often called the point-spread function, but we reserve that for a different (related) quantity below. For an ideal lens, the amplitude spread function depends only on the aperture size of the lens. Ignoring phase factors which do not affect the intensity distribution of the image and assuming shift invariance of the system, the amplitude-spread function is the Fourier transform of the pupil function $P(\boldsymbol{k})$,

$$h(\boldsymbol{r}) = -\frac{M}{4\pi^2} \int d^2\boldsymbol{k} P(\boldsymbol{k}) e^{-i\boldsymbol{r}\cdot\boldsymbol{k}}.$$

An ideal lens of radius R has a pupil function

$$P(\boldsymbol{k}) = \begin{cases} 1 & k \leq k_{max} \\ 0 & k > k_{max} \end{cases}$$

where the cutoff $k_{max} \equiv \frac{2\pi}{\lambda d_i} R$ is determined by the lens aperture. Based on the convolution theorem, we find a very simple interpretation of Eqn. 2.1 in Fourier space,

$$\tilde{U}_i(\boldsymbol{k}) \propto P(\boldsymbol{k}) \tilde{U}_o(M\boldsymbol{k}) \tag{2.2}$$

where the image field amplitude at a particular wavevector is simply the object amplitude multiplied by the Pupil function (after appropriately accounting for the magnification). For the ideal lens, the image field is simply a magnified version of the object field with all features beyond the cutoff wavevector removed.

The essential difference between a realistic imaging system and the ideal lens above is the form of the pupil function $P(\boldsymbol{k})$. Generally, there is still a cutoff k_{max} set by the smallest aperture along the optical axis. However, the phase and amplitude of the pupil function will also vary across the aperture as a result of the aberrations due to realistic (imperfect) optical elements and misalignments. For example, consider the pupil function of the imaging system in our apparatus. In scaled polar coordinates ($\rho \equiv \frac{k}{k_{max}}$) one can write the pupil function as $P(\rho, \theta) = T(\rho, \theta) e^{i\Theta(\rho,\theta)}$ in terms of its amplitude and phase. We generally model the transmittance function as $T(\rho, \theta) = H(1-\rho) e^{-\rho^2/\tau^2}$. Moreover, including spherical aberration of strength S_0, astigmatism of strength α and angle ϕ, and defocusing of strength β, one can write the phase term as $\Theta(\rho, \theta) = S_0\rho^4 + \alpha\rho^2 cos(2\theta - 2\phi) + \beta\rho^2$. Nonzero aberrations and attenuation within the aperture distort and generally broaden the corresponding amplitude spread function, limiting the fidelity of the imaging system.

In our experiment we use strong saturation absorption imaging to detect the atomic density distribution [130, 83]. In this scheme the atoms are illuminated with a resonant beam whose intensity $I \gg I_{\rm sat}$ is much greater than the saturation intensity $I_{\rm sat}$ of the atomic transition. We use a CCD to measure the intensity distribution in the image plane $I_i(\boldsymbol{u}) = |U_i(\boldsymbol{u})|^2$ with ($I_{\rm out}$) and without ($I_{\rm in}$) the atoms. We extract the measured density distribution $n_{\rm meas}$ based on the modified Beer-Lambert law,

$$n_{\rm meas}(\boldsymbol{x})\sigma_0 = -\ln \frac{I_{\rm out}(\boldsymbol{x})}{I_{\rm in}(\boldsymbol{x})} + \frac{I_{\rm in}(\boldsymbol{x}) - I_{\rm out}(\boldsymbol{x})}{I_{\rm sat}}, \tag{2.3}$$

where σ_0 is the resonant cross section. For absorption imaging with a strong imaging beam, the intensity profile of the image is primarily determined by the interference of the dark field scattered by the atoms with the strong imaging beam, as long as the scattered field is not too large compared to the field of the imaging beam (equivalently, the linear term dominates, $I_{\rm out}/I_{\rm in} \ll 1$). In this approximation, the measured atomic density is the convolution of the true density $n(\boldsymbol{x})$ with the point spread function $\mathcal{P}(\boldsymbol{x})$,

$$n_{\rm meas}(\boldsymbol{x}) \equiv \int d\boldsymbol{x}' n(\boldsymbol{x}')\mathcal{P}(\boldsymbol{x} - \boldsymbol{x}'). \tag{2.4}$$

The point spread function $\mathcal{P}(\boldsymbol{x}) = \mathcal{R}(h(\boldsymbol{x}))$ is the real part of the amplitude spread function. Note that the breakdown of this approximation may lead to artifacts which distort the apparent atomic distribution for high optical densities.

We typically characterize the imaging system by measuring the modulation transfer function (MTF) $M(k) = |\tilde{\mathcal{P}}(k)|$ which is the absolute value of the fourier transform of the point spread function [75, 83]. We typically extract the MTF from a measurement of the fluctuation power spectrum of a thermal gas, using the relationship,

$$\langle |\delta n_{\rm meas}(k)|^2 \rangle = NS(k)M^2(k), \tag{2.5}$$

where N is the particle number and $S(k)$ is the structure factor. At sufficiently large temperatures, we can approximate the structure factor of the thermal gas as a constant $S(k) = 1$. Therefore, the modulation transfer function is directly proportional to the measured power spectrum and can be extracted based on the equation above.

Characterizing our imaging system yields many benefits. First of all, by measuring the MTF we obtain clear feedback by which to optimize the objective alignment and maximize the imaging resolution. However, even with perfectly optimized alignment, we are still often interested in features of our gases at length scales comparable to the resolution. If the key features being measured are even of the same order of magnitude as the resolution limit, then one must account for the point spread function in order to obtain quantitatively reliable results. This fact is especially true when measuring scaling exponents for the dependence of a length scale on some parameter, since the systematic shift from the resolution is nonlinear and will thereby distort the scaling exponent. We take the point spread function into account when analyzing the scaling of spin correlations in the shaken lattice (see Sec. 4.3.4) and the width of jets in Bose Fireworks (see Sec. 5.3).

Finally, a few words of caution. There are a few, slightly different approaches to both the theory and practice of imaging. Therefore some of the definitions and results here may not be entirely standard. So, when reading, look for the mathematical definitions and think carefully before proceeding.

2.3 Controlling interactions with magnetic Feshbach resonances

The interaction strength between ultracold atoms is typically parameterized by the s-wave scattering length a. In many cases, the scattering length can be thought of as controlling the collision cross section, which is

$$\sigma = 8\pi a^2 \tag{2.6}$$

for pairs of identical bosons. Moreover, since the atoms undergo pure s-wave scattering, the low energy and long wavelength physics can be understood by approximating the interaction between atoms using the Fermi pseudo-potential [122],

$$V(\boldsymbol{r}) \equiv g\delta(\boldsymbol{r}), \tag{2.7}$$

where $\delta(\boldsymbol{r})$ is the Dirac delta function and we have defined the interaction strength

$$g \equiv \frac{4\pi\hbar^2 a}{m}. \tag{2.8}$$

In this convenient approximation we can write the interaction energy of the gas in second-quantized form as simply,

$$H_{\text{int}} = \frac{g}{2}\int d\boldsymbol{r}\psi^\dagger(\boldsymbol{r})\psi^\dagger(\boldsymbol{r})\psi(\boldsymbol{r})\psi(\boldsymbol{r}) \tag{2.9}$$

for field operator $\psi(\boldsymbol{r})$. In the mean-field approximation which is generally appropriate for weakly-interacting, dilute BECs, the interaction energy density is simply $\epsilon_{\text{int}}(\boldsymbol{r}) = g\frac{n(\boldsymbol{r})^2}{2}$ for a gas with density $n(\boldsymbol{r})$. Notably, when the scattering length is negative the energy is also negative, and the interactions are effectively attractive.

One of the most remarkable features of ultracold atomic gases is the possibility to tune the scattering length using Feshbach resonances [36]. Simply by varying the magnetic field near a magnetic Feshbach resonance (MFR) the scattering length can be made as large or small as desired and even flipped from positive to negative. Among their many groundbreaking applications, MFRs enabled Bose-Einstein condensation of atomic species like ^{85}Rb [54] and ^{133}Cs [152]. Indeed, without MFR it would not be possible to form cesium BECs at all due to the enormous background scattering length. MFR also enabled the formation of ultracold molecules [37, 72, 88], exploration of the BEC-Bardeen Cooper Schrieffer crossover [129, 171, 16], and tests of Efimov physics [93].

A Feshbach resonance arises when a low-energy bound state in a different scattering channel approaches the scattering threshold of the free atoms. Near the field B_0 at which the bound state and scattering threshold meet, the scattering length takes the form [36],

$$a(B) = a_{\mathrm{bg}}\left(1 - \frac{\Delta}{B - B_0}\right) \tag{2.10}$$

where B is the magnetic field, a_{bg} is the scattering length far from resonance and Δ is the width of the resonance.

We make frequent use of MFR in this experiment. Most notably, as a result of a broad $\Delta = 28.7$ G Feshbach resonance at $B_0 = -11.7$ G (where the direction of the magnetic field is defined by the requirement that the atoms are in the absolute ground state $|F, m_F\rangle = |3, 3\rangle$ for positive fields) and a background scattering length of 1720 a_0, the Cs scattering length for small fields is extremely large and negative $a \approx -2400\ a_0$. Both the three-body loss rate which scales as a^4 and the collapse of BECs with negative scattering lengths [54] make it impossible to form a stable BEC under those conditions, which is a major reason why Cs was the last of the stable alkali atoms to be Bose-Einstein condensed [152]. At the end of dRSC we typically set the magnetic field to 20.8 G such that the scattering length is moderate and positive $a = 210\ a_0$ during evaporation. This choice is optimal because it is positive to prevent collapse, sufficiently large to yield a reasonable collision rate for thermalization during the evaporation stage, and corresponds to a local minimum of the three-body loss rate due to the Efimov effect [93]. Another common use of MFR is during time-of-flight (TOF) experiments. There, we set the scattering length to $a = 0$ immediately after releasing the atoms from the trap, such that interactions do not distort the momentum distribution during the TOF.

In this thesis we also introduce some new uses of MFR, including the use of an oscillating scattering length to induce Bose Fireworks (see Ch. 5). To induce oscillating scattering lengths at frequencies comparable to the bandwidth of the main coils, we must first calibrate

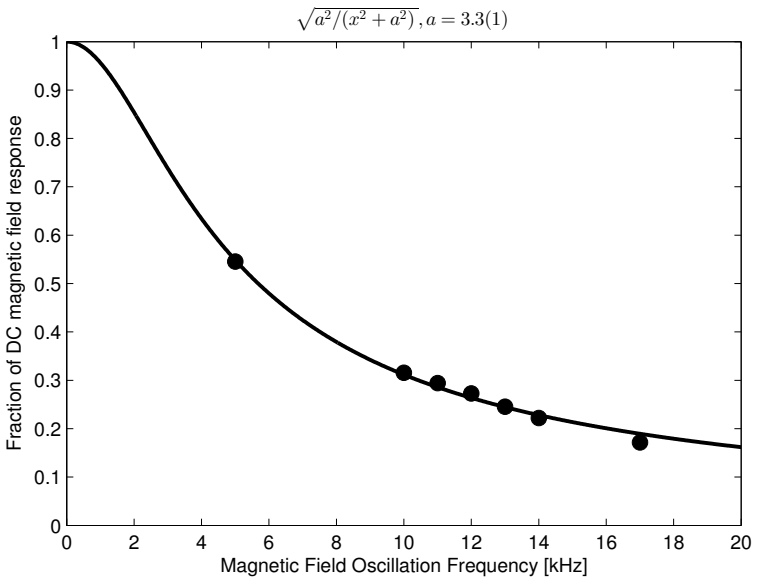

Figure 2.2: A plot of the amplitude $B_{\mathrm{AC}}(f)$ of the oscillating magnetic field relative to its DC amplitude B_{DC} for the same driving amplitude. The magnetic field response follows $B_{\mathrm{AC}}(f)/B_{\mathrm{DC}} = \sqrt{f_0^2/(f^2+f_0^2)}$ where $f_0 = 3.3(1)$ kHz is the -3 dB bandwidth of the power in the oscillating field.

the magnitude of the oscillating field at the atoms as a function of the frequency of the current driving the coils. Attenuation at high frequencies results from the inductance of the coils and eddy currents. We can calibrate the response by taking advantage of the extremely rapid three-body loss which occurs near the narrow Feshbach resonance at 19.84 G [36]. We begin by shifting the DC magnetic field to be $\Delta B = 500$ mG away from the narrow resonance. Then, starting at small modulation amplitudes where the BEC has a long lifetime, we increase the amplitude until we suddenly observe rapid loss of the BEC. The onset of loss indicates that the oscillation amplitude has exceeded ΔB such that the atoms spend time near 19.84 G. The magnitude of the field response extracted from such a measurement is shown in Fig. 2.2.

While MFR is an extremely powerful technique, its spatial and temporal resolution tend to be limited by the size of practical magnetic field coils. In Ch. 6 we discuss our development of a new technique for spatiotemporally controlling interactions by using a laser to optically

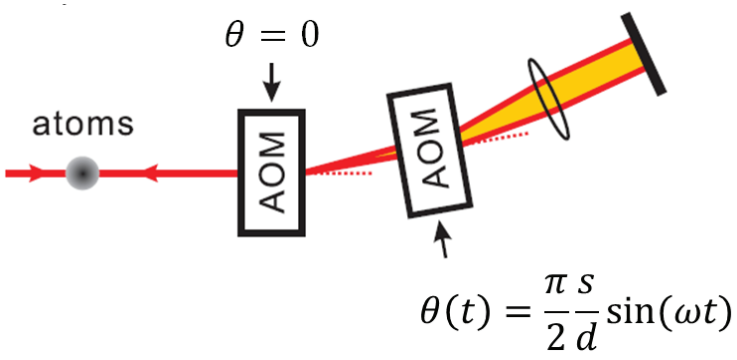

Figure 2.3: Lattice shaking via phase modulation of an acousto-optic modulator (AOM). Along both the x- and y-axes, an optical lattice with spacing $d = 532$ nm is formed by retroreflecting the dipole trapping laser. Two AOMs in the path enable depth and position control of the lattice. Specifically, we use the -1 diffraction order of one AOM and the $+1$ order of the second AOM, such that the frequency shifts from the two AOMs cancel each other. Phase modulating the RF which drives the second AOM by $\theta_2(t) = \frac{\pi}{2}\frac{s}{d}\sin(\omega t)$ directly shifts the phase of the diffracted beam, such that the retroreflection picks up a phase of $2\theta_2(t)$ after passing that AOM twice. This results in oscillation of the optical lattice position as $\Delta x = \frac{s}{2}\sin(\omega t)$ for peak-to-peak shaking amplitude s.

control a Feshbach resonance.

2.4 Shaken optical lattices

Shaking optical lattices can be used to engineer effective band structures with desirable properties, as discussed in Ch. 3. We shake the lattice by phase modulating the RF used to drive one of the AOMs, see Fig. 2.3. The n'th diffracted order from an AOM is phase shifted by $n\phi(t)$ with respect to the 0'th order, where $\phi(t) = ft + \theta(t)$ is the phase of the acoustic wave in the AOM crystal with RF drive carrier frequency f and RF phase modulation $\theta(t)$. In our setup, the final retroreflected beam has been diffracted twice as the -1 order of the first AOM and twice as the $+1$ order of the second AOM. The total resulting phase shift of the beam is $\Delta\theta(t) = 2(f_2 t + \theta_2(t) - f_1 t - \theta_1(t))$. We set the carrier frequencies $f_1 = f_2$ to be equal, and don't phase modulate the first AOM. We phase modulate the second AOM as $\theta_2(t) = \frac{\pi}{2}\frac{s}{d}\sin(\omega t)$ which leads to a total phase shift $\Delta\theta(t) = \pi\frac{s}{d}\sin(\omega t)$ and therefore a

periodic translation of the lattice position by $\frac{s}{2}\sin(\omega t)$. Note that the absolute position of the lattice can drift slowly over time since the total optical path length is extremely sensitive to thermal drifts. However, since we do not resolve individual lattice sites the absolute position of the lattice is not important.

When performing shaking experiments we make two key adjustments to experimental parameters to minimize the effects of heating (see Sec. 3.1.3). Here, heating primarily corresponds to scattering events in which pairs of atoms collide and absorb at least one quantum of energy $\hbar\omega$ (often called a "photon" in the literature) from the shaking. First, since the rate of such collisions scales as a^2 [38, 40, 39] we typically reduce the heating rate by using a scattering length $a = 40\ a_0$, much smaller than the scattering length $a = 210\ a_0$ used during evaporation. Note that, for reasonable shaking amplitudes, it is certainly still possible to work at larger scattering lengths as demonstrated in Sec. 4.4.5. A second valuable step is to ensure that the vertical trap depth is sufficiently small to allow high energy atoms to escape the trap. This constant "evaporation" allows atoms which undergo heating collisions to leave without further disturbing the remaining atoms.

A number of other technical improvements related to the shaken lattice setup are presented in Ch. 4 in the context of studying critical dynamics.

2.5 Arbitrary potentials with a digital micromirror device

Digital micromirror devices (DMDs), most commonly used in commercial projectors, are becoming an extremely popular tool for shaping beams in cold atom experiments [104, 154, 76, 167, 67, 95, 80]. The DMD is an array of small mirrors, 7.6 μm across in the DLP3000 chip that we use. Each mirror can be independently programmed to orient at either the "on-state" angle or the"off-state" angle, which are typically separated by 24°. Generally, one shines light on the DMD from an angle such that outgoing light from the on-state mirrors is perpendicular to the array while outgoing light from off-state mirrors leaves at a large angle

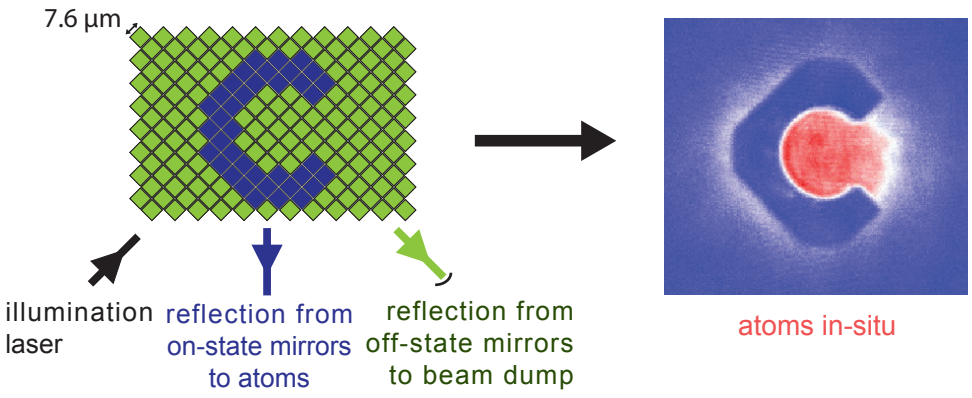

Figure 2.4: Illustration of creating arbitrary potentials with a digital micromirror device. A laser reflecting off of the digital micromirror device (left) becomes patterned depending on which mirrors are at the "on-state" angle (blue) or the "off-state" angle (green). The real device has many more mirrors (415,872) than are depicted in this illustration. We image the patterned, blue-detuned laser onto the atom plane, creating a repulsive potential proportional to the laser intensity. In the example shown (right) the atoms (red) in an otherwise harmonic trap are repelled from the C-shaped, blue-detuned laser.

and can be blocked. The large number of mirrors, 608×684 for DLP3000, enables precise control of the intensity profile of the reflected light. Moreover, the pattern can be rapidly changed (4 kHz for DLP3000) in order to create time-dependent intensity profiles.

In our lab we use the DMD to create arbitrary potentials for the atoms by shaping a blue-detuned laser (the "DMD laser") with wavelength 788 nm to create repulsive potentials corresponding to the distribution of on-state mirrors, see Fig. 2.4. To achieve this effect we image the blue laser pattern at the DMD plane onto the atom plane using the high-resolution vertical objective, as shown in Fig. 2.5. First, a non-polarizing beamsplitter cube combines the DMD laser with a second gaussian beam, which is available for flattening the curvature of the normal dipole traps but is typically not used. Just before the eyepiece lens, the DMD laser is reflected from a steering mirror (Optics in Motion OIM 101) which can be used to fine-tune the position of the DMD potential relative to the atoms. After the eyepiece lens the laser transmits through a dichroic mirror (Thorlabs DMSP805) which enables us to simultaneously use the high-resolution objective lens for pattern projection at

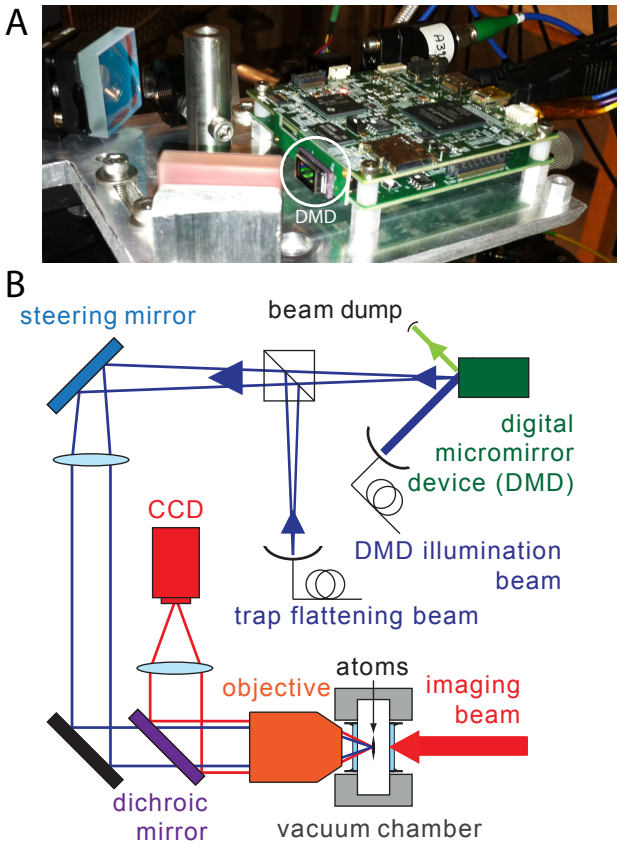

Figure 2.5: Setup of the DMD in our apparatus. (**A**) A photograph of the DMD and its electronic control boards mounted with the fiber and mirrors used to illuminate it. (**B**) A schematic of the DMD as it is arranged in our apparatus.

a wavelength of 788 nm and imaging at 852 nm. Overall, the projection optics achieve a total demagnification of 36× such that the 7.6 μm pitch of the DMD mirrors corresponds to a distance of 0.21 μm in the atom plane.

It is often useful to create optical lattices using the DMD. When the DMD pattern encodes a lattice structure, in whichs the density of on-state mirrors varies periodically across the array, the reflected laser is diffracted from the lattice into many orders, see Fig 2.6. With no aberrations these beams would interfere on the atoms to match the original intensity pattern on the DMD, but aberrations change the relative phase between the different orders and severely alter the resulting intensity pattern. By using a beam-selection mask in a Fourier

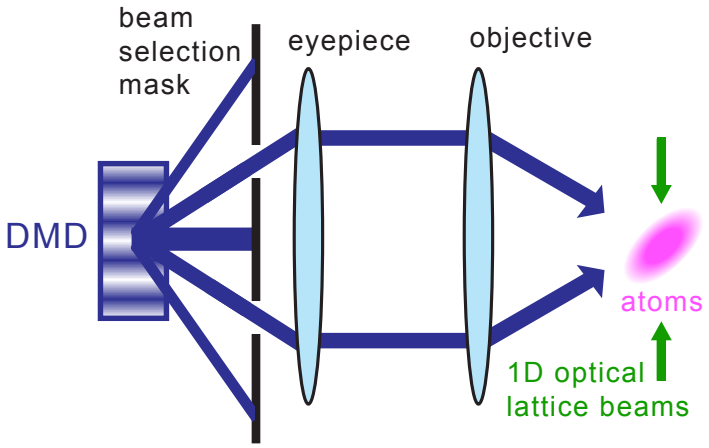

Figure 2.6: Beam blocking scheme for creating clean DMD lattices in the presence of aberrations. When forming 1D lattice patterns using the DMD, we place a beam-selection mask in a Fourier plane along the optical path of the DMD projection which transmits only the two desired diffraction orders. Aberrations still cause a phase shift between the two remaining beams, but can only affect the position of the resulting lattice and not its depth or spacing.

plane we block all but two of the diffracted beams. Phase shifts between the two remaining beams can affect the position of the resulting lattice but not its depth or spacing. Therefore, blocking the undesired beams is very useful for creating DMD optical lattices which are not significantly affected by any residual aberrations. A similar approach is effective for 2D lattices from the DMD: the lattice potential from any three non-collinear beams will not change as a result of aberrations, except for an overall translation.

Presently, our DMD projection suffers from aberrations. We characterize the aberrations via the phase profile $\Theta(\boldsymbol{k})$ of the pupil function $P(\boldsymbol{k})$ of the DMD projection, see Fig. 2.7. In an ideal imaging system, the phase is uniform across the pupil function and as a result one achieves the narrowest possible point spread function. To extract the phases of the experimental pupil function, we begin by projecting clean DMD lattices composed of the interference between the zeroth order beam and a first order beam of various wavevectors and angles. In each case the center position of the programmed lattice pattern is the same. While the phase of the zeroth order beam is fixed, each first order beam gets a phase shift

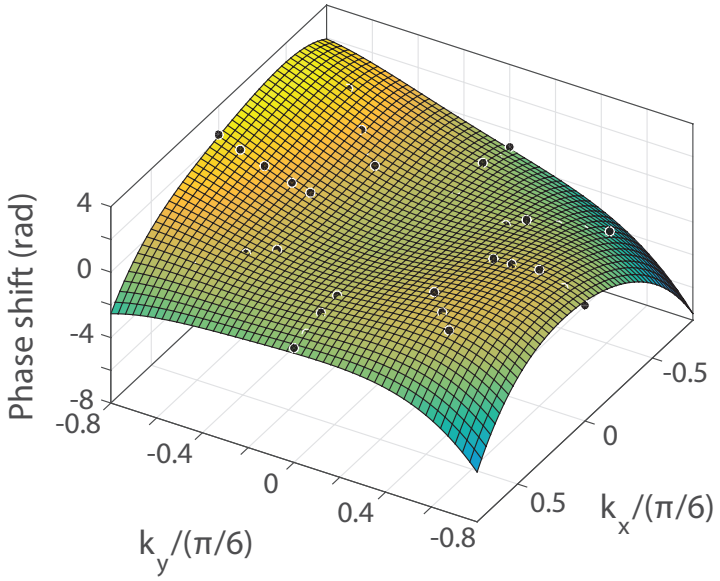

Figure 2.7: Measurement of aberrations in the DMD projection. The phase shifts $\Theta(\boldsymbol{k})$ (circles) at various locations across the pupil of the DMD projection optical path. Phase shifts are detected by creating lattice patterns on the DMD and measuring the position of the resulting lattice on the atom plane relative to its expected position based on the DMD pattern.

$\Theta(\boldsymbol{k})$ depending on its wavevector as it passes through the projection system (Eqn. 2.2). When the two beams interfere on the atoms, the position of the lattice potential will be shifted by $\lambda_{\mathrm{lat}}\Theta(\boldsymbol{k})/2\pi$ where λ_{lat} is the wavelength of the interference. By measuring the density profile of atoms loaded into many of these DMD lattices we can determine the shift of each lattice and thus the phases $\Theta(\boldsymbol{k})$ which characterize the aberrations. Future users of the system may wish to implement a phase plate or adaptive optics in order to compensate the phase shifts and thereby remove the aberrations. For now, our primary applications of the DMD (discussed in the next sub-section) are effective even in the presence of these small aberrations. Another intriguing alternative is to work with the DMD in a Fourier plane, where one can sacrifice laser power in order to cancel aberrations and create very precise potentials [167].

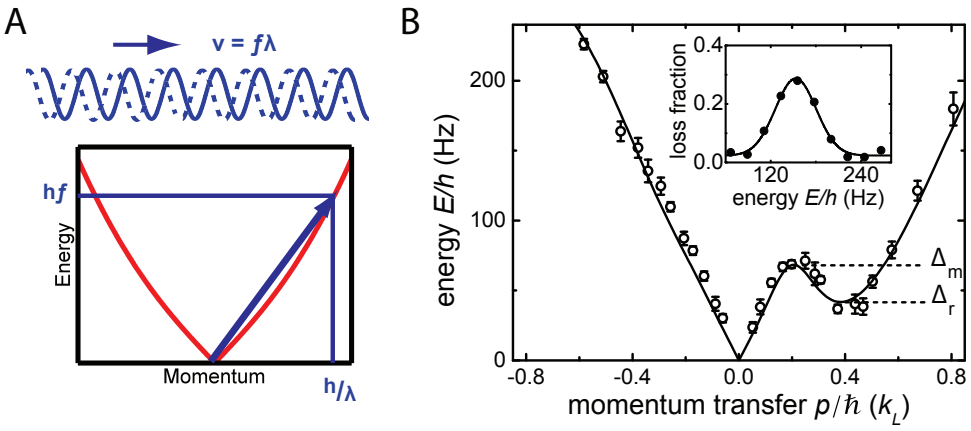

Figure 2.8: Measuring roton-maxon dispersion by using a DMD to perform Bragg spectroscopy. (A) An illustration of the scheme for Bragg spectroscopy. DMD lattices of wavelength λ moving at a speed v strongly excite the gas when they are on resonance with the quasiparticle spectrum. (B) The excitation spectrum for BECs in the shaken optical lattice, which have a roton-maxon dispersion relation, measured using moving DMD lattices [76].

2.5.1 Dynamic potentials

Many powerful applications of the DMD involve creating dynamic potentials by cycling through a series of DMD patterns during the experiment. The built-in control electronics for the DLP Lightcrafter 3000 are designed to store up to 96 patterns and can be externally triggered to switch to the next pattern at rates up to 4 kHz. More expensive devices can have switching rates nearly 10 times faster. For most applications one wants to create smooth changes in the potential; the desired smooth motion is best approximated by using a series of patterns in which each pattern creates a potential which is only slightly different from the previous one. The maximum number of patterns and switching rate limit the smoothness. However, in many cases the response of the atoms to changes in the potential is sufficiently slow that the difference between the series of discrete jumps and the desired smooth evolution can be ignored. For example, see the discussion of aliasing in Bragg spectroscopy below.

Our first application of dynamic DMD potentials was the use of moving DMD lattices to perform Bragg spectroscopy, as illustrated in Fig. 2.8 [76]. In Bragg spectroscopy the dispersion relation for small excitations of the gas is measured by looking for resonances in

the response of the atoms to moving potentials with a well-defined wavelength (momentum) and frequency (energy) [118]. To perform Bragg spectroscopy with the DMD we program a series of optical lattice patterns with the same wavelength but with each lattice slightly displaced from the previous one. The series is cyclic, returning to the first pattern each time the lattice position has shifted by one complete wavelength. The excitation energy imparted by the moving lattice hf depends on the frequency f at which the DMD cycles through the full set of patterns, and the momentum h/λ corresponds to the wavelength λ of the lattice. We typically use sets of 9 lattice patterns, so that each pattern switch corresponds to a lattice phase shift of $2\pi/9$. To better smooth the motion, especially for long wavelengths, one can increase the number of patterns involved. The dispersion relation shown in Fig. 2.8 corresponds to the points in wavevector and frequency space at which we observe resonant heating of the atom cloud. We determine those points by probing the atomic sample at a fixed wavevector and scanning the DMD triggering frequency. For the experiments corresponding to Fig. 2.8B we applied the exciting optical potential to the cloud for 40 ms, then performed 30 ms TOF to determine the number of atoms remaining in the condensate. Note that we also implemented a closely related technique with a moving speckle potential to measure the critical velocity in the same work [76].

It is worth noting that our approach to Bragg spectroscopy with the DMD maps directly onto the usual approach, using the interference of two beams whose relative angle defines the wavelength and whose frequency difference defines the imparted energy, when we use the beam blocking scheme shown in Fig. 2.6. The wavelength of the programmed lattice determines the angle between the diffracted beams, and the motion of the programmed lattice effectively creates a frequency difference between the beams. The major advantage of our approach to Bragg spectroscopy lies in the ease of varying the wavelength and frequency over a wide range simply by reprogramming the DMD. The disadvantage to generating the beams with the DMD is aliasing; the discrete jumps between the DMD lattice patterns also

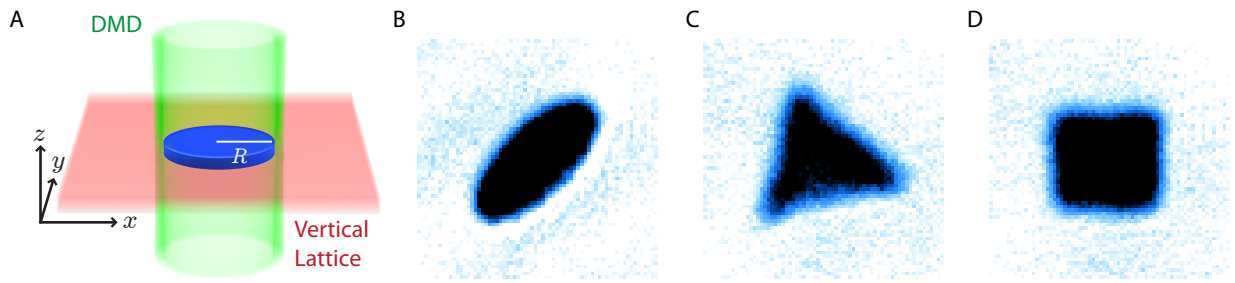

Figure 2.9: Forming homogeneous gases of arbitrary shape using DMD compression. (A) In this trapping configuration, the vertical lattice (red) and a magnetic field gradient along the z-axis are used to provide tight vertical confinement without significant horizontal confinement. The only potential in the horizontal plane is provided by a repulsive DMD boundary (green). In the end we obtain a thin disk-shaped BEC (blue) of controllable radius R. We can change the shape of the DMD boundary to create homogeneous gases of arbitrary shapes. Example images from experiments show homogeneous elliptical (B), triangular (C), and square (D) BECs.

create higher harmonics in the frequency difference between the beams. If the sequence includes N patterns, then in addition to the desired excitation at f there will also excitation at Nf, $2Nf$, etc. Generally, even within the constraints of the DMD these higher harmonics can easily be made both very small and very far off-resonant, and therefore negligible.

Our second major application of dynamic DMD potentials is the creation of homogeneous gases of arbitrary size and shape, see Fig. 2.9. After the normal evaporation sequence, our gas is in an elliptical harmonic trap dominated by the ZDT beam. Here, we use the combination of magnetic gradient levitation and the vertical lattice to provide all of the vertical confinement without creating significant horizontal confinement. Then, we can turn off the XDT, YDT, and ZDT beams such that the gas is essentially free horizontally, except for a hard repulsive boundary created by the DMD. In order to ensure that the entire gas is confined, we start with a DMD boundary which is large compared to the original gas, and later use pattern switching to shrink the boundary and thus compress the gas to the desired size and shape.

Our typical procedure for creating homogeneous gases of arbitrary size and shape is as

follows. First, we project a DMD potential which is zero everywhere except for a hard "wall" or boundary, which at this stage is larger than the initial BEC. We then turn on the vertical lattice and levitation gradient, such that the ZDT trap is not necessary for vertical confinement. We then switch the DMD once through a series of 40 patterns, which shrink the DMD boundary down to the desired final size, in steps of roughly 200 nm every 2 ms. Subsequently we slowly turn off the XDT, YDT, and ZDT beams, so that the BEC expands to homogeneously fill the boundary set by the DMD potential. In the end, the trap consists only of the vertical lattice, the magnetic field gradient, and the DMD boundary, as shown in Fig. 2.9A. Note that the homogeneity of the sample breaks down at the edge due to the finite resolution of the projected DMD potential.

Not only does this technique enable us to create homogeneous gases, but it allows us to control both the shape and size of the gas. For example, elliptical, triangular, and square samples created in this way are shown in Fig. 2.9B-D. In Ch. 5 the use of circular, homogeneous samples enables us to make a quantitative comparison between our results and theory. Furthermore, we use this technique to test the effect of the size of the disk on the width of the emitted jets, as shown in Fig. 5.17.

One disadvantage of this trap configuration is that we cannot easily create an optical lattice because we have turned off the XDT and YDT dipole traps. Turning these trapping beams back on would disturb the homogeneity of the sample. However, it may actually be possible to turn on lattices in which the incident and retro-reflected beams have the same intensity, which minimizes the strength of the harmonic trapping for a given lattice depth. The resulting trap potential in the region within the DMD boundary shouldn't be relevant as long as it is small compared to the chemical potential of the sample. Depending on the details of the desired application, one could in principle turn on at least a weak optical lattice and still treat the sample as effectively homogeneous.

CHAPTER 3

BOSONS IN SHAKEN OPTICAL LATTICES

Driven optical lattices provide exciting opportunities for engineering interesting Hamiltonians in atomic quantum gases [68, 105, 58]. Groundbreaking examples include dynamical control of tunneling to drive the superfluid to Mott insulator transition [161], the simulation of frustrated magnetism [142], the creation of artificial gauge fields [4, 143, 3, 112], and the realization of topological band structures [89].

In the Chin lab we have developed a powerful new approach to creating desirable band structures with shaken lattices: by shaking the lattice at frequencies slightly large than a band gap we strongly couple two or more bands [119, 164, 76, 42, 106, 7, 62]. In this chapter we discuss the the theoretical background and early experiments on bosons in this near-detuned shaken lattice. First, in Sec. 3.1 we explain Floquet theory, which describes some powerful, generic features of systems with periodic Hamiltonians. We then apply Floquet theory to calculate the effective band structure for single particles in the near-detuned shaken lattice. Next, in Sec. 3.2 we explain the effectively ferromagnetic quantum phase transition which arises for repulsively interacting bosons in the shaken lattice; this phase transition is the platform for our study of critical dynamics in Ch. 4. In Sec. 3.3 we discuss the influence of micromotion on the interaction energy which has enormous consequences for the experiments discussed in Sec. 7.1. Finally, in Sec. 3.4 we briefly mention our work on understanding the nature of the domain walls which appear in the ferromagnetic phase.

3.1 Floquet theory for atoms in shaken optical lattices

A crucial starting point for understanding the behavior of atoms in the one-dimensional shaken lattice is to calculate the single-particle steady-states and the corresponding energy spectrum. With a time-independent Hamiltonian the best approach is usually to diagonalize

the Hamiltonian, obtaining eigenstates whose time evolution is a simple phase winding at a rate proportional to the corresponding eigenvalue (energy). However, time-dependent Hamiltonians do not have any true eigenstates - an eigenstate at a time t_1 will not generally remain an eigenstate at a later time t_2. Therefore, we need a different approach to handle the time-dependent Hamiltonian for each atom in the shaken lattice,

$$H(t) = -\frac{\hbar^2}{2m}\frac{\partial^2}{\partial x^2} + U_0 \sin^2\left(k_{\mathrm{L}}[x - x_0(t)]\right) \tag{3.1}$$

where U_0 is the lattice depth, k_{L} is the wavevector at the band edge $k_{\mathrm{L}} = \frac{\pi}{d}$ for lattice spacing d, and $x_0(t)$ is the time-dependent offset of the lattice position. Note that we generally perform sinusoidal shaking (Sec. 2.4) such that $x_0(t) = \frac{s}{2}\sin(\omega t)$ where s is the peak-to-peak shaking amplitude.

A great tutorial for understanding the concepts in this section can be found in Ref. [79], and a wider review of experiments and theories in this area is found in Ref. [58].

3.1.1 Two-Band Approximation

We can gain valuable intuition by using a band hybridization model of the shaken lattice [75, 106]. Assuming that the amplitude is small ($k_{\mathrm{L}}s \ll 1$) we can expand the Hamiltonian as $H(t) = H_0 + H'(t)$ where H_0 is the static Hamiltonian for a stationary lattice of depth U_0 and $H'(t) \approx -\frac{k_{\mathrm{L}}sU_0}{2}\sin(2k_{\mathrm{L}}x)\sin(\omega t)$ is a time-dependent perturbation due to the lattice shaking. The static lattice Hamiltonian has the usual band structure familiar from condensed matter physics [13]: the energy eigenstates $|\Psi_n(q)\rangle$ form bands $E_n(q)$ where n is the band index and the quasimomentum q is within the Brillouin zone $-q_{\mathrm{L}} < q \leq q_{\mathrm{L}}$ with $q_{\mathrm{L}} = \hbar k_{\mathrm{L}}$.

Because we shake the lattice at a frequency just slightly greater than the band gap $E_2(0) - E_1(0)$ at $q = 0$ (motivating the term "blue-detuned" shaking), the time-dependent perturbation $H'(t)$ will primarily lead to coupling between the first two bands, see Fig. 3.1. In a sufficiently deep lattice the Bloch waves look very similar to harmonic oscillator states

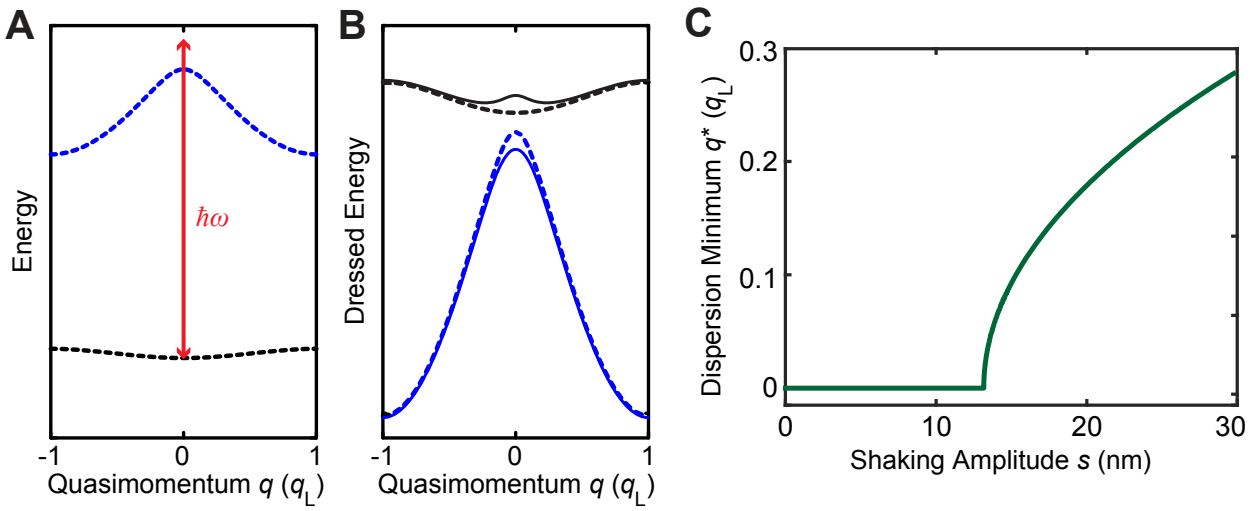

Figure 3.1: Band structure of atoms in the shaken optical lattice. (**A**) An illustration shows how shaking the lattice at a frequency ω slightly greater than the band gap at $q = 0$ couples the ground band $E_1(q)$ (black dashed curve) to the first excited band $E_2(q)$ (blue dashed curve). The lattice momentum is $q_{\mathrm{L}} = h/\lambda$ where $\lambda = 1064$ nm is the wavelength of the lattice laser. (**B**) In a dressed picture the coupling leads to level repulsion between the bands which results in the effective ground $\epsilon_1(q)$ (solid black) and excited $\epsilon_2(q)$ (solid blue) bands. With sufficient shaking amplitude the effective ground band develops a double well with minima at $q = \pm q^*$. (**C**) The effective ground band minimum q^* is calculated from the Floquet theory based on our experimental parameters. Above the critical point $s > s_c$, q^* closely follows the threshold law $q^* \propto (s - s_c)^{1/2}$ in the plotted range.

within each lattice site, and therefore we can approximate the coupling matrix element as $\langle \psi_2(q)| H'(t) |\psi_1(q)\rangle \approx -k_{\mathrm{L}} s U_0 \left(\frac{\hbar^2 k_{\mathrm{L}}^2}{8 U_0 m}\right)^{1/4} \sin(\omega t) \equiv -W \sin(\omega t)$ which defines the coupling strength W. For example, under typical conditions ($U_0 = 8.86\ E_{\mathrm{R}}$, $s = 32$ nm, $d = 532$ nm) we find $W = h \times 120$ Hz. With this matrix element we can approximate the full Hamiltonian using a two band model,

$$H_{2b} = \begin{pmatrix} E_1(q) & -W \sin(\omega t) \\ -W \sin(\omega t) & E_2(q) \end{pmatrix}. \tag{3.2}$$

To further simplify the Hamiltonian we transform into a rotating frame where $|\psi_2(q)'\rangle = e^{-i\omega t} |\psi_2(q)\rangle$. In this frame we can perform the rotating wave approximation, dropping terms which have rapidly oscillating phases to obtain the time-independent Hamiltonian

$$H_{\mathrm{RWA}} = \begin{pmatrix} E_1(q) & W/2 \\ W/2 & E_2(q) - \hbar\omega \end{pmatrix}. \tag{3.3}$$

We can diagonalize this Hamiltonian to obtain the energies of the eigenstates in the rotating frame,

$$\epsilon_{\pm}(q) = E_1(q) + \frac{\hbar\delta(q)}{2} \pm \frac{\sqrt{\hbar^2\delta(q)^2 + W^2}}{2} \tag{3.4}$$

where $\delta(q) = E_2(q)/\hbar - E_1(q)/\hbar - \omega$ is the quasimomentum-dependent detuning of the shaking from resonantly coupling the two bands. In essence, the near-resonant coupling between the first two bands leads to level repulsion with a strength W proportional to the shaking amplitude.

The double-well excitation spectrum in the effective ground band $\epsilon_1(q) \equiv \epsilon_+(q)$ results from the interplay between the momentum-dependent detuning and the normal single-well structure of the un-shaken ground band, see Fig. 3.1B. Because the shaking is blue-detuned, the ordinary ground band has higher energy than the excited band in the rotating frame, and therefore level repulsion causes the ground band energy to increase. Near the center of the bands the detuning is small, and the ground band energy increases dramatically; away from the center the detuning grows quickly, and the ground band energy is barely affected by level repulsion at all. For a sufficiently large shaking amplitude s the repulsion is sufficient to convert $\epsilon_q(0)$ into a local maximum and thus make the dispersion into a double-well with two new minima at $q = \pm q^*$. The quasimomentum q^*, as determined from the more thorough treatment in the next section, is plotted in Fig. 3.1C.

This treatment captures the essence of the double-well excitation spectrum, and one could skip the next two sub-sections and essentially still understand most of work described in Ch. 4. However, the more comprehensive treatment of the Floquet quasi-energy spectrum in the following sub-sections is essential for accurately calculating $\epsilon_1(q)$, for predicting the

results of strong shaking pulses discussed in Sec. 4.3.1, and for treating the interplay of interactions and micromotion in Sec. 3.3. We will also attempt to put the assumption that atoms evolve within the single effective ground band $\epsilon_1(q)$ and the treatment of its minima as "ground states" on somewhat more solid footing.

3.1.2 Single-particle effective Hamiltonian

Before specializing to a discussion of our particular system, it is helpful to discuss a few general principles of the Floquet theory for systems with time-periodic Hamiltonians $H(t + T) = H(t)$. If we wished to understand a system with a time-independent Hamiltonian, we would generally diagonalize the Hamiltonian to find eigenstates which evolve over time with a simple phase winding. We cannot directly diagonalize the Hamiltonian H since it is time-dependent. However, if we can find states which return to themselves (up to a complex phase) after a single Floquet period T, then they are guaranteed to continue returning to themselves after each subsequent Floquet period as well. If we examine the system stroboscopically such that we only consider the state after time-evolution in intervals of duration T, then such a state will appear very similar to an ordinary eigenstate with a simple complex phase winding over time; we call such states Floquet steady-states.

Floquet theory explains that it is indeed possible to calculate a complete basis of Floquet steady-states for a periodic Hamiltonian [79]. For a steady-state to return to itself after each period it must be an eigenstate of the time evolution operator, $U(T) = \mathcal{T} e^{-\frac{i}{\hbar}\int_0^T dt' H(t')}$, where $\mathcal{T}$ is the time-ordering operator. Therefore, the steady states $|n\rangle$ must satisfy $U(T)\,|n\rangle = e^{i\epsilon_n T/\hbar}\,|n\rangle$, where we have written the eigenvalue in a suggestive form since the operator U is unitary and therefore its eigenvalues must lie on the unit circle. In this form, the stroboscopic dynamics appears to be generated by an effective Hamiltonian H_e defined such that $H_\mathrm{e}\,|n\rangle = \epsilon_n\,|n\rangle$. The eigenvalues ϵ_n are called quasi-energies, because they essentially play the role of energy but are only defined up to integer multiples of $\hbar\omega$ since

the complex logarithm is multivalued. To complete this picture, the full time-dependent Floquet states also include a micromotion component, the Floquet function $|u_n(t)\rangle = P(t)\,|n\rangle$ where $P(t) = \left[\mathcal{T} e^{\frac{-i}{\hbar}\int_0^t dt' H(t')}\right] e^{\frac{i}{\hbar}H_e t}$ is periodic with period T since we have removed the quasi-energy winding from the full time evolution. Together, the steady states, their quasi-energies, and the corresponding Floquet functions describing the micromotion fully specify the time-evolution of the system. Analogous to the typical approach for time-independent Hamiltonians, we can decompose an arbitrary state $|\psi(t)\rangle$ into its component Floquet states,

$$|\psi(t)\rangle = \sum_n a_n\,|\psi_n(t)\rangle = \sum_n a_n\,|u_n(t)\rangle\, e^{-i\epsilon_n t/\hbar} \tag{3.5}$$

and the coefficients a_n will be time-independent. Since the micromotion is periodic on the (presumably) fast timescale of the Floquet period, it is instructive to look at the evolution of states $|\phi(t)\rangle \equiv P^{-1}(t)\,|\psi(t)\rangle$ in a frame where the micromotion has been removed. That time evolution is determined by the time-independent effective Hamiltonian as $-i\hbar\partial_t\,|\phi(t)\rangle = H_e\,|\phi(t)\rangle$.

In order to calculate the effective Hamiltonian and the Floquet steady-states for atoms in a shaken lattice, we must diagonalize the time-evolution operator over a full period $U(T)$ [119, 79]. Our typical approach is to perform the diagonalization numerically. We first calculate the band structure $E_m(q)$ and quasi-momentum states $|\Psi_m(q)\rangle$ for the average Hamiltonian $H_0 = \langle H\rangle$ (see Eq. 3.1). This basis is extremely convenient because the full Hamiltonian, including the shaking, commutes with quasimomentum, so we can calculate independent time-evolution operators $U(q,t)$ among the states at each quasimomentum. We break up the Floquet period into N discrete time steps $\Delta t = T/N$ ($N = 100$ is typically sufficient) and computer the time-evolution operators as a Trotter product. In fact, we can assemble time-evolution operators for arbitrary (discrete) times using the exact evolution from H_0 and a first order approximation of evolution from the remaining $H'(t) = H(t) - H_0$

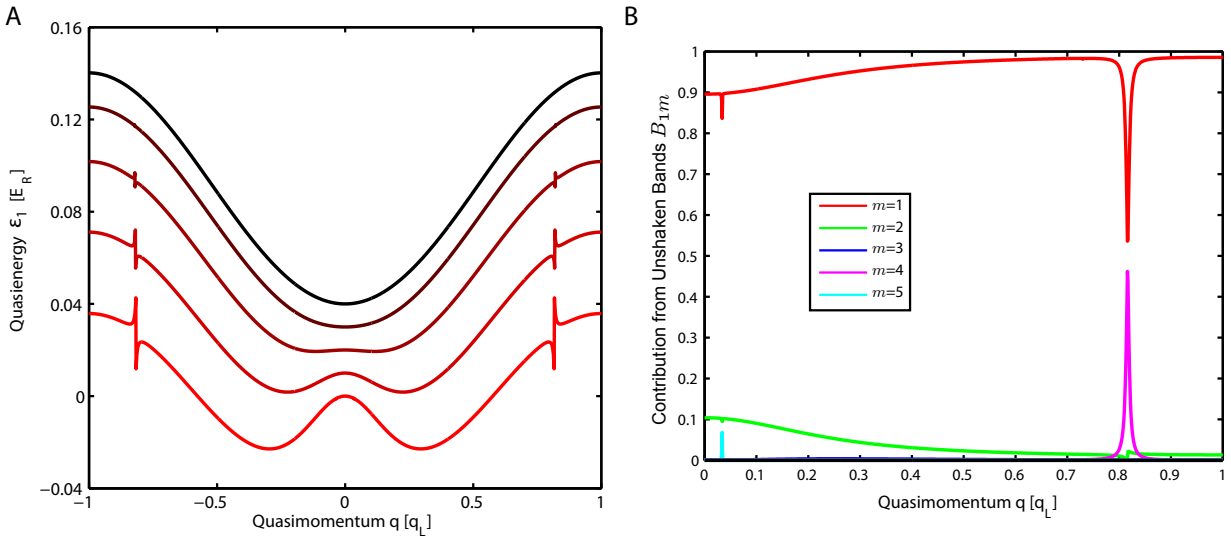

Figure 3.2: Quasienergy and contribution from unshaken bands based on the full Floquet calculation. (**A**) The quasienergy in the effective ground band calculated based on the approach in Sec. 3.1.2 with lattice spacing $d = 532$ nm, depth 8.86 E_{R}, shaking frequency $f = 8.0$ kHz and shaking amplitudes of $s = 0$, 8, 16, 24, and 32 nm increasing from the top curve to the bottom curve. (**B**) The time-averaged wavefunction contribution from states in the unshaken bands to the effective ground band for $s = 32$ nm. Each color corresponds to a different unshaken band, as indicated by the inset legend. Note that the narrow features in both panels correspond to avoided crossings of the first Floquet band with the fourth band (near $q \approx 0.8 q_{\mathrm{L}}$) and the fifth band (near $q \approx 0.03 q_{\mathrm{L}}$).

at each time step,

$$U(q, M\Delta t) \approx \prod_{n=0}^{M-1} \left(e^{iH_0(q)\Delta t/\hbar} \right) \left(1 + iH'(q, n\Delta t)\Delta t/\hbar \right). \tag{3.6}$$

By diagonalizing the time-evolution operator over a full period, $U(q, T)$, we obtain the Floquet steady-states $|\psi_n(q, 0)\rangle$ at time zero and the corresponding quasi-energies $\epsilon_n(q)$ which comprise the effective Hamiltonian H_e. We can readily obtain the full time-dependent Floquet states using the time-evolution operators at intermediate times,

$$|\psi_n(q, t)\rangle = U(q, t) \, |\psi_n(q, 0)\rangle \, , \tag{3.7}$$

thus recovering the micromotion component. In many cases the effects of micromotion are

negligible, but in others it plays a crucial role in determining the energies of many-body states once we account for interactions (see. Secs. 3.3 and 7.1). Note that we can readily extend this calculation, which amounts to a numerical solution of the time-dependent Schrödinger equation, to predict time-evolution for rapid changes in shaking amplitude during which the Hamiltonian is not periodic (see Sec. 4.3.1). The quasienergy bands calculated in this way significantly improve on the two-band approximation and provide sufficient quantitative accuracy for interpreting our experiments.

The ground quasienergy band $\epsilon_1(q)$ from this calculation is shown in Fig. 3.2A for various shaking amplitudes. Since the Floquet states are composed of superpositions of the unshaken quasimomentum states, $|\psi_n(q,t)\rangle = \sum_m b_{nm}(t)\,|\Psi_m(q)\rangle$, we identify the m'th Floquet band as the one which maximizes the time averaged contribution $B_{nm} = \int_0^T dt|b_{nm}(t)|^2/T$ to the Floquet state from the m'th band of the unshaken lattice. That is, the "first" Floquet state is the state which looks most like the unshaken first state most of the time. As can be seen in Fig. 3.2B, for most quasimomenta $B_{11} + B_{12} \approx 1$, supporting the two-band approximation described in the previous subsection.

An important difference between the calculated Floquet ground band and that which would be found from the two-band approximation is the existence of additional crossings with other bands. In the example shown in Fig. 3.2A, there is a noticeable crossing with the fourth Floquet band near $q \approx 0.8q_{\mathrm{L}}$, signified by the sharp feature in the quasienergy spectrum and the peak in B_{14} (Fig. 3.2B). An additional, very narrow crossing is apparent in the peak of B_{15} at small q. These Floquet band crossings tend to be associated with heating [7]. It is therefore desirable to operate under conditions in which the crossings are small and far away from quasimomenta typically occupied by the atoms. Aside from heating, these crossings can be largely ignored when interpreting our experiments.

3.1.3 Interpreting the quasi-energy bands in an interacting system

How should we interpret the quasienergy bands in a system with many interacting atoms? It is easy to get confused, since many treatments of Floquet theory focus on single particle examples. The single particle calculations above are highly suggestive: we still have a "ground band", and we're working with ultracold bosons, so we expect them to condense in the minimum energy state. However, in reality the single particle calculation is inadequate for supporting such a claim. On its own, the calculation above says that single particles in the shaken lattice should stay in a Floquet steady-state forever. That is, if we prepare atoms at $q = 0$ in the unshaken ground band, and ramp on the shaking lattice at an appropriate rate (slow compared to the coupling between the first and second bands but quickly compared to the small avoided crossings with far-off-resonant bands), then atoms should occupy the Floquet state $|\psi_1(0,t)\rangle$ perpetually. Specifically, the state of the atoms would not change even if the quasi-energy band acquired a double well and $\epsilon_1(0)$ became a local maximum. For single or non-interacting particles, one could envision a situation in which an external force (such as the dipole trap) should eventually cause the quasimomentum to change. One could predict subsequent dynamics based on the size of external forces compared to the widths of various avoided crossings in the band structure. While these are often the sorts of effects explored by explicit treatments of Floquet theory, none of them relate much to bosons condensing in the minimum energy state. To make matters worse, energy is not conserved for a time-dependent Hamiltonian, and there is no true minimum of quasi-energy since it is only defined up to multiples of $\hbar\omega$; from that perspective, even the question of into which state bosons should condense becomes murky.

The key to resolving the aforementioned issues is to recognize that the dynamics in the shaken optical lattice are largely driven by interactions. It is not an external force which drives the atoms away from $q = 0$ when it becomes a local maximum, but rather the interactions which enable pairs of atoms to transition into states with (opposite) finite

momenta. In that case, our treatment of the system in terms of atoms limited to the effective ground band should be appropriate as long as the interactions couple atoms to other states in the ground band much faster than they couple atoms to states in other bands. We generally consider transitions into other bands, which involve the absorption of a quantum of energy $\hbar\omega$ from the shaking, to be a "heating" process. To be precise, one can consider the energy that such a process would leave behind in the system even after removing the shaking lattice. Extensive work has been done to estimate the rates of heating processes in the near-detuned shaken lattice [38, 40, 39]. With these processes in mind, as long as dynamics in the effective ground band are fast compared to the heating, the interacting time-periodic system should still behave like an interacting time-independent system in the effective band.

Once we are limited to a single band and as long as the band-width is small compared to $\hbar\omega$, quasi-energy is clearly ordered and we can determine an effective ground state. Our expectation from statistical mechanics that bosons should condense into the ground state should be met on timescales comparable to the couplings from interactions within the effective ground band. Eventually, on the (presumably longer) timescale at which interactions can couple atoms into other bands, this metastable condensate should decay. Experimentally, we find that for typical parameters and blue-detuned shaking the dynamics of atoms within the effective ground band take place over $1 \sim 10$ ms timescales, while heating takes $10 - 100\times$ longer [119]. This separation of timescales is an essential feature of any useful Floquet-engineered system.

3.2 Effectively ferromagnetic quantum phase transition

It is very interesting to consider what happens to a BEC with a double-well single-particle excitation spectrum [119, 164]. As discussed in the previous section, we expect bosons to condense in the minimum of the effective band, but the bosons still have two degenerate minima at $q = \pm q^*$ to choose between. For non-interacting bosons and ignoring the micro-

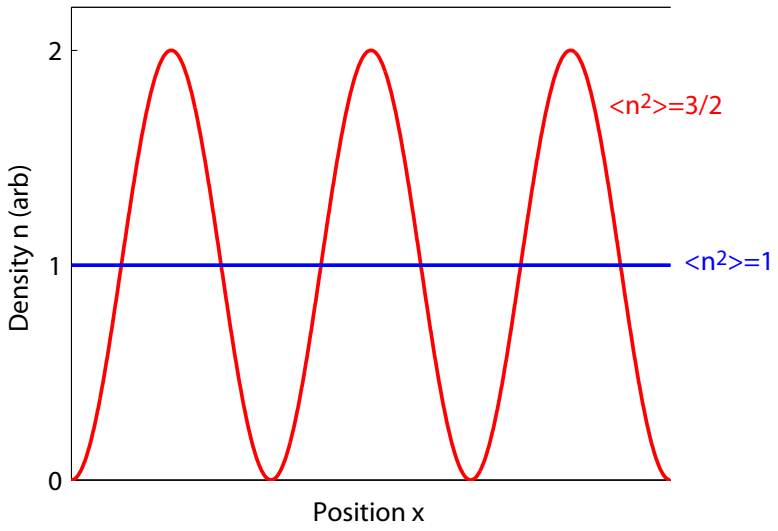

Figure 3.3: Illustration of possible ground states of the condensate in a double-well energy band. When the atoms are repulsively interacting $g > 0$, the condensate will occupy only a single minimum ($|A_\pm|^2 = 1$ and $|A_\mp|^2 = 0$) which yields a flat density profile (blue) that minimizes the positive interaction energy. When the atoms are attractively interacting $g < 0$, the system could in principle occupy both wells equally ($|A_+|^2 = |A_-|^2 = 0.5$), forming a density wave (red) in order to make the interaction energy more negative.

scopic structure at the scale of lattice sites, there are a wide variety of degenerate states (any superposition of the two minima) $\Psi_{\rm mf}(x) = \sqrt{\bar{n}}\left(A_+ e^{ik^*x} + A_- e^{-ik^*x}\right)$ (recalling $q^* = \hbar k^*$) into which the bosons could condense, assuming a homogeneous average density $\bar{n}$. So, which of these states should form?

The interactions almost entirely break the degeneracy and determine the nature of the double-well phase. For bosons with interaction strength g the interaction energy per particle is $E_{\rm int} = \frac{g}{2}\left\langle n(x)^2\right\rangle_x / \left\langle n(x)\right\rangle_x$ [122] where the density $n(x) = |\Psi(x)|^2$ and the angle brackets $\langle\rangle_x$ denote spatial averaging. The many-body ground state should minimize $E_{\rm int}$. By plugging in the ansatz $\Psi_{\rm mf}(x)$ and noting that proper normalization requires $|A_+|^2 + |A_-|^2 = 1$, we find

$$E_{\rm int} = \frac{g\bar{n}}{2}\left(1 + 2|A_+|^2|A_-|^2\right). \tag{3.8}$$

If the bosons are repulsively interacting ($g > 0$) then $E_{\rm int}$ is minimized by setting $|A_\pm|^2 = 1$ and $|A_\mp|^2 = 0$ such that $E_{\rm int} = \frac{1}{2} g\bar{n}$; that is, in the absolute ground state all of the bosons occupy a single minimum. The form of the interaction energy can be understood by looking at the density profile, see Fig. 3.3. By only occupying a single minimum, the bosons avoid the density wave (and the corresponding higher interaction energy) which arises from interference when atoms occupy both wells simultaneously. This scenario makes the double-well phase effectively ferromagnetic; we can treat the atoms as a pseudo-spin system in which spin up (down) corresponds to q^* ($-q^*$), and like a ferromagnet the energy is minimized if all atoms adopt the same pseudo-spin. We will almost exclusively discuss this scenario for the rest of the thesis.

Before moving on, it is worth mentioning that for attractive interactions ($g < 0$) one expects a very different behavior. In that case the interaction energy is negative, and it is minimized by setting $|A_+|^2 = |A_-|^2 = 0.5$ such that $E_{\rm int} = \frac{3}{4} g\bar{n}$. This choice of coefficients corresponds to a density wave, see Fig. 3.3. The phase of the density wave (which can be thought of as the location of its peaks and valleys) breaks an additional $U(1)$ symmetry of the Hamiltonian. Indeed, such a phase would in many ways look like a supersolid [26, 102, 103], with the spontaneously broken translation invariance of a solid appearing in a superfluid phase, and be fascinating to study. Unfortunately, the density wave is only the ground state under the assumption that the coarse grained density is homogeneous, implicit in our ansatz above. So far we have been unable to stabilize the density wave against the collapse of the condensate which typically occurs in BECs with attractive interactions [54].

The essential features of the effectively ferromagnetic quantum phase transition were first explored in Ref. [119]. The key observations are that a BEC in a double-well energy band will split up to occupy the minima at $q = \pm q^*$, see Fig. 3.4A. In the ferromagnetic phase the atoms form domain structures, an example of which is shown in Fig. 3.4B. Within each domain the atoms all share the same quasimomentum of either q^* or $-q^*$, but the pattern

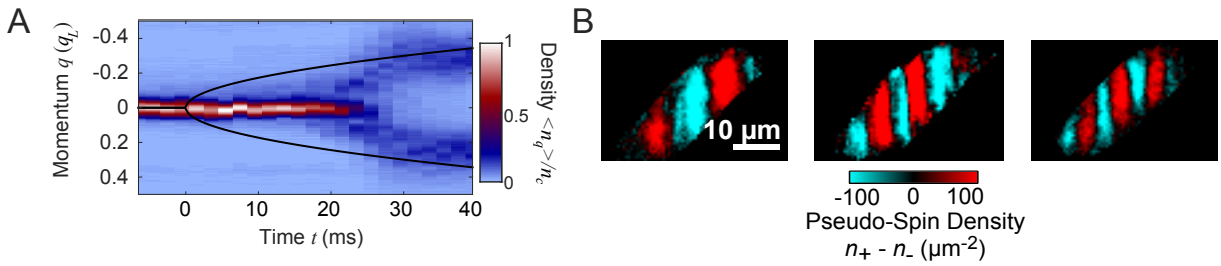

Figure 3.4: Essential features of the effectively ferromagnetic phase transition. A) After crossing into the ferromagnetic phase due to a linear increase of the shaking amplitude, the condensate remains at $q = 0$ for a delay time (see Sec. 4.1) before bifurcating to occupy the two minima $q = \pm q^*$ whose instantaneous positions are indicated by the solid black curves. The density in momentum-space n_q is measured using a focused TOF technique, averaged over many iterations of the experiment, and compared to the peak momentum-space density of the condensate n_q. This figure appears in Ref. [62]. B) Three example domain structures formed after crossing into the ferromagnetic phase. For more details see Sec. 4.3.1.

of the domains is unpredictable from shot to shot. The dynamics which lead to formation of domain structures (and the corresponding topological defects) in systems crossing symmetry-breaking phase transitions turns out to have many interesting universal features, as typically discussed in the framework of the famous Kibble-Zurek mechanism (KZM) [91, 168]. Those universal dynamics will be the primary topic of Ch. 4.

Another noteworthy feature is that the phase transition is biased by the initial velocity distribution of the gas. If the entire gas is initially moving in one direction, then its non-zero momentum is mostly conserved as the gas crosses the phase transition. The easiest way to analyze such a scenario is to work in the co-moving frame, in which the gas is stationary and the energy is shifted by $\Delta E_{\text{bias}}(q) = -qv$. This shift creates an energy difference of approximately $\Delta E_{\text{bias}}(q^*) - \Delta E_{\text{bias}}(-q^*) = -2q^*v$ between the two previously degenerate minima. With an initial nonzero velocity, there is now a single ground state with quasimomentum in the same direction as the initial velocity. As a result, the system preferentially occupies that state when it enters the ferromagnetic phase. We frequently use this effect for calibration (for example, see Sec. 4.3.1). One can also make use of this effect to deterministically generate more exotic domain structures, as shown in Fig. 3.5. This

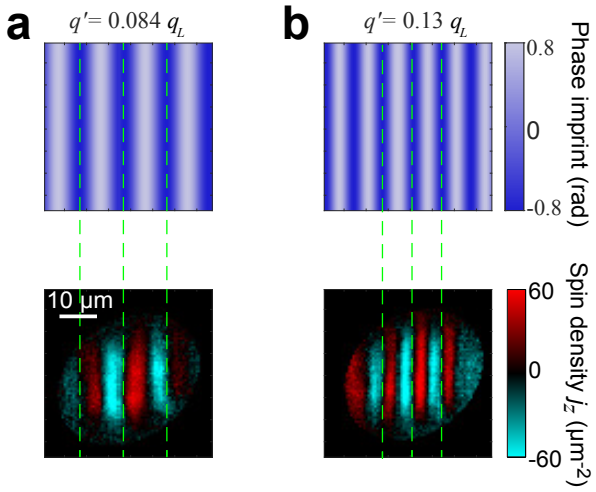

Figure 3.5: Deterministic domain structure formation. Briefly pulsing on a lattice potential with wavevector q' formed by the DMD (top row) creates an oscillating initial velocity distribution. If the gas subsequently crosses the effectively ferromagnetic quantum phase transition, the initial velocity distribution locally biases the gas toward one well or the other, as explained in the text. The local biasing leads to deterministic formation of a corresponding domain structure in the ferromagnetic phase (bottom row). The columns show examples of this effect for (a) $q' = 0.084\ q_{\mathrm{L}}$ and (b) $q' = 0.13\ q_{\mathrm{L}}$. The dashed green lines illustrate that domain boundaries match up with extrema of the lattice potential used for biasing.

capability presents exciting opportunities for studying the dynamics of domain walls in the ferromagnetic phase; see Sec. 7.1.1 for more discussion of the specific case in which domains tend to grow (coarsen) over time. However, biasing from nonzero initial velocity distributions (especially fluctuating ones) must be carefully avoided in order to observe universal critical dynamics; see Sec. 4.3.2 for more details.

3.3 Micromotion and Interactions

Understanding the micromotion of the Floquet steady states is important for developing an intuitive picture of the states involved in the effectively ferromagnetic phase transition. Moreover, in certain situations the micromotion will play a crucial role in determining the interaction energy of the system and have a huge impact on its bulk behavior. For example,

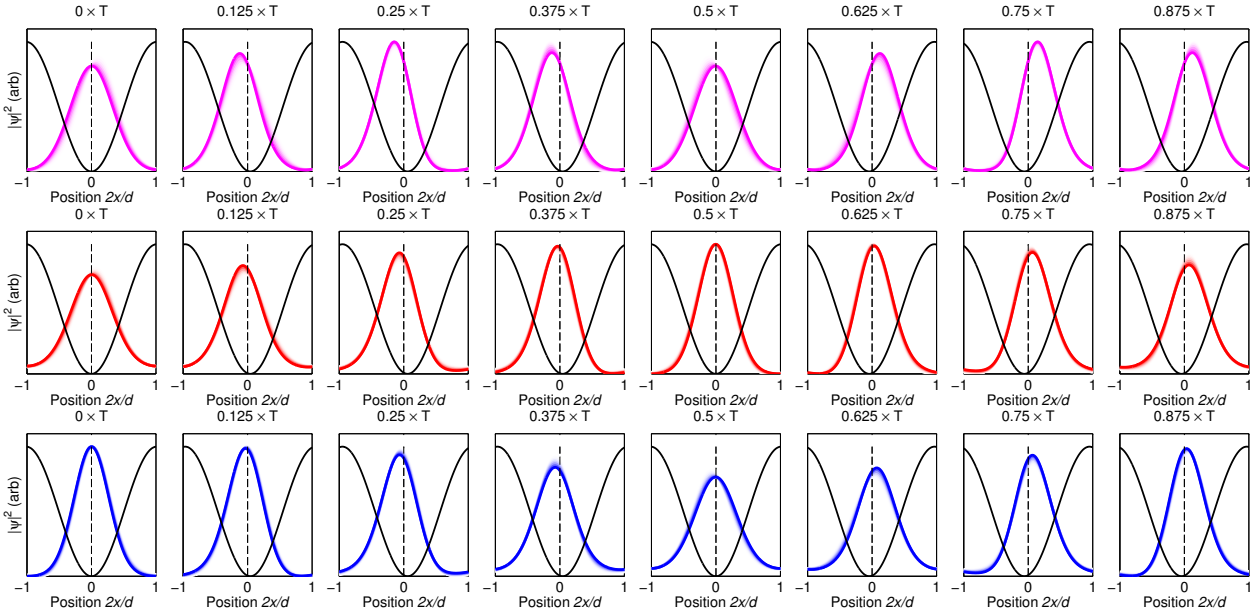

Figure 3.6: Micromotion in the shaken lattice. Plots of the density in the Floquet steady states with $q = 0$ (top), $q = q^*$ (middle), and $q = -q^*$ (bottom) over one shaking period and within a single lattice site. The fading curves indicate the density profiles at previous times within the $T/8$ step between each plot, making the motion more apparent. Calculated with lattice spacing $d = 532$ nm, depth 8.86 E_{R}, shaking frequency $f = 8.0$ kHz, and shaking amplitude $s = 32$ nm.

interaction effects from micromotion can be used to drive the system across a phase transition in the red-detuned shaking lattice, break the symmetry between the four minima in the two-dimensional shaken lattice, and engineer density-dependent synthetic gauge fields. We will discuss those very interesting situations in Sec. 7.1. Here, we develop a basic understanding of micromotion and its effects on interaction energy using the example of steady-states in the blue-detuned, one-dimensional shaken lattice.

We plot the Floquet functions $u_{nq}(x,t)$ which encode the micromotion for states at $q = 0$ and at the minima $q = \pm q^*$ in Fig. 3.6. The states share a few common features. As one generally expects for an oscillator driven at a frequency well above resonance, the peak density always oscillates directly out of phase with the lattice motion. While the shaking is sufficiently near detuned that contributions from other bands can be largely neglected, the detuning is still large compared to the damping and the coupling strength, and thus the

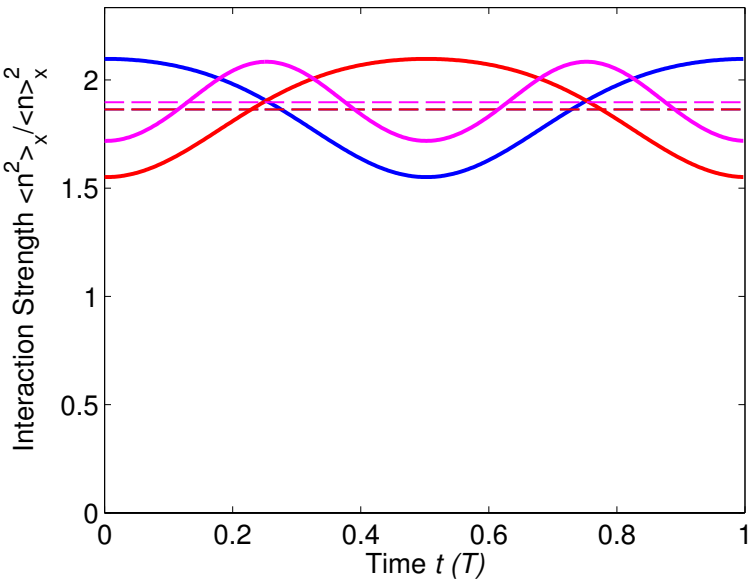

Figure 3.7: Interaction energy during micromotion. A plot of the instantaneous ratio $\langle n(t)^2 \rangle_x \,/\, \langle n(t) \rangle_x^2$ of the average interaction energy in the $q = 0$ (magenta), $q = q^*$ (red) and $q = -q^*$ (blue) Floquet steady-states to the interaction energy of a state with flat microscopic density over one Floquet period. The horizontal dashed lines indicate the respective averages over the full Floquet period - note that the averages for $q = \pm q^*$ are identical. Calculated with lattice spacing $d = 532$ nm, depth 8.86 E_{R}, shaking frequency $f = 8.0$ kHz, and shaking amplitude $s = 32$ nm.

response is out of phase. It is tempting to make an analogy to a driven pendulum. The peak in the $q = 0$ state bounces back and forth during the period, like normal pendulum motion. In contrast, in the $q = q^*$ ($-q^*$) states the density peak executes clockwise (counter-clockwise) motion, reminiscent of a pendulum driven "over the top" which also executes either clockwise or counter-clockwise motion. At this level, it's not clear that the analogy provides much value, but at least it doesn't seem harmful. Finally, note that these plots verify that the Floquet states satisfy an unusual symmetry of the Hamiltonian, in which space is inverted and time is translated by half of a period $T/2$ [79].

More important in terms of the observable consequences is the effect of micromotion on the interaction energy. As we did in Sec. 3.2, it is often most useful to treat bulk properties of the system by coarse-graining over the microscopic structures (at the scale of the lattice sites). When we take this approach in the lattice, we must use a modified

interaction strength in order to account for the micromotion. In the simplest case we assume that atoms still condense into a single quasimomentum state (or at least into domains of a single quasimomentum) and that the interactions are too weak to modify the microscopic wavefunction. In that case we define a renormalized interaction strength $g'_{nq} \equiv \eta_{nq} g$ where the interaction strength for atoms in free space is $g = 4\pi\hbar^2 a/m$ [122] and the modifier $\eta_{nq} \equiv \frac{1}{T}\int_0^T dt \, \langle |u_{nq}(x,t)|^4 \rangle_x \, / \, \langle |u_{nq}(x,t)|^2 \rangle_x^2$ accounts for the fact that the density in a lattice site is higher than it would be for a microscopically homogeneous gas.

The instantaneous interaction modification factor over time for blue-detuned shaking is shown in Fig. 3.7. By comparing this plot to the wavefunctions in Fig. 3.6 one sees that large modifiers correspond to a tall and narrow microscopic density distribution. The modifiers η_{nq} are shown as dashed lines in Fig. 3.7 and correspond to the time-averages of the instantaneous modifiers. Under the conditions used in this example, the modifier for the states $q = \pm q^*$ is slightly smaller than the modifier for $q = 0$. In principle, this means that higher density increases the energy of the $q = 0$ state relative to $q = \pm q^*$ and therefore shifts the critical point to smaller shaking amplitudes [164]. In practice, the shift of the critical point is quite small (see Sec. 4.1). Moreover, the interactions do not break the symmetry between the two minima $q = \pm q^*$. These points make the micromotion effects difficult to observe for 1D, blue-detuned shaking. However, the interaction effects become very interesting in other scenarios. For example, in the case of 2D shaking the micromotion depends sensitively on the relative phase of the shaking between the two lattice directions, and can break the four-fold symmetry (see Sec. 7.1.3). Finally, in the case of red-detuned shaking, the micromotion makes it possible to drive the system across the phase transition by increasing the scattering length (see Sec. 7.1.2).

3.4 Domain Walls

We have performed a detailed theoretical study of the domain walls in the ferromagnetic phase in Tongtong Liu, Logan W Clark, and Cheng Chin, "Exotic domain walls in bose-einstein condensates with double-well dispersion", *Physical Review A*, 94(6):063646, 2016 (Copyright 2016 by the American Physical Society). Based on the one dimensional Gross-Pitaevskii equation we performed numerical calculations to find the domain wall wavefunctions which minimize the energy. We also derived analytical forms for the domain wall wavefunction in the limits of weak and strong interactions.

Interestingly, the nature of the domain walls is quite different in the two limits. With weak interactions the superfluid minimizes its energy by forming "density wave domain walls" which avoid populating states near zero quasimomentum due to the high kinetic energy barrier. Since the quasimomentum must be well localized near the minima, in this limit bosons in the double-well dispersion are closely analogous to an immiscible two-component BEC [77, 140, 146, 12]. The density wave forms due to the interference between $+q^*$ and $-q^*$ at the domain wall. Indeed, the domain wall wavefunction in this limit takes the approximate form,

$$\psi_{\text{weak}}(x) \approx \sqrt{\rho_+(x)}e^{ik^*x} + \sqrt{\rho_-(x)}e^{-ik^*x} \tag{3.9}$$

where $\rho_\pm$ are the density envelopes of the positive/negative momentum components $k = \pm k^*$. The envelope functions have a width which scales as $L \propto (\mu/\epsilon)^{-1/2}/k^*$, where μ is the interaction energy and ϵ is the height of the kinetic energy barrier at $k = 0$. Moreover, the energy E_{weak} of the domain walls depends on the interaction strength $E_{\text{weak}} \propto \sqrt{\mu^3\epsilon}$.

In the strong interaction regime, the system forms "phase domain walls" as just a small perturbation of the density allows the system to support a smooth winding of the quasimomentum across the kinetic energy barrier. In this limit the wavefunction takes the form

$$\psi_{\text{strong}}(x) = \sqrt{\rho_\infty + \delta\rho(x)}e^{i\phi(x)} \tag{3.10}$$

where ρ_∞ is the density far from the domain wall. The density variation is

$$\delta\rho(x) = \frac{\epsilon}{g}(6 - 4\cosh 2k^*x)\text{sech}^4 k^*x \tag{3.11}$$

where g parameterizes the interaction strength and the perturbation vanishes for large interactions [106]. The presence of the domain wall is primarily encoded in the wavefunction phase,

$$\phi(x) = \ln\left(e^{k^*x} + e^{-k^*x}\right). \tag{3.12}$$

In this limit, the width of the domain wall is fixed at $L \approx 0.81\pi/k^*$, the minimum width which satisfies the uncertainty principle for a wavefunction interpolating smoothly between the two minima. The energy of the domain wall is also fixed,

$$E_{\text{strong}} = \frac{8}{3}\frac{\mu\epsilon}{gk^*}. \tag{3.13}$$

This work can provide a valuable guide for future studies focused on the dynamics of domain walls in the ferromagnetic phase. For example, one could attempt to understand the coarsening behavior, including the rotation of domain walls toward the short axes of the condensate (see Sec. 7.1.1), based on the energies of domain walls in a two dimensional extension of this calculation. For more details on these calculations and their possible implications see Ref. [106].

CHAPTER 4

SCALING SYMMETRY OF CRITICAL DYNAMICS

Much of the content in this chapter is based on our published work in Ref. [42]: Clark, L. W., Feng, L., & Chin, C. Universal space-time scaling symmetry in the dynamics of bosons across a quantum phase transition. *Science*, 354(6312):606-610, 2016. The thesis author played the primary role in the work described in this chapter.

The dynamics of many-body systems spanning condensed matter, cosmology, and beyond are hypothesized to be universal when the systems cross continuous phase transitions. The universal dynamics are expected to satisfy a scaling symmetry of space and time with the crossing rate which is essentially a result of the Kibble-Zurek mechanism. In this chapter we discuss a test of this symmetry based on Bose condensates crossing the effectively ferromagnetic quantum phase transition in the shaken lattice. We measure the growth of (pseudo-)spin fluctuations and the spatial spin correlations for ramping rates varied over two orders of magnitude. Beyond the critical point we observe delayed development of ferromagnetic spin domains with long-range anti-ferromagnetic correlations due to the bunching of the domain sizes, which is not expected in a thermal distribution of ferromagnets. The times and lengths characterizing the critical dynamics agree with the scaling predicted by the Kibble-Zurek mechanism. The measured fluctuations and correlations collapse onto single curves in scaled space and time coordinates, supporting the universality hypothesis.

This chapter is organized as follows. First, in Sec. 4.1 we provide a detailed explanation of the Kibble-Zurek mechanism (KZM). We emphasize three key features of our system which had been largely unexplored experimentally in the context of the KZM: 1) it involves a quantum (rather than classical) phase transition, 2) it is a Floquet system, and 3) the system is inhomogeneous. Next, in Sec. 4.2 we derive the mean-field prediction for the scaling exponents in our system. We then describe the technical details of our experiments in Sec. 4.3, detailing a number of improvements to the stability of our apparatus and our

detection methods which enabled this study. Then, we arrive at the main results of the study, exploring the temporal scaling of the unfreezing process in Sec. 4.4.1 and the spatial scaling of pseudo-spin correlations in Sec. 4.4.2. We then discuss the breakdown of the KZM at extreme parameters in Sec. 4.4.3, and derive the critical exponents within their regime of validity in Sec. 4.4.4. In Sec. 4.4.5 we demonstrate that dynamics over a wide range of interaction strengths are captured by the same universal functions. In 4.4.6 we briefly present the results of simulations of the critical dynamics using the Gross-Pitaevskii equation of the complete shaken lattice system.

4.1 Background

4.1.1 The Kibble-Zurek Mechanism

Critical phenomena near a continuous phase transition reveal fascinating connections between seemingly disparate systems that can be described via the same universal principles. Such systems can be found in the contexts of superfluid helium [168], liquid crystals [41], biological cell membranes [148], the early universe [91], and cold atoms [165, 124]. An important universal prediction is the power-law scaling of the topological defect density with the rate of crossing a critical point, as first discussed by T. Kibble in cosmology [91] and extended by W. Zurek in the context of condensed matter [168]. Their theory, known as the Kibble-Zurek mechanism, has been the subject of intense experimental study that has largely supported the scaling laws [50]. Recent theoretical works further propose the so-called universality hypothesis, according to which the collective dynamics across a critical point should be invariant in the space and time coordinates that scale with the Kibble-Zurek power-law [92, 33, 64].

The Kibble-Zurek mechanism provides a powerful insight into quantum critical dynamics. According to this theory, when the time remaining to reach the critical point inevitably

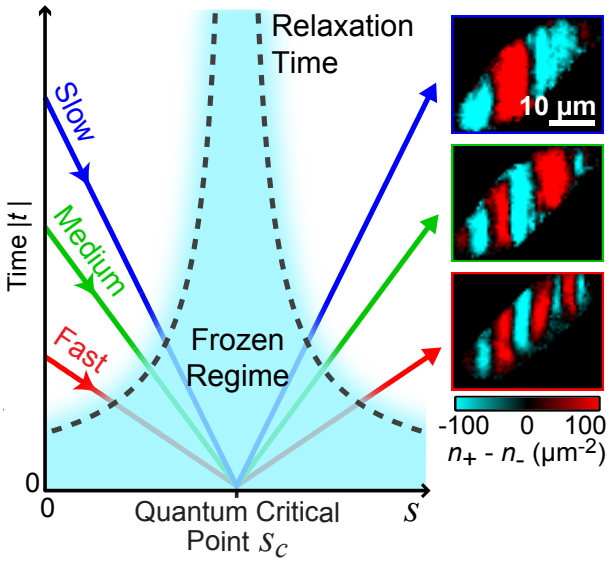

Figure 4.1: Kibble-Zurek picture. Evolution of a system crossing a continuous phase transition becomes diabatic in the frozen regime (cyan) when the time t remaining to reach the critical point is less than the relaxation time. Faster ramps cause freezing farther from the critical point, limiting the system to smaller domains. Sample domain images are shown for slow, medium, and fast ramps.

becomes shorter than the relaxation time, the system becomes effectively frozen, see Fig. 4.1. The system only unfreezes at a delay time t_{KZ} after passing the critical point, when relaxation becomes faster than the ramp. At this time topological defects become visible, and the typical distance d_{KZ} between neighboring defects is proportional to the equilibrium correlation length. The Kibble-Zurek mechanism predicts that t_{KZ} and d_{KZ} depend on the quench rate $\dot{s}$ as,

$$t_{\mathrm{KZ}} \propto \dot{s}^{-a},\ a = \frac{z\nu}{1+z\nu}, \tag{4.1}$$

$$d_{\mathrm{KZ}} \propto \dot{s}^{-b},\ b = \frac{\nu}{1+z\nu}, \tag{4.2}$$

where z and ν are the equilibrium dynamical and correlation length exponents given by the universality class of the phase transition. While the details of this picture may not describe

every phase transition, similar predictions hold for a variety of quench types across the transition [57] and for phase transitions which break either continuous or discrete symmetries [50].

For slow ramps t_{KZ} and d_{KZ} diverge and become separated from other scales in the system, making them the dominant scales for characterizing the collective critical dynamics [92, 33, 64]. This idea motivates the universality hypothesis, which can be expressed as

$$f(x,t;\dot{s}) \propto F\left(\frac{x}{d_{\mathrm{KZ}}}\ ,\ \frac{t}{t_{\mathrm{KZ}}}\right), \tag{4.3}$$

indicating that the critical dynamics of any collective observable f obeys the scaling symmetry and can be described by a universal function F of the scaled coordinates x/d_{KZ} and t/t_{KZ}. In a system satisfying the universality hypothesis, the only effect of changing the quench rate or any other microscopic parameter is to modify the length and time scales.

4.1.2 Testing the KZM in Quantum, Floquet, and Inhomogeneous systems

A key topic of recent interest has been the application of the KZM to describe dynamics across quantum phase transitions. Quantum phase transitions have been observed to exhibit critical scaling in equilibrium similar to the classical case [165, 163]; in fact, in general a quantum phase transition can be mapped onto a classical phase transition in higher dimensions [134]. Since the dynamical scaling of the KZM is a direct extension of the equilibrium critical scaling, one might therefore expect the KZM to apply to systems crossing quantum phase transitions as well. Indeed, early theoretical works suggested that the KZM was compatible with quantum phase transitions [56, 48, 170, 123]. Atomic quantum gases provide a clean, well-characterized, and controlled platform for testing this conjecture [24, 57, 124]. They have previously enabled experiments on the formation of topological defects across the Bose-Einstein condensation transition [153, 96, 45, 114] as well as critical dynamics across quantum

phase transitions [135, 20, 34, 115, 28, 110]. Indeed, shortly before our work was completed a very exciting test of some aspects of the KZM in a spinor BEC was reported [11].

The Kibble-Zurek mechanism also had not previously been experimentally tested in a Floquet-engineered phase transition [133]. Considering that Floquet systems present many challenges even to our understanding of equilibrium statistical mechanics [99, 47, 58], as discussed in the previous chapter, the expected behavior of critical dynamics in Floquet systems is even more uncertain. Previously, we have seen that for timescales short compared to heating the near-equilibrium behavior of atoms in the shaken lattice is indeed consistent with expectations from statistical mechanics in a time-independent double well dispersion [119, 76]. In much the same way, below we find that the KZM approach to critical dynamics is quite successful in our Floquet system as long as heating remains small.

It is often expected that the KZM should fail or be drastically modified in inhomogeneous systems, such as our ultracold Bose gas in the harmonic trap. However, in most cases when the presence of a harmonic trap modifies the critical dynamics, the primary cause is the inhomogeneity of the value of the critical parameter across the sample. For example, inhomogeneity has a huge effect on the critical dynamics of systems crossing the Bose-Einstein condensation transition [96, 45, 114, 53]. In those cases, the critical temperature $T_{\mathrm{c}} \propto n^{2/3}$ for density n, and therefore varies enormously across a harmonically trapped gas, dropping all the way to zero at the edge [169]. In our case the critical shaking amplitude is almost independent of the density. From our calculation (recall Sec. 3.3) the value of s_c is constant within 5% across the whole gas. We will see below that the effect of shifting sc by 5% on our scaling is within our existing error bars. In addition, throughout the experiment, we are working in the limit where the domain size is much smaller than the sample size, see Fig. 3D. Thus, it is a noteworthy feature of our experiments that the essentially homogeneous critical shaking amplitude allows the KZM scaling to survive even in an inhomogeneous gas.

4.2 Mean-Field Theoretical Scaling

The partition function Z of our system near the critical point where $\alpha \to 0$ and $\beta > 0$ can be written in the path integral form as [164]

$$\begin{aligned} Z &= \int D\Psi D\Psi^* e^{-\int dx d\tau L} \\ L &= \Psi^* \partial_\tau \Psi + \alpha |\partial_x \Psi|^2 + \beta |\partial_x^2 \Psi|^2 - \mu \Psi^* \Psi + \frac{g}{2}(\Psi^* \Psi)^2, \end{aligned}$$

where L is the mean field Lagrangian density, $\mu = g\rho_0$ is the chemical potential, g is the interaction parameter and $\tau = it/\hbar$.

Given a fluctuating order parameter $\Psi = \sqrt{\rho} e^{i\theta}$ around the equilibrium value $\Psi_0 = \sqrt{\rho_0}$ and $\rho = \rho_0 + \tilde{\rho}$, we have

$$\begin{aligned} \Psi^* \partial_\tau \Psi &= i\rho \partial_\tau \theta + \partial_\tau \rho/2 \\ |\partial_x \Psi|^2 &= \rho (\partial_x \rho)^2 + \frac{1}{4\rho}(\partial_x \theta)^2 \\ |\partial_x^2 \Psi|^2 &= \rho^{-3} \left(\frac{(\partial_x \rho)^2}{4} - \frac{\rho \partial_x^2 \rho}{2} + \rho^2 (\partial_x \theta)^2 \right)^2 + \rho^{-1} (\rho \partial_x^2 \theta - \partial_x \theta \partial_x \rho)^2 \\ -\mu \Psi^* \Psi + \frac{g}{2}(\Psi^* \Psi)^2 &= \frac{g}{2}(\tilde{\rho}^2 - \rho_0^2). \end{aligned}$$

Eliminating terms like $\partial_\tau \rho$ and $\rho_0 \partial_\tau \theta$ that contribute to constants after integration over τ, we have

$$\begin{aligned} L = i\tilde{\rho} \partial_\tau \theta + \frac{\alpha}{\rho} \left(\rho^2 (\partial_x \rho)^2 + \frac{(\partial_x \theta)^2}{4} \right) \\ + \frac{\beta}{\rho^3} \left(\frac{(\partial_x \tilde{\rho})^2}{4} - \frac{\rho \partial_x^2 \tilde{\rho}}{2} + \rho^2 (\partial_x \theta)^2 \right)^2 + \frac{\beta}{\rho} (\rho \partial_x^2 \theta - \partial_x \theta \partial_x \tilde{\rho})^2 + \frac{g}{2} \tilde{\rho}^2. \end{aligned}$$

Since the amplitude excitations are gapped and the angular excitations are gapless, we can assume $\partial_x \tilde{\rho} = 0$ in the long wavelength limit, which gives

$$L = i\tilde{\rho}\partial_\tau \theta + \alpha\rho\frac{(\partial_x\theta)^2}{4} + \beta\rho(\partial_x\theta^2)^2 + \beta\rho(\partial_x^2\theta)^2 + \frac{g}{2}\tilde{\rho}^2$$

Completing the path integral over $\tilde{\rho}$, we obtain to leading order in θ

$$L_\theta = \frac{1}{2g}(\partial_\tau\theta)^2 + \frac{\alpha}{4}\rho_0(\partial_x\theta)^2 + \beta\rho_0(\partial_x^2\theta)^2.$$

The mean field correlation length exponent $\nu = 1/2$ can be derived from the spatial scaling symmetry with $\partial_\tau\theta = 0$:

$$\alpha \to \lambda^{-1}\alpha, x \to \lambda^\nu x.$$

At the critical point $\alpha = 0$, the dynamical critical exponent $z = 2$ is determined by applying the following scaling transformation to the effective Lagrangian L_θ,

$$x \to \lambda x, t \to \lambda^z t,$$

and noting that L_θ is invariant when $z = 2$, except for an overall multiplicative factor λ^{-4}. Notably $z = 2$ results from the dominance of the quartic term $\beta|\partial_x^2\Psi|^2$ at the critical point.

Given $z = 2$ and $\nu = 1/2$, the Kibble-Zurek temporal and spatial exponents from Eqs. 4.1 and 4.2 are given by $a = 1/2$ and $b = 1/4$, respectively. It is generally expected that there are beyond-mean-field corrections to the critical exponents, but, as we will see below, the

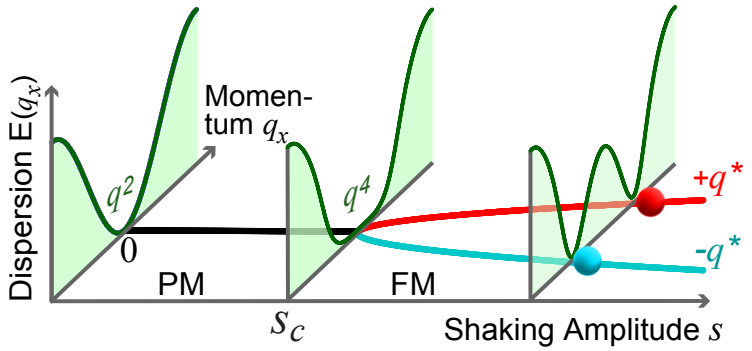

Figure 4.2: Evolution of the single atom excitation spectrum across the effectively ferromagnetic phase transition. The effectively ferromagnetic phase transition occurs when the ground band evolves from quadratic for $s < s_c$ (paramagnetic (PM) phase), through quartic at the quantum critical point $s = s_c$, to a double-well for $s > s_c$ (ferromagnetic (FM) phase) with two minima at $q_x = \pm q^*$ [42].

corrections appear to be smaller than we can resolve with our present experiments.

4.3 Experiment Setup

For this experiment we form 3D condensates at the crossing of the XDT, YDT, and ZDT dipole traps (see Sec. 2.1). After evaporation the condensates are nearly pure, consisting of 30 000 to 40 000 atoms with temperatures less than 10 nK in a trap with frequencies of $(\omega_{x'}, \omega_{y'}, \omega_z) = 2\pi \times (12,\ 30,\ 70)$ Hz, where the long (x') and short (y') axes are oriented at 45^o with respect to the x and y coordinates (Fig. 4.3). The tight confinement along the vertical z-axis suppresses non-trivial dynamics in that direction (see the discussion on the dynamics in the y-direction below) which is also the optical axis of our imaging system. We adiabatically load the condensates into a one-dimensional (1D) optical lattice [24] of depth 8.86 E_R by retro-reflecting the YDT trapping beam which propagates along the x-axis (and provides primarily y-axis trapping, motivating its name).

To induce the effectively ferromagnetic quantum phase transition explained in the previous chapter, we modulate the phase of the lattice beam to periodically translate the lattice potential by $\Delta x(t) = (s/2)\sin(\omega t)$, where s is the peak-to-peak shaking amplitude and the

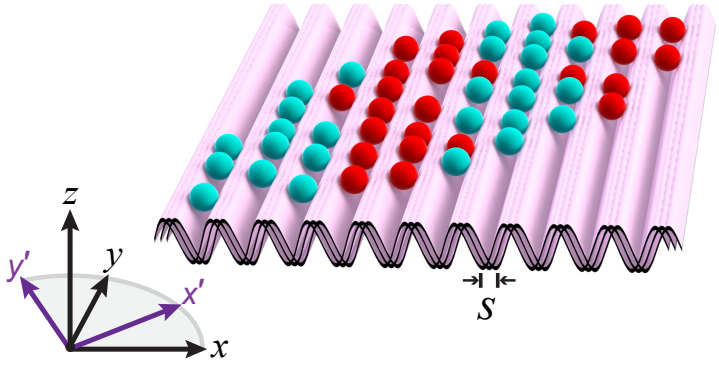

Figure 4.3: A BEC of cesium atoms (spheres) in a 1D optical lattice (pink surface) shaking with peak-to-peak amplitude s can form ferromagnetic domains (blue and red regions). The elliptical harmonic confinement has principal axes rotated 45^o from the lattice [42].

modulation frequency ω is tuned to mix the ground and first excited lattice bands, as explained in Sec. 2.4. These experiments rely on a careful choice of the parameters governing the shaking optical lattice. We set the shaking frequency $\omega = 2\pi \times 8.00$ kHz slightly above the zero-momentum band gap $E_2(0) - E_1(0) = h \times 7.14$ kHz, such that shaking raises the energy near the center of the ground band. Based on the lattice depth and shaking frequency, we calculate the critical shaking amplitude $s_c = 13.1$ nm using Floquet theory (Sec. 3.1.2). The hybridized single-particle ground band energy ϵ can be modelled for small quasimomentum $\mathbf{q} = (q_x,\ q_y,\ q_z)$ by

$$\epsilon(\mathbf{q}; s) = \alpha(s) q_x^2 + \beta(s) q_x^4 + \frac{q_y^2 + q_z^2}{2m}, \tag{4.4}$$

where m is the atomic mass, and the coefficients of its quadratic (α) and quartic (β) terms depend on the shaking amplitude (Fig. 4.2). During shaking we reduce the scattering length to $a = 2.1$ nm using a Feshbach resonance to lower the heating rate [38, 40, 39]. Finally, immediately before time-of-flight (TOF) we reduce the scattering length to $a = 0$ to prevent collisions while the atoms separate into distinct Bragg peaks.

As a brief side note, we have significant freedom to tune many parameters of the shaken lattice. While the shaking must be near-resonant and blue-detuned to create the double-

well, without enormous difficulty we have observed the phase transition for lattice depths from $4 \sim 11\ E_R$ with an appropriate shift in the shaking frequency. Given this freedom, one surprisingly useful condition worth maintaining is that the least common multiple of the shaking period and the time steps of the computer controller be small. The least common multiple tells us how long we must wait before the phase of the shaking, and equivalently the phase of the micromotion, repeats itself at a subsequent controller time step. For the shaking period $T = 125\ \mu$s used in this experiment and our time steps of 20 μs, the least common multiple is 500 μs. We can therefore shift phase-sensitive procedures, such as the detection method discussed in the next section, by as little as 500 μs without affecting their performance. This is a crucial feature for experiments like this one testing the KZM, in which the physics of interest requires careful, precise control over the timing of detection. For comparison, many of our original shaking experiments in the lab were done with a lattice depth of 7 E_R and $f = 7.3$ kHz; under those conditions, the micromotion phase only lined up with the controller time step every 10 ms, providing insufficient flexibility in setting the detection time.

In the next section we explain the pseudo-spin reconstruction technique which enables us to analyze the spin density distribution $j_z(\mathbf{r}) = n_+(\mathbf{r}) - n_-(\mathbf{r})$ based on the density $n_{+/-}$ of atoms with pseudo-spin up/down.

4.3.1 Improved domain reconstruction with a hard shaking pulse

Reconstruction enables us to study the *in-situ* spin density distribution, including the domain structure. A previous study demonstrated that local variations in the distribution of density among the Bragg peaks after a short TOF could be used to reconstruct the pseudo-spin domains [119].

We improve upon the original domain reconstruction scheme by adding an amplification stage before TOF. After linearly ramping the shaking amplitude at ramp rate $\dot{s}$ until $t =$

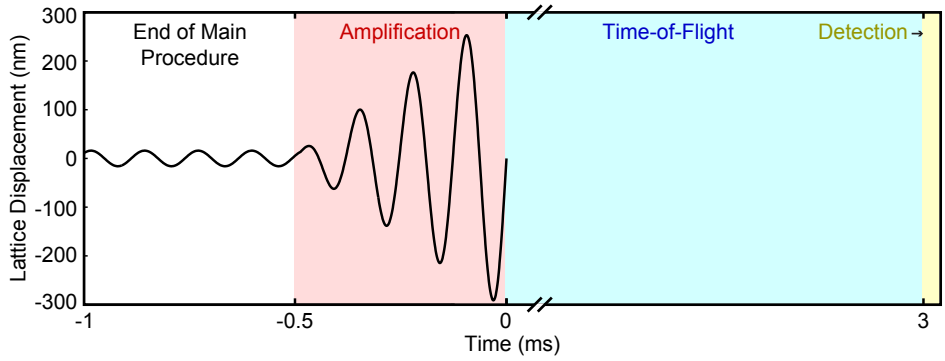

Figure 4.4: Illustration of shaking waveform to amplify domains for reconstruction. At the end of the main procedure, which generates a gas with a domain structure that we wish to probe, we apply an additional amplification stage in which the shaking amplitude increases linearly before performing a short time-of-flight and acquiring an absorption image. The amplification stage dramatically increases the signal to noise ratio for domain reconstruction.

1.4 t_d when domains have fully formed, we rapidly increase the shaking amplitude by as much as a factor of 15 over only 0.5 ms (Fig. 4.4). The rapid increase in shaking amplitude excites the atoms to higher bands while leaving their quasimomentum approximately the same. For a proper choice of the shaking amplitude and timing during this amplification stage, the atoms are efficiently transferred to the second excited band before they are released for TOF. In the second excited band, pseudo-spin down atoms ($q = -q^*$) will mostly appear in the -1 Bragg peak while pseudo-spin up atoms ($q = +q^*$) will mostly appear in the $+1$ Bragg peak, making them easy to distinguish after the short TOF.

To examine how the amplification process occurs, after initializing the gas entirely into either the left or right well we collect a series images at different stages during the amplification ramp, see Fig. 4.5. We then compare the fraction of atoms in each Bragg peak to a single-particle numerical simulation of the Schrödinger equation using the complete shaking waveform during the amplification stage, see Fig. 4.6. Allowing for some deviation of the actual shaking waveform from the programmed waveform, the theory nicely captures the evolution of the Bragg peaks during the experiments.

We can understand the time-evolution of the Bragg peaks as follows. First, at times

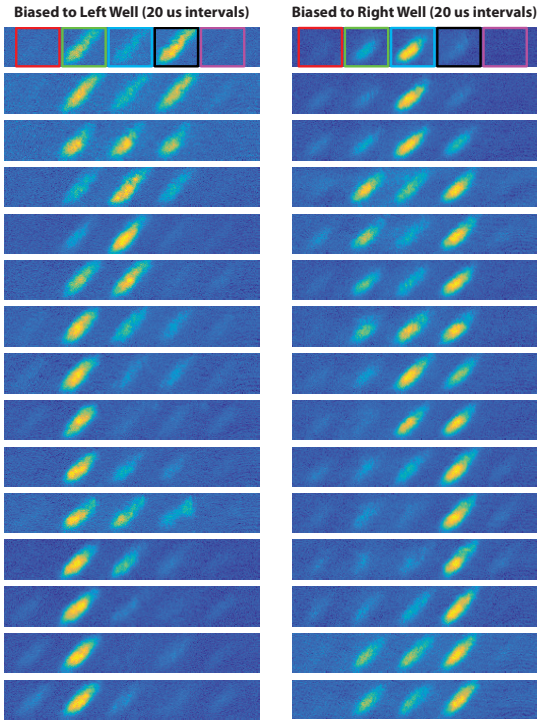

Figure 4.5: Image series of atom diffraction peaks after 5 ms time-of-flight for condensates released from the trap and lattice during the amplification stage. After initializing the system such that the entire BEC has quasimomentum $-k^*$ (left column) or $+k^*$ (right column) we linearly increase the shaking amplitude from $s_\mathrm{i} = 32$ nm at time $t = 0$ to $s_\mathrm{f} = 230$ nm at $t = 700$ μs, followed by an additional 100 μs held at constant shaking amplitude. These images correspond to release times from $t = 500$ μs (top) to $t = 780$ μs (bottom). The lattice depth was 7 E_R and shaking frequency 7.3 kHz. The colored squares indicate the regions integrated to determine the number of atoms in each Bragg peak, which is used to create Fig. 4.6.

$t < 0$ before the amplification pulse begins, we see the small oscillations between the Bragg peaks which represent the normal micromotion of a Floquet steady state (Sec. 3.3) and were discussed in the context of the original reconstruction scheme [119]. Later, at times $t > 0$ the large amplitude shaking of the lattice during the amplification stage deterministically drives diabatic transitions of atoms from the ground Floquet band to a superposition of excited bands. While the state of the atoms is rapidly oscillating between different superpositions, a properly shaped pulse will eventually place a large majority of atoms in the desired Bragg peak for a duration of about 40 μs. We empirically choose a time during this brief interval

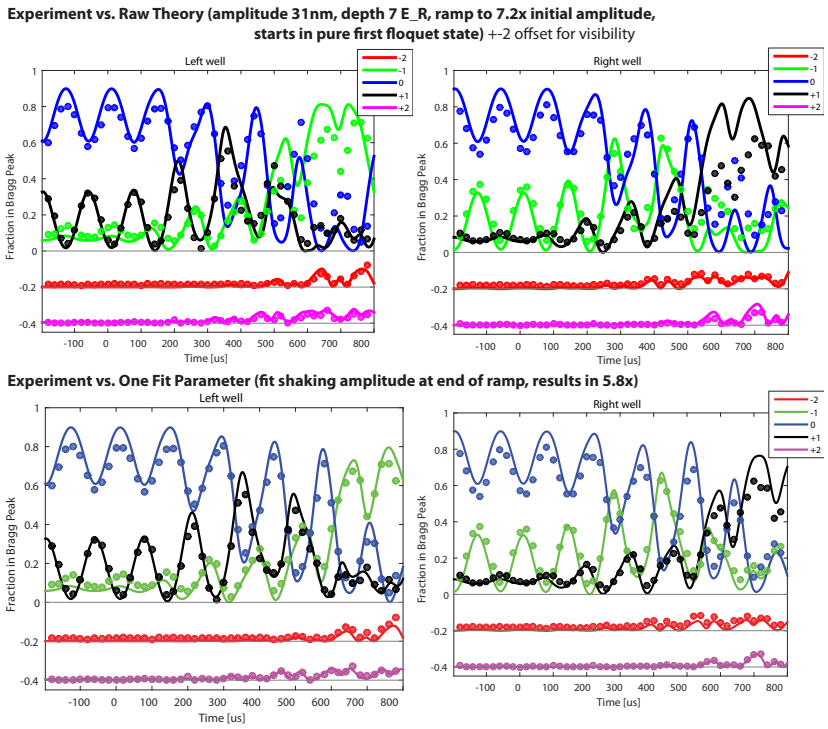

Figure 4.6: Comparison of amplification time series to Schrödinger equation. We extract the fraction of atoms in each Bragg peak (circles) from images as in Fig. 4.5 throughout the amplification stage for BECs with $k = -k^*$ (left) and $k = +k^*$ (right). The populations of the ± 2 Bragg peaks are offset for clarity. In the top row, solid curves show the theoretical prediction based on numerical simulations of the Schrödinger equation (Sec. 3.1.2) for the conditions listed in the caption of Fig. 4.5 with no free parameters. In the bottom row, solid curves show the best fit to numerical simulations of the Schrödinger equation with the final shaking amplitude s_f as a free parameter, yielding $s_\mathrm{f} = 186$ nm. Note that, in these plots, $t = 0$ marks the beginning of the amplification pulse.

to remove the shaking lattice and the trap, after which the populations in each Bragg peak are constant because momentum states are eigenstates for free atoms. A subsequent TOF separates the Bragg peaks spatially so that we can detect their density distributions.

We do not fully understand why we need to include the final shaking amplitude as a fitted parameter in order to capture the experimental results. One might be concerned that interaction effects modify the time evolution. However, we did not observe significant density dependence of this process; that is, the bragg peak occupations seem to be the same for the high density central regions and the low density outer regions of the gas. This observation

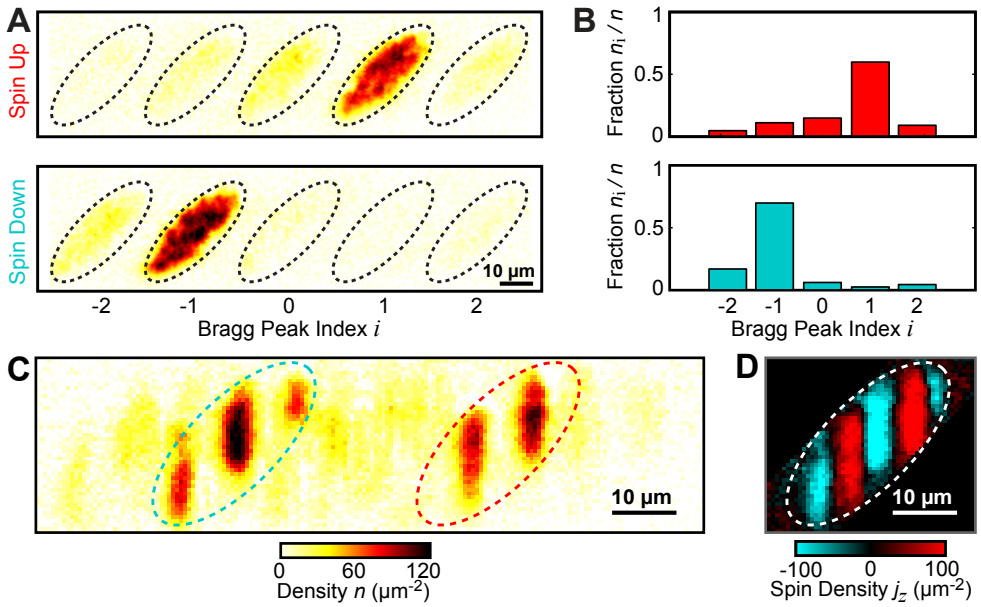

Figure 4.7: We amplify the distinction between the pseudo-spin states by rapidly increasing the shaking amplitude over 0.5 ms before time-of-flight (TOF). After 3 ms TOF we detect the density distribution by absorption imaging. The examples shown in this figure correspond to lattice depth $V = 8.86\ E_{\mathrm{R}}$, shaking frequency $f = 8.0$ kHz and amplitude $s = 32$ nm before amplification. (**A**) Sample images used to calibrate the occupation of each Bragg peak are taken with all of the atoms in pseudo-spin up (top) or down (bottom). Ellipses identify the Bragg peaks. For these images we use a longer TOF lasting 5 ms. Each spin predominantly occupies a different Bragg peak. (**B**) The fraction of density n_{i}/n in each Bragg peak distinguishes spin up (top) and down (bottom). (**C**) A sample image shows the density distribution after 3 ms TOF for a condensate with five domains. The ellipses mark the two most important Bragg peaks and are colored to indicate the spin state which dominates each peak. (**D**) Reconstruction based on the fractions in panel C produces the spin density distribution corresponding to the TOF image in panel D.

suggests that the deviation is not a result of ignoring interactions in the simulation. We suspect that the deviation results from nonlinearity of the position response of the optical lattice to the frequency modulation of the AOMs, since these data were collected before switching our shaking setup to the more reliable phase-modulation scheme described in Sec. 2.4. Regardless, while the theory can provide a useful guess for the parameters of the amplification pulse, we determine the optimal parameters for maximizing the signal empirically.

Depending on the shaking amplitude immediately before the amplification stage, we

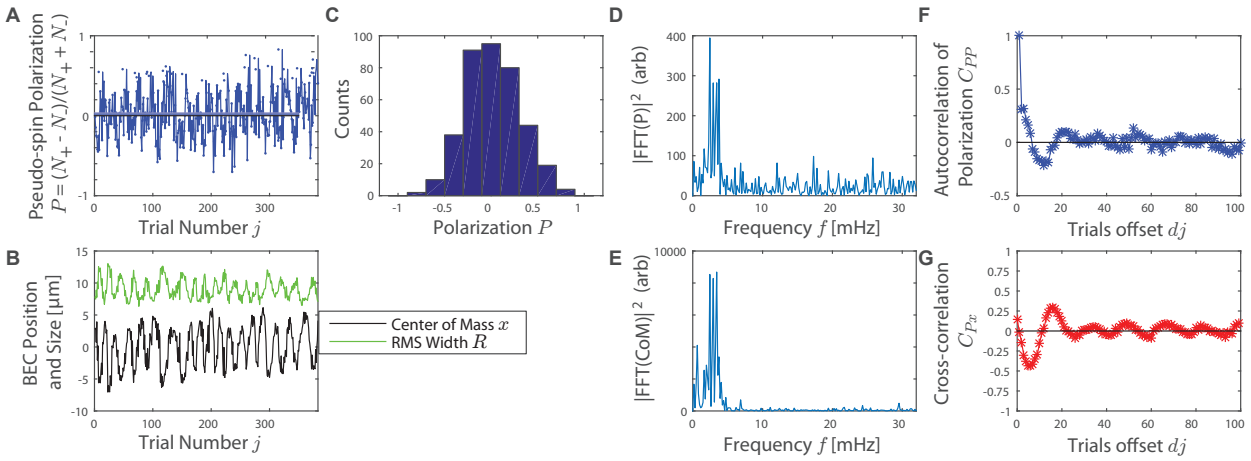

Figure 4.8: A series of analyses revealing the systematic biasing of domain structures. See text for details.

adjust the amplification waveform in order to maximize the distinguishability of the two spin states. We use images of condensates with uniform spin (Fig. 4.7A) to calibrate the projection of each spin state onto Bragg peaks (Fig. 4.7B). We then adjust the duration and the final shaking amplitude of the amplification pulse in order to maximize the fraction of atoms transferred to the desired Bragg peak. In comparison to the procedure without enhanced shaking used in Ref. [119], the amplification stage improves the fraction of atoms which distinguish the spin states from 23% to about 71%, corresponding to an increase in signal by more than a factor of three as well as a reduction in the density of background atoms by a similar factor.

During normal operation, after the enhanced shaking period, we perform a 3 ms TOF and measure the density in each Bragg peak (Fig. 4.7C), from which we can reconstruct the spin density distribution (Fig. 4.7D) using an algorithm similar to that described in Ref. [119].

While this technique provides a powerful probe for the domain structure in the ferromagnetic phase, it cannot be used in every situation. In particular, it assumes that the atoms are almost entirely at $q = \pm q^*$ and will not provide useful results at early times before that condition is met. Moreover, due to the uncertainty principle it is not possible for the quasimomentum in a domain to be well localized near $q = \pm q^*$ unless the size l of the

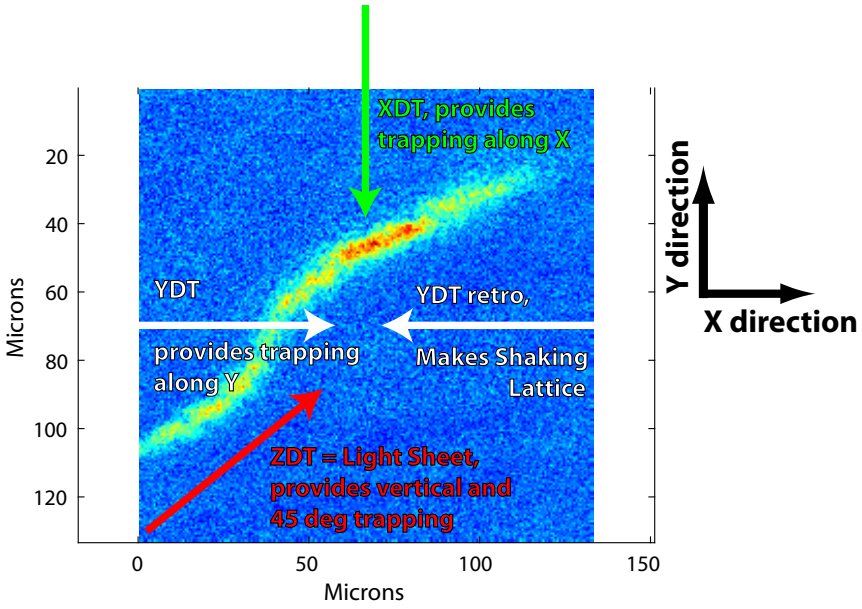

Figure 4.9: Example image revealing the dipole trap fringes as they appeared in conditions close to our normal experiment procedure, before correction (see below). The "snake"-like atomic density profile results from a four beam trap, with the contributing beams marked as arrows. The trap profile is dominated by the trapping from ZDT, which propagates at 45° in this image, and large scale fringes which only appeared when the YDT retro beam was present.

domain satisfies $l \gg 1/k^*$. In the work described in this chapter, at sufficiently late times ($t = 1.4t_d$, see below for details), we observe density distributions after TOF consistent with nearly all atoms arranging into sufficiently large domains with $q = \pm q^*$, enabling us to treat them as pseudo-spins and calculate the spin density just after the system unfreezes using the approach detailed in this section.

4.3.2 Eliminating moving fringes

One of the most serious problems plaguing the lab's original studies of the effectively ferromagnetic quantum phase transition was technical noise. In particular, it was found that a systematic biasing, presumably caused by an offset of the initial velocity of the gas, would lead to artificial symmetry breaking and result in most gases becoming completely polar-

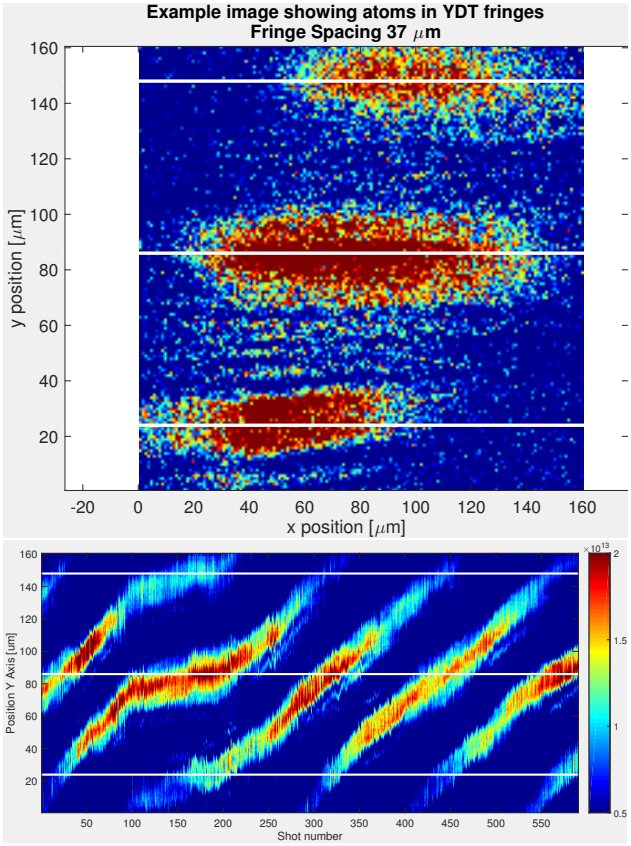

Figure 4.10: Characterization of large scale fringes due to YDT retroreflection. (top) By removing the ZDT beam and adjusting our loading procedure, we can cause the gas to split between multiple long wavelength fringes caused by the YDT retroreflection. From this image we found that the spacing between the fringes was 37 μm. (bottom) Here we show a series of nearly 600 images averaged over the x-axis, revealing the systematic drift of the position of the fringes due to the slow warming up of the optical table over the course of the day. These images span approximately 2.5 hours.

ized to one pseudo-spin or the other [119]. Moreover, while the effects were correlated on timescales of about 10 trials of the experiment, the magnitude and direction of the effect was inconsistent over time. This biasing would destroy the scaling of the domain structure which is predicted by the Kibble-Zurek mechanism by creating artificial correlations in the local current across the gas before the system even approaches the phase transition [62]. I am going to tell the full story of correcting this problem here, because it might be instructive for future users of this or similar systems.

We analyzed this biasing effect quantitatively for nearly 400 consecutive experiment trials

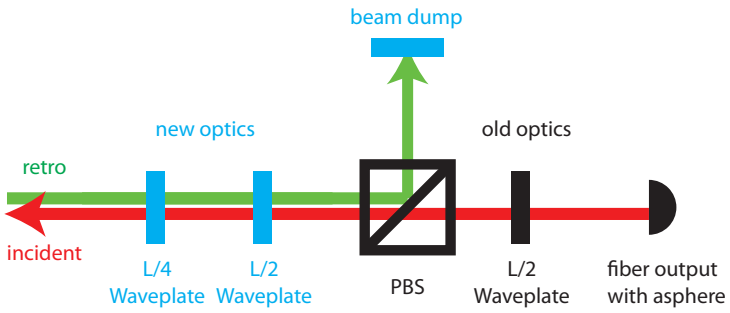

Figure 4.11: New optics to remove the large fringes in the YDT lattice. The large fringes were caused by reflection of the YDT retro beam from the fiber tip. To remove them, we inserted two new waveplates in the beam path, such that the retro beam reflected from a PBS into a beam dump instead of returning to the fiber. Note that there was insufficient space to insert an optical isolator in the existing path. Note also that additional waveplates were added on the opposite side of the chamber to ensure that the polarization is linear entering the AOMs.

in Fig. 4.8. First, in Fig. 4.8A we plot the total spin polarization $P = \int j_z(\vec{R})d\vec{R} / \int n(\vec{R})d\vec{R}$ of each reconstructed image. It is troubling that a large number of shots have a polarization far from zero, as show in Fig. 4.8C. Perhaps even more troubling is the clear oscillatory trend with trial number. Comparing the trend in polarization to the trends in the center of mass position x and RMS width R of the gas, see Fig. 4.8B, they appear to have fluctuation on a similar timescale. We can confirm this quantitatively by looking at the power spectrum of polarization fluctuations (Fig. 4.8D) and center of mass position fluctuations (Fig. 4.8E) which exhibit strong peaks at precisely the same frequency. Note that we calculate the frequency by accounting for the delay of about 15 seconds between each trial. Finally, by calculating correlation functions $C_{AB} = \langle A(j)B(j+dj)\rangle_j / \sqrt{\langle A(j)^2\rangle_j \langle B(j)^2\rangle_j}$ we confirm that there is a strong shot-to-shot correlation in the total polarization (Fig. 4.8F) and that the polarization and center-of-mass fluctuation are strongly correlated, though they are phase shifted (Fig. 4.8G).

This analysis strongly suggested that removing the source of center of mass fluctuations should dramatically decrease the systematic biasing of the polarization. We eventually found that the center of mass fluctuation was only present when the YDT retro-reflection, which

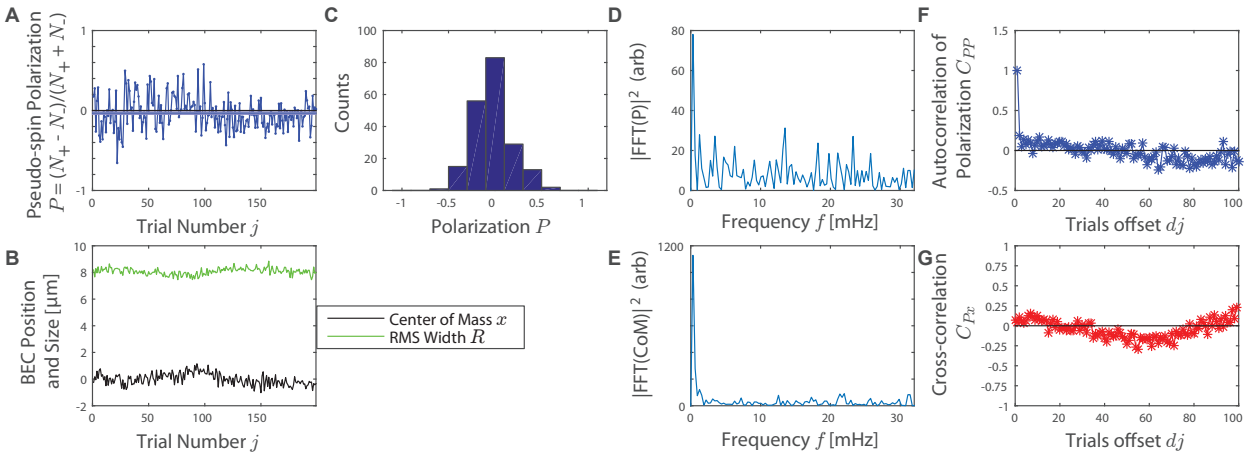

Figure 4.12: A series of analyses revealing the reduction in biasing of domain structures after eliminating the large, moving fringes caused by the YDT retroreflection. See text for details.

creates the shaking optical lattice, was turned on. To isolate that effect, we loaded BECs while almost completely turning off the XDT confinement, resulting in "snake"-like density profiles, see Fig. 4.9. This observation suggested that the YDT retro-reflection, in addition to creating the desired $d = 532$ nm lattice, was also creating some very long wavelength fringes due to small angle interference, which we assumed came from an unintentional reflection from a lens or window surface. The total trapping potential from those interference fringes and the ZDT beam propagating at a 45° angle had a snake-like appearance. By carefully turning down the power in ZDT as well, we were able to load atoms into a dipole trap which primarily took the shape of the long wavelength fringes (Fig. 4.10) which turned out to have a spacing of about $d' = 37$ μm. The relationship $d' = \lambda_L/2\sin(\theta/2)$ yields the small angle $\theta \approx 1.6°$ of the interference. Moreover, repeating this experiment for a couple of hours we saw the fringes drift systematically in one direction, suggesting that the fluctuation was a result of slow thermal drift of the optical path length difference between the beams responsible for the interference. This drift is likely a result of slow thermal expansion of the optical table over the course of each day, caused by the air-cooled MOT coils which are the only significant heat source on the optical table.

Our first approach to fixing the problem was to attempt to make the fringes stationary.

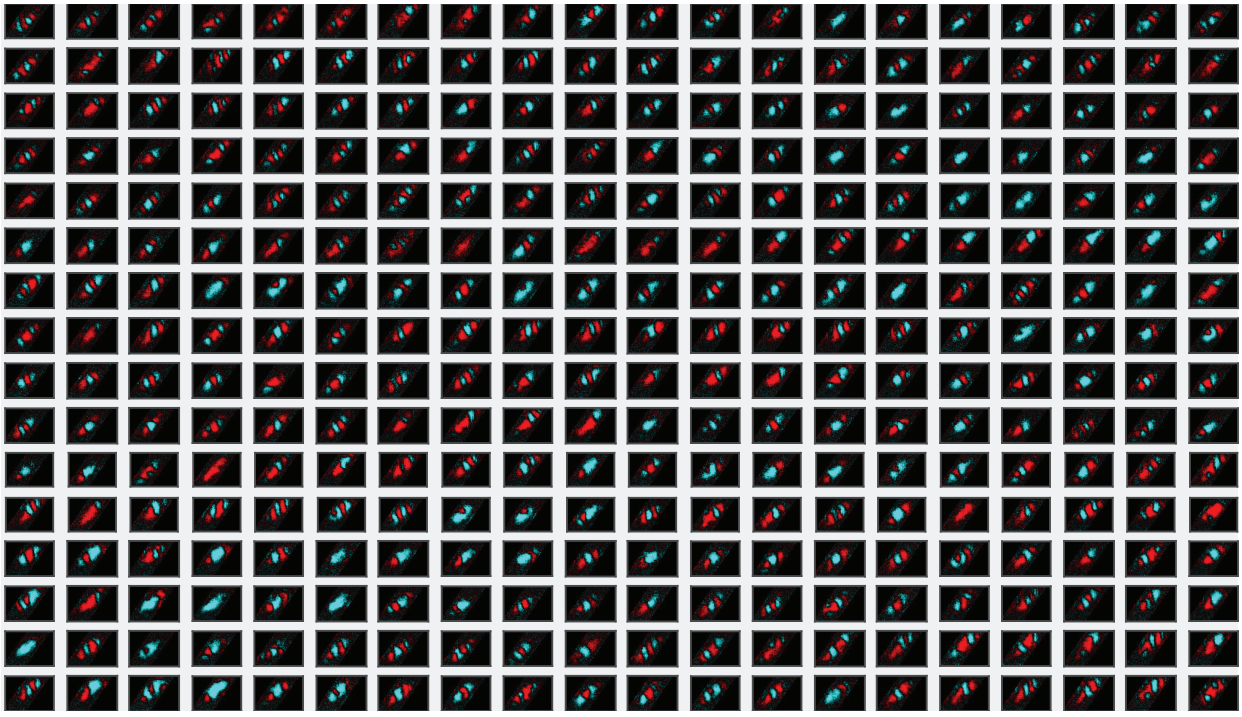

Figure 4.13: Example domain structures biased by the moving fringes due to the YDT retro beam. Images are time ordered, starting from the top left and moving right.

We spent quite a while seeking out tiny reflections of the YDT and YDT-retro beams off of windows, cubes, or lenses which might have intersected the main beams at the position of the atoms and been responsible for the fringes. We would then interfere each tiny reflection with a fraction of the main retro beam on a quadrant photodiode and lock the relative phase between the beams by feeding back on the phase of the retro beam using an AOM. We were never able to eliminate the motion of the fringes in this way.

Eventually, we discovered that the fringes were coming from a small reflection of the YDT-retro beam off of the fiber. Even better, rather than phase locking this reflection we simply removed it by preventing the YDT-retro beam from reaching the fiber in the first place, see Fig. 4.11. In the original setup, shown in black, the retro beam in this region had the same polarization as the incident beam and would normally transmit the PBS to reach the fiber mount; subsequent reflections from the fiber could transmit the PBS once again and reach the atoms. By adding the waveplates shown in blue, the retro and incident

Figure 4.14: Example domain structures after the large, moving fringes were eliminated. Images are time ordered, starting from the top left and moving right.

beams at the location of the atoms still have approximately the same polarization (up to errors caused by dichroic mirrors, AOMs, etc.) and therefore we still have an optical lattice, but the YDT-retro beam reflects from the PBS into a beam dump and never reaches the fiber. Note that we also added additional waveplates before the two AOMs responsible for controlling the retro power, so that the polarization would be linear as the beam passed through the AOMs. Also note that the ideal solution is to add an isolator directly after the fiber, but there was no space to implement that solution in the YDT beam path. We did add an isolator after the fiber in the XDT beam path.

To confirm that we had correctly diagnosed and solved the problem, we repeated the biasing analysis, see Fig. 4.12. In short, the magnitude of typical fluctuations of both the polarization and the shape and size of the gas was dramatically reduced. Moreover, the strong peaks from $2 \sim 4$ mHz in the fourier transforms were eliminated, and the main features in

C_{PP} and C_{Px} has been eliminated. Note that the correlations data still appear to show much weaker systematic trends on much longer timescales, but these are primarily caused by slow drifts of the total atom number (and the fact that there are only about 200 trials included in this dataset). To gain further intuition for the improvement, we have provided figures showing many domain structures in the previous strongly biased case (Fig. 4.13) and the much less biased case after eliminating the moving fringes (Fig. 4.14).

In order to focus the study described below on the dynamics across an unbiased quantum phase transition, we perform post-selection based on the total spin polarization $P = \int j_z(\vec{R})d\vec{R} / \int n(\vec{R})d\vec{R}$ of each reconstructed image, which is expected to be close to zero for unbiased samples. Indeed, under most conditions ($0.16 \leq \dot{s} < 1.0$ nm/ms) we find that more than 90% of images have total polarization $|P| < 0.3$. The correlation analysis excludes the remaining biased images with $|P| > 0.3$. For very slow ramps ($\dot{s} < 0.16$ nm/ms) starting from $s = 0$, we find that many samples are biased, likely due to increased susceptibility to a small, uncontrolled velocity between the condensate and the lattice. We have excluded data from these conditions to avoid poor statistics.

4.3.3 Lattice Depth Drift and Inhomogeneity

While it is always important to calibrate the lattice depth, it was especially important when testing the Kibble-Zurek mechanism because the critical shaking amplitude is extremely sensitive to lattice depth, see Fig. 4.15. Near our typical operating parameters, a change in the lattice depth by just 0.1 E_R or roughly 1% causes the critical shaking amplitude s_c to shift by nearly 0.5 nm or 4%, which can significantly effect the critical dynamics which occurs very close to the critical point for slow ramps.

To calibrate the lattice depth we load the BEC into the ground state of the optical lattice and then suddenly shift the position of the lattice by a small amount. This shift transfers atoms to a superposition of the ground and first excited bands in the lattice, leading to

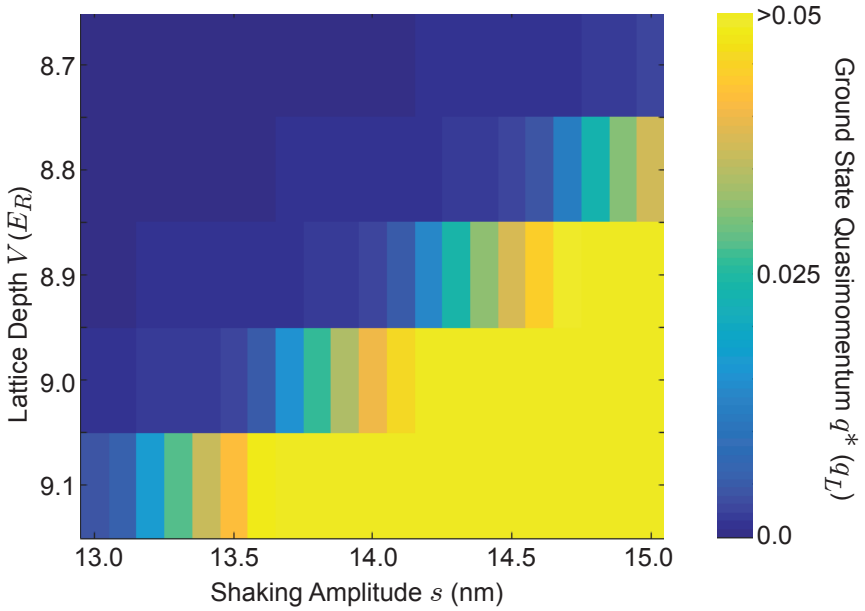

Figure 4.15: A heatmap of the ground state quasimomentum q^* as a function of the lattice depth and shaking amplitude, based on the Floquet calculation in Sec. 3.1. For a given lattice depth the critical shaking amplitude corresponds to the smallest amplitude at which $q^* > 0$.

oscillation of the atom number in the Bragg peaks at a frequency $f_{\text{cal}} = (E_2(0) - E_1(0))/h$, see Fig. 4.16. By fitting the oscillation of the peak imbalance over time with a sinusoid we can extract that frequency, equivalent to the $q = 0$ band gap, which uniquely specifies the lattice depth.

To account for slow drifts in our apparatus we re-calibrated the lattice depth approximately every 30 minutes to keep variation of the lattice depth at $\Delta U_0 < 0.1E_R$ while collecting data for the experiments described below.

In addition to the temporal stability of the lattice depth, similar problems can arise when the lattice depth varies significantly across the gas. We can detect this variation by splitting the data taken for lattice depth calibration into three segments, corresponding to the "top", "middle', and "bottom" of the gas, see Fig. 4.17A. We can then measure the oscillation of the peak imbalance over time separately for each segment and extract independent oscillation frequencies (corresponding to lattice depths) for each region of the gas. The measurement

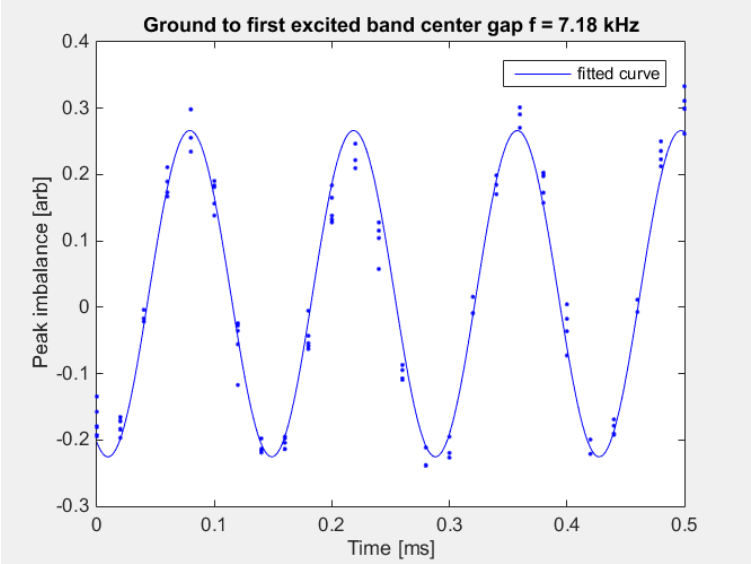

Figure 4.16: A plot of the atom number imbalance between the Bragg peaks $\Delta = (N_1 - N_{-1})/(N_1 + N_0 + N_{-1})$ after a sudden jump of the lattice position. The oscillation frequency determined from a sinusoidal fit (solid curve) indicates the energy difference between the first and second bands at $q = 0$, $hf_{\mathrm{cal}} = E_2(0) - E_1(0)$, from which we extract the lattice depth.

of the state of the system before correction is shown in Fig. 4.17B, and indicates a change in the lattice depth from one end of the gas to the other of approximately 0.5 E_R. Before performing the experiments described below, we carefully adjusted the alignment of the retroreflected beam to make the frequencies in each region equal. After this correction, the spatial inhomogeneity of the lattice depth is now less than the $\sim$0.1 E_R temporal fluctuation.

4.3.4 Accounting for Finite Imaging Resolution

Below, we study the one-dimensional domain structures along the lattice direction (x) by taking cuts $g_{\mathrm{meas}}(x)$ along the long-axis of the measured, normalized correlation functions $g(\mathbf{r})$. Since the domain walls are predominantly oriented along the non-lattice direction (y), long axis cuts maximize the range of the correlation functions that we can evaluate but still reflect the structure along the lattice direction.

To obtain the physical spin correlations we must remove the systematic effects of our finite

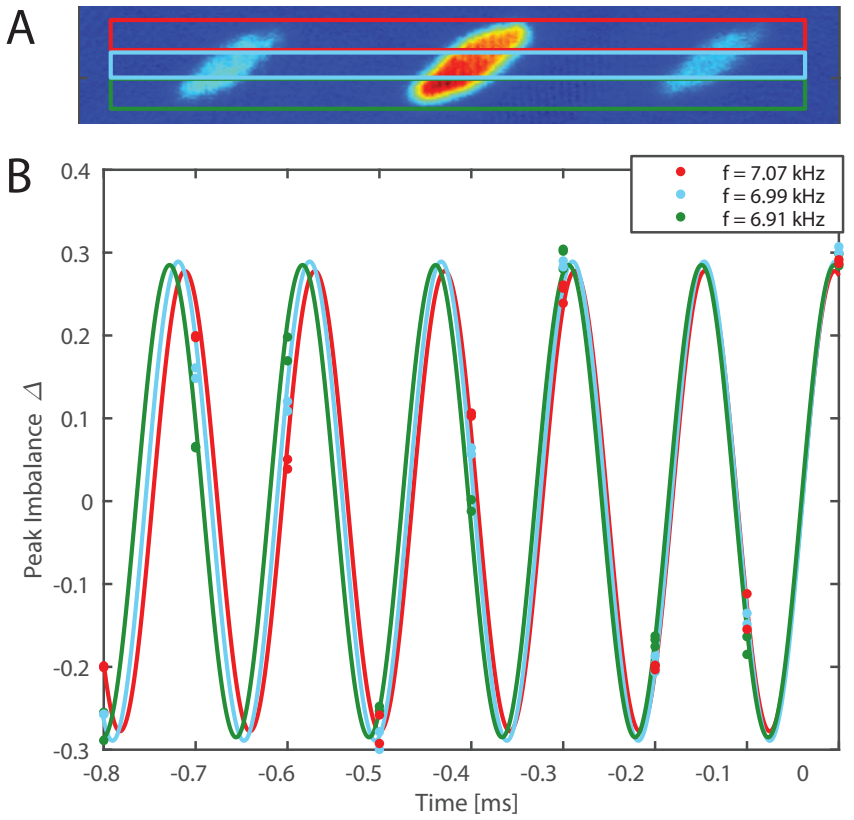

Figure 4.17: Measurement of lattice depth inhomogeneity. (A) We split the Bragg peaks into top (red), middle (cyan), and bottom (green) sections and calculate the peak imbalance Δ (see Fig. 4.16) in each section. (B) The peak imbalance over time for each section (circles) is fitted with a sinusoid (solid curves) to determine the local depth of the lattice, represented by the frequencies indicated at the top-right corner. In this example, the lattice depth is decreasing from the top to the bottom of the gas.

imaging resolution. Since the correlation functions depend on the spin density at both ends of the displacement vector, the measured correlations $g_{\mathrm{meas}}(x)$ are the physical correlations $g(x)$ convolved with the point spread function $P(x)$ twice [83]. We calculate the Fourier transform of the deconvolved correlation function $\tilde{g}(k) = \tilde{g}_{\mathrm{meas}}(k)/\tilde{P}^2(k)$ from the Fourier transforms of the measured correlations $\tilde{g}_{\mathrm{meas}}(k)$ and of the point spread function $\tilde{P}(k)$. Inverting the Fourier transform produces the correlation functions $g(x)$ shown in Fig. 4.24. Furthermore, from the peak position k_p in $\tilde{g}(k)$ we extract the typical domain size $d = \pi/k_p$, and from the full width at half maximum Δk of the peak we extract the correlation length

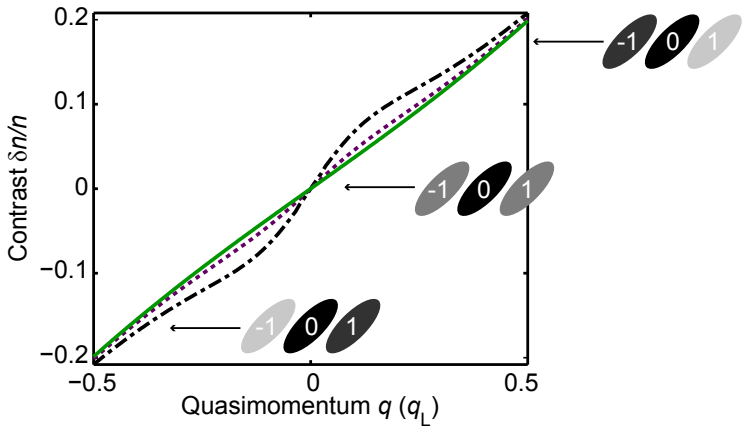

Figure 4.18: Detection of quasimomentum via density deviation. The contrast $\delta n/n$ between the ± 1 Bragg peaks can be used to assess the quasimomentum q, according to a calculation of the Floquet eigenstates in the shaken lattice (Sec. 3.1.2). The contrast only weakly depends on shaking amplitude, shown for $s = 0$ (solid), $s = s_c$ (dotted), and $s = 2s_c$ (dot-dashed). The illustrations represent the density in the three relevant Bragg peaks after time-of-flight.

$\xi = \pi/\Delta k$.

4.4 Results

4.4.1 Temporal Scaling of Phase Fluctuations

We begin our study of critical dynamics by testing the the scaling symmetry of time via the emergence of quasimomentum fluctuations at different quench rates. Here, fluctuations refer to deviations of quasimomentum from zero which vary across space and between individual samples; fluctuations should saturate to a large value when domains having $q = \pm q^*$ are fully formed. After loading the condensates into the lattice, we ramp the shaking amplitude linearly from $s = 0$ to values well above the critical amplitude $s_c = 13.1$ nm and interrupt the ramps at various times to perform a brief time-of-flight (TOF) before detection. After TOF we measure the density profiles of the Bragg peaks; $n_i(\mathbf{r})$ is the profile of the i'th Bragg peak.

We use the density fluctuation in the Bragg peaks to detect quasimomentum fluctuation

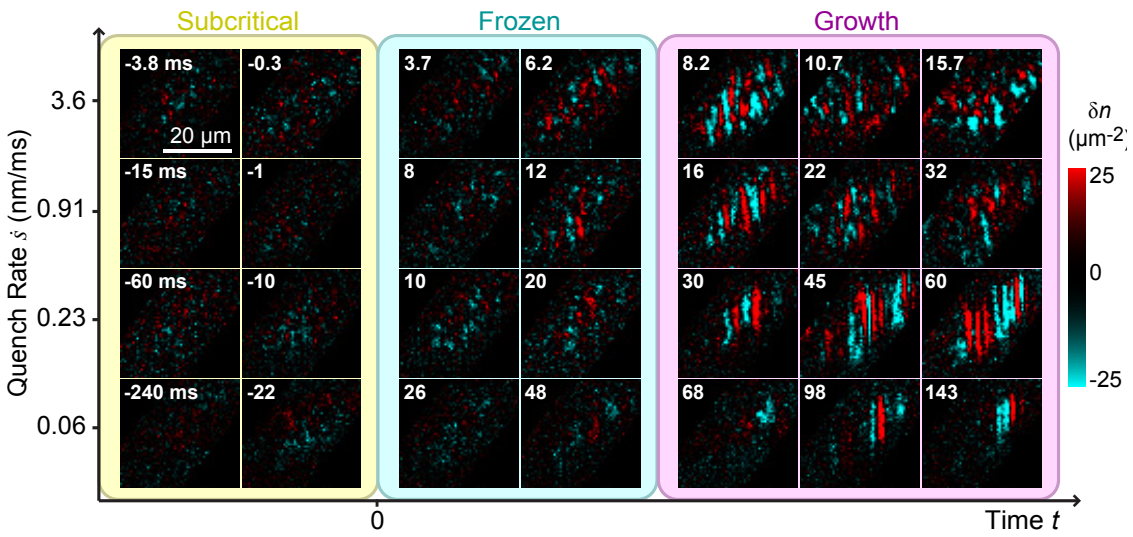

Figure 4.19: Sample images show the emergence of non-zero local quasimomentum via the density deviation between Bragg peaks δn as the system is linearly ramped across the ferromagnetic phase transition; four ramps with increasing quench rates (bottom to top) are shown. Each ramp exhibits three regimes: a subcritical regime before the transition, a frozen regime beyond the critical point where the fluctuation remains low, and a growth regime in which fluctuation increases and saturates, indicating domain formation. Time $t = 0$ corresponds to the moment when the system reaches the critical point.

in the gas. Non-zero local quasimomentum q changes the local density difference between Bragg peaks. To detect this change we perform a brief TOF with duration $t_{\mathrm{TOF}} = 5$ ms, which is long enough to separate the Bragg peaks but short enough that spatial information is preserved. From our images we calculate the density difference $\Delta n(\mathbf{r}) = n_{-1}(\mathbf{r}) - n_1(\mathbf{r})$ where $n_i(\mathbf{r})$ is the density of the i'th Bragg peak. To remove the small offset in Δn which exists at momentum $q = 0$, we calculate the density deviation $\delta n(\mathbf{r}) = \Delta n(\mathbf{r}) - \langle \Delta n(\mathbf{r}) \rangle$, where the angle brackets denote averaging over multiple images. The deviation δn is nearly proportional to the local quasimomentum regardless of the shaking amplitude (Fig. 4.18). Finally, we calculate the contrast fluctuation $\Delta c = \langle \delta n^2 / n^2 \rangle$ which closely tracks quasimomentum fluctuation in our condensates, where $n(r)$ is the total density. In this case, the angle brackets denote averaging over many images and over the position within each sample.

In order to remove spurious sources of fluctuation such as photon and atom shot noise,

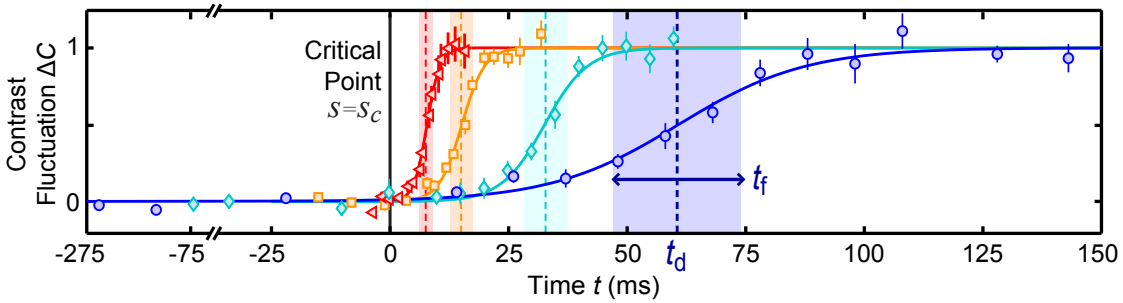

Figure 4.20: Quasimomentum fluctuation for ramp rates $\dot{s} = 3.6$ (triangles), 0.91 (squares), 0.23 (diamonds), and 0.06 (circles) nm/ms arises at a delay time $t = t_{\mathrm{d}}$ over a formation time t_{f}. Fluctuation is normalized for each ramp rate to aid comparison. The solid curves show fits based on Eq. 4.5. Error bars indicate one standard error.

we calculate the normalized fluctuations $\Delta C = (\Delta c - \Delta c_{\mathrm{i}})/(\Delta c_{\mathrm{f}} - \Delta c_{\mathrm{i}})$. Here we subtract the baseline value Δc_{i} for each ramp rate, which is given by the average of the three measurements at the earliest times taken below the critical point. Furthermore, even though quasimomentum fluctuation should continue to grow as q^{*2} with increasing shaking amplitude, where $\pm q^*$ are the quasimomenta of the ground states, we find that Δc appears to saturate to a nearly constant value for times well beyond t_d. We attribute saturation to the typical displacement $q^* t_{\mathrm{TOF}}/m$ during TOF becoming larger than the correlation length, such that fluctuation is dominated by the motion rather than the density of the Bragg peaks. We normalize Δc to its saturated value Δc_f at each ramp rate for convenient comparison. We determine Δc_f by averaging the latest three measured values, which are taken well beyond the delay time t_d.

Over a wide range of quench rates the evolution of quasimomentum fluctuation can be described in three phases (Fig. 4.19). First, below the critical point, quasimomentum fluctuation does not exceed its baseline level. Second, just after passing the critical point, critical slowing keeps the system "frozen", and fluctuation remains low. Finally, the system unfreezes and quasimomentum fluctuation quickly increases and saturates, indicating the emergence of ferromagnetic domains. We quantify this progression by investigating the growth of the fluctuation of contrast (Fig. 4.20). We find empirically that the growth of

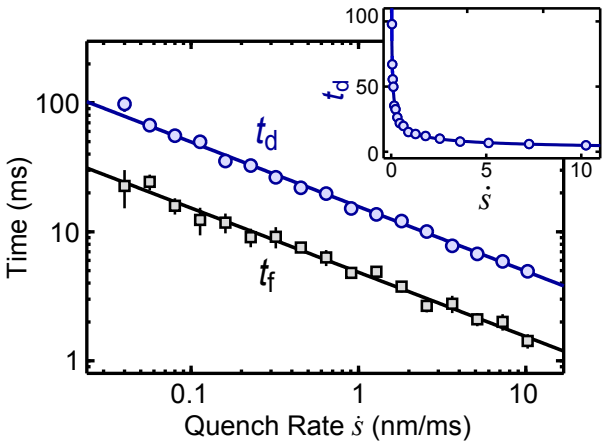

Figure 4.21: The dependence of $t_{\rm d}$ (circles) and $t_{\rm f}$ (squares) on the quench rate is well fit by power-laws (solid curves) with scaling exponents of $a_{\rm d} = 0.50(2)$ and $a_{\rm f} = 0.50(6)$, respectively. The inset shows $t_{\rm d}$ on a linear scale. Error bars indicate one standard error.

normalized fluctuations is well fit by the function

$$\Delta C(t) = \frac{1}{2} + \frac{1}{2}\tanh\left(\frac{t - t_{\rm d}}{t_{\rm f}}\right), \tag{4.5}$$

where the time t is defined relative to when the system crosses the critical point at $t = 0$, $t_{\rm d}$ characterizes the delay time when the system unfreezes, and $t_{\rm f}$ is the formation time over which the fluctuation grows.

The measurement of fluctuation over time provides a critical test for both the Kibble-Zurek scaling and the universality hypothesis. First, both t_d and t_f exhibit clear power-law scaling with the quench rate $\dot{s}$ varied over more than two orders of magnitude (Fig. 4.21). Power-law fits yield the exponents of $a_{\rm d} = 0.50(2)$ and $a_{\rm f} = 0.50(6)$, respectively. The nearly equal exponents are suggestive of the universality hypothesis, which requires all times to scale identically. Indeed, the growth of contrast fluctuation ΔC follows a universal curve when time is scaled by $t_{\rm d}$ (Fig. 4.22), strongly supporting the universality hypothesis (Eq. 4.3). Note that any observable time characterizing the collective dynamics can be chosen as $t_{\rm KZ}$ in Eq. 4.3, including $t_{\rm d}$ and $t_{\rm f}$.

Note that it is not possible to reconstruct the spin density under these conditions because

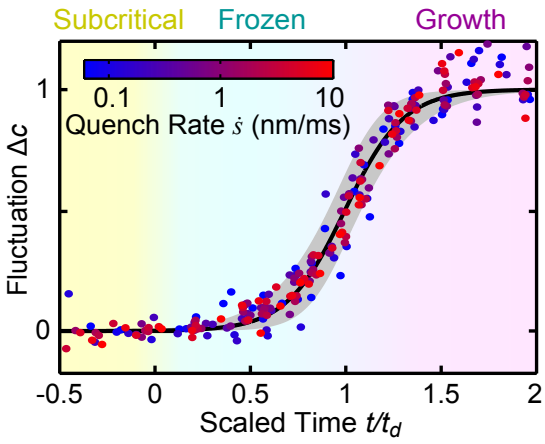

Figure 4.22: Fluctuations measured for 16 ramp rates from 0.06 to 10.3 nm/ms collapse to a single curve when time is scaled by t_{d} based on the power-law fit. The solid curve shows the best fit based on the empirical function (Eq. 4.5), and the gray shaded region covers one standard deviation.

the atoms have not yet settled primarily to $q = \pm q^*$ (Sec. 4.3.1). Here, our intention is to show the growth of quasi-momentum fluctuations across the critical point and thus the observable needs to be well defined even in the subcritical and frozen regime. The advantage of the chosen detection method is that it is particularly sensitive near the critical point when the quasimomentum just starts deviating from zero, indicating the emergence of fluctuations in the ferromagnetic phase where the ground states have non-zero quasimomentum. However, this method has some disadvantages when the quasimomentum becomes large. Specifically, while ΔC is proportional to q^2 for small quasimomentum, that relationship no longer holds once quasimomentum is large and the motion of atoms with different momentum during TOF dominates ΔC. It is actually that motion which should dominate the saturated value of ΔC in our dataset. Moreover, at an intermediate ramp rate of approximately 0.4 nm/ms the expected displacement for atoms with q^* at $t = 1.4\ t_d$ becomes equal to the typical domain size, and we expect the saturated value of ΔC to become essentially independent of q.

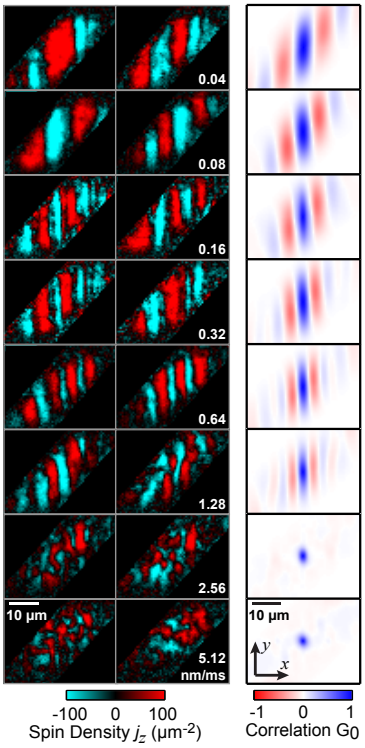

Figure 4.23: (Left) Two sample images at each quench rate exemplify spin domains measured near the time $t = 1.4\ t_{\rm d}$ after crossing the phase transition. These images correspond to linear ramps starting at $s = 0$ ($\dot{s} = 0.32$-5.12 nm/ms) and $s = s_c$ ($\dot{s} = 0.04$-0.16 nm/ms). (Right) Spin correlation functions $G_0(\mathbf{r}) = G(\mathbf{r})/G(0)$ (Eq. 4.6) are calculated from ensembles of 110-200 images.

4.4.2 Spatial Scaling of Pseudo-spin Correlations

We next test the spatial scaling symmetry based on the structures of pseudo-spin domains that emerge after the system unfreezes. Here, we cross the critical point with two different protocols: the first is a linear ramp starting from $s = 0$, while the second begins with a jump to $s = s_c$, followed by a linear ramp. We detect domains near the time $t = 1.4\ t_{\rm d}$ in the spin density distribution $j_z(\mathbf{r}) = n_+(\mathbf{r}) - n_-(\mathbf{r})$ based on the density $n_{+/-}$ of atoms with spin up/down (Sec. 4.3.1). At this time the spin domains are fully-formed and clearly separated by topological defects (domain walls), as shown in Fig. 4.23. Furthermore, choosing this time just after domain formation minimizes the time available for non-universal relaxation processes. We characterize the domain distribution with the spin correlation function [135,

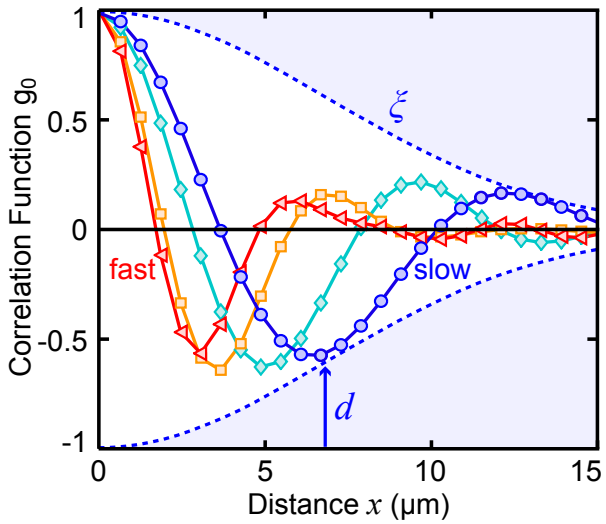

Figure 4.24: Cuts across the density-weighted correlation functions $g_0(x) = g(x)/g(0)$ are shown for quench rates $\dot{s} = 1.28$ (triangles), 0.45 (squares), 0.16 (diamonds), and 0.056 nm/ms (circles). Solid curves interpolate the data to guide the eye. The typical domain size d and the correlation length ξ are illustrated for 0.056 nm/ms by the arrow and dashed envelope, respectively.

119],

$$G(\mathbf{r}) = \left\langle \int j_z(\mathbf{R}+\mathbf{r}) j_z(\mathbf{R}) d\mathbf{R} \right\rangle, \tag{4.6}$$

averaged over multiple images. Both ramping protocols lead to similar correlation functions, suggesting that the domain distribution is insensitive to increases in the quench rate below the critical point.

The spin correlations reveal rich domain structure that strongly depends on the quench rate, see Fig. 4.23. For slower ramps $\dot{s} < 1.3$ nm/ms the structures are predominantly one-dimensional and the density of topological defects increases with the quench rate. The tighter confinement and finite speed of sound near the critical point along the $y-$ and z-axes allow spin correlations to span the gas in those directions. The dynamics thus appear one-dimensional. When the quench rate exceeds 1.3 nm/ms, defects start appearing along the y-axis, and the domain structures become multi-dimensional. We discuss this effect further in Sec. 4.4.3. For most of this chapter (and the remainder of this section) we focus on the

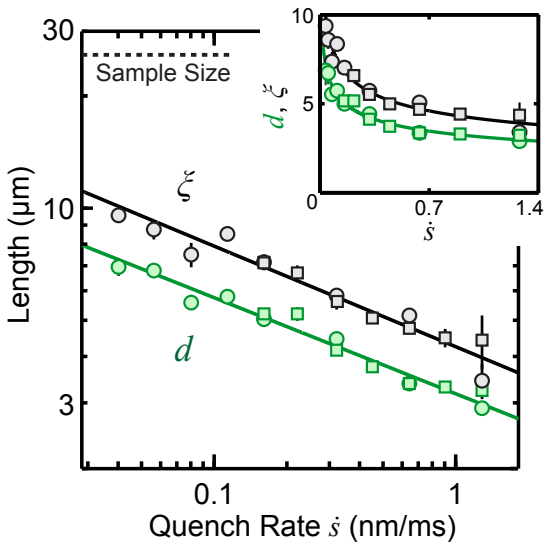

Figure 4.25: Kibble-Zurek scaling of characteristic lengthscales. The dependence of d (green) and ξ (black) on the quench rate is well fit by power-laws (Eq. 4.2) with spatial scaling exponents of $b_{\mathrm{d}} = 0.26(2)$ and $b_{\xi} = 0.26(5)$, respectively. Marker shape indicates linear ramps starting at $s = 0$ (squares) or at $s = s_c$ (circles). The inset shows the results on a linear scale. Error bars indicate one standard error.

slower quenches and investigate the spin correlations along the x-axis.

We examine the one-dimensional correlations using line cuts of the density-weighted correlation functions $g(\mathbf{r}) = G(\mathbf{r})/\langle \int n(\mathbf{R}+\mathbf{r})n(\mathbf{R})d\mathbf{R}\rangle$ [135, 119]. The results exhibit prominent decaying oscillation (Fig. 4.24). We extract two essential length scales from the correlation functions: the average domain size d, or equivalently the distance between neighboring topological defects, and the correlation length ξ, indicating the width of the envelope function. These two scales are determined from the position and width of the peak in the Fourier transform of $g(x)$, see Sec. 4.3.4.

These length scales enable us to test the spatial scaling symmetry. The lengths d and ξ both display power-law scaling consistent with the Kibble-Zurek mechanism, see Fig. 4.25, with fits yielding exponents $b_{\mathrm{d}} = 0.26(2)$ for the domain size and $b_{\xi} = 0.26(5)$ for the correlation length. Similarly, the correlations, measured at the same scaled time, collapse to a single curve in spatial coordinates scaled by the domain size d (Fig. 4.26). This result

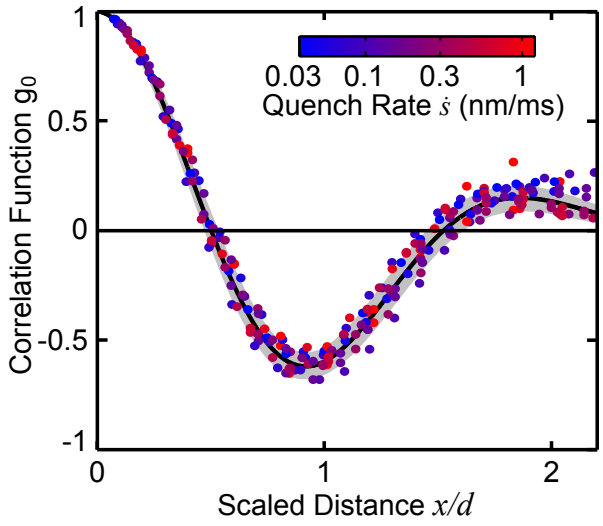

Figure 4.26: Collapse of pseudo-spin correlations in scaled space-time. Correlation functions for $\dot{s} = 0.04$-1.28 nm/ms collapse to a single curve when distance is scaled by the domain size extracted from the power-law fit in Fig. 4.25. The solid curve shows the fit based on Eq. 4.7; the gray shaded area covers one standard deviation.

strongly supports the spatiotemporal scaling from the universality hypothesis (Eq. 4.3). An empirical curve,

$$g_0(x) = \exp\left(-\frac{1}{2\sigma^2}\frac{x^2}{d^2}\right)\cos\left(\frac{\pi}{\gamma}\frac{x}{d}\right), \tag{4.7}$$

provides a good fit to the universal correlation function, yielding $\sigma = 1.01(1)$ and $\gamma = 1.04(1)$, indicating that the width of the envelope is close to the typical domain size.

The most striking feature of the universal correlation function is the emergence of oscillatory, anti-ferromagnetic order in the ferromagnetic phase. In thermal equilibrium, ferromagnets are expected to have a finite correlation length but no anti-correlation. The appearance of strong anti-correlation at $x = d$ suggests that domains of size d form preferentially during the quantum critical dynamics.

To better understand the process which generates domain walls we calculate the domain size distribution from our images. We identify domain walls by integrating the spin density along the y-direction, filtering noise at the single pixel scale (0.6 μm) which is below our

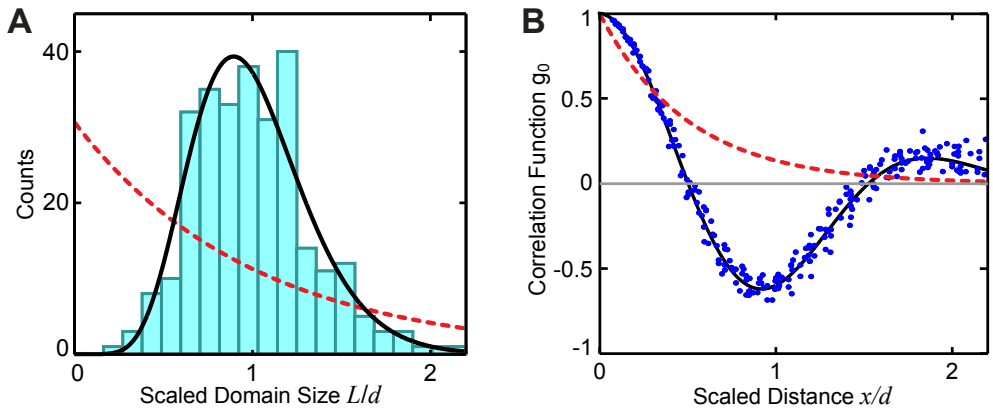

Figure 4.27: Sub-Poisson generation of domain walls. (**A**) The distribution of domain sizes L for 110 samples with quench rate $\dot{s} = 0.08$ nm/ms is bunched near the average domain size d. The solid curve shows a fit based on the function $A(L/d)^{a-1}e^{-aL/d}$, where the coefficient $A = a^a/\Gamma(a)$, which interpolates between the exponential ($a = 1$) and delta ($a \to \infty$) distributions. The fit yields $a = 10(1)$ for the measured distribution. For comparison, the dashed curve shows an exponential distribution ($a = 1$) corresponding to Poisson generation of defects. (**B**) Poisson generation of defects would lead to exponential decay of spin correlations as $g_{\mathrm{P}}(x) = e^{-2x/d}$ (dashed curve), which does not exhibit the anti-correlation seen in the data from Fig. 3E (blue points). The solid curve shows the fit to the measured correlations based on Eq. 7.

resolution limit, and locating where the spin density changes sign. We calculate the domain sizes from the distances between neighboring walls.

Since the correlation functions in scaled space are invariant with quench rate we focus on a single rate $\dot{s} = 0.08$ nm/ms, for which the domains are relatively large ($d = 6.0$ μm) and easy to resolve. The resulting domain size distribution (Fig. 4.27A) is tightly bunched around its mean. Indeed, the standard deviation $\sigma_d = 0.31(2)d$ is well below the mean. This bunching would not be expected for a Poisson process, which should exhibit an exponential distribution due to the constant probability of forming a domain wall at any location. Similarly, Poisson generation of domain walls would lead to exponentially decaying correlations that are qualitatively distinct from the oscillatory correlations observed in our experiments (Fig. 4.27B).

The direct identification of domain walls presents intriguing possibilities for future studies

of the topological defects generated during critical dynamics. These opportunities would be particularly interesting if the shaking technique is extended to higher dimensions in such a way that the transition breaks a continuous symmetry. In addition, the scaling of the correlation functions suggests that the anti-ferromagnetic order may be a shared feature of quantum critical dynamics for phase transitions in the same universality class, meriting future experiments.

4.4.3 Breakdown of KZM Scaling

We seem to observe a breakdown of the Kibble-Zurek scaling for extremely slow ($\dot{s} <\sim$ 0.04 nm/ms) and extremely fast ($\dot{s} >\sim$ 1.28nm/ms) quench rates. For the slowest ramp, it is likely that the inhomogeneity of the density and the finite size of the gas are becoming relevant. Specifically, while interaction effects only shift the critical point in our system by a few percent from the center to the edge (see Secs. 3.3 and 4.1), eventually this shift represents a significant fraction of the distance of the shaking amplitude s_d at which the system is unfreezing from the critical amplitude s_c. Moreover, the combination of the trapping potential and small changes of the interaction strength during the slow ramp of the shaking amplitude may lead to small collective motions which could bias the system as it crosses the phase transition. Finally, even in a homogeneous system one would expect finite size effects to prevent scaling beyond the point when the domain size is comparable to the system size.

Generically, for fast ramps the KZM scaling should break down when the microscopic scales of the system become comparable to the scales characterizing macroscopic dynamics. Specific to our experiments, the breakdown of scaling could result from the impossibility of localizing the quasimomentum q within a finite domain whose size $d_{\min}$ approaches the limit from the Heisenberg uncertainty principle, $d_{\min} \approx \hbar/q$. Specifically, to localize the quasimomentum in a domain at the level of $q = 0.1q_{\mathrm{L}}$ we find $d_{\min} \approx 2$ μm. which is close to the expected domain size for the fastest ramps measured (2.56$\sim$5.12 nm/ms, see

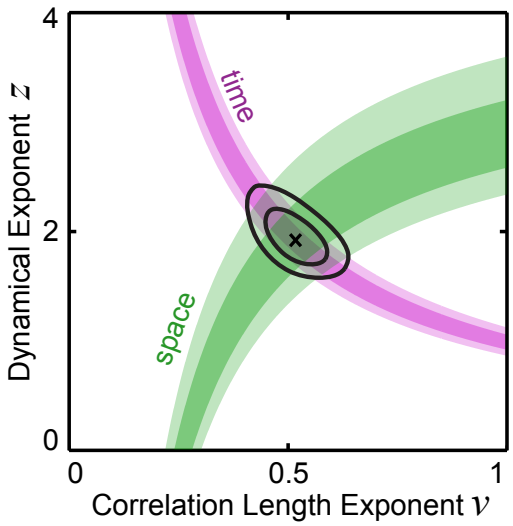

Figure 4.28: Constraints on the equilibrium critical exponents based on dynamics. The temporal scaling exponents a_d and a_f from Fig. 4.21 (magenta) and the spatial scaling exponents b_d and b_ξ from Fig. 4.25 (green) constrain the critical exponents ν and z according to Eqs. 4.8 and 4.9 with 68% (dark) and 95% (light) confidence intervals. The cross marks the best values with contours of 68% and 95% overall confidence.

Fig. 4.23). Instead of observing domains covering just a small number of lattice sites, we see the breakdown of the universal scaling due to the relevance of the microscopic length scale. It is intriguing to note that the temporal scaling seems to continue unperturbed even beyond this limit, see Fig. 4.21.

4.4.4 Critical Exponents

The combined scaling exponents of space and time allow us to extract the equilibrium critical exponents based on the Kibble-Zurek mechanism [157] (Fig. 4.28). From the measured temporal scaling exponent $a = 0.50(2)$ and Eq. 4.1 we derive the constraint,

$$z = \frac{a}{(1-a)\nu}, \tag{4.8}$$

indicated in magenta in Fig. 4.28. From the measured spatial scaling exponent $b = 0.26(2)$ and using Eq. 4.2 we derive the second constraint,

$$z = \frac{\nu - b}{\nu b}. \tag{4.9}$$

indicated in green in Fig. 4.28. More precisely, to determine the constraints on z and ν presented in Fig. 4.28, we first calculate the relative likelihood of different values of the dynamic exponents (a and b) based on the reduced chi-squared values for using power-laws to explain the experimental data in Figs. 4.21 and 4.25. We then convert the likelihood of the dynamic exponents into the likelihood of the equilibrium exponents, from which we determine the confidence intervals shown.

The combination of both constraints yields,

$$\nu = \frac{b}{1-a}, \tag{4.10}$$

$$z = \frac{a}{b}. \tag{4.11}$$

Combining the two constraints we obtain the dynamical exponent $z = 1.9(2)$ and correlation length exponent $\nu = 0.52(5)$, which are close to the mean-field values $z = 2$ and $\nu = 1/2$ up to our experimental uncertainty. Note that the dynamical critical exponent $z = 2$ results from the unique quartic kinetic energy $\epsilon = \beta q_x^4$ of our system at the critical point (Sec. 4.2).

4.4.5 Universality vs Interaction Strength

The power of the universality hypothesis (Eqn. 4.3) is that it strictly limits the possible effects of changing microscopic system parameters. The length- and time-scales characterizing the dynamics may change, but the functional form of any observable should not. Therefore, as long as we remain within the universal range (Sec. 4.4.3), the unfreezing process should

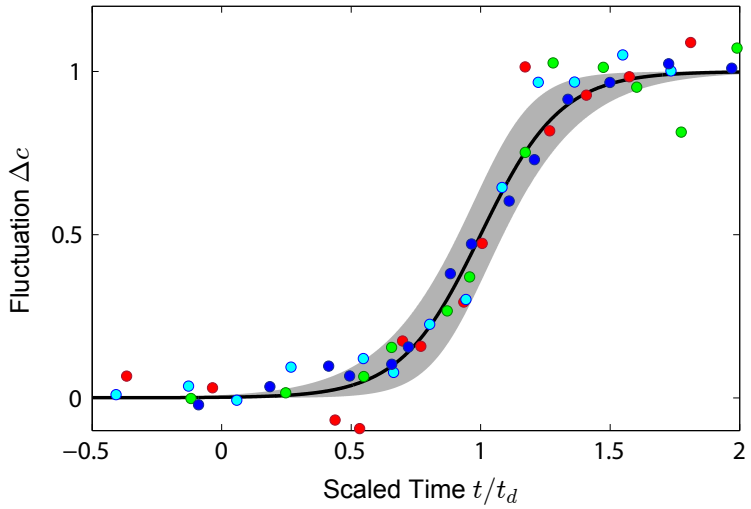

Figure 4.29: Universality of the unfreezing function with scattering length. Contrast fluctuations for linear ramps across the phase transition with scattering lengths 20 a_0 (blue), 60 a_0 (green), 100 a_0 (cyan), and 200 a_0 (red). Time is scaled by $t_{\mathrm{d}}(a)$ extracted from independent fits based on Eq. 4.5 to the data at each scattering length. The solid curve and shaded region indicate the universal function and its uncertainty from Fig. 4.22.

follow the universal function shown in Fig. 4.22 and the pseudo-spin correlations should match the form in Fig. 4.26.

Here we test that prediction by characterizing the critical dynamics for different interaction strengths. Before shaking the lattice we adiabatically ramp the scattering length from its usual starting value of 40 a_0 to final values between 20 a_0 and 200 a_0. In the Thomas-Fermi approximation for a harmonic trap the interaction energy scales as $\mu \propto a^{2/5}$; therefore, over this range we vary the interaction energy by a factor of approximately 2.5. For each final scattering length we follow the procedure described in Sec. 4.4.1 to measure the growth of contrast fluctuations (Fig. 4.29). For each contrast curve, t_d was extracted and time was scaled to t_d. The delay times were found to be t_d = 22.8 ms(200a0), 23.7 ms (100 a_0), 26.0 ms (60 a_0), 35.9 ms (20 a_0). The growth of contrast does appear to be approximately consistent with the universal function in scaled time across all of the different interaction strengths.

Next, we followed the procedure described in Sec. 4.4.2 to measure the pseudo-spin corre-

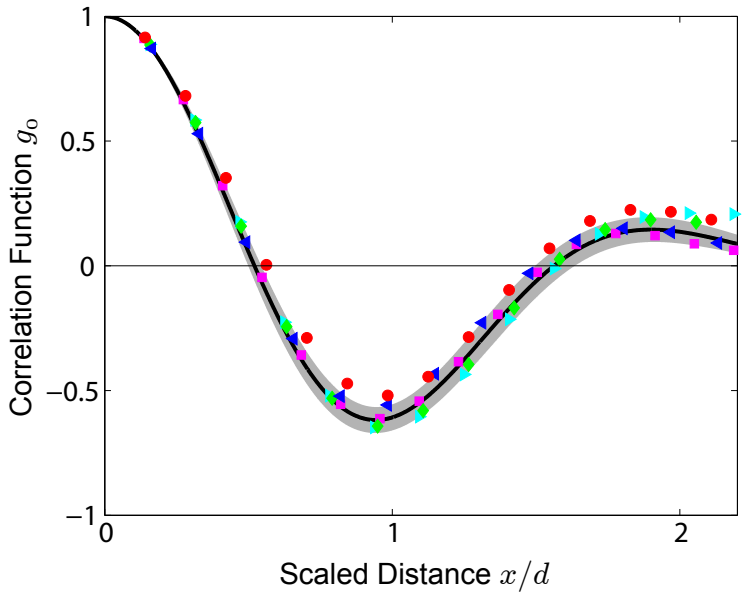

Figure 4.30: Universality of pseudo-spin correlations with scattering length. Correlation functions at $t = 1.4\ t_d$ calculated from domain structures formed for linear ramps starting at $s = s_c$ with scattering lengths 20 a_0 (blue $\triangleleft$), 40 a_0 (magenta $\square$), 60 a_0 (green $\diamond$), 100 a_0 (cyan $\triangleright$), and 200 a_0 (red $\circ$). The typical domain size d is extracted independently for the data at each scattering length based on its fourier transform, as discussed in Sec. 4.4.2. The solid curve and shaded region indicate the universal function and its uncertainty from Fig. 4.26.

lations for different scattering lengths (Fig. 4.30). For each correlation curve, d was extracted and space was scaled to that specific d. All data were collected for 0.32 nm/ms ramps after jumping to the critical point. The spatial correlation functions appear consistent with the universal function, within one standard deviation, for scattering lengths from 20 a_0 to 200 a_0. The dependence of the length scale on scattering length is quite weak: the domain sizes for each dataset are 3.69 μm (20 a_0), 3.82 μm (60 a_0), 3.87 μm (100 a_0), 4.30 μm (200 a_0). However, the dependence is at least monotonic in the expected direction (larger scattering lengths lead to bigger domains). Overall, we find that the universal functions still appear to describe both the unfreezing and the correlations even after a dramatic change in the interaction strength.

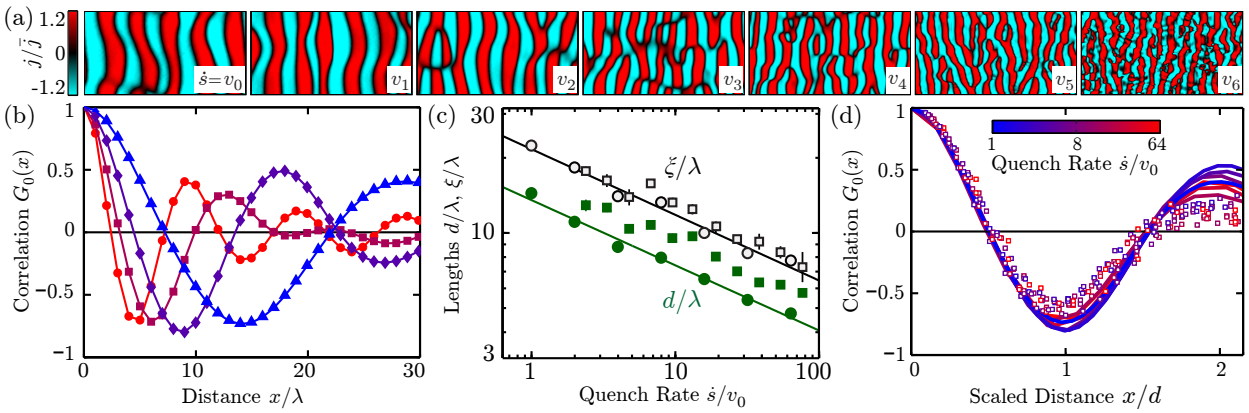

Figure 4.31: Comparison of correlation functions between simulation and experiment. (a) Simulated domain structures showing a snapshot of the local current density j normalized to its RMS value $\bar{j}$. Each snapshot corresponds to a different quench rate indicated at the bottom right, with $v_n = 2^n v_0$ and $v_0 = 0.98 s_c \omega/(2^8 50\pi)$. (b) Plots of the normalized correlation functions before rescaling the distance, cf. Fig. 4.24. (c) Scaling of the typical domain size d (solid circles) and the correlation length ξ (open circles) extracted from the simulations, compared with the corresponding experimental results (squares). (d) In scaled spatial coordinates x/d, the correlation functions for every quench rate collapse onto a single curve (solid lines), consistent with the experimental results (squares), cf. Fig. 4.26. See Ref. [7] for more details.

4.4.6 Simulations of the critical dynamics

We have performed simulations of condensates crossing the effectively ferromagnetic quantum phase transition, which are presented in Brandon M. Anderson, Logan W Clark, Jennifer Crawford, Andreas Glatz, Igor S Aranson, Peter Scherpelz, Lei Feng, Cheng Chin, and K Levin, "Direct lattice shaking of bose condensates: Finite momentum superfluids", *Physical Review Letters*, 118(22):220401, 2017 (Copyright 2017 by the American Physical Society). We briefly summarize that work here.

We simulate ultracold bosons in the shaken lattice using the Gross-Pitaevskii equation (GPE), which describes the time-evolution of a Bose condensate under the mean-field approximation. Unlike our simulations of domain walls (see Sec. 3.4), for which we used an effective model where the GPE is directly modified to include quadratic and quartic terms in the dispersion, in this work we time evolve the GPE with an explicit lattice potential which

oscillates over time. With this approach we can directly observe evolution of the superfluid in the shaken lattice without making assumptions about its effects, aside from the mean-field approximation implicit in the GPE. As a result, these simulations also manifest effects like heating due to absorption of shaking "photons" which would not ordinarily appear in an effective model. Note that a naive GPE simulation does not accurately capture the behavior of our system, because it does not include the fluctuation which seeds the domain structures that form in the ferromagnetic phase. In practice, we approximate this fluctuation using phenomenological noise and dissipation terms. We find that the simulations capture quite a few of the key features observed in the experiments, in particular yielding similar scaling exponents and universal correlation function, see Fig. 4.31. For further discussion of our simulation results, please see Ref. [7].

10.1038/nature24272

CHAPTER 5

BOSE FIREWORKS

Much of the content in this chapter is based on our published work [43], which can currently be found as a preprint arXiv:1706.05560 will appear in *Nature* with doi:10.1038/nature24272. The thesis author played the primary role in the work described in this chapter.

5.1 Background

Scattering experiments have frequently provided fascinating insights into fundamental questions of physics. Scattering in many-body quantum systems presents a new frontier, in which the interplay of many collision events can create phenomena which appear completely different from the underlying pair scattering processes. In this chapter we report on a new such phenomenon, in which collisions in Bose-Einstein condensates with periodically modulated interaction strength lead to ejection of matter-wave jets. The emitted jets form a remarkable, fireworks-like structure (Fig. 5.1) even though the underlying microscopic process is simply isotropic, s-wave scattering. Surprisingly, this behavior is robust across a huge range of modulation frequencies and belongs to a new class of processes analogous to superradiance that has not been observed in former experiments.

Ultracold atomic gases provide a powerful platform in which control over pair-wise interactions empowers us to investigate scattering in quantum many-body systems [36]. Past experiments on colliding Bose-Einstein condensates have revealed many important features, including matter-wave interference [10, 6], halos of scattered atoms [35, 30], four-wave mixing [51, 149], and correlations between counter-propagating pairs [120, 121, 87]. However, a regime with strong stimulation of spontaneous collisions [126, 55, 147, 14, 166, 116, 117, 52, 151, 132] analogous to superradiance [85, 113, 138] has proven elusive. Here we access that regime, finding that runaway stimulated collisions in condensates with modulated interaction

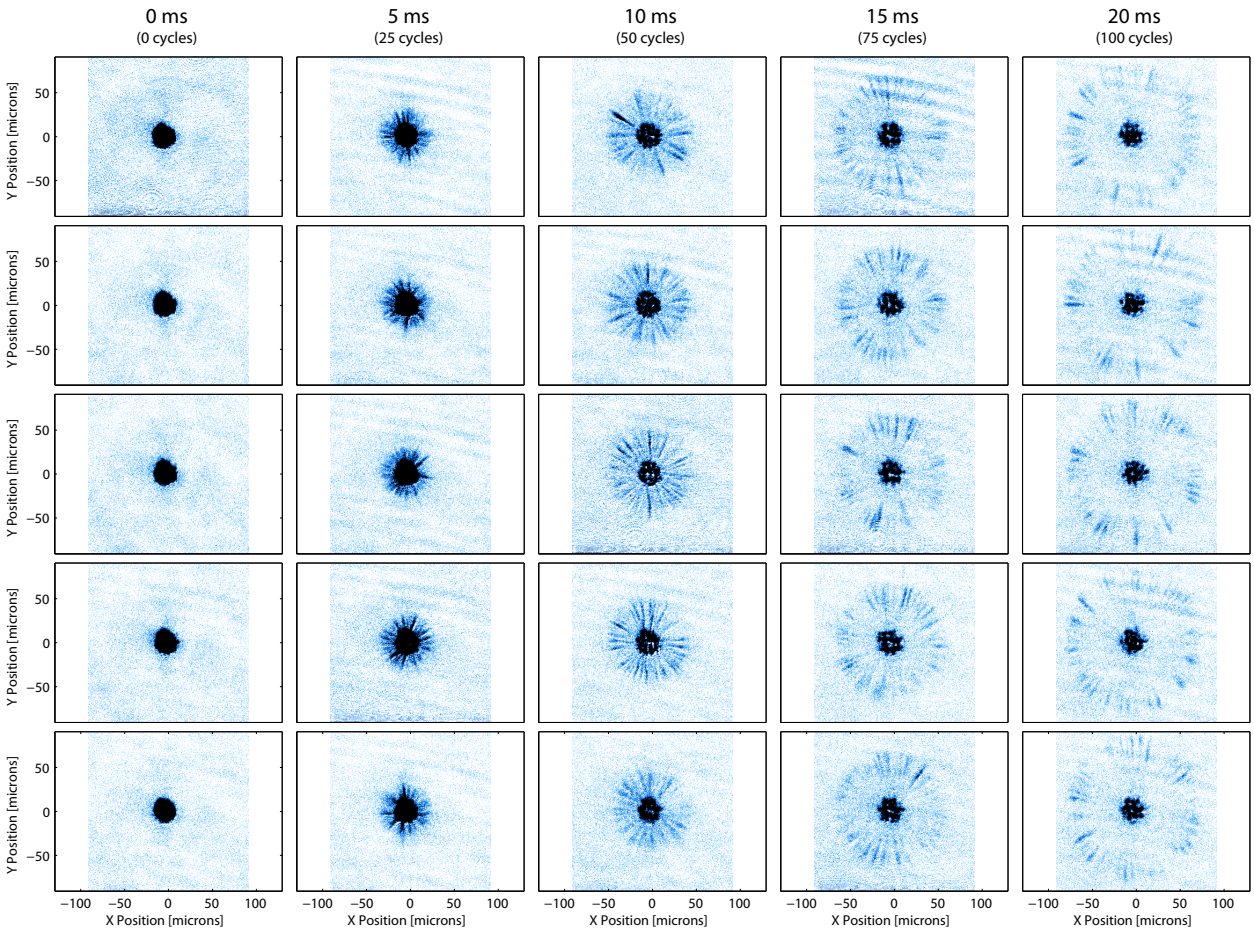

Figure 5.1: Example image series of Bose fireworks in a harmonic trap with approximately symmetric horizontal trap frequency $\omega_r = 2\pi \times 6$ Hz and tight vertical trapping $\omega_z = 2\pi \times 260$ Hz. The conditions are $a_{\rm dc} = 10\ a_0$, amplitude $a_{\rm ac} = 40\ a_0$, and $f = 5$ kHz.

strength cause the emission of matter-wave jets which resemble fireworks. In spite of the isotropic nature of the underlying s-wave collisions, the jets are also spontaneously directed such that they only propagate in the plane of the disk-shaped condensate. Moreover, jets appear only above a threshold modulation amplitude and their correlations are invariant even as the ejected atom number grows exponentially. Hence, we show that the structures and occupations of the jets stem from the quantum fluctuations of the condensate. Our findings demonstrate the conditions for runaway stimulated collisions and reveal the quantum nature of the matter-wave emission.

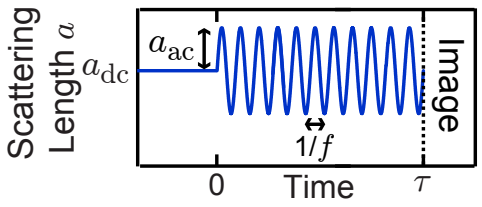

Figure 5.2: In a typical experiment we modulate the scattering length as $a(t) = a_{\rm dc} + a_{\rm ac}\sin(\omega t)$ where $\omega \equiv 2\pi f$ for a time τ before collecting an image of the resulting density distribution.

5.2 Theory

The interplay between spontaneous and stimulated scattering events underpins many interesting physical phenomena. In general, spontaneous events dominate for low scattering rates. When the scattering rate exceeds a threshold, stimulated processes can "run away", leading to exponential amplification of outgoing particles. As a result, the character of the emission dramatically changes. A well-known example is the laser, in which a sufficient rate of stimulated emission results in a coherent wave of photons. Here, we show that runaway stimulation of collective atom-atom scattering in a driven Bose-Einstein condensate causes it to emit a burst of matter-wave jets.

5.2.1 Condensate filling space

Before treating the realistic, finite size system below, we can gain valuable intuition by treating a condensate which fills all of space. Here, we will find that the oscillating interaction strength induces a dynamical instability which allows pairs of atoms to collide and populate modes with opposite momentum and total energy close to one quantum of the oscillating field. As a result, the populations of those modes grow exponentially and there is a strong correlation between pairs of modes with opposite momentum.

To treat the infinite system, the general Hamiltonian with which we begin is,

$$H = \sum_{\boldsymbol{k}} \frac{\hbar^2 k^2}{2m} b^\dagger_{\boldsymbol{k}} b_{\boldsymbol{k}} + \frac{g(t)}{2V} \sum_{\boldsymbol{k_1 k_2 q}} b^\dagger_{\boldsymbol{k_2+q}} b^\dagger_{\boldsymbol{k_1-q}} b_{\boldsymbol{k_1}} b_{\boldsymbol{k_2}}$$

where $b_{\boldsymbol{k}}$ are annihilation operators for bosons with momentum $\boldsymbol{k}$, V is the volume of space, and we modulate the scattering length $a(t) = a_{\rm dc} + a_{\rm ac}\cos(ft) = a_{\rm dc} + \frac{a_{\rm ac}}{2} e^{i\omega t} + \frac{a_{\rm ac}}{2} e^{-i\omega t}$, which we have taken internally to calling "wiggling," for lack of a better, convenient shorthand, with angular frequency $\omega = 2\pi f$. This modulation corresponds to an oscillating interaction strength $g(t) = \frac{4\pi\hbar^2 a(t)}{m} = g_{\rm dc} + \frac{g_{\rm ac}}{2} e^{i\omega t} + \frac{g_{\rm ac}}{2} e^{-i\omega t}$. Note that we expect the phase of the modulation to be unimportant since the dynamics will generally be slow compared to the modulation period.

We make the Bogoliubov approximation by setting $b_0 = b_0^\dagger = \sqrt{N}$ where N is the number of particles in the condensate. In so doing, we assume a macroscopic occupation of the ground state which is not significantly depleted by the dynamics. This approximation fails once the depletion of the original condensate mode becomes significant. However, it is very useful for predicting the essential features of spontaneous jet formation and amplification. Generally, even at the stage when depletion becomes significant the primary effect is to reduce the amplification rate.

For a time-independent interaction strength the typical Bogoliubov treatment would proceed by re-writing the Hamiltonian as

$$H = \sum_{\boldsymbol{k}\neq 0} \frac{\hbar^2 k^2}{2m} b^\dagger_{\boldsymbol{k}} b_{\boldsymbol{k}} + \frac{N g(t)}{2V} \sum_{\boldsymbol{k}} (b^\dagger_{\boldsymbol{k}} b^\dagger_{-\boldsymbol{k}} + b_{\boldsymbol{k}} b_{-\boldsymbol{k}} + 2 b^\dagger_{\boldsymbol{k}} b_{\boldsymbol{k}})$$

from which we split off the terms which include $\boldsymbol{k}$ and $-\boldsymbol{k}$ to obtain:

$$H_{\boldsymbol{k}} = (\frac{\hbar^2 k^2}{2m} + n g(t))(b^\dagger_{\boldsymbol{k}} b_{\boldsymbol{k}} + b^\dagger_{\boldsymbol{-k}} b_{\boldsymbol{-k}}) + n g(t)(b^\dagger_{\boldsymbol{k}} b^\dagger_{\boldsymbol{-k}} + b_{\boldsymbol{k}} b_{\boldsymbol{-k}})$$

where we have defined $n \equiv N/V$. If the condensate fills space, these pairs of modes are

completely independent of other modes. At this point we diverge from the typical Bogoliubov treatment because of the time-dependent interaction term.

We use the Heisenberg equation of motion

$$\dot{b}_{\boldsymbol{k}} = \frac{i}{\hbar}[H, b_{\boldsymbol{k}}] = -\frac{i}{\hbar}(E(k) + ng(t))b_{\boldsymbol{k}} - \frac{i}{\hbar}ng(t)b^{\dagger}_{-\boldsymbol{k}}$$

where we have defined $E(k) \equiv \frac{\hbar^2 k^2}{2m}$. In order to focus on the essential features of Bose fireworks we approximate $g_{\rm dc} = 0$ since, in the experiments described below, $ng_{\rm dc} \ll \hbar\omega, ng_{\rm ac}$. We transform to a rotating frame by defining $b_{\boldsymbol{k}} \equiv e^{-iE(k)/\hbar}c_{\boldsymbol{k}}$. Substituting these new operators we obtain

$$\dot{c}_{\boldsymbol{k}} = -\frac{i}{\hbar}n(\frac{g_{\rm ac}}{2}e^{i\omega t} + \frac{g_{\rm ac}}{2}e^{-i\omega t})c_{\boldsymbol{k}} - \frac{i}{\hbar}n(g_{\rm dc} + \frac{g_{\rm ac}}{2}e^{i\omega t} + \frac{g_{\rm ac}}{2}e^{-i\omega t})e^{2iE(k)/\hbar}c^{\dagger}_{-\boldsymbol{k}}$$

and we are now in position to invoke the rotating-wave approximation. We will drop all terms oscillating with frequencies of ω or faster, keeping only terms which oscillate at the detuning $\delta \equiv \frac{2E(k)}{\hbar} - \omega \ll \omega$. Making the rotating-wave approximation we obtain,

$$\dot{c}_{\boldsymbol{k}} = -i\frac{ng_{\rm ac}}{2\hbar}e^{i\delta t}c^{\dagger}_{-\boldsymbol{k}} \equiv -i\frac{\gamma}{2}e^{i\delta t}c^{\dagger}_{-\boldsymbol{k}},$$

where we define the growth rate $\gamma \equiv \frac{ng_{\rm ac}}{\hbar}$. At this stage it is already clear that we should see growth of modes with small detuning, corresponding to ejected atoms with roughly half of a quantum ($\hbar\omega/2$) of the oscillating magnetic field. Note that this aggressive rotating-wave approximation is well justified as long as the dynamics are slow compared to the modulation frequency; that is, the modulation amplitude should satisfy $ng_{\rm ac} \ll \hbar\omega$.

From the coupled time-evolution equations in the rotating-wave approximation we can

obtain the uncoupled second-order differential equation,

$$\ddot{c}_{\boldsymbol{k}} - i\delta\dot{c}_{\boldsymbol{k}} - \left(\frac{\gamma}{2}\right)^2 c_{\boldsymbol{k}} = 0$$

Ignoring, for the moment, that $c_{\boldsymbol{k}}$ are operators, we see that this differential equation takes a familiar form. The solution has the familiar form of exponentially growing and decaying terms. The occupation numbers $|c_{\boldsymbol{k}}|^2$ should have exponentially growing and decaying terms with exponents (assuming $\delta < \gamma$)

$$\lambda_{\pm} = \pm\sqrt{\gamma^2 - \delta^2}.$$

As we anticipated, the resonant modes with $\delta = 0$ have purely exponential growth and decay solutions with rate $\lambda_{\pm} = \pm\gamma$. In this approximation, the apparent "linewidth" of amplification comes entirely from power broadening; growth drops to zero when $\delta \geq \gamma$.

5.2.2 Correlations of jets in a finite BEC

While treating a finite size system is more challenging than the infinite system above, there are a couple of key advantages that make our system significantly more accessible theoretically than the closely related colliding condensates [126, 55, 147, 14, 166]. First of all, the mean-field(s) in the case of colliding condensates are moving through each other over the course of their collision. As a result, the region in which the outgoing modes are being amplified, which corresponds to the region where the condensates overlap, has inherent anisotropy and time-dependence. In our case, we can make the condensate mean-field nearly homogeneous and circular, and its only time-dependence comes from depletion due to the fireworks themselves (which we neglect here). Therefore, in this section we are able to derive an analytical form for the correlation functions which explains the autocorrelation peak (near $\theta = 0$) quite well (Fig. 5.13).

For a finite size system, the many-body Hamiltonian describing our system is,

$$H = \int d^3\boldsymbol{r}\Psi^\dagger(\boldsymbol{r},t)\frac{p^2}{2m}\Psi(\boldsymbol{r},t) + \int d^3\boldsymbol{r}\Psi^\dagger(\boldsymbol{r},t)V(\boldsymbol{r})\Psi(\boldsymbol{r},t) + \frac{g(t)}{2}\int d^3\boldsymbol{r}\Psi^\dagger(\boldsymbol{r},t)\Psi^\dagger(\boldsymbol{r},t)\Psi(\boldsymbol{r},t)\Psi(\boldsymbol{r},t)$$

where Ψ is the bosonic field operator, $V(\boldsymbol{r})$ is a static external potential which determines the initial shape of the condensate, and m is the mass. Dynamics are driven by an oscillating interaction strength $g(t) = \frac{4\pi\hbar^2 a(t)}{m}$ where the scattering length follows $a(t) = a_{\mathrm{dc}} + a_{\mathrm{ac}}\sin(\omega t)$, see Fig. 5.2.

We begin by invoking a few key assumptions. First, since most of this work can be understood in the regime where the depletion of the condensate is negligible, we will use the Bogoliubov approximation of a fixed, macroscopically occupied condensate. Therefore, we decompose the field operator into a quantum field describing the excited modes $\Psi_e(\boldsymbol{r})$ and a classical field $\psi_0(\boldsymbol{r},t)$ which corresponds to the condensate wavefunction. Second, since we do not observe significant ejection of atoms outside the horizontal plane, we will assume that the emission is only into horizontal modes and ignore the vertical structure of the gas. Further assuming an idealized trap and ignoring the healing length, we can approximate the condensate as a homogeneous cylinder of radius R and density n, such that the classical field describing the condensate is $\psi_0(\boldsymbol{r}) \equiv \sqrt{n}\rho(\boldsymbol{r})$ where

$$\rho(\boldsymbol{r}) = \begin{cases} 1 & r \leq R \\ 0 & r > R \end{cases}$$

in cylindrical coordinates with the horizontal radius r. Since the trap potential $V(r)$ primarily serves to contain the condensate and does not significantly affect jet propagation, we will neglect its effects on the time evolution of the excited modes. Moreover, it is convenient

to work in Fourier space, using the transformations

$$\rho(\boldsymbol{r}) = \frac{1}{(2\pi)^{3/2}} \int d^3k e^{i\boldsymbol{k}\cdot\boldsymbol{r}} \tilde{\rho}(\boldsymbol{k}),$$

$$\Psi_e(\boldsymbol{r}, t) = \frac{1}{(2\pi)^{3/2}} \int d^3k e^{i\boldsymbol{k}\cdot\boldsymbol{r}} b(\boldsymbol{k}, t).$$

We can now invoke the rotating wave approximation. We define $b(\boldsymbol{k}, t) \equiv e^{-i\omega t/2} c(\boldsymbol{k}, t)$. Time evolution of the rotating operators $c(\boldsymbol{k}, t)$ is governed by the Hamiltonian $H_c = H - \int d^3k \frac{\hbar\omega}{2} c^\dagger(\boldsymbol{k}, t) c(\boldsymbol{k}, t)$ in which we drop terms which oscillate at multiples of ω. We also drop the elastic scattering term proportional to $a_{\rm dc}$, which is negligible in this work. Together, these steps yield the Hamiltonian:

$$\begin{aligned} H_c = &\frac{\hbar^2}{2m} \int d^3\boldsymbol{k} (k^2 - k_f^2) c^\dagger(\boldsymbol{k}) c(\boldsymbol{k}) \\ &+ \frac{\hbar\gamma}{4} \int d^3k_1 d^3k_2 \left(c^\dagger(\boldsymbol{k}_1) c^\dagger(\boldsymbol{k}_2) \frac{\tilde{\rho}(\boldsymbol{k_1} + \boldsymbol{k_2})}{(2\pi)^{3/2}} + \text{h.c.} \right) \end{aligned}$$

where the excitation rate is

$$\gamma = \frac{2hna_{\rm ac}}{m}.$$

Below, in the absence of the decay term, the excitation rate will appear as the rate of exponential growth for the excited atom number.

The time evolution of the excited field in the Heisenberg representation yields, which yields

$$\dot{c}(\boldsymbol{k}) = -i\frac{\hbar}{2m}(k^2 - k_f^2) c(\boldsymbol{k}) - i\frac{\gamma}{2} \int d^3k_1 \frac{\tilde{\rho}(\boldsymbol{k} + \boldsymbol{k_1})}{(2\pi)^{3/2}} c^\dagger(\boldsymbol{k_1}),$$

where $k_f \equiv \sqrt{\omega m/\hbar}$ is the carrier wavenumber.

The first term contains the kinetic energy of the excited atoms and the second term contains the interactions which populate the excited modes.

The kinetic energy term primarily leads to two effects: the resonance condition and the threshold behavior. While we will see that resonant modes with $k = k_f$ can grow exponentially, this term prevents the growth of modes which are sufficiently far from resonance. Therefore, even in the finite-size case treated here, we expect the dynamics to be dominated by wavepackets whose carrier momentum is on resonance while their envelopes take the shape of the condensate. For such wavepackets the first term also encodes their motion out of the condensate. Those parts of the wavepacket which leave the condensate no longer grow, leading to the threshold behavior. While a full solution becomes challenging in this case, approximate treatments incorporating the threshold behavior have been discussed, for example, in Ref. [13].

Here, for the purpose of calculating the correlation function, we impose the resonance condition and assume that the system is sufficiently above the threshold that the kinetic energy term is negligible here. Furthermore, notice that the integral effectively performs a projection onto the homogeneous condensate density profile $\rho(\boldsymbol{r})$; that is, $\int d^3k_1 \frac{\tilde{\rho}(\boldsymbol{k}+\boldsymbol{k_1})}{(2\pi)^{3/2}} c^\dagger(\boldsymbol{k_1}) = c^\dagger_{in}(-\boldsymbol{k})$ where the subscript "in" denotes a projection onto the inside of the condensate boundary and we can decompose the operator as $c(\boldsymbol{k}) = c_{\rm out}(\boldsymbol{k}) + c_{\rm in}(\boldsymbol{k})$. The evolution equation is then

$$\dot{c}_{\rm in}(\boldsymbol{k}) + \dot{c}_{out}(\boldsymbol{k}) = -i\frac{\gamma}{2} c^\dagger_{in}(-\boldsymbol{k}).$$

This equation has the solution

$$c_{out}(\boldsymbol{k}, t) = c_{out}(\boldsymbol{k}, 0),$$

$$c_{in}(\boldsymbol{k},t) = c_{in}(\boldsymbol{k},0)\cosh(\frac{\gamma}{2}t) - i\,c_{in}^{\dagger}(-k,0)\sinh(\frac{\gamma}{2}t), \tag{5.1}$$

in which all amplitudes inside the condensate boundary grow, and those outside do not. The thermal fluctuation at the relevant energies is expected to be negligible, so we can assume that the initial state is the vacuum and all of the excited modes are initially empty. Therefore we have

$$c(\boldsymbol{k}_1,0)\,|0\rangle = 0$$

$$\left\langle c(\boldsymbol{k}_1,0)c^{\dagger}(\boldsymbol{k_2},0)\right\rangle = \delta(\boldsymbol{k_1}-\boldsymbol{k_2}).$$

The correlation function is defined as

$$g^{(2)}(\boldsymbol{k_1},\boldsymbol{k_2},t) \equiv \frac{\left\langle c^{\dagger}(\boldsymbol{k_1},t)c^{\dagger}(\boldsymbol{k_2},t)c(\boldsymbol{k_2}t)c(\boldsymbol{k_1},t)\right\rangle}{\langle n(\boldsymbol{k_2},t)\rangle\,\langle n(\boldsymbol{k_1},t)\rangle}.$$

Using Wick's theorem, which applies because the time evolution is linear (Eq. 5.1), we can rewrite the correlation function as,

$$g^{(2)}(\boldsymbol{k_1},\boldsymbol{k_2},t) = 1 + \frac{|n(\boldsymbol{k_1},\boldsymbol{k_2},t)|^2 + |m(\boldsymbol{k_1},\boldsymbol{k_2},t)|^2}{\langle n(\boldsymbol{k_2},t)\rangle\,\langle n(\boldsymbol{k_1},t)\rangle},$$

where $n(\boldsymbol{k_1},\boldsymbol{k_2},t) = \left\langle c^{\dagger}(\boldsymbol{k_1},t)c(\boldsymbol{k_2},t)\right\rangle$ is the contribution from the density matrix, we have defined $n(\boldsymbol{k},t) \equiv n(\boldsymbol{k},\boldsymbol{k},t)$, and $m(\boldsymbol{k_1},\boldsymbol{k_2},t) = \langle c(\boldsymbol{k_1},t)c(\boldsymbol{k_2},t)\rangle$ is the anomalous contribution. Substituing the solution for the excited field from Eq. (5.1), we obtain,

$$n(\boldsymbol{k_1},\boldsymbol{k_2},t) = \frac{\tilde{\rho}(\boldsymbol{k_1}-\boldsymbol{k_2})}{(2\pi)^{3/2}}\sinh^2(\frac{\gamma}{2}t),$$

for the density matrix. Note that $\sinh^2(\frac{\gamma}{2}t)$ contains one term which is exponentially growing at a rate γ. Accounting for the effects of the kinetic energy term, which leads to the threshold behavior, yields a reduced exponential growth rate satisfying $\gamma' = 2hn(a_{\rm ac}-a_{\rm t})/m$,

consistent with our observations in Fig. 5.15.

Furthermore, far above the threshold we obtain

$$m(\boldsymbol{k_1}, \boldsymbol{k_2}, t) = -i\frac{\tilde{\rho}(\boldsymbol{k_1} + \boldsymbol{k_2})}{(2\pi)^{3/2}}\cosh(\frac{\gamma}{2}t)\sinh(\frac{\gamma}{2}t)$$

for the anomalous contribution. Combining these results, we find the correlation function

$$g^{(2)}(\boldsymbol{k_1}, \boldsymbol{k_2}, t) = 1 + \frac{|\tilde{\rho}(\boldsymbol{k_1} - \boldsymbol{k_2})|^2}{\tilde{\rho}(0)^2} + \frac{|\tilde{\rho}(\boldsymbol{k_1} + \boldsymbol{k_2})|^2}{\tilde{\rho}(0)^2}\coth^2(\frac{\gamma}{2}t).$$

We can simplify the correlation function by assuming that $|\boldsymbol{k}_1| = |\boldsymbol{k}_2| = k_f$ and calculating the correlations as a function of the angle ϕ between $\boldsymbol{k}_1$ and $\boldsymbol{k}_2$. Furthermore, taking into account the disk-shape of our condensates and noting that our observations are made at times satisfying $\gamma t \gg 1$, we obtain the time-independent correlation function:

$$g^{(2)}(\phi) = 1 + \left|\frac{2J_1(k_f R\phi)}{k_f R\phi}\right|^2 + \left|\frac{2J_1(k_f R(\phi - \pi))}{k_f R(\phi - \pi)}\right|^2, \tag{5.2}$$

where J_n are the Bessel functions of the first kind and in our experiments the coefficient $k_f R \gg 1$ is sufficiently large that we have made small angle approximations for the last two terms.

While the approximation of ignoring the motion of the outgoing wavepackets (that is, mostly dropping the kinetic energy term except for the resonance condition) was discussed above, it is crucial to note that this approximation is likely responsible for discrepancies between the experiment and theory. It is possible that finding a way to incorporate the motion of the outgoing wavepackets into the theory will account for the suppression and broadening of the peak at 180°, for example. The motion of the outgoing jets almost certainly also plays important roles in determining the average density and fluctuations in the remnant condensate which is left behind after the jets are ejected, in setting the threshold for secondary collisions, and in the effects of excitations such as vortices in the initial condensate on the

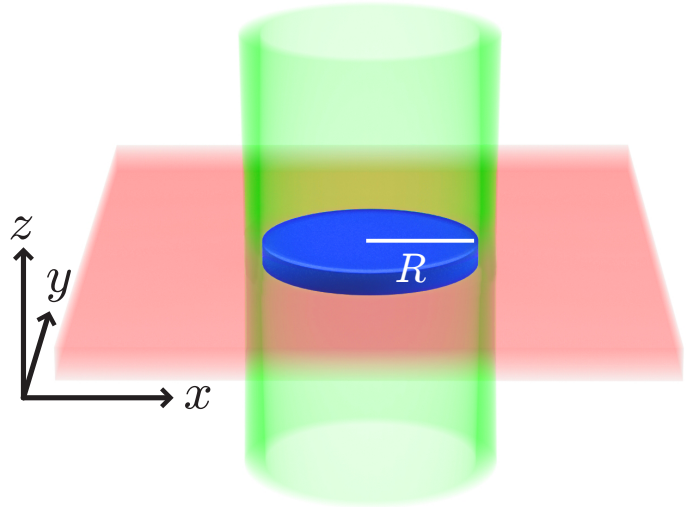

Figure 5.3: Disk-shaped Bose-Einstein condensates (blue) of radius R are trapped at the intersection of two lasers, which create a repulsive cylindrical shell (green) and an attractive sheet (red).

fireworks pattern (see Sec. 7.2).

5.3 Experiment Setup

To observe jets we typically perform experiments on thin, pancake-shaped condensates of 30 000 cesium atoms (Fig. 5.3). The condensates homogeneously fill a circle of typical radius $R = 8.5$ μm in the horizontal plane while being tightly, harmonically confined vertically to a root-mean-squared radius of 0.5 μm. The trap depth in all directions is sufficient to confine the condensates, but weak enough to allow ejected atoms to propagate nearly undisturbed. Note that the fireworks appear qualitatively similar in more ordinary harmonic traps, as shown in Fig. 5.1. Here, the use of homogeneous disk traps facilitates data analysis and quantitative comparisons with theory.

Horizontal confinement is provided by a repulsive 780 nm laser which is shaped into a circle of controllable radius by a digital micromirror device (DMD) before being projected onto the atoms through the high-resolution objective lens, see Sec. 2.5.1. The resulting barrier has a height of $h \times 150$ Hz and thickness of 4 μm. Vertical (z-axis) confinement is

approximately harmonic with frequency $\omega_z = 2\pi \times 210$ Hz and depth $h \times 500$ Hz.

After loading the condensates into this trap we modulate the magnetic field around 17.22 G, near the zero-crossing a Feshbach resonance, at frequency f which causes the s-wave scattering length a of the atoms to oscillate [125], see Fig. 5.2 and Sec. 2.3. Below, except where explicitly discussed, we maintain a small, positive average scattering length $a_{\rm dc} = 5\, a_0$, in terms of the Bohr radius a_0. For typical experiments we hold the modulation amplitude at a constant value $a_{\rm ac}$ for a duration τ before imaging the atomic density distribution.

5.3.1 Defringing

While methods for defringing have been well established and are commonly used in cold atoms (for example, see Ref. [94]), such that they don't need to be rehashed here, the use of defringing for analyzing fireworks images deserves a crucial message of warning. Since the density in fireworks is typically small, especially when they have propagated far enough away from the remnant condensate to be easily resolved, the signal to noise ratio may not be very large; as a result, fringes in the absorption imaging beam may create artifacts in images comparable in magnitude to the fireworks themselves. It is quite appropriate to use defringing to remove these artifacts, and when generating images for simple visual inspection there is not much harm to be done. However, when processing images in order to perform quantitative analysis, such as calculating atom numbers or correlations, one must use extreme caution to ensure that there are not any atoms in the region chosen as the "background" for defringing. Because the emission of jets begins slowly, with a small number of atoms, the atoms in the leading edge of the jets may not be visually apparent due to their extremely low density. However, they can easily lead to defringing artifacts which ruin the results of any further quantitative analysis of the primary jet signal. Note that secondary collisions could also eject small numbers of atoms into regions which one expected to be empty. One must be absolutely certain that no atoms are in the background region before applying defringing

at the beginning of any quantitative analysis. For this work, we implement defringing only when there is a large region at the boundary of our images which is too far away for any ejected atoms to have reached during the modulation time.

5.3.2 Correlations

Below, we calculate the angular correlation functions

$$g^{(2)}(\phi) = \frac{\langle \int d\theta n(\theta) \left[n(\theta + \phi) - \delta(\phi) \right] \rangle}{\langle \int d\theta n(\theta) \rangle^2}, \tag{5.3}$$

where $n(\phi)$ is the angular density of atoms emitted at an angle ϕ, $\delta(.)$ is the Dirac delta function, and the angle brackets denote averaging over ensembles of many images. To calculate these correlations from our data we use discrete angular slices of width 10 mrad. Moreover, for each condition we include only atoms within an annulus whose inner and outer radii are symmetric around the distance at which ejected atoms are most dense. For Fig. 5.13 the annulus has thickness 10 μm, whereas for Fig. 5.17 the thickness increases to 20 μm to improve the signal strength for conditions with few jets.

Especially when calculating correlations for conditions in which the jet density is very low, it is important to remove spurious contributions to the correlation from small, fluctuating backgrounds (including fringes in the imaging beam). In each trial of the experiment with atoms present, we are actually measuring $n_{\text{meas}}(\theta) = n_{\text{real}}(\theta) + n_{\text{bkg}}(\theta)$ where $n_{\text{real}}(\theta)$ represents the signal from our atoms and $n_{\text{bkg}}(\theta)$ is some fluctuating, correlated background corresponding to technical noise. In that case, the correlation function that we would naively calculate from raw data would be (temporarily ignoring the δ-function contribution for simplicity),

$$g^{(2)}(\phi)_{\text{naive}} = \frac{\langle \int d\theta (n_{\text{real}}(\theta) + n_{\text{bkg}}(\theta))(n_{\text{real}}(\theta + \phi) + n_{\text{bkg}}(\theta + \phi)) \rangle}{\langle \int d\theta (n_{\text{real}}(\theta) + n_{\text{bkg}}(\theta)) \rangle^2}, \tag{5.4}$$

which deviates from the physical correlation function because of the contributions from the background. In order to remove the background, we first acquire an additional set of images with no atoms present, effectively measuring $n_{\mathrm{bkg}}(\theta)$ independently (in practice, we intersperse these background-only images within each real dataset to account for slow drifts in performance of the experiment). Then, to ensure that the background does not contribute to the denominator, we subtract the average background from the measured data $n'_{\mathrm{meas}}(\theta) = n_{\mathrm{meas}}(\theta) - \langle n_{\mathrm{bkg}}(\theta)\rangle$ and the background-only data $n'_{\mathrm{bkg}}(\theta) = n_{\mathrm{bkg}}(\theta) - \langle n_{\mathrm{bkg}}(\theta)\rangle$. Next, as long as we assume that the fluctuations in the real signal and the background are uncorrelated, we can remove the background-only correlations by calculating the real correlations as,

$$g^{(2)}(\phi)_{\mathrm{real}} = \frac{\langle \int d\theta n'_{\mathrm{meas}}(\theta) n'_{\mathrm{meas}}(\theta+\phi)\rangle - \langle \int d\theta n'_{\mathrm{bkg}}(\theta) n'_{\mathrm{bkg}}(\theta+\phi)\rangle}{\langle \int d\theta n'_{\mathrm{meas}}(\theta)\rangle^2}. \tag{5.5}$$

Two other subtleties in calculating the correlations deserve mention. First, the half-widths at half-maximum shown in Figs. 5.14 and 5.17 are corrected for small systematic shifts due to our finite imaging resolution of 1.4 μm similar to the case of the pseudo-spin correlations in the effectively ferromagnetic phase (see Sec. 4.3.4). Since we use narrow annuli for correlation analysis, we approximate the angular resolution by considering the point spread function for atoms at the midpoint of the two radii defining the annulus.

Second, unlike in the case of pseudo-spin correlations treated in the previous chapter, here we are often calculating correlations between regions containing small atom numbers, and as a result it is important to remove the autocorrelation of atoms when comparing to the theory (this corresponds to accounting for the term containing the δ-function in Eq. 5.3). The width of the point spread function is not insignificant compared to the width of the angular slices; for example, the width of a 10 mrad angular slice at a distance of 70 μm from the center is 0.7 μm, smaller than our imaging resolution of about 1.4 μm. Therefore, before subtracting the delta-function contribution we must convolve it with the point-spread-

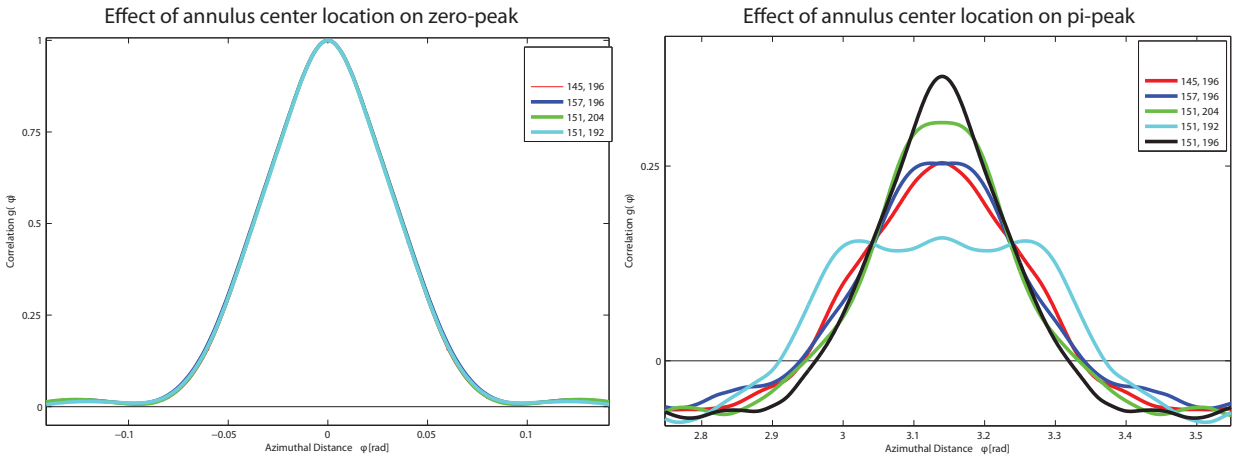

Figure 5.4: When calculating angular correlation functions from images of fireworks, the choice of the center relative to which we define the angular density can lead to systematic effects. While the correlations at small angles (left) are essentially unaffected, correlations near 180° (right) change significantly when the center is shifted by microns. The values in the legend denote the coordinates of the corresponding annulus center; the units are camera pixels, which correspond to 0.60 μm in the atomic plane.

function; note that this also means that the delta-function affects $g^{(2)}$ for small angles, not just $g^{(2)}(0)$.

5.3.3 Systematic Distortions of the Fireworks Pattern

The calculated correlations can depend very sensitively on small distortions of the fireworks pattern. Experimentally, we suppress these as much as possible by turning off the XDT, YDT, and ZDT dipole traps and shifting the residual trapping (a sum of the weak magnetic antitrapping and a horizontal weak trapping from the vertical lattice) to be concentric with the DMD circle by offsetting the bias field. Even so, slight distortions generally remain, such that the center of the fireworks pattern is not exactly the center of the remnant BEC (this is the lowest order effect; other distortions are also possible). Since the residual potentials are very weak, the distortions are only relevant for atoms which have traveled large distances apart. Therefore, the systematic effects have the strongest influence on the appearance of the correlation peak at 180° (which we call the π-peak). Equivalently, this effect can be

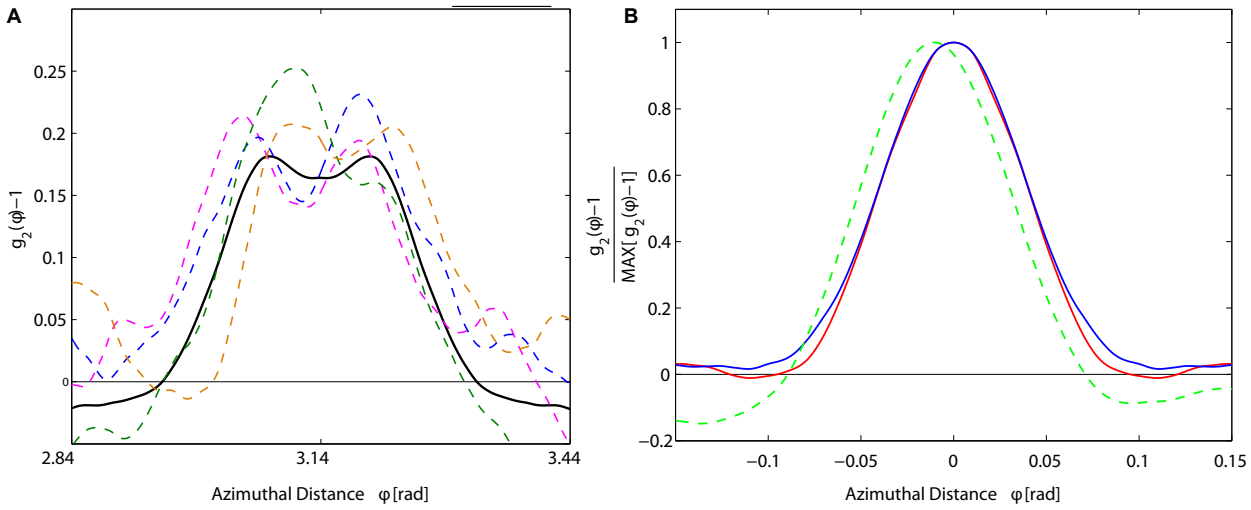

Figure 5.5: Two tests for systematic issues in Fireworks correlation functions. A) An example calculation of the π-peak for a complete dataset (black solid curve) as well as four independent sets of opposing 45° angular slices of the data (colored, dashed curves). B) Correlations calculated within two independent annuli of thickness 20 μm centered around radii R = 95 μm (red) and R = 130 μm (blue) as well as the cross-correlation between the angular densities in the two annuli (dashed green). All correlations were measured only within a finite angular slice of width $\pi/4$.

seen in the distortion of the calculated correlations when the center of the annulus used for data analysis is translated, see Fig. 5.4. Shifts of the center position by a few microns have no significant effect on the peak at 0° (0-peak) but dramatically distort the π-peak. This observation is especially troubling because the π-peaks in our primary data (see Fig. 5.13) are shorter and wider than expected. Ideally, we would like to ensure that these effects do not result from technical issues.

While we certainly cannot completely rule out technical distortions as the cause of the short, broad π-peaks in general, we have made significant effort to rule out technical issues which could account for the π-peaks. Here we will describe two noteworthy examples. First, in Fig. 5.5A we compare the π-peak correlations calculated for the entire sample with correlations calculated for narrow angular slices of the data. For example, the magenta dashed curve was calculated using the angular density $n(\theta)$ limited to absolute angles from 0 to $\pi/4$ and from π to $5\pi/4$. If there were large-scale (i.e. not too much rapid spatial variation)

systematic distortions of the fireworks profile which were consistent from trial to trial, we would expect to see taller, narrower π-peaks within each of these independent angular slices. Any such effect in the example data shown (and in every dataset that we have tested) is very small and insufficient to account for the deviation of the π-peak from theory.

In the second example shown in Fig. 5.5B we illustrate how we can determine the most appropriate center location for the analysis annulus based on cross-correlations in the angular densities measured using independent annuli at two different radii. We partition the angular density into 8 independent angular slices of width $\pi/4$ and in each slice generate a plot as shown in the example Fig. 5.5B. If the center is positioned properly, and the fireworks are propagating radially away from the center, then the cross-correlation between the inner and outer annuli (the dashed green curve) should also be centered at $\phi = 0$. If it is not (in the example it is offset by 10 mrad), then we can try to reposition the center to minimize the offsets measured across all of the angular slices. With the optimal choice of center location we can generally limit the offsets to less than 5 mrad in every slice, which is insufficient to account for the π-peak.

5.3.4 Frequency Limits

In this chapter we will discuss fireworks experiments performed at frequencies $f = 1 \sim 10$ kHz. In theory, nothing fundamentally limits us from using lower or higher frequencies. On the low frequency end, the behavior of the fireworks should not qualitatively change until the frequency approaches either the trap depth or the chemical potential. On the high frequency end, one might not expect a qualitative change until the magnetic field oscillation frequency reached the binding energy of a Cs_2 molecular state, at which point additional features due to the binding of molecules should appear. However, in practice the low frequency limit is reached when we start to excite collective modes of the trap in the vertical direction, leading to rapid variation of the density and a flow of atoms leaving the

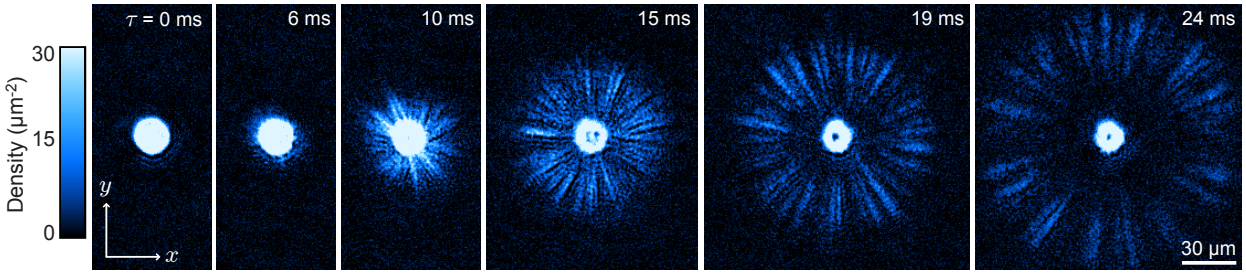

Figure 5.6: Top-down images of condensates after modulating the scattering length at $f = 3.5$ kHz and $a_{\mathrm{ac}} = 60\ a_0$ show condensates ejecting a sudden burst of narrow jets. Note that the internal structure of the remaining condensate suffers from imaging artifacts due to the extremely high density. Each image corresponds to a single, independent realization of the experiment.

trap vertically. Moreover, the practical high frequency limit occurs because the threshold modulation amplitude necessary to achieve fireworks (rather than just spontaneous emission) becomes unreasonably high (and the background of spontaneously emitted atoms becomes very large even when the amplitude exceeds threshold). Either limit could probably be overcome if someone felt a strong urge to do so. For instance, one could change the vertical trap configuration to adjust the resonance positions or increase the density of the gas.

5.4 Results

5.4.1 Essential Features

When we monitor the behavior of the condensate under the typical experimental procedure (Fig. 5.2), for the first few milliseconds of modulation little change is observed, until suddenly the jets emerge and propagate radially away from the condensate, see Fig. 5.6. The specific pattern of jets appears to be random in each repetition of the experiment. Even so, the jets have similar angular widths, and jets often appear to be accompanied by a partner propagating in the opposite direction. Side-view images of the condensates indicate that atoms are predominantly ejected in the horizontal plane, see Fig. 5.7. All of these behaviors are observed throughout a wide range of frequencies $f = 1 \sim 10$ kHz.

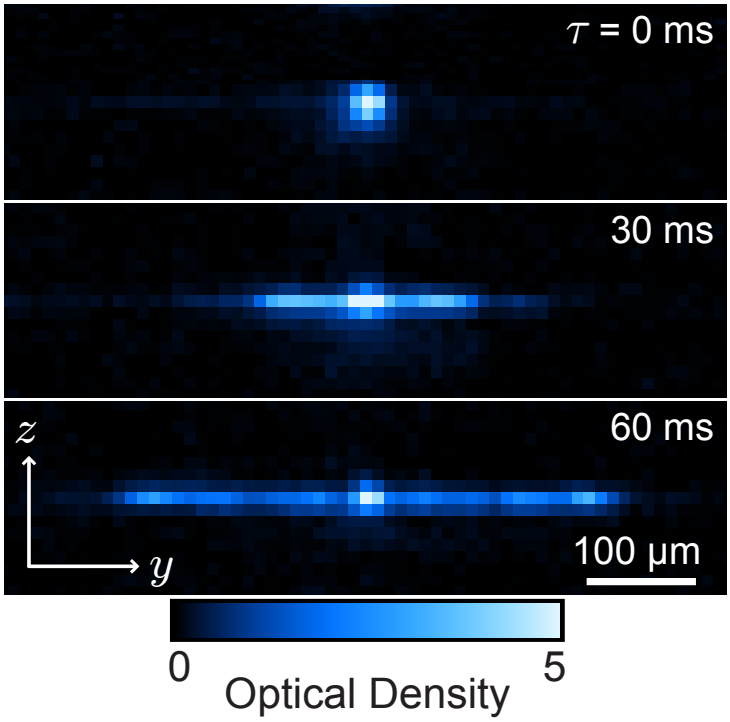

Figure 5.7: Side-view images of the condensates taken at $f = 3.5$ kHz show atoms emitted predominantly in the horizontal plane. Each image corresponds to a single, independent realization of the experiment.

To understand the microscopic process responsible for ejection of atoms, we extract the kinetic energy per atom by monitoring their distance from the condensate over time. We find that each atom has half of a quantum of the oscillating field, $E_{\mathrm{k}} = hf/2$ where h is the Planck constant (Fig. 5.8). This relationship confirms our expectations that the ejected atoms come from collisions in which two atoms absorb and equally share an energy of hf from the modulation and are ejected in opposite directions. From this microscopic perspective, the situation is similar to collisions between two condensates, during which counter-propagating pairs of atoms are ejected while conserving momentum and energy[35].

The preferential emission in the horizontal plane and the jet structure are salient and indicative of a collective collision process occurring throughout the condensate; uncorrelated, s-wave collisions should generate a diffuse, spherical shell of outgoing atoms. The observed features suggest that atoms produced in each collision stimulate further scattering into the

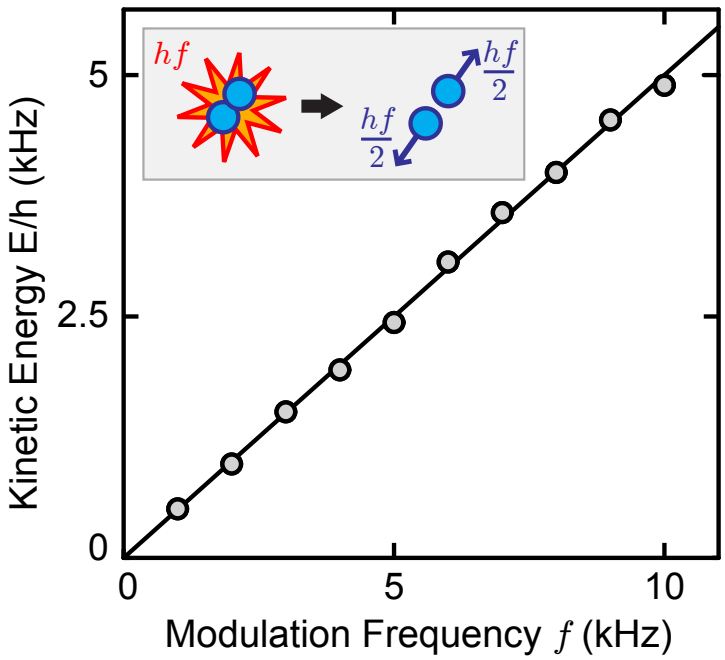

Figure 5.8: The measured kinetic energy per emitted atom for a range of modulation frequencies. The standard error is smaller than the symbol size. The inset illustrates the microscopic process leading to jets, in which two atoms collide, absorb one quantum from the oscillating field, and are ejected in opposite directions.

same outgoing direction. Sufficient driving makes this stimulation run away and causes large numbers of atoms to go in particular directions and appear as jets while other directions have far fewer atoms and appear nearly empty. Note that the small, constant average scattering length is important for suppressing elastic collisions which scatter the atoms out of the jets. With sufficiently large positive or negative average scattering lengths a_{dc} we no longer observe jets.

The disk shape of the condensates precludes strong stimulation for atoms emitted vertically, which rapidly escape the condensate before stimulating further collisions. This anisotropy results in the predominantly horizontal emission which we observe. However, for sufficiently high frequencies and modulation amplitudes the atoms from spontaneous collisions are detectable in side-view images as a low density halo out of the plane, see Fig. 5.9. The vertical lattice is almost certainly responsible for the apparent gap between the main

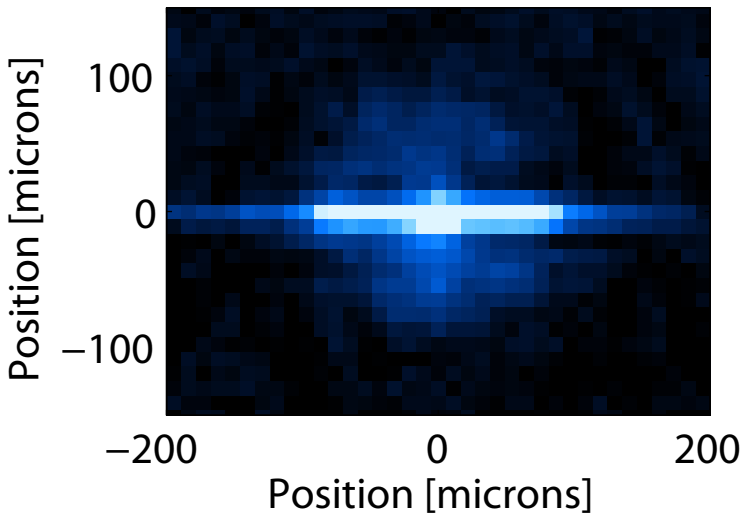

Figure 5.9: An example side-view image of fireworks from the disk trap with $R = 8.5$ μm, modulation amplitude $a_{\rm ac} = 100\, a_0$, and frequency $f = 8$ kHz. A low density halo containing approximately 40% of the total ejected atoms is visible outside of the horizontal plane.

horizontal emission and the halo, since atoms emitted at small vertical angles cannot leave the primary well of the lattice.

The atoms ejected out-of-plane should be kept in mind when analyzing the images from the vertical camera. Under the conditions of the figure shown, the out-of-plane emission contains approximately 40% of total ejected atom number. Since we are forced to image the column density, these atoms can contribute a large uncorrelated background which reduces the height of peaks in the calculated correlation functions (see Sec. 5.3.2). It might be possible to eliminate this background by using microwaves to repump only the in-plane atoms (due to the large magnetic field gradient) before imaging. We were unable to remove this background in the results reported below.

There seems to be a common misconception (hopefully only slightly exacerbated by our explanations) that there is a dichotomy between modes containing jets and modes which are empty. No such dichotomy exists; we observe modes with large occupations, modes with small occupations, and modes in between. The appearance of jets merely reflects the large variance. To illustrate this, we present a histogram of the atom numbers in 20 mrad slices

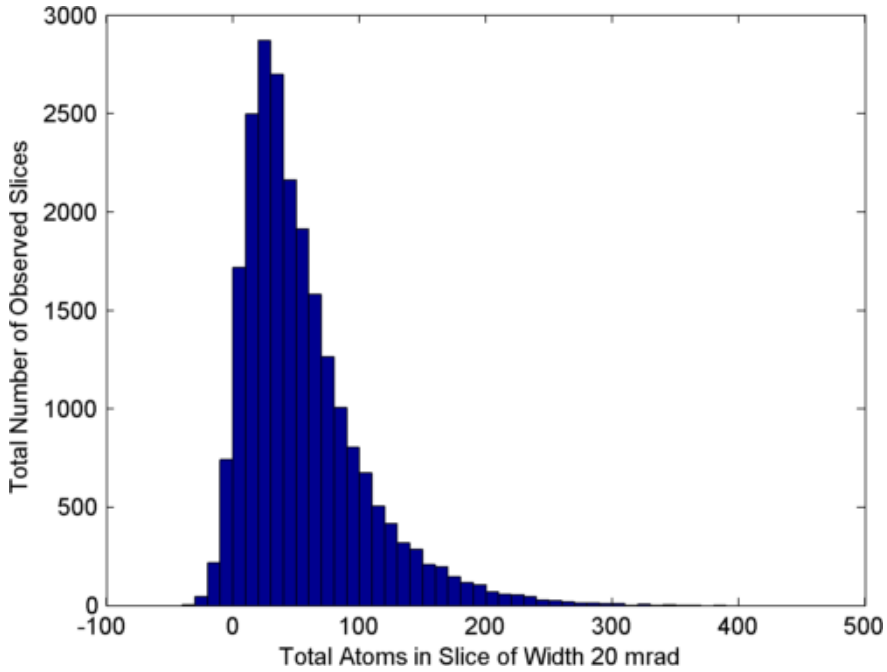

Figure 5.10: A histogram of the atom numbers measured in 20 mrad angular slices from 73 images of fireworks with $f = 1.9$ kHz.

from typical images in Fig. 5.10. If there were two types of modes, containing jets or nothing, we would generally expect a bimodal distribution with a peak near zero and another peak with large occupation. Since there is actually a smooth distribution of occupations, reflecting the distribution which results from amplified quantum fluctuation (see below), the histogram is instead unimodal. The distribution of occupations should be unimodal for any system in which all of the modes are equivalent. In particular, the sample should be isotropic and all modes should share the same unimodal distribution of initial occupations (in this case, the modes are all initially empty).

5.4.2 Threshold

Runaway stimulated scattering only occurs when outgoing atoms stimulate further collisions faster than they escape the condensate. We estimate that the ejected atoms escape at a rate $\Gamma = \alpha \frac{v}{R}$ where

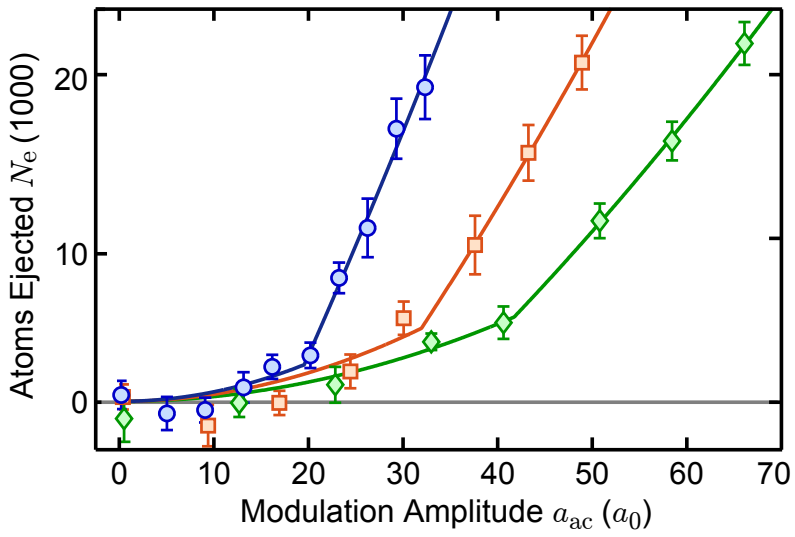

Figure 5.11: Examples of threshold behavior at three frequencies. A plot of the number of ejected atoms N_e for modulation at frequency $f = 1.3$ kHz for duration $\tau = 46$ ms (blue circles), $f = 4.5$ kHz for $\tau = 25$ ms (orange squares), and $f = 8.2$ kHz for $\tau = 19$ ms (green diamonds). Solid curves show fits based on Eq. 5.8 (methods).

$$v = \sqrt{\frac{hf}{m}} \tag{5.6}$$

is the velocity of an ejected atom with mass m and α is a dimensionless constant of order unity[147]. Moreover, a careful theoretical treatment yields an excitation rate for the ejected population $\gamma = \frac{2hna_{ac}}{m}$ which is proportional to the modulation amplitude and the density n of the condensate (see Sec. 5.2). Therefore, runaway stimulation occurs if the gain is larger than the loss $\gamma > \Gamma$. When only the modulation amplitude is varied, we can recast the threshold condition as $a_{ac} > a_t$ where

$$a_t = \alpha \frac{m}{2h} \frac{v}{Rn} \tag{5.7}$$

is the threshold amplitude.

To test for the existence of a threshold for jet formation we measured the number of atoms ejected from the condensate at many different modulation amplitudes, see Fig. 5.11.

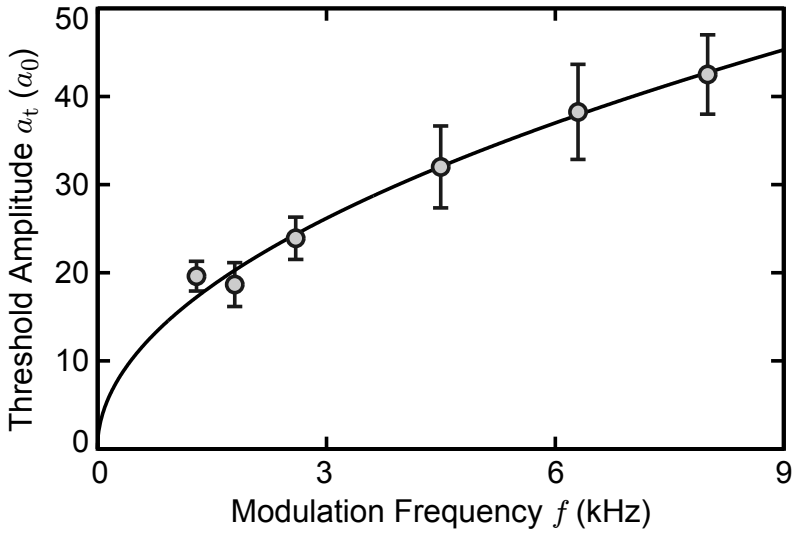

Figure 5.12: Threshold amplitudes extracted from fits as shown in Fig 5.11. The solid curve shows a fit based on Eq. 5.7 which yields the value of the numerical coefficient $\alpha = 2.1(1)$. All error bars show standard errors.

To determine the threshold at each frequency, we measure the number of atoms ejected as a function of the modulation amplitude. Here, the total duration τ of the experiment is set to the time an atom takes to travel 80 μm to the edge of our field of view. We fit the results using an empirical model,

$$N_{\mathrm{e}} = A a_{\mathrm{ac}}^2 + B(a_{\mathrm{ac}} - a_{\mathrm{t}})\Theta(a_{\mathrm{ac}} - a_{\mathrm{t}}), \tag{5.8}$$

where A and B characterize the strength of the spontaneous and strongly stimulated contributions to emission, respectively, and Θ is the Heaviside step function.

Below the threshold only a few atoms are ejected in a diffuse cloud, primarily from spontaneous scattering. Above a certain amplitude, which we identify as the threshold amplitude, the condensate suddenly starts ejecting many more atoms in the form of narrow jets. We further test the predicted behavior of the threshold (Eq. 5.7) by varying the modulation frequency to change the velocity of outgoing atoms (Eq. 5.6), see Fig. 5.12. Our results verify the expected dependence $a_{\mathrm{t}} \propto \sqrt{f}$ and yield an empirical value $\alpha = 2.1(1)$.

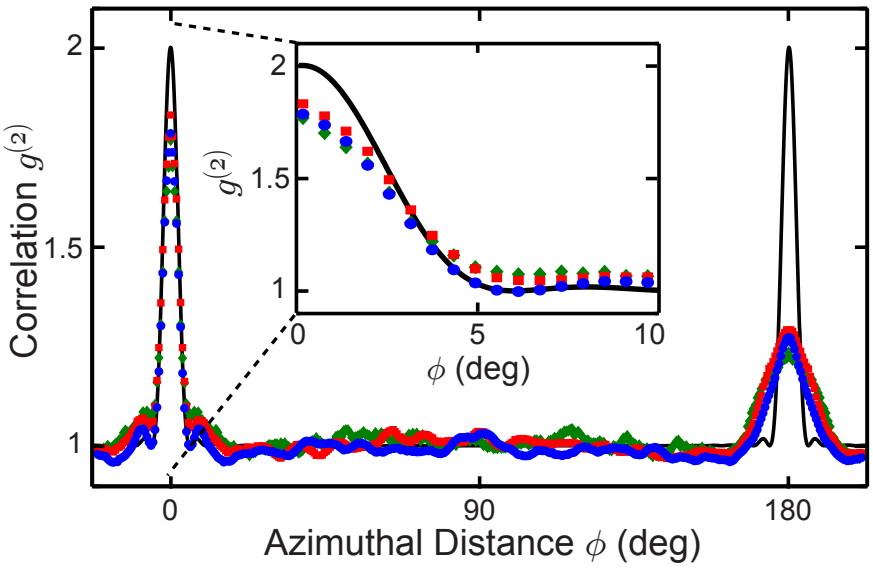

Figure 5.13: Azimuthal density-density correlations calculated from 90 images of jets emitted from condensates driven at $f = 1.9$ kHz and $a_{\rm ac} = 60\ a_0$ for modulation durations of 4.4 ms (green diamonds), 5.6 ms (red squares), and 8.0 ms (blue circles). The solid curve shows the theoretical correlation function based on Eq. 5.2. The inset magnifies the peak near $\phi = 0°$.

5.4.3 Correlations among Jets

Many essential features of the jets are characterized by their correlations[126, 55, 147, 14, 166, 116, 117, 52, 151, 113]. Specifically, we plot angular correlation functions (see Sec. 5.3.2) in Fig. 5.13. As expected, we consistently detect two peaks in the measured correlation functions, one near $\phi = 0°$ (the 0-peak) and the other near $\phi = 180°$ (the π-peak). The 0-peak results from collectively stimulated collisions, which lead to preferential bunching of the ejected atoms into the same modes. The π-peak appears because forward and backward jets are mutually stimulating as a result of conservation of momentum in the underlying pair scattering process.

The 0-peaks are in close agreement with the prediction for runaway stimulation, see Fig. 5.13 inset. The slight reduction in the height of $g^{(2)}(0)$ is likely a result of our finite imaging resolution and the aforementioned spontaneous emission out of the plane.

In addition to the jet profile, the correlation function (see Eq. 5.3) also indicates the

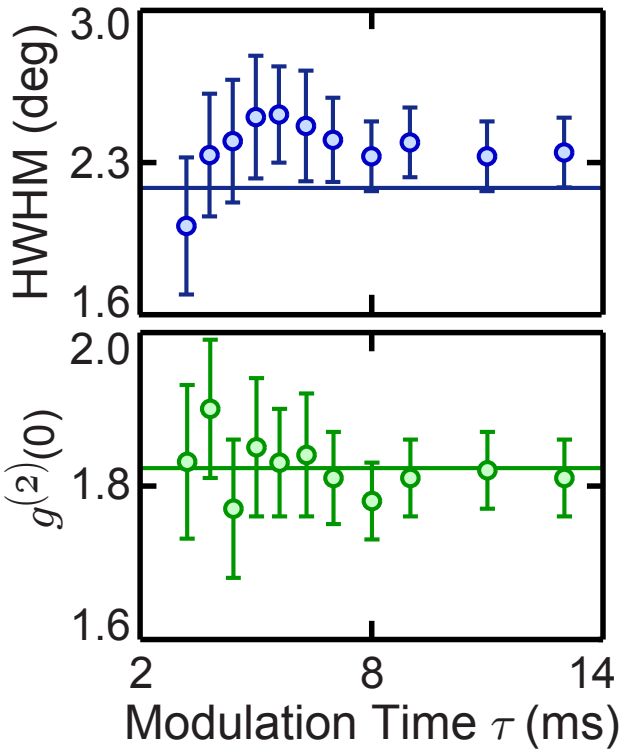

Figure 5.14: The half-width at half-maximum (HWHM, top) and height (bottom) of the peak near $\phi = 0°$ are constant within error bars, which represent one standard error. The solid lines represent the theoretical width (top) and the average measured height (bottom).

variance $\sigma^2 = \left[g^{(2)}(0) - 1\right] \langle N_\theta \rangle^2 + \langle N_\theta \rangle$ of the atom number N_θ ejected in a direction θ. For runaway stimulation and many ejected atoms, the standard deviation $\sigma \propto N$ is proportional to the number of ejected atoms, supporting the observed jet-like appearance. This contrasts with the case of spontaneous scattering, where the fluctuation $\sigma \propto \sqrt{N}$ comes only from shot noise, leading to a diffuse halo.

The correlation function is remarkably consistent throughout the amplification process even as the number of atoms in jets grows by an order of magnitude, see Fig. 5.15. When the modulation duration varies from $\tau = 2 \sim 14$ ms we find that both the width and height of the zero peak remain constant. This observation is consistent with the expectation that the gain in our system is isotropic in the horizontal plane; as a result, the stimulated emission into each horizontal mode depends only on its occupancy and the runaway stimulation does

not change the jet structure.

5.4.4 The π-Peak

Conservation of momentum in pair scattering should in principle cause each jet to be accompanied by a counter-propagating partner, such that the π-peak has the same area as the 0-peak. Taking the ratio of the areas we obtain $A(180^\circ)/A(0^\circ) = 70 \sim 85\%$, suggesting that this expectation is largely met. However, the peaks near $\phi = 180^\circ$ are shorter and wider than those near $\phi = 0^\circ$. We note that the profiles of the peaks near $\phi = 180^\circ$ are much more sensitive to technical distortions of the atom trajectories, since this peak comes from atoms on opposite sides of the image which are separated by approximately 150 μm at the time of detection. In addition, broadening of the correlation peaks has been predicted for analogous system[117].

Our preliminary results suggest that the π-peak gets broader and shorter for larger gases. Unfortunately fireworks from larger gases may also be more sensitive to systematic effects in the loading of the homogeneous gas. Even so, it is quite possible that the reduction of the π-peak is physical and not technical; the trend in the π-peak most likely results from the motion of outgoing jets which is not properly accounted for in the theory. Investigation into the nature of the π-peak is currently ongoing in the lab.

5.4.5 Fireworks seeded by Quantum Fluctuations

Since the correlations appear to be time-independent, the distribution of atoms in the amplified jets should reflect the fluctuation of the original condensate. The thermal fluctuations are expected to be negligible since the thermal population $\frac{1}{e^{E_\mathrm{k}/k_\mathrm{B}T}-1} \leq 0.03$ atoms per outgoing mode is small for our condensate with a temperature of $T = 7$ nK and modulation frequencies $f \geq 1$ kHz. As a result, quantum fluctuation should dominate the initial population, suggesting that we observe parametric amplification of the vacuum fluctuation. To

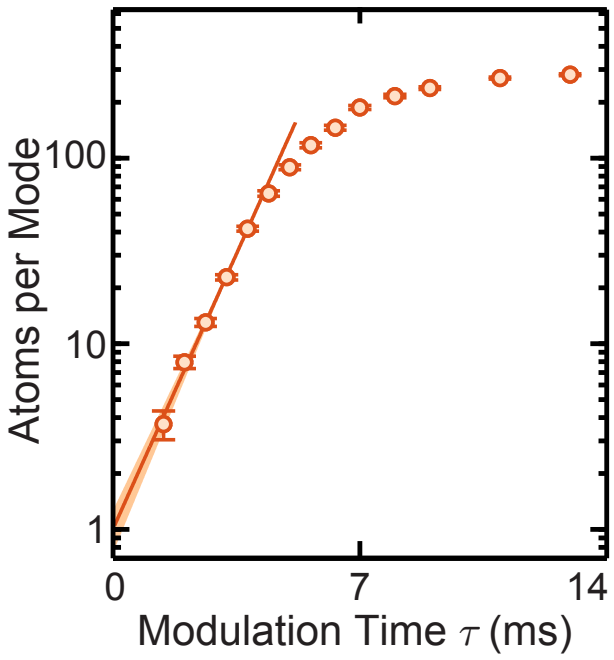

Figure 5.15: The number of atoms per mode (circles) grows rapidly over time before saturating when the condensate is depleted. An exponential fit to the first five data points (solid curve) extrapolates to an initial level of 1.0(3) atoms per mode; the shaded region covers one standard error.

further probe this feature we calculate the apparent number of atoms per outgoing mode as a function of the driving time, see Fig. 5.15. Here we estimate the number of outgoing modes as $M \approx 180^\circ/\Delta\theta = 78$ where $\Delta\theta = 2.3^\circ$ is the measured half-width at half-maximum of the peak at $g^{(2)}(0)$. The growth of the atom number over time is well described by an exponential until the depletion of the condensate becomes relevant. An exponential fit extrapolates to an apparent initial number of 1.0(3); in the case of quantum fluctuation this value represents a virtual population.

5.4.6 Fireworks Scaling Saturates Uncertainty Limit

An important prediction is that the width of the jets has a simple relationship to the size of the condensate and the modulation frequency by the Heisenberg uncertainty principle, see Fig. 5.16. In particular, the uncertainty principle suggests that the lower limit of the

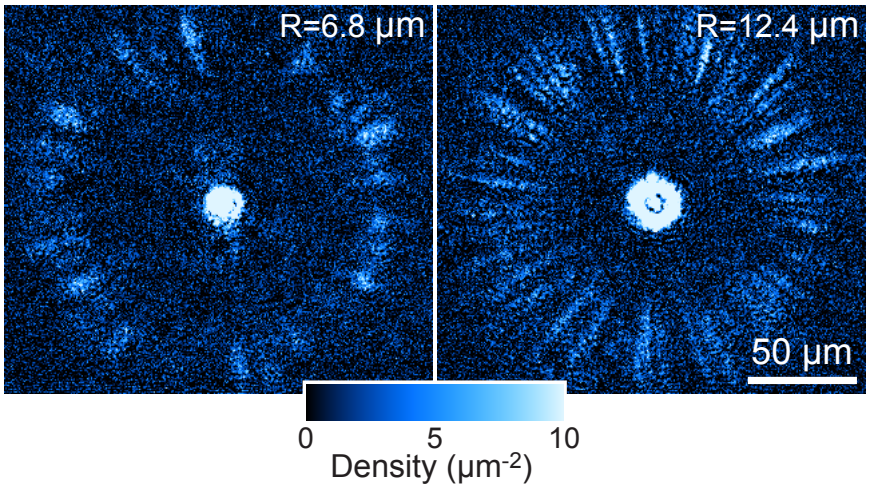

Figure 5.16: Example images of jets ejected from condensates of different radii with modulation frequency $f = 1.9$ kHz and amplitudes of $a_{\mathrm{ac}} = 70$ and 80 a_0 respectively.

transverse spread of momentum in a jet $\Delta k \propto 1/R$ is set by the radius of the condensate, and the radial momentum $k_f \propto 1/\sqrt{f}$ is determined by the oscillation frequency. As a result, the uncertainty-limited angular width follows $\Delta\theta = \Delta k/k_f \propto 1/(Rk_f)$. The complete calculation, see Eq. 5.2, yields $\Delta\theta \approx 1.62/(Rk_f)$. The measured angular widths of jets emitted from condensates of various sizes and oscillation frequencies saturate this uncertainty limit, see Fig. 5.17.

Note that the condensates of $R = 6.8$ μm and 12.4 μm used in Fig. 5.17 typically contain $N = 26\,000$ and $41\,000$ atoms, respectively. Even with these slight differences in atom number, the density of the gas with $R = 12.4$ μm is approximately half as that of gases with $R = 6.8$ μm. We did not make any effort to keep the density constant between the different radii, because density is not expected to affect the width of the jets; it only affects their growth rate. This expectation seems to be validated by the results, which all agree with the density-independent prediction.

Finally, it is interesting t note that the angular width of the jets does not appear to depend on their distance from the condensate. Specifically, our theoretical predictions (Sec. 5.2) are made for the so-called "far-field" scenario, in which the jets have propagated sufficiently

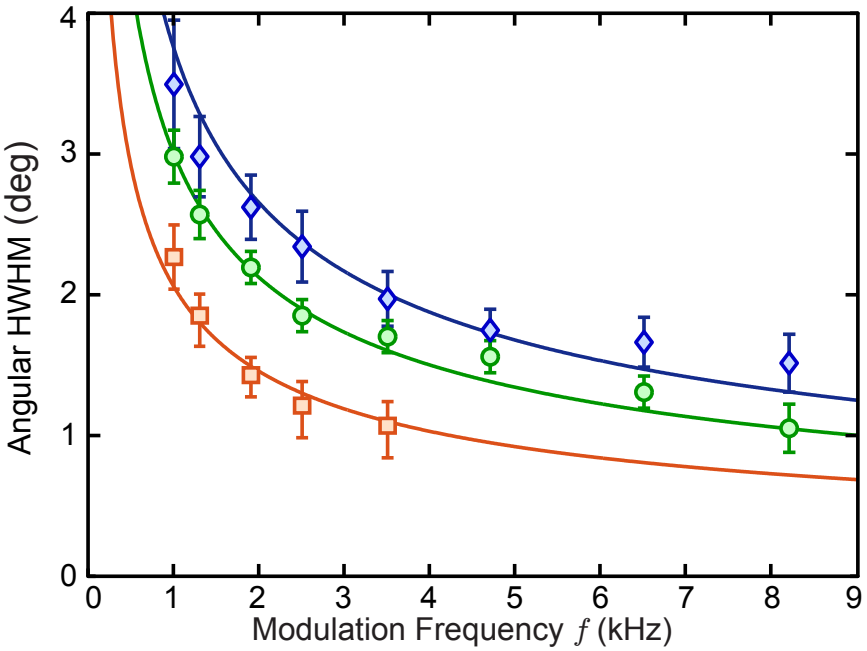

Figure 5.17: The deconvolved widths of the peaks at $g^{(2)}(0)$ for condensates with radius $R = 6.8$ (blue diamonds), 8.5 (green circles), and 12.4 μm (orange squares). Solid curves indicate the theoretical widths based on Eq. 5.2. Error bars indicate one standard error. For details on experimental parameters refer to the methods.

far from the remnant condensate that their width is dominated by their initial spread of momentum, rather than their initial spread in space. In the far-field, the modes should not be significantly overlapping in space. In the so-called "near-field" region in which the width of the jets is less than the width of the original gas (which matches the width of the mode envelopes), our theory would seemingly indicate that many modes are still overlapping. We can quantify the "field" of particular experimental conditions by comparing the typical half-width of a jet $r\Delta\theta$ where r is the distance of the jet from the center of the condensate to the radius R of the condensate. The results shown in Fig. 5.17 span a wide range $r\Delta\theta/R \approx 0.1 \sim 0.6$, though they are generally closer to the near-field. Surprisingly, we still observe excellent agreement with the far-field theory. It would be interesting for future theoretical work to attempt to explain this observation.

The jet emission process can be further investigated as a function of the coherence length,

shape, or collective motion of the gas. One could probe the excitations present in more exotic states of matter by amplifying them into more readily detectable jets. Moreover, the observation that jets come from parametric amplification of the vacuum fluctuation suggests that this is a promising new platform to generate twin matter waves for metrological applications[27, 108, 74]. Jet emission should also be taken into account in schemes for Floquet engineering which utilize oscillating interactions[128, 109]. The observation that jets result from amplified quantum fluctuations suggests that this system overcomes the challenge of generating a scenario in which all other sources of excitations are suppressed. The suppression of other sources of noise makes this system well suited for amplifying the fluctuations which appear in more exotic states of matter than the ordinary BECs tested here.

CHAPTER 6

SPATIOTEMPORAL CONTROL OF THE INTERACTION STRENGTH

Much of the content in this chapter is based on our published work [44]: Clark, L. W., Ha, L.-C., Xu, C.-Y. & Chin, C, "Quantum dynamics with spatiotemporal control of interactions in a stable Bose-Einstein condensate," Phys. Rev. Lett. 155301, 9, 2015 (Copyright 2015 by the American Physical Society). The thesis author played the primary role in the work described in this chapter.

6.1 Background

Feshbach resonances play an essential role in many exciting experiments on atomic quantum gases, as discussed in Sec. 2.3. Indeed, none of the work described in this thesis would have been possible without the ability to tune the scattering length using Feshbach resonances. The fundamental reason is that one cannot even dream of forming condensates of ^{133}Cs without tuning the scattering length away from its large and negative background value[152, 36]. Moreover, the surprisingly sophisticated dynamics of Bose fireworks described in the previous chapter result from a simple oscillation of the scattering length. Even the shaken lattice experiments described in Ch. 3 and 4 relied on Feshbach resonances in subtle but crucial ways. First, the small average scattering length during shaking kept the heating of the gas due to inter-band collisions manageable[119, 38, 40, 39]. Second, the domain detection technique described in Sec. 4.3.1 only works because the scattering length is tuned to zero and thus interactions are negligible during time-of-flight[42].

In light of the many applications already discussed for relatively slow, global changes of the scattering length, it is easy to imagine that fast, local control of interactions would bring a plethora of new quantum-mechanical phenomena into the realm of ultracold atomic

gases. Indeed, temporal modulation of interactions has been theoretically proposed as a route for creating anyonic statistics for atoms in optical lattices [69, 73] as well as new types of quantum liquids [1, 136] and excitations [139, 127, 2]. Spatial modulation would grant access to unusual soliton behavior [131, 21], controlled interfaces between quantum phases [78], stable nonlinear Bloch oscillations [137], and even the dynamics of acoustic black holes [15]. Oscillating interactions could also provide a powerful tool in Floquet engineering, specifically for creating density-dependent synthetic gauge fields [128, 109], see Sec.7.1.

Unfortunately, the conventional technique of magnetic Feshbach resonance (MFR) [84, 36] is usually unable to provide the desired spatiotemporal control of interactions. In most setups MFR is limited because the magnetic coils are too large for very fast or local modulation of the field. Specific to our setup, the main field coils have a bandwidth of just a few kHz (see Fig. 2.2) and are essentially limited to producing global fields and linear gradients[81].

A promising approach to overcome the limitations of MFR is optical control of Feshbach resonances (OFR), with which high speed, spatially resolved control of interactions can be realized. Early work in this direction [61, 25, 60, 144] focused on direct optical coupling of the atomic scattering state to an excited molecular bound state. Others have used the narrow intercombination transition in alkaline-earth-like atoms [160, 59, 158, 23, 159] where OFR has the additional benefit of providing control of interactions to species in which MFRs do not exist. Another approach is to provide a bound-to-bound optical coupling which shifts a state already coupled to the continuum [18, 17].

While these past efforts have shown significant promise, they generally encountered two major obstacles. First, in previous experiments OFR has limited the quantum gas lifetime to the millisecond timescale [17, 159, 66] due to optical excitation to molecular states. Short lifetimes prevent quantum gases from reaching equilibrium or evolving normally over typical dynamical timescales. Second, the change of interaction strength from OFR is often accompanied by an optical potential. This potential can result in a parasitic dipole force which

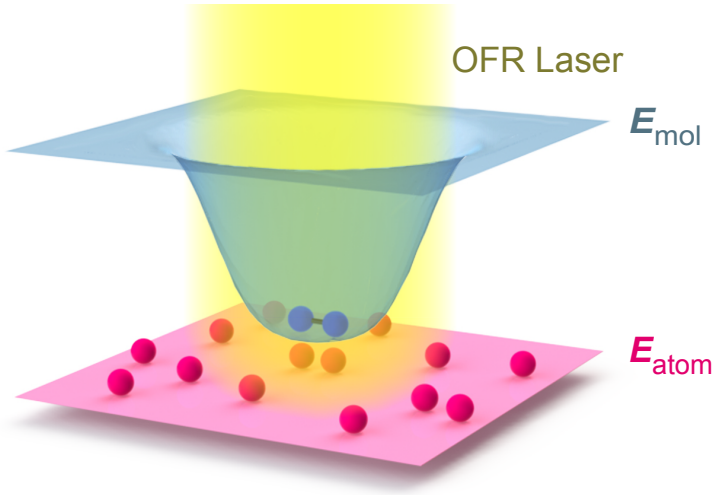

Figure 6.1: Illustration of scheme for optical control of Feshbach resonances. A Feshbach resonance occurs when a laser (yellow) brings a molecular energy level (blue surface) close to the atomic scattering threshold (red surface). Here, the atom-molecule coupling makes atomic interactions more attractive at higher laser intensity. When operating at the tune-out wavelength, the beam does not shift the energy of single atoms.

dominates the dynamics when the interactions are spatially modulated [158].

In this chapter we develop and implement a new scheme for optically controlling interactions while maintaining a long quantum gas lifetime and negligible parasitic dipole force. Using this scheme we can achieve a change of the scattering length by 180 Bohr radii with only a slow radiative loss of 1.6 s^{-1}. In the next Sec. 6.2 we describe our scheme in detail and predict its performance in ^{133}Cs. Following that in Sec. 6.3 we explain the technical challenges to implementing this scheme, both in general and specific to our apparatus. Then, in Sec. 6.4, we present our results confirming the excellent performance of our scheme and implementing it to perform interaction modulation spectroscopy and explore the dynamics of condensates with locally attractive interactions.

6.2 Scheme for optically controlling Feshbach resonances

We optically control Feshbach resonances by using a far detuned laser to light shift molecular states near the atomic scattering threshold (Fig. 6.1). The large detuning from all atomic

and molecular transitions offers low heating and loss rates for the quantum gas. For a laser with intensity I, the total light shifts of atoms (subscript a) and molecules (subscript m) are given by [100]

$$\begin{aligned}\delta E_{\mathrm{a}} = &\quad (\alpha_{\mathrm{a}} + \beta_{\mathrm{a}}\mu_{\mathrm{a}})I \\ \delta E_{\mathrm{m}} = &\quad (\alpha_{\mathrm{m}} + \beta_{\mathrm{m}}\mu_{\mathrm{m}})I,\end{aligned}$$

where α is the scalar polarizability and the vector polarizability $\beta\mu$ depends on the magnetic moment μ. The polarizabilities are calculated based on the laser detuning and the polarization-dependent dipole matrix elements of the transitions to the excited states below. Since our target molecular states are very weakly bound, they have similar polarizability to free atoms: $\alpha_{\mathrm{m}} \approx 2\alpha_{\mathrm{a}}$ and $\beta_{\mathrm{m}} \approx \beta_{\mathrm{a}} \equiv \beta$. Assuming the molecular and atomic magnetic moments differ $\mu_m \neq 2\mu_a$, the vector light shift can bring the molecular states closer to the scattering state, inducing a resonant atom-molecule coupling. In the past, optical shifts of a magnetic Feshbach resonance have been achieved using specific bound-to-bound transitions [18, 17, 66, 156] and recently using a far detuned laser [32]. Here, since this scheme does not rely on proximity to any atomic or molecular transitions, in principle the lifetime is only limited by the one-body off resonant scattering rate. Moreover, we choose a tune-out wavelength λ_{T} to eliminate the dipole force on the atoms ($\delta E_{\mathrm{a}} = 0$) [101, 154], such that only the molecular shift

$$\delta E_{\mathrm{m}} \approx \beta(\mu_{\mathrm{m}} - 2\mu_{\mathrm{a}})I \tag{6.1}$$

remains (Fig. 6.1). Under these conditions the laser can shift the energies of molecular states without creating parasitic dipole forces for free atoms. This scheme can be implemented in atomic species with a magnetic Feshbach resonance and a tune-out wavelength far-detuned from electronic transitions, see Sec. 6.4.7.

The effect of such a laser on the scattering length can be conveniently understood by

Transition	$\omega_{fi}/2\pi$ (THz)	$\lvert\langle f\rvert\rvert d\rvert\rvert i\rangle\rvert$ (10^{-29} C·m)	$\Gamma_f/2\pi$ (MHz)	C_{fi}^{+}	C_{fi}^{-}
D1	335.116	3.81	4.557	$\frac{7}{24}$	$\frac{1}{24}$
D2	351.726	5.36	5.219	$\frac{5}{48}$	$\frac{11}{48}$

Table 6.1: The parameters used to calculate the polarizability and scattering rate for the D1 and D2 transitions of Cs.

recognizing that the molecular shift (Eqn. 6.1) is equivalent to that caused by an effective magnetic field

$$B_{\text{eff}}(I) = \beta I \tag{6.2}$$

proportional to the laser intensity. Therefore, near a magnetic Feshbach resonance the scattering length follows [36] (see Sec. 2.3),

$$a(I) = a_{\text{bg}}\left[1 - \frac{\Delta}{B(I) - B_0}\right], \tag{6.3}$$

where $B(I) = B_{\text{ex}} + B_{\text{eff}}(I)$ is the total field including the real external magnetic field B_{ex}, Δ is the width of the resonance, and B_0 is the resonance position.

6.2.1 Theoretical calculation of light shift and scattering rate

To predict the tune-out wavelength λ_{T} and the effective field shift (Eqn. 6.3) from OFR we calculate the scalar and vector polarizabilities. Our Cs atoms are prepared in the absolute hyperfine ground state $|F = 3,\ M_F = 3\rangle$ where the total angular momentum $F = J+I$ is the sum of electron angular momentum $J = 1/2$ and nuclear spin $I = 7/2$, and M_K ($K = F,\ J$) is the projection onto the quantization axis. At low field we have $|F = 3,\ M_F = 3\rangle = -\sqrt{7/8}\,|M_J = -1/2,\ M_I = 7/2\rangle + \sqrt{1/8}\,|M_J = 1/2,\ M_I = 5/2\rangle$.

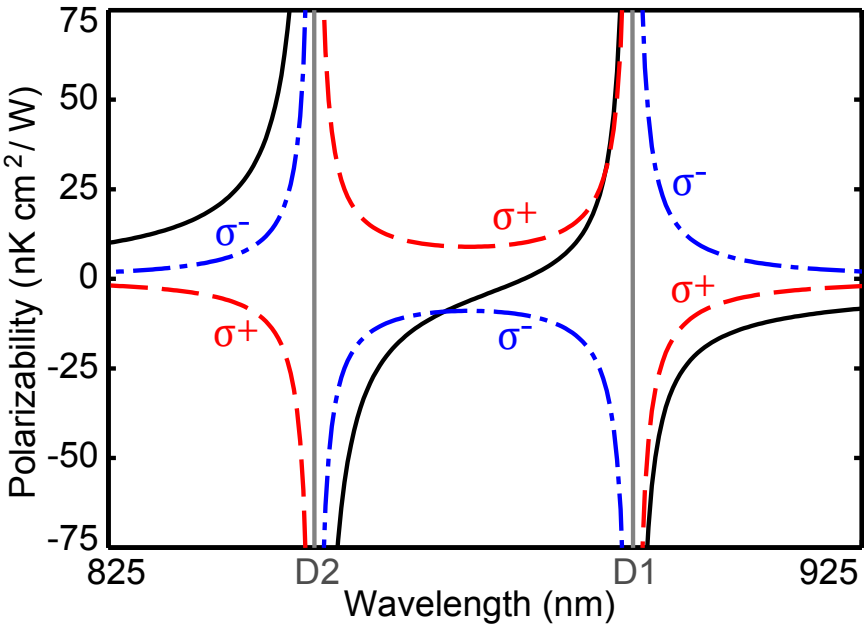

Figure 6.2: Theoretical polarizability. Scalar (solid), σ^+ vector (dashed), and σ^- vector (dot-dashed) polarizabilities in the absolute ground state of Cs, see equations 6.4 and 6.5. Only the D1 (894 nm) and D2 (852 nm) lines are included in the calculation. Two possible tune-out wavelengths exist with circularly polarized light, 869.7 nm for σ^+ and 891.0 nm for σ^- polarization. We employ σ^+ polarization for this work.

The scalar (α) and vector ($\beta\mu$) AC polarizabilities of an atom for detuning which is large compared to the hyperfine splitting are [100]

$$\begin{aligned}\alpha_i =& \frac{(-1)^{J_i}}{2\hbar\epsilon_0 c\sqrt{3(2J_i+1)}} \\ &\times \sum_f (-1)^{J_f} \left\{ \begin{array}{ccc} 1 & 0 & 1 \\ J_i & J_f & J_i \end{array} \right\} |\langle f||d||i\rangle|^2 \\ &\times \left(\frac{1}{\omega_{fi}-\omega} + \frac{1}{\omega_{fi}+\omega} \right)\end{aligned} \tag{6.4}$$

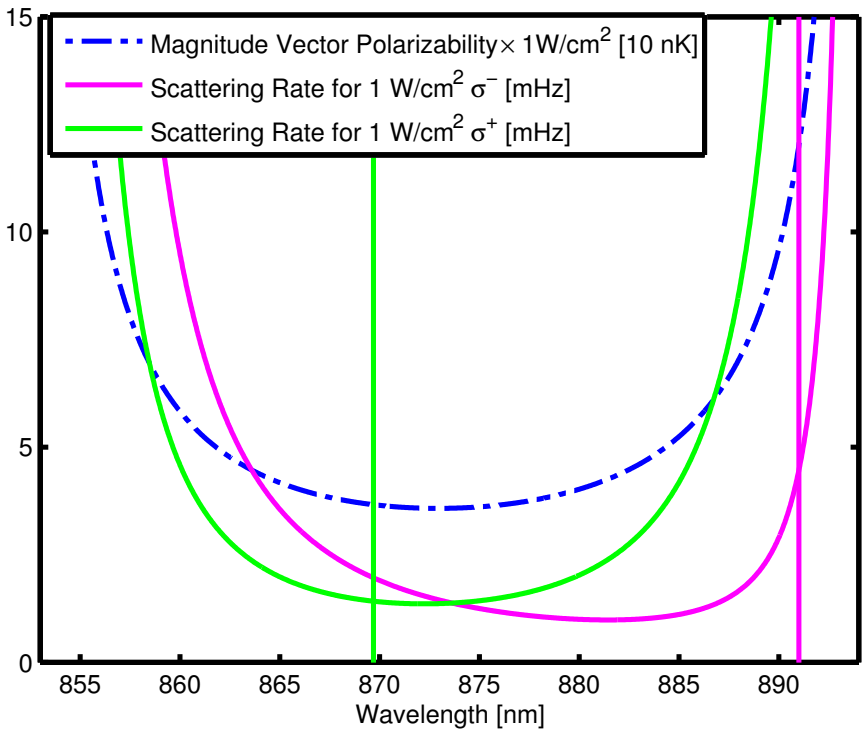

Figure 6.3: Scattering rate in comparison to vector polarizability. A plot of the magnitude of the vector polarizability (blue dot-dashed) compared with the theoretical one-body scattering rates for photons of polarization σ^- (green) and σ^+ (purple). The vertical lines of each color indicate the corresponding tune-out wavelengths.

$$\begin{aligned}\beta_i\mu_i =& \frac{(-1)^{J_i}}{2\hbar\epsilon_0 c}\sqrt{\frac{3J_i}{2(J_i+1)(2J_i+1)}}\left(\frac{AM_J}{J_i}\right)\\ &\times\sum_f(-1)^{J_f}\left\{\begin{array}{ccc}1 & 1 & 1\\ J_i & J_f & J_i\end{array}\right\}|\langle f||d||i\rangle|^2\\ &\times\left(\frac{1}{\omega_{fi}-\omega}-\frac{1}{\omega_{fi}+\omega}\right),\end{aligned} \tag{6.5}$$

where $|f\rangle$ represents a relevant excited state, ϵ_0 is the vacuum permittivity, c is the speed of light, $\left\{\begin{array}{ccc}j_1 & j_2 & j_3\\ j_4 & j_5 & j_6\end{array}\right\}$ is the Wigner 6-j symbol, $|\langle f||d||i\rangle|$ and ω_{fi} are the reduced dipole matrix element and resonance frequency for the transition from $|i\rangle$ to $|f\rangle$ (Table 6.1), ω is

the laser frequency, M_J is the projection of J_i onto the laser propagation direction, and $A = (I_{\sigma^+} - I_{\sigma^-})/I$ accounts for the beam polarization. We include in the calculation only the D1 and D2 transitions, which dominate in the wavelength range that we consider. The next most significant excited state provides a correction at the 10^{-3} level, which is negligible for our purposes. We set M_J to its expectation value of $\langle M_J \rangle = -3/8$ for atoms in the $|F = 3,\ M_F = 3\rangle$ state. The calculated polarizabilities are shown in Fig. 6.2.

The total off-resonant photon scattering rate $s(I)$ is,

$$s(I) = \frac{I}{2\hbar^2 \epsilon_0 c} \sum_f \frac{d_{fi}^2 \Gamma_f}{(\omega_{fi} - \omega)^2}, \tag{6.6}$$

where $d_{fi}^2 = C_{fi}^{\pm} |\langle f||d||i\rangle|^2$ is the squared dipole matrix element, $C_{fi}^{\pm}$ is a numerical factor primarily accounting for the Clebsch-Gordan coefficients with beam polarization $\sigma^{\pm}$, and Γ_f is the spontaneous emission rate of the excited state $|f\rangle$ (Table 6.1).

6.2.2 Optimal performance of OFR

The figure of merit M for choosing the wavelength and polarization of the laser is the ratio of the effective field shift $B_{\text{eff}} = \beta I$ from OFR to the photon scattering rate $s(I)$,

$$M = \frac{\beta I}{s(I)} \tag{6.7}$$

A larger absolute value of M indicates a greater shift in molecular states for a particular quantum gas lifetime. M is optimized by using pure circular polarization. The tune-out wavelengths for σ^+ and σ^- polarization are both suitable choices with almost identical M to within 5%, see Fig. 6.3. The two choices remain differentiated by the sign of the change in scattering length, $da/dI < 0$ for σ^+ and $da/dI > 0$ for σ^-. In the experiments

described below we employ σ^+ polarization with $M = -130$ mG·s at the tune-out wavelength $\lambda_T = 869.7$ nm.

Optimal performance of the full OFR scheme is obtained when a laser with maximum M is employed near a proper magnetic Feshbach resonance. The sensitivity of scattering length to the effective field shift from OFR (based on Eqn. 6.3) is

$$\left.\frac{da}{dB_{\text{eff}}}\right|_{|a/a_{\text{bg}}|\ll 1} = \frac{a_{\text{bg}}}{\Delta} \tag{6.8}$$

near the zero crossing $B(I) = B_0 + \Delta$ where the condensate can be stable. This result suggests that a narrow resonance with a large background scattering length will offer wide tunability for a given laser intensity. However, one must be cautious to avoid extremely narrow resonances which can greatly enhance the three-body recombination rate. In this work we choose the Feshbach resonance at 47.8 G, for which we have $a_{\text{bg}}/\Delta = 6.6\ a_0/\text{mG}$ from coupled channel calculations [22].

Overall, optimal performance is obtained via the independent optimizations of M, which is determined by the laser, and $da/d(\beta I)$, which is determined by the choice of Feshbach resonance. For Cs atoms near the Feshbach resonance at 47.8 G and a laser of σ^+ polarization at the tune-out wavelength $\lambda_T = 869.7$ nm, the product of these two factors yields $Ma_{\text{bg}}/\Delta = -860\ a_0$·s. This value indicates that a change of the scattering length by 860 a_0 should be possible while inducing a scattering rate of 1/s.

6.3 Experiment Setup

In this section we will explain some technical details of our implementation, which may interest both others who wish to implement OFR and future users of this particular apparatus, to varying degrees. First, we provide the parameters of the system specific to these experiments. Second, we will explain our strategy for forming stable condensates near the

47.8 G Feshbach resonance. Third, we relate some brief cautionary tales about the "spot of death" and the drift of the coil temperature which caused us a few headaches. Fourth, we demonstrate a convenient method for reliably measuring the intensity profile of the OFR laser at the plane of the atoms. Finally, we show the intensity modulation bandwidth that we were able to achieve with an acousto-optic modulator (AOM) and future prospects for a speedup using an electro-optic modulator (EOM).

6.3.1 Experiment Setup

The experiments in this chapter are performed in a 3D trap composed of the XDT, YDT, ZDT, and vertical lattice beams. This harmonic trap has fixed horizontal frequencies $(\omega_x, \omega_y) = 2\pi \times (12, 30)$ Hz. We tune the vertical frequency ω_z from $2\pi \times 70$ Hz to $2\pi \times 470$ Hz using the vertical lattice intensity, which we vary to suit the needs of individual experiments. Our samples typically contain from $3{\sim}10{\times}10^3$ atoms with peak densities from $1{\sim}4{\times}10^{13}$ cm^{-3}. When we test the response of condensates in optical lattices to oscillating OFR intensity, one of the horizontal trapping beams is retro-reflected to create a 1D optical lattice with spacing $d = 532$ nm and depth $h \times 9.28$ kHz. For most of the experiments described in this chapter we form our BECs near the d-wave magnetic Feshbach resonance at 47.8 G [97] with a small and positive scattering length of $a = 200{\sim}300\ a_0$. The magnetic field in our system is stable to within 1 mG with systematic calibration error of 5 mG, sufficient to form stable BECs even at this narrow resonance (see the next subsection for more information).

We optically control interactions with the intensity of the OFR laser, which propagates along the magnetic field direction. The change of scattering length due to OFR is insensitive to small changes in the wavelength and polarization of the OFR laser. However, both parameters must be carefully controlled to eliminate the residual light shift. The source of the laser is a free-running single-mode diode with 100 mW output power, which can be tuned

via its temperature. We determine the laser frequency using a wavemeter with an accuracy of 100 MHz, sufficient to make the residual light shift negligible.

6.3.2 Magnetic fields and the formation of stable condensates near the 47.8 G Feshbach resonance

This experiment presents a number of challenges in the realm of magnetic field control due to our need to work near the moderately narrow 47.8 G Feshbach resonance. First of all, we need to be able to form stable BECs slightly above the zero crossing. However, it is not possible to simply "jump" the magnetic field there after forming a BEC at the usual lower magnetic field of $\sim$ 20 G, because the gas heats up enormously (compared to its few nK temperature) even if it quickly crosses the narrow resonance. Perhaps a better way to say that is that we cannot cross the resonance quickly enough.

Therefore, for this experiment we adjust the evaporation procedure in order to jump the magnetic field across the 47.8 G Feshbach resonance before the end of evaporation. However, this presents additional challenges. We normally perform evaporation by slowly reducing the magnetic field gradient which counteracts gravity [81], and only at the end of evaporation does the gradient go to zero. Unfortunately, near the narrow resonance the presence of a field gradient creates a corresponding scattering length gradient, making it difficult to achieve efficient evaporation. In light of these issues, we form condensates as follows: 1) increase the initial dipole trap depth by increasing the intensity of the ZDT beam, 2) ramp the gradient down to zero to perform an efficient initial evaporation at low field, 3) jump the field to slightly above 47.8 G where the scattering length is roughly $a \approx 200a_0$, and 4) slowly ramp down the ZDT intensity toward its normal value to complete evaporation. This procedure is still less efficient than the usual procedure, but can produce cold condensates containing $N \approx 10\,000$ atoms. Note that jumping back across the resonance down to low field for imaging also seems to significantly disturb the atoms; therefore, it is preferable to

recalibrate the imaging and repumper laser frequencies and perform the imaging at the same field at which experiments are performed.

A few other magnetic field issues are worth mentioning. First, when using the expansion during TOF to measure the scattering length as in Sec. 6.4.2, we would ordinarily (i.e. away from the narrow resonance) use a levitation gradient of $B' \approx 31$ G/cm to prevent the BEC from falling out of focus for the high resolution vertical imaging. However, near the zero crossing of the narrow resonance a gradient of that magnitude causes the scattering length to vary by $\Delta a \approx 100\ a_0$ over a distance of 5 μm which is comparable to the vertical diameter of the gas. This magnitude of variation would ruin the measurement, and therefore we must allow the gas to drop under the influence of gravity. Dropping the gas makes the vertical imaging useless, so we use the lower resolution horizontal imaging instead. We also take special care to ensure that the magnetic field is constant within a few mG while the gas drops.

The last noteworthy magnetic field issue is caused by the slow drift of the main coil temperature over the course of the day. Because the coils are air cooled, they heat up very slowly over the course of a few hours if the experiment is running (the primary heating occurs while a large magnetic field gradient is present). While the controller keeps the current in the coils consistent, thermal expansion causes the magnetic field experienced by the atoms to drift. Therefore, while performing these experiments, we tried to keep the duty cycle of the experiment consistent such that the coils would reach equilibrium and the magnetic field would be constant. We monitored the temperature of the coils in real time and adjusted the duty cycle to maintain a constant temperature within $\delta T \approx 0.1$ K, corresponding to a magnetic field uncertainty of $\delta B \approx 1$ mG. Finally, the magnetic field near our atoms shifts by approximately 7 mG when the building elevators are in the sub-basement [162]; it was important to make sure that the field controller which cancels this effect is operating correctly when performing these experiments. If one observes occasional trials which jump

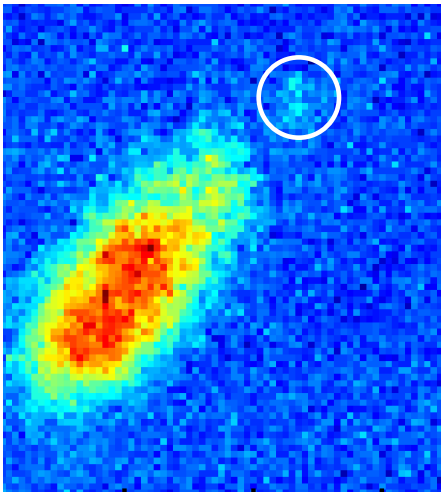

Figure 6.4: Lossy region formed by a focused reflection of the OFR beam from the objective lens, whose position in the atom plane is indicated by a small clump of atoms circled in white. Originally, the laser for optical control of Feshbach resonance was partially reflected and focused by the first surface of the objective lens, resulting in a strongly attractive potential and rapid atom loss.

by a consistent amount away from the expected behavior, it may be caused by the elevator.

6.3.3 Lifetime Issues

Before achieving the lifetime performance presented below, two serious issues were limiting the lifetime of the atoms in the presence of the OFR laser. First, these experiments were performed using a diode laser (Eagleyard EYP-RWL-0870) which tend to have a pedestal of extremely weak emission covering a wide range of frequencies. The fraction of pedestal light near the D1 and D2 lines of Cs caused rapid scattering of the laser and loss of atoms. Sending the laser through an interference filter (Semrock FF01-910, at an angle of approximately 36°) before the fiber removes the worst components of the pedestal.

The second issue was much more exotic. Whenever we turned on the OFR laser, we would see faster loss rates than expected and an extra "spot" of atoms a few microns away from the main BEC, as shown in Fig. 6.4. Eventually, we realized that the spot was actually the (approximate) focus of the small fraction of OFR laser light reflected from the first

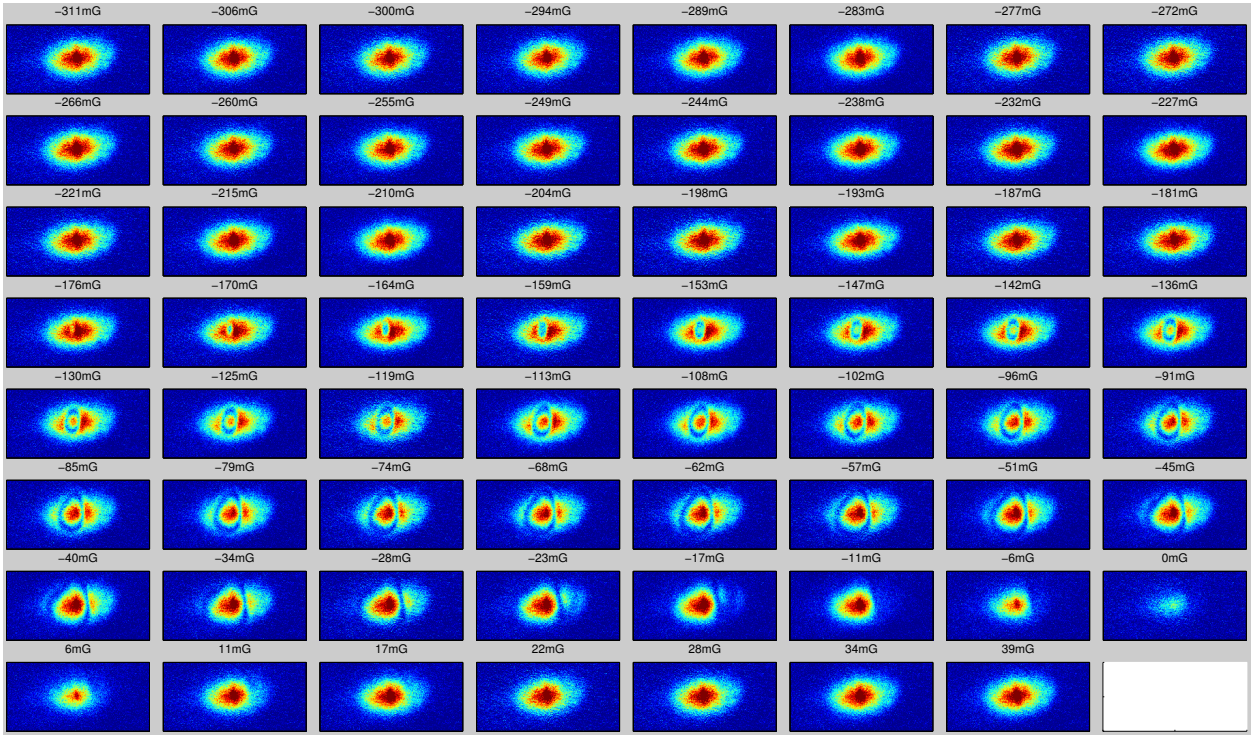

Figure 6.5: Example of OFR beam tomography using the shift of a microwave resonance. In each image, atoms are depleted from locations at which the OFR laser provides the effective magnetic field labeled above each image. See text for details on the procedure.

surface of the objective lens. Moreover, as a result of the waveplate and polarizer below the objective lens (whose primary purpose is to reflect the vertical MOT laser [75]) the reflected light had approximately the opposite circular polarization. As a result the reflection was far from the tune-out wavelength for its polarization, creating a strongly attractive potential, and it induced rapid loss of the atoms it attracted because the beam was focused to high intensity. We resolved the issue by translating the objective lens horizontally in order to move the reflected spot far away from the BEC.

6.3.4 Beam profiling using microwave tomography

The OFR laser in our system propagates vertically through the atoms, approximately along the optical axis of the vertical imaging and in the same direction as the imaging beam. As

a result, coarse alignment and profiling of the beam can be done using the vertical camera. However, chromatic aberrations distort the results sufficiently that we need a better approach when the details of the beam profile are crucial, such as for the local collapse measurement in Sec. 6.4.6.

In order to obtain a reliable beam profile, we can directly measure the influence of the OFR beam on the local effective magnetic field using a microwave resonance, see Fig. 6.5. First, we load a large 2D gas with weak horizontal trapping. We then turn on deep optical lattices along XDT and YDT to minimize the motion of the atoms. After slowly turning on the OFR beam, we apply a weak microwave pulse over tens of ms to excite some atoms from the ground $|3,3\rangle$ state to the excited $|4,2\rangle$ state. In regions where atoms are resonant with the microwaves, they end up in a mixture of spin states, causing them to undergo rapid loss due to spin-exchange collisions. By scanning the microwave frequency we can measure the resonance frequency at each location in the gas relative to its resonance with zero laser intensity (marked 0 mG in the figure) and therefore extract the local effective magnetic field shift due to the OFR laser.

6.3.5 Intensity modulation bandwidth

The temporal modulation experiment (see Fig. 6.11 below) requires rapid control of the beam intensity. We send the OFR beam through an acousto-optic modulator (Isomet 1205C-1) and use a fast RF switch (Mini-Circuits ZFSWA-2-46) to control the acoustic wave which drives the modulator. We measure the 3 dB bandwidth of intensity modulation to be 10 MHz using a fast photodiode, see Fig. 6.6.

6.3.6 Polarization Purity

One of the most difficult challenges when implementing this scheme, particular when one wants high resolution features to create spatial patterns of the scattering length, is to avoid

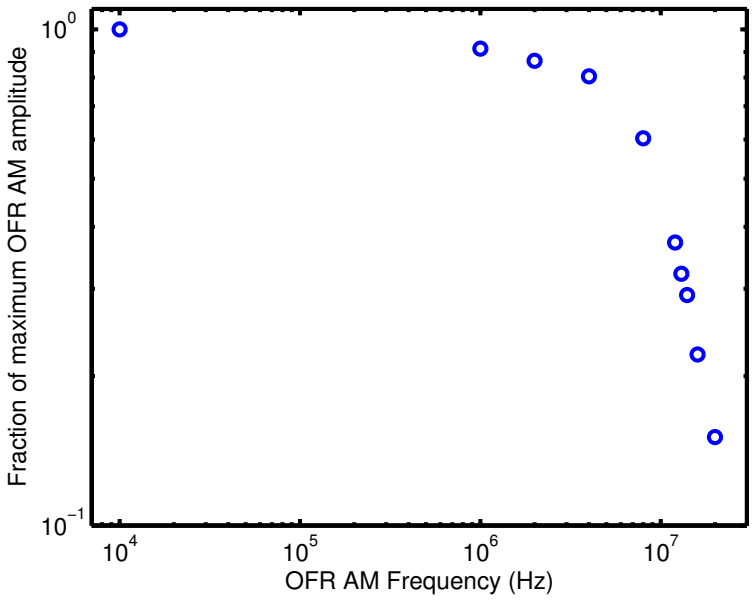

Figure 6.6: Intensity modulation bandwidth of the OFR laser. A plot of the fraction of the maximum intensity modulation of the OFR laser which can be achieved by modulating the RF power driving an acousto-optic modulator.

inhomogeneities of the beam polarization which lead to a position-dependent tune-out wavelength. While a global change in the polarization can be compensated with a change in the wavelength, it is much harder to account for inhomogeneity. Polarization inhomogeneity is inevitable as a result of polarization- and angle- dependent reflection from both mirror and lens surfaces, for example. At the very least, it is important to make sure that the beam is well collimated when passing through polarization optics (such as cubes or waveplates) so that their effects are as homogeneous as possible. One can estimate the necessary polarization purity for a given experiment by noting how the potential changes with polarization near the tune-out wavelength. For example, the dipole potential for the 115 W/cm^2 beam used in Sec. 6.4.6 follows $dV \approx -dA k_{\mathrm{B}} \times 1\ \mu$K where $dA = I_{\sigma^-}/I$ represents the fraction of intensity at the wrong polarization. Given that our gases typically have chemical potentials on the order of $k_{\mathrm{B}} \times 10$ nK, we are sensitive to even a 0.1% variation in the intensity at the wrong polarization across the beam, which would perturb the density profile by 10%.

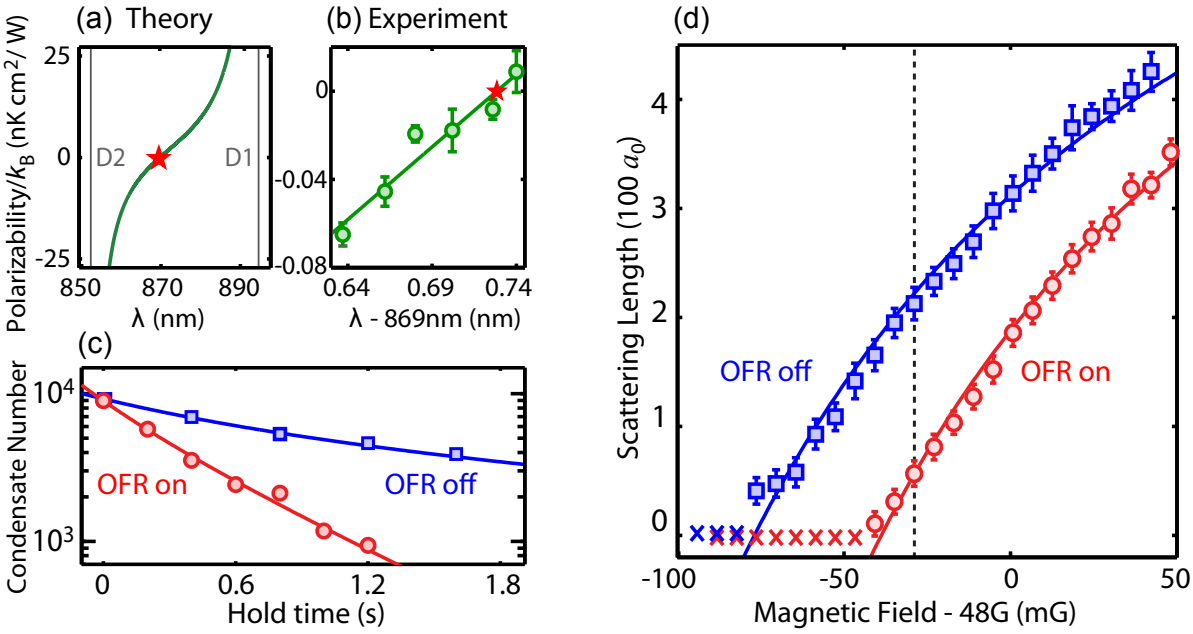

Figure 6.7: Stable optical control of scattering length at a tune-out wavelength λ_T. (a) Theoretical polarizability of Cs atoms in the absolute ground state for σ^+ polarization (Sec. 6.2). The star marks the tune-out wavelength where polarizability is zero. (b) Measured polarizability (circle). A linear fit yields $\lambda_T = 869.73(2)$ nm (star). (c) Number of condensed atoms remaining over time with (circle) and without (square) exposure to OFR at a magnetic field of 48.19 G. We fit the decay dynamics (solid curves) and find that OFR exposure adds a one-body loss process with a time constant of 0.63(2) s (see Sec. 6.4.3) at intensity $I = 225$ W/cm^2. (d) Scattering length a determined from the free expansion of BECs with (circle) and without (square) exposure to the OFR laser. When the scattering length becomes negative ($a < 0$) the condensate collapses (cross). The solid curves derive from a single fit to all $a > 0$ data using Eq. (6.11), which yields $\Delta = 157(3)$ mG, $B_0 = 47.766(4)$ G, and $\beta I = -38(1)$ mG. All error bars indicate standard error.

6.4 Results

6.4.1 Tune-out wavelength

For cesium atoms one possible tune-out wavelength is 869.7 nm with a σ^+ polarized laser, which is far detuned from atomic transitions but maintains a large vector polarizability (Fig. 6.7a). To confirm the tune-out wavelength experimentally, we measure the atomic polarizability at different wavelengths. To test the polarizability we measure the displace-

ment of the BEC caused by an intensity gradient OFR laser. At the tune-out wavelength, the beam should not move the condensate. For this experiment we operate at $B = 22$ G where the dependence of interactions on the OFR shift is negligible. We prepare the OFR beam with a waist of 70 μm, which is large compared to the BEC, and displace the beam to achieve a slope of $dI/dx = 5$ (W/cm^2)/μm across the sample. A finite total polarizability $\gamma = \alpha + \beta\mu$ leads to a force of $F = \gamma dI/dx$ on the atoms, which offsets the center of the harmonic trap by $\Delta x = F/m\omega_x^2$. By measuring the shift in the center of the BEC, we extract the polarizability

$$\gamma = \frac{m\omega_x^2 \Delta x}{dI/dx}, \tag{6.9}$$

yielding the data shown in Fig. 6.7b.

We find the tune-out wavelength to be $\lambda_{\mathrm{T}} = 869.73(2)$ nm for σ^+ polarization, in fair agreement with the prediction of 869.66 nm. We attribute the difference to the electronic transitions not included in the calculation and the imperfect beam polarization; we estimate that $I_{\sigma^-} \approx 0.005I$. Therefore, at the intensity $I = 225$ W/cm^2 used for most of this chapter, we estimate that the residual dipole potential $k_{\mathrm{B}} \times 1$ nK is negligible compared to our typical chemical potential of $k_{\mathrm{B}} \times 10$ nK, where k_{B} is the Boltzmann constant.

In addition, at the tune-out wavelength we test the assumption that $\beta_m \approx \beta_a \equiv \beta$ for weakly-bound molecular states. We measure the effective field shift βI induced by the laser using microwave spectroscopy. We compare the microwave result to the shifts in energy of g-wave and d-wave molecular states. Within 5% all methods yield values which are consistent with the theoretical prediction (Eq. (6.5)).

6.4.2 Extracting scattering length from BECs after free expansion

A precise way to measure the scattering length is to release the BEC from the harmonic trap, simultaneously switch the magnetic field and OFR beam intensity, and measure the BEC

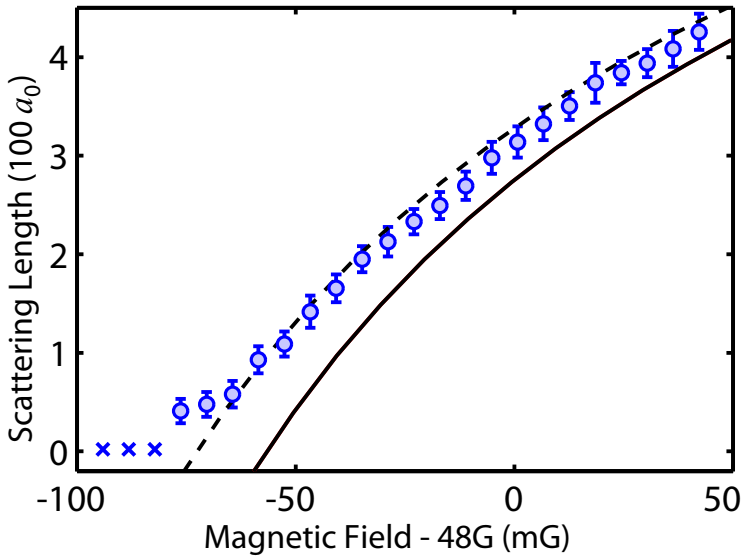

Figure 6.8: Comparison of scattering length from free expansion to a coupled channel model. The scattering length extracted from free expansion with no OFR laser (circle) compared to the scattering length based on the coupled channel calculations in Ref. [22] (solid curve). The dashed curve shows the calculated scattering length shifted by -16 mG, which is within the model uncertainty. Error bars show standard error.

radius after a period of free expansion. This method yields measured radii R which scale as $a^{1/2}$, making it more sensitive than *in situ* measurements or free expansion measurements with constant magnetic field which yield $R \propto a^{1/5}$ [150]. Ref. [31] shows that, during expansion, the BEC density profile is parabolic with time-dependent Thomas-Fermi radii R_k $(k = x, y, z)$. The time evolution of the ratios $\lambda_k(t) \equiv R_k(t)/R_k(0)$ is described by the three coupled differential equations,

$$\ddot{\lambda_k} = \frac{a_f}{a_i} \frac{\omega_k^2}{\lambda_x \lambda_y \lambda_z \lambda_k} \tag{6.10}$$

where ω_k is the trap frequency before release, $a_i = 250 a_0$ is the scattering length before release, and a_f is the scattering length during expansion which is determined by the magnetic field and OFR intensity. Note that there is one equation for each λ_k and the trap frequencies are independently calibrated, such that the only unknown variable is the scattering length.

To determine a_f as a function of magnetic field and OFR intensity, we execute the

experimental procedure over a range of magnetic fields with and without exposure to the OFR beam at $I = 225$ W/cm^2. For this experiment we use a vertical trapping frequency of $\omega_z = 2\pi \times 105$ Hz much greater than the horizontal frequencies of $(\omega_x, \omega_y) = 2\pi \times (14, 31)$ Hz, which causes the vertical expansion to dominate after release. Thus, after an expansion time of 16 ms we measure only the vertical radius of the gas. For each combination of magnetic field and OFR intensity, we determine the scattering length a_f by comparing the measured radius to the numerical solution of Eq. (6.10).

The resulting scattering lengths with and without the OFR laser are shown in Fig. 6.7d. We fit the scattering lengths with a theoretical model [36]

$$a(I) = a_{\rm bg}\left[1 - \frac{\Delta}{B(I) - B_0}\right], \tag{6.11}$$

where $B(I) = B_{\rm ex} + \beta I$ is the effective magnetic field including the contribution βI from OFR (Eq. (6.1)) and the external field $B_{\rm ex}$, $a_{\rm bg} \approx 950\ a_0$ is the background scattering length at this Feshbach resonance [22], Δ is the width of the resonance, and B_0 is the resonance position. The fit yields $\beta I = -38(1)$ mG, sufficient to shift from $a = 180\ a_0$ to zero. In the absence of the OFR beam we compare our results to coupled channel calculations [22], see Fig. 6.8.

6.4.3 Condensate lifetime with OFR

In the presence of the OFR laser, we expect the lifetime to be limited by one-body off-resonant scattering of photons, since our scheme does not rely on proximity to resonant atomic or molecular transitions. In practice, while we predict the one-body loss process to have extremely weak wavelength dependence, we find significant wavelength dependence of the lifetime within the tuning range of our laser, see Fig. 6.9. We attribute this observation to the two-body loss caused by photoassociation or molecular resonances which happen to be within the tested wavelength range. After finding a wavelength which minimizes this loss,

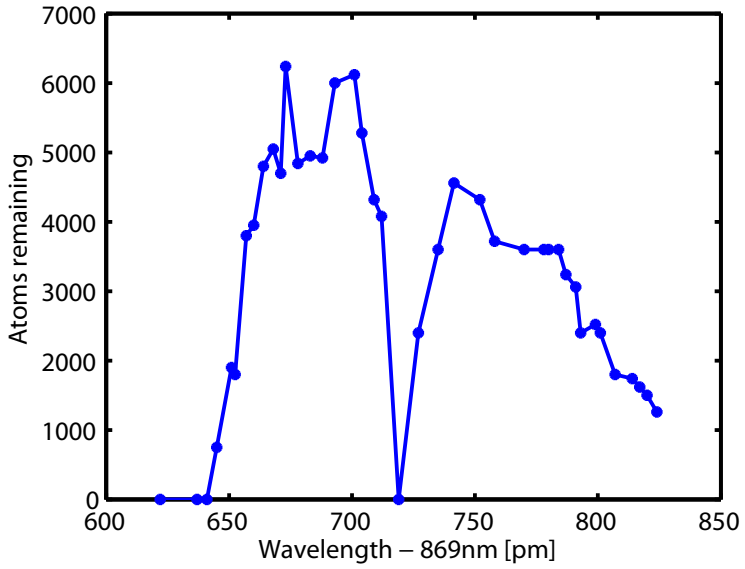

Figure 6.9: A plot of the number of atoms remaining in a BEC initially containing 10 000 atoms after exposure to the OFR laser tuned over a range of wavelengths near the tune-out condition.

we make minute adjustments to our laser polarization to shift the tune-out wavelength to the loss minimum. The required change in polarization is small, such that its effect on the effective field shift is negligible.

Having minimized two-body loss, we model the lifetime by accounting for the one-body loss process induced by OFR and the pre-existing three-body loss process. With both processes the decay of density n is described by the differential equation

$$\frac{\partial n(\boldsymbol{r},t)}{\partial t} = -L_1 n(\boldsymbol{r},t) - L_3 n(\boldsymbol{r},t)^3, \tag{6.12}$$

where L_1 (L_3) is the one-(three-)body decay constant. We assume that the loss is slow such that the system remains in equilibrium. Integrating the Thomas-Fermi density profile [122] over space with fixed scattering length and absorbing trap-dependent factors into the modified decay constant L_3' we obtain,

$$\frac{dN}{dt} = -L_1 N - L_3' N^{9/5} \tag{6.13}$$

which describes the decay of total atom number in the presence of one- and three-body loss. Note that the one-body lifetime is independent of trap geometry.

To determine the lifetime experimentally, we compare the decay of condensate number with and without exposure to the OFR laser at $B_{\mathrm{ex}} = 48.19$ G (Fig. 6.7c). We chose this field to obtain realistic decay rates near the Feshbach resonance but be far enough away to avoid inducing condensate dynamics or significantly altering the three-body loss with the OFR beam. We keep the trap depth constant throughout the decay, so that the BEC continues to evaporate and maintain an approximately constant temperature while exposed to the laser. With no OFR exposure we fit the decay to the numerical solution of Eq. (6.13) with negligible L_1 and find $L_3' = 5.6 \times 10^{-4}$ s^{-1} in our trap geometry. We use this fixed value to fit the decay in the presence of OFR to Eq. (6.13) and obtain $L_1 = 1.58(4)$ s^{-1}, corresponding to a time constant of $\tau = 1/L_1 = 0.63(2)$ s, with OFR intensity 225 W/cm^2.

The fitted time constant represents more than an order of magnitude improvement over existing OFR schemes, but it is still shorter than the off-resonant scattering time constant of 3.2 s (Eq. (6.6)). We expect that the lifetime is shorter than the scattering time constant because the recoil heating from a single scattering event is $k_B \times 200$ nK, much larger than the critical temperature $T_C \approx 30$ nK of the condensate. Thus each scattering event can lead to the loss of multiple atoms from the condensate. There may also be a contribution from photoassociation resonances or molecular transitions which remain near the chosen wavelength.

6.4.4 Extraction of scattering length from in-situ BEC density profiles

The long lifetime of BECs exposed to the OFR laser allows us to corroborate the change of scattering length based on *in situ* measurements of the density profile. We slowly ramp on the OFR beam to four different final intensities over 200 ms and measure the resulting density profiles (Fig. 6.10a). Higher intensities of the OFR laser shrink the BEC and increase

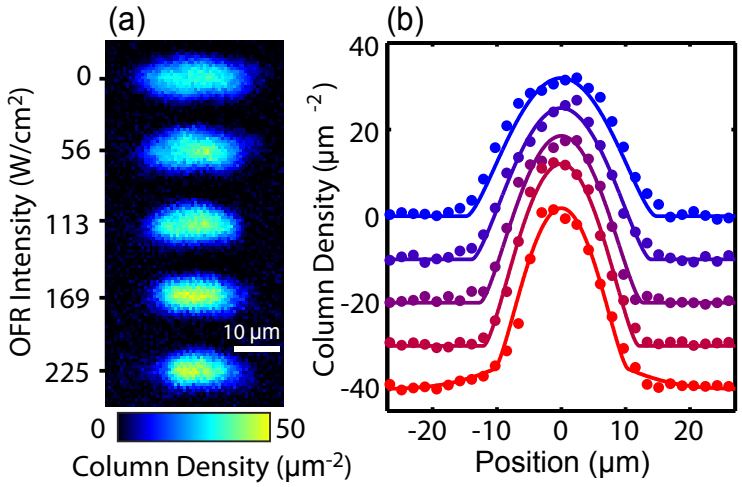

Figure 6.10: Effect of OFR on in situ density profiles. (a) *In situ* images of BECs at 47.97 G after ramping on the intensity of the OFR laser over 200 ms. Each image is the average of 10 trials. (b) Horizontal line cuts (circle) obtained by averaging the middle five pixels from each image in panel (a), similarly arranged from top (no OFR laser) to bottom (225 W/cm^2). The solid curves are the corresponding cuts from a fit to each image with Eq. (6.14). For the 225 W/cm^2 case we first perform a Gaussian fit to the wing to account for thermal atoms before fitting the remaining BEC. The fitted scattering lengths, in order of increasing beam intensity, are a = 230(33), 175(25), 120(16), 96(13), and 78(16) a_0 in good agreement with the free expansion result.

its density, consistent with weakening the repulsive interactions.

We fit the measured *in-situ* column density of BECs with a Thomas-Fermi density profile [122]

$$n(x,y) = n_0 \left(1 - \frac{x^2}{R_x^2} - \frac{y^2}{R_y^2}\right)^{3/2}, \tag{6.14}$$

where

$$n_0 = \left(\frac{1}{2\pi}\right)(5N\omega_x\omega_y)^{3/5}\left(\frac{m^2}{3\hbar^2 a\omega_z}\right)^{2/5}, \tag{6.15}$$

is the peak column density and the Thomas-Fermi radii are

$$R_k = \omega_k^{-1}(15\hbar^2 m^{-2} N\omega_x\omega_y\omega_z a)^{1/5}. \tag{6.16}$$

The only free parameter is the scattering length a which appears in n_0 and R_k, while the atom number $N = 3500$ and trap frequencies $(\omega_x, \omega_y, \omega_z) = 2\pi \times (10, 22, 75)$ Hz are calibrated independently. We compare horizontal line cuts of the images to the corresponding cuts from the fit in Fig. 6.10b. The extracted scattering lengths are in excellent agreement with the free expansion result in Sec. 6.4.2.

6.4.5 Interaction Modulation Spectroscopy

The stability of this scheme enables us to explore temporal and spatial control of interactions in a quantum gas. We first perform interaction modulation spectroscopy by recording the response of the BEC to an OFR beam with oscillating intensity. We perform these experiments either in the bulk, with the vertical trap frequency ω_z increased to $2\pi \times 470$ Hz, or in a weak one-dimensional optical lattice in the horizontal plane with spacing 532 nm and lattice depth $h \times 9.28$ kHz, in which the system remains a superfluid [76]. For this experiment only we introduce the optical lattice in order to test the consequences of modulated interactions in a lattice gas, as discussed in many theoretical proposals [69, 2, 73]. Combining the experiments in both geometries, we observe a variety of resonance features over a wide range of timescales, as shown in Fig. 6.11, highlighting the versatility of this technique.

At lower frequencies we observe excitations in the trap and in the optical lattice. The oscillating scattering length drives parity-conserving transitions to the second excited state in the vertical trap at 890(10) Hz and the second excited band of the optical lattice at 8.18(2) kHz. This demonstrates that the plentiful theoretical proposals [69, 73, 1, 136, 2, 139, 127] which require rapid oscillation of scattering length in the bulk or in the lattice are well within reach of our scheme.

At higher frequencies the oscillating intensity of the OFR beam induces formation of molecules. We identify a broad resonance at 133(7) kHz corresponding to a virtual molecular state embedded in the continuum, as well as narrow resonances at 197(1) kHz and

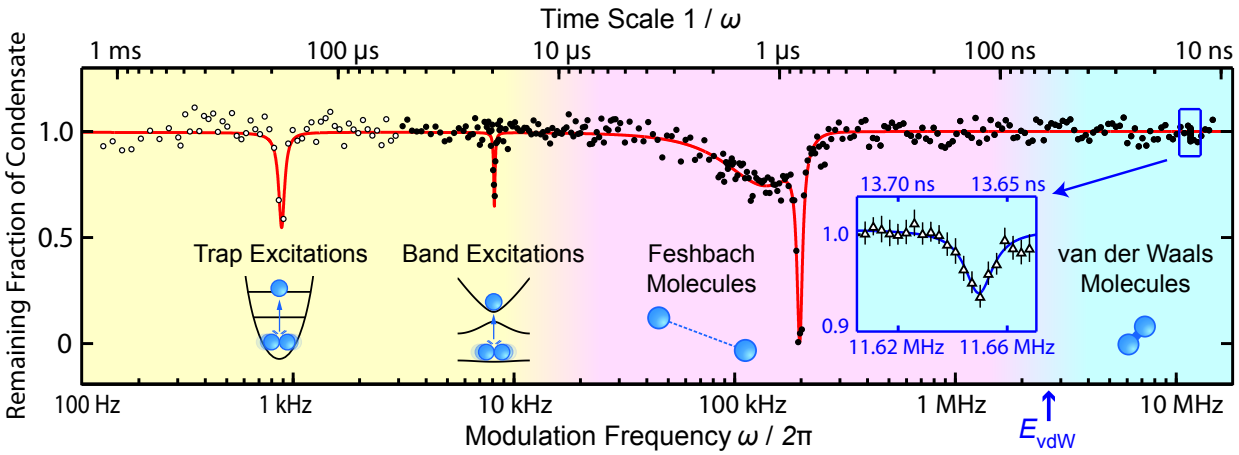

Figure 6.11: Interaction modulation spectroscopy. The BEC at 47.976 G is exposed for a hold time t to the OFR laser, which is intensity modulated at frequency $\omega/2\pi$. We measure the number of condensed atoms remaining after exposure, normalized to the off-resonant number, under three conditions: (open circle) $t = 100$ ms with no optical lattice, (filled circle) $t = 20$ ms with a one dimensional optical lattice of depth $h \times 9.3$ kHz, (open triangle) $t = 500$ ms with no optical lattice. Resonances are observed at 0.89(1), 8.18(2), 133(7), 197(1), and 11,649(2) kHz, determined from fits (solid curve) to each resonance (Gaussian for 133 kHz, Lorentzian for others). The illustrations indicate the nature of each resonance. The van der Waals energy scale is $E_{\mathrm{vdW}} = h \times 2.7$ MHz for Cs molecules.

11.649(2) MHz corresponding to a weakly-bound Feshbach molecular state and a deeply-bound van der Waals molecular state, respectively. All observed resonance positions are in excellent agreement with theoretical calculations given below. These resonances provide direct evidence that OFR can access interaction physics on timescales as short as 10 ns.

We have determined the origin of each of the resonances excited by interaction modulation spectroscopy (Fig. 6.11). The first resonance at 890(10) Hz corresponds to excitation in the vertical harmonic trap. Since the BEC density is even across the trap center, the oscillating interaction strength provides an even perturbation which can only excite the gas to states with the same parity as the ground state; thus the first excited state is forbidden. The ratio of the resonance frequency to the vertical trapping frequency of 470 Hz is 1.9, suggesting that the samples are close to the quasi-2D regime (chemical potential $\mu \ll 470$ Hz) and OFR is driving excitations to the 2nd excited harmonic oscillator state.

The second resonance at 8.18(2) kHz corresponds to excitations to the second excited

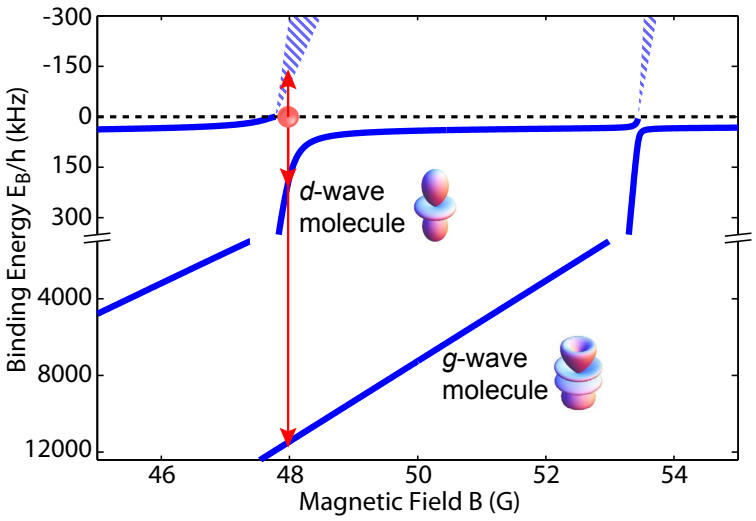

Figure 6.12: Energy levels for Cs_2 molecules. A schematic of the three molecular resonances observed in our experiment, based on the energy levels in ref. [97]. The red ball indicates the condensate, and arrows represent the coupling to three molecular states by interaction modulation spectroscopy.

band of the optical lattice. For comparison we perform band structure calculations for our lattice depth of $h \times 9.28$ kHz, yielding energies of $h \times 6.58$ kHz and $h \times 8.18$ kHz for the zero quasimomentum states in the first and second excited bands, respectively. The observed resonance is consistent with transitions to the second excited band; no resonance appears at the first excited band energy because the parity of the ground state is again conserved. Transitions to higher parity-allowed bands are also not observed, which we attribute to the weaker coupling strength to those states.

The highest three resonances correspond to coupling of the free atoms to Cs_2 molecular states. The process is analogous to the binding of dimers with an oscillating magnetic field [145]. The locations of the observed features are consistent with known Cs_2 molecular states (Fig. 6.12). We compare our data to coupled channel calculations [22] at the average effective magnetic field $B = 47.957$ G. The 133(7) kHz resonance corresponds to a molecular state above the atomic threshold, with an energy of 95 kHz based on extrapolation of coupled channel calculations into the continuum. The feature is broad because the molecular state is embedded in the continuum. The 197(1) kHz resonance corresponds to a primarily d-wave

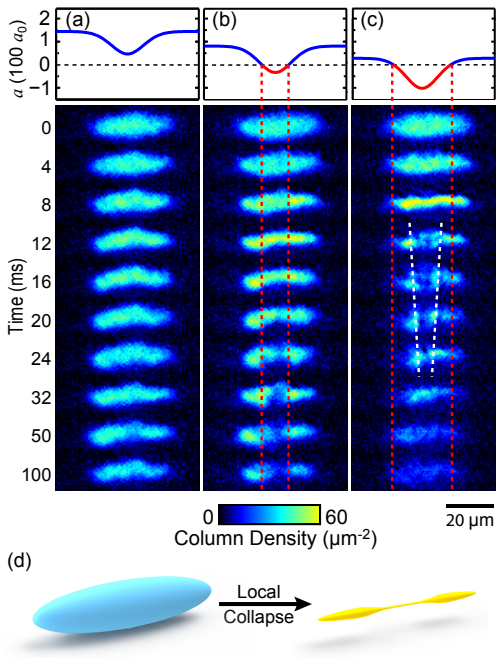

Figure 6.13: Condensate dynamics with spatially modulated interactions. Time series of *in situ* images of BECs with $N = 12000$ atoms after a quench from uniform $a = 200\ a_0$ at 47.965 G to the spatially modulated a shown in the top panels. The OFR beam has peak intensity of 115 W/cm^2 and a waist of 14 μm, while the final magnetic fields are (a) 47.949 G, (b) 47.935 G, and (c) 47.925 G. Each image is the average of 6 or 7 trials. The red dashed lines show where a equals zero. The white dashed lines in panel (c) guide the eye to the motion of the solitonic wave towards the trap center. (d) Illustration of the local collapse dynamics, in which the initial BEC (left) undergoes transverse compression followed by localized central collapse (right).

bound state calculated to be at 208 kHz and the 11.649(2) MHz resonance corresponds to a g-wave bound state calculated at 11.731 MHz [22]. These molecules are individually stable, but their collisions with each other and the remaining atoms lead to net loss of atoms from the trap.

6.4.6 Local Collapse

Next, we demonstrate spatial modulation of the interaction strength within a quantum gas. For this experiment we employ an OFR beam which is small compared to the size of the BEC, leading to a reduced scattering length only in the center of the gas. After preparing the BEC

we quickly turn on the OFR beam and simultaneously change the magnetic field. We study the subsequent dynamics of the sample by measuring its *in situ* density profile over time (Fig. 6.13). For example, when the interactions remain repulsive throughout the condensate, we observe collective excitations for the duration of the experiment (Fig. 6.13(a)). For all images the small distortion at the center of the gas results from the dipole potential due to slightly non-uniform laser polarization (Sec. 6.3).

Intriguing dynamics occur when the interactions become locally attractive. When the scattering length is negative in a small region near the center of the trap (Fig. 6.13b), we observe a brief period of transverse compression followed by a rapid drop in central density between 20 and 32 ms after the quench, signaling local collapse of the condensate (illustrated in Fig. 6.13d). A large fraction of the sample survives at the edges for more than 100 ms. With even stronger attractive interactions (Fig. 6.13c), faster central collapse occurs after 8 ms. Subsequently, the dense remnants at the edge of the sample move toward the center of the trap (see white dashed lines in Fig. 6.13c). Beyond 32 ms only thermal gas survives, indicating that the remnants have undergone further collapse. This behavior is reminiscent of bright matter wave solitons [141, 90, 46]; the remnants form at a small negative scattering length but become unstable as they move toward the center where the scattering length is more negative. Further investigation into the nature of these remnants provides an intriguing course for future work. Moreover, the variety of behaviors observed in this experiment establishes the richness of the quantum dynamics accessible with space dependent interactions.

6.4.7 Implementing OFR with other atomic species

Our scheme for OFR is quite general and should perform well with a variety of atomic species. For example, calculations based on ^{87}Rb in the absolute ground state $|F = 1, M_F = 1\rangle$ yield the figure of merit $M = -45$ mG·s. Moreover, past experiments with ^{87}Rb sug-

gest two potential candidates for the Feshbach resonance. For ^{87}Rb in $|F = 1, M_F = 1\rangle$, the 1007.4 G resonance [18] has a sensitivity of $da/d(\beta I) = 0.5\ a_0$/mG [36], which would allow a change of scattering length by 100 a_0 with a 5/s one-body scattering rate. If a tune-out wavelength is not required, then the interstate Feshbach resonance at 9.13 G [155] offers $da/d(\beta I) = 6.7\ a_0$/mG, where a is the scattering length between the $|F = 1,\ M_F = 1\rangle$ and $|F = 2,\ M_F = -1\rangle$. This resonance allows a change of 300 a_0 with a 1 s^{-1} scattering rate, which is only about three times worse than the tunability in Cs condensates.

Beyond alkali atoms, quantum gases of heavy, magnetic atomic species like erbium and dysprosium [107, 5] are promising candidates for OFR. Their rich sets of optical transitions provide many options for obtaining a favorable ratio of the vector light shift to the scattering rate. Moreover, such highly magnetic elements have an abundance of Feshbach resonances [65, 19], many of which could provide favorable properties for implementing OFR.

CHAPTER 7

FUTURE DIRECTIONS

Many interesting ideas arose over the course of completing the work described above. Some of them show quite a lot of promise, and we have pursued them to varying degrees. The purpose of this chapter is present the most promising ideas, with a particular focus on those with preliminary experimental results or at least some interesting theory. Perhaps we will have an opportunity to finish some of these projects in the future. However, my real hope is that future students will be inspired by some of these ideas and continue the work themselves. The ideas involve either the shaken lattice, and are presented in Sec. 7.1, or the Bose Fireworks, and are presented in Sec. 7.2.

7.1 Shaking Lattice

7.1.1 Coarsening of domain structure

Many systems which cross a phase transition will form intricate structures of finite domains separated by topological defects, as discussed in Ch. 4. In general, the structures which form are not in true thermal equilibrium, but the defects are topologically stable and therefore typically persist on timescales much longer than the timescale of the critical dynamics. However, in many systems the domains will tend to slowly grow over time, a process called coarsening or phase ordering [29].

The coarsening process is expected to satisfy the dynamic scaling hypothesis, in which the domain structures present at later times look statistically identical to those at early times except for an increase in the length scale [29]. For example, the correlation function should satisfy,

$$g(\boldsymbol{r}, t) = f(\boldsymbol{r}/L(t)), \tag{7.1}$$

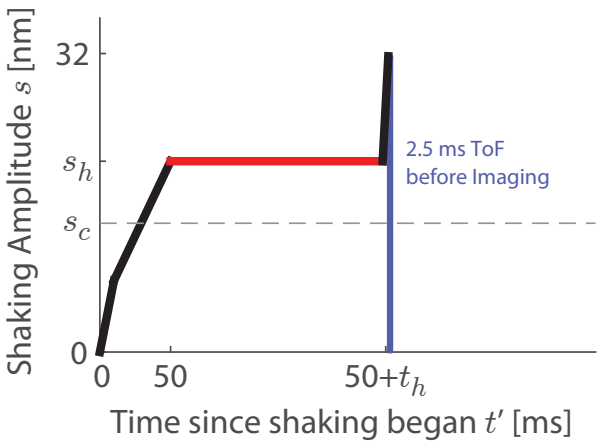

Figure 7.1: A schematic of the procedure used for preliminary coarsening experiments. After preparing the BEC we increase the shaking amplitude to its hold value $s_{\mathrm{h}} > s_{\mathrm{c}}$ in 50 ms. After a variable hold time t_{h} during which the shaking amplitude is constant, we rapidly increase the shaking amplitude to $s = 32$ nm before performing a 2.5 ms time-of-flight and acquiring an absorption image.

where the function f describes the form of the correlations and the single characteristic length scale $L(t)$ grows over time. Moreover, the length scale typically grows as a power law over time. Much like in the case of the Kibble-Zurek mechanism, there is no general proof of this hypothesis. Therefore, it is quite valuable to test it experimentally in many systems with diverse properties in order to elucidate when and why it does (or does not) succeed. Studying the appearance of finite, metastable domain structures and their subsequent coarsening may also shed light on the process of prethermalization and the subsequent evolution toward true thermal equilibrium in near-integrable quantum systems [98]. Furthermore, in general the universal correlation function observed immediately after unfreezing and that which appears through the coarsening process may differ, and it would be interesting to study the transition between these two regimes.

In our original study of the Kibble-Zurek mechanism (Ch. 4), we avoided coarsening effects by measuring the domain structures at a fixed point in scaled time. However, when left to evolve for a longer time after the phase transition, we clearly observe coarsening of the domain structure. Here, we discuss a few preliminary experiments which provide an overview

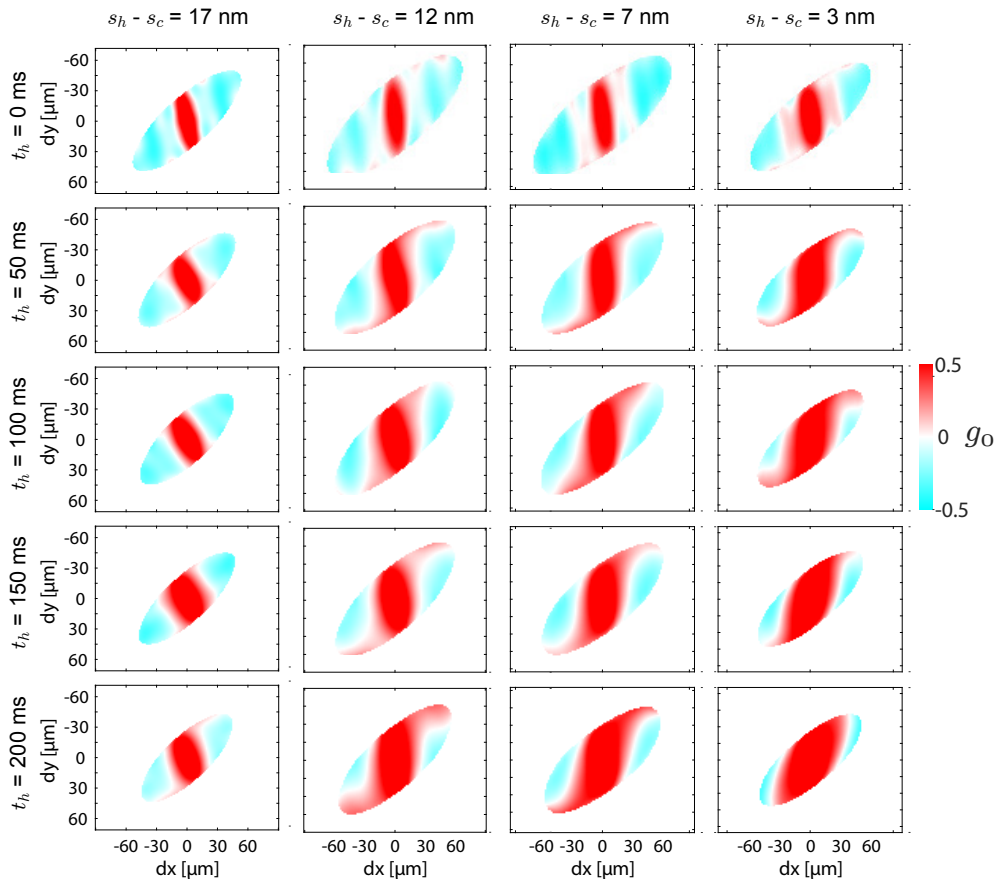

Figure 7.2: Correlation functions during coarsening at four shaking amplitudes. Normalized correlation functions $g_0(dx, dy)$ calculated from ensembles of 60 images collected after procedures as shown in fig. 7.1.

of coarsening behaviors that we have observed in the ferromagnetic phase, and which can perhaps provide a foundation for future work using this system to study this important topic.

We studied the coarsening process using the experimental procedure shown in Fig. 7.1. In a fixed time of 50 ms we ramped on the shaking across the critical amplitude $s_c = 13.1$ nm to a holding amplitude s_h. We then held the system at s_h for a variable hold time t_h, followed by a rapid ramp to $s = 32$ nm for detection. For various values of s_h and t_h we performed 60 iterations of the experiment, reconstructed the pseudo-spin distribution using the procedure described in Sec. 4.3.1, and calculated the normalized pseudo-spin correlation functions shown in Fig. 7.2. The top row shows the initial correlation functions, which are

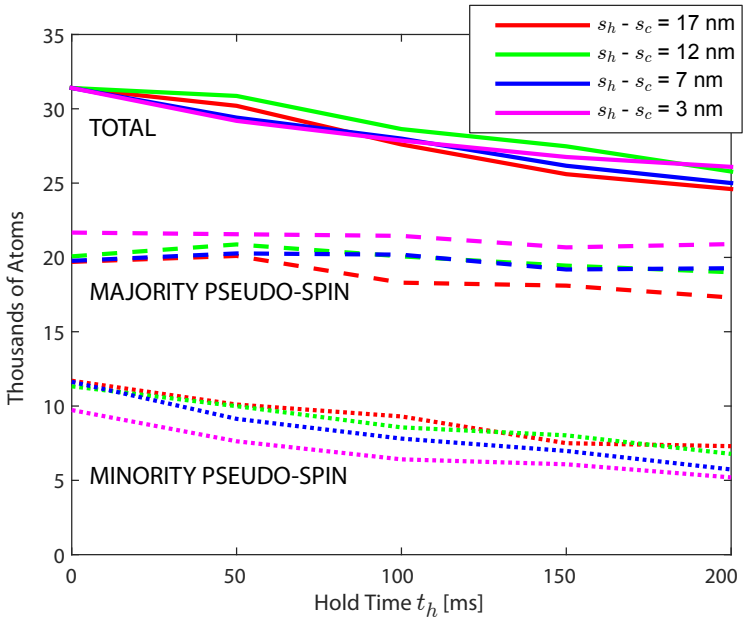

Figure 7.3: Decay of the atom number during the coarsening process. We measure the total atom number, atom number in the dominant pseudo-spin state, and atom number in the minority pseudo-spin state as a function of the coarsening time for four different shaking amplitudes (indicated in the legend). Atoms appear to be preferentially lost from the minority pseudo-spin during coarsening.

not quite identical (nor do they quite match the universal form seen in Fig. 4.23) due to the differences in the quench rate across the transition and a short coarsening time between the unfreezing time and reaching s_h. See the last two paragraphs of this section for suggestions for improving the procedure. For now, we will assume that the initial domain distributions are essentially the same. In every case, the domains clearly grow over time.

Many intriguing features can be seen in the pseudo-spin correlation functions. Regardless of the hold amplitude s_h, the domains clearly coarsen over time, as indicated by the expansion of the central region with positive correlations. Moreover, the coarsening rate appears to be greatest when the system is held as close as possible to the critical point. We have found that the energy of a domain wall shrinks as the system approaches the critical point (from the ferromagnetic side) due to the shrinking of the kinetic energy barrier at $q = 0$, see Sec. 3.4 and Ref. [106]. One might speculate that the domain walls have a correspondingly

smaller effective mass closer to the critical point. In that way the domain walls can move around more quickly, and thereby enable the domains to coarsen more quickly as well. With this dataset we have not attempted to make a quantitative test of the scaling hypothesis, due to imperfections in the procedure and finite size effects as the domain size approaches the system size at later times. However, our system appears well suited to further studies exploring the scaling hypothesis.

Coarsening in this system appears to involve the expulsion of atoms in regions of minority pseudo-spin from the trap, see Fig. 7.3. Regardless of the holding amplitude, the number of atoms in the majority pseudo-spin state appears to remain nearly constant over time, while the number of atoms in the minority pseudo-spin state drops. This suggests that coarsening proceeds not just by increasing the domain size, but also by increasing the overall polarization of the gas. However, this may be predominantly a finite size effect; it seems unlikely that the non-zero overall polarization could be relevant (or even present) in the case of an infinite system.

We observe an interesting evolution of the orientation of the domain walls during coarsening. We have ample evidence that the initial domain wall orientation is always predominantly perpendicular to the shaking lattice. For example, if we shake the XDT lattice instead of the usual YDT lattice, the domain walls just after unfreezing are rotated by 90°, as shown in Fig. 7.4. Moreover, when the hold amplitude is sufficiently close to the critical point, the domain walls seem to remain predominantly in this orientation. We see this behavior at $s_h - s_c = 7$ nm and 3 nm, where the positively correlated region in the center of the correlation functions is oriented nearly vertically until it becomes distorted by the finite size of the sample (two rightmost columns in Fig. 7.2). However, for larger shaking amplitudes the domain walls appear to rotate quickly to the short axis of the trap. In the leftmost column of Fig. 7.2 showing $s_h - s_c = 17$ nm, even though the correlated region remains small, it clearly rotates by about 45° in less than 100 ms. The predominance of domain walls along

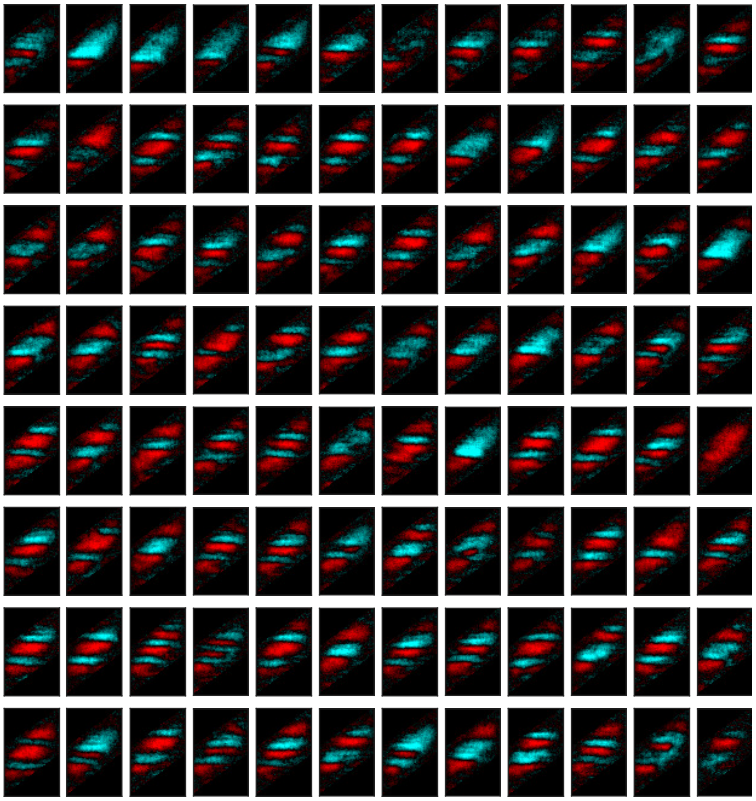

Figure 7.4: Example images of domain structures soon after unfreezing when shaking the XDT lattice. As usual, the domain walls are preferentially orientated perpendicular to the axis of the shaking lattice.

the short axis was originally observed in Ref. [119]. We suspect that domain walls have lower energy if they are perpendicular to the shaken lattice when the system is close to the critical point, but that for sufficiently large shaking amplitudes the domain wall energy is lowered by minimizing its area, which is achieved by rotating toward the short axis of the gas. Since this effect relies on the finite size of the gas, it might distort the behavior predicted by the scaling hypothesis.

While we can often simplify our analysis by looking only at the structure along one dimension, as we did in Ch. 4, the rotation of the domain walls is a valuable reminder that the domain structure can become nontrivial in 2D or even 3D. Since the excitation spectrum of the gas is fundamentally anisotropic as a result of the 1D shaken lattice, we should consider the possibility that scaling laws are anisotropic as well. For example, it is natural to predict

anisotropic Kibble-Zurek scaling exponents in this system. While the system can have only one unfreezing timescale, the speed of sound is different along the x- and y-axes (and only the x-axis speed of sound depends on the shaking amplitude). This difference might lead one to observe a different spatial scaling exponent for the y-axis than the one we measured along the x-axis, if the domains were not limited by the finite size of the gas along that axis.

The experiments presented in this chapter were not performed with an ideal procedure. The primary issue is that these experiments were performed before correcting the biasing issues discussed in Sec. 4.3.2. A second issue is that the duration (50 ms) of the ramp to s_h is fixed, rather than the ramp rate. Since the ramp rate varies between conditions, the initial domain structures at the beginning of the hold time vary depending on s_h, as can be seen in the variation in the correlations measured at $t_h = 0$ in the top row of Fig. 7.2. Ideally the quench rate should be held constant, and the ramp to the desired holding amplitude s_h should become fast immediately after unfreezing, so that the initial domain distribution is independent of s_h. In addition, it is not necessary to include the ramp to $s = 32$ nm for detection, since we can perform amplified detection at any shaking amplitude (see Sec. 4.3.1).

In order to test the coarsening hypothesis (Eqn. 7.1), it would be best to initialize the system in the ferromagnetic phase with the smallest possible domains so that the domains have room to grow before becoming comparable to the size of the gas. It might be even more interesting to initialize the system with various deterministic domain structures by biasing the initial velocity distribution, as demonstrated in Fig. 3.5, to test how long the memory of the initial distribution lasts during the coarsening process.

7.1.2 Interaction-driven phase transition and condensation in a single particle excited state

The behavior of Bose-Einstein condensates in a red-detuned shaking lattice is quite different from that in the usual case of blue-detuned shaking. With red-detuned shaking, a phase

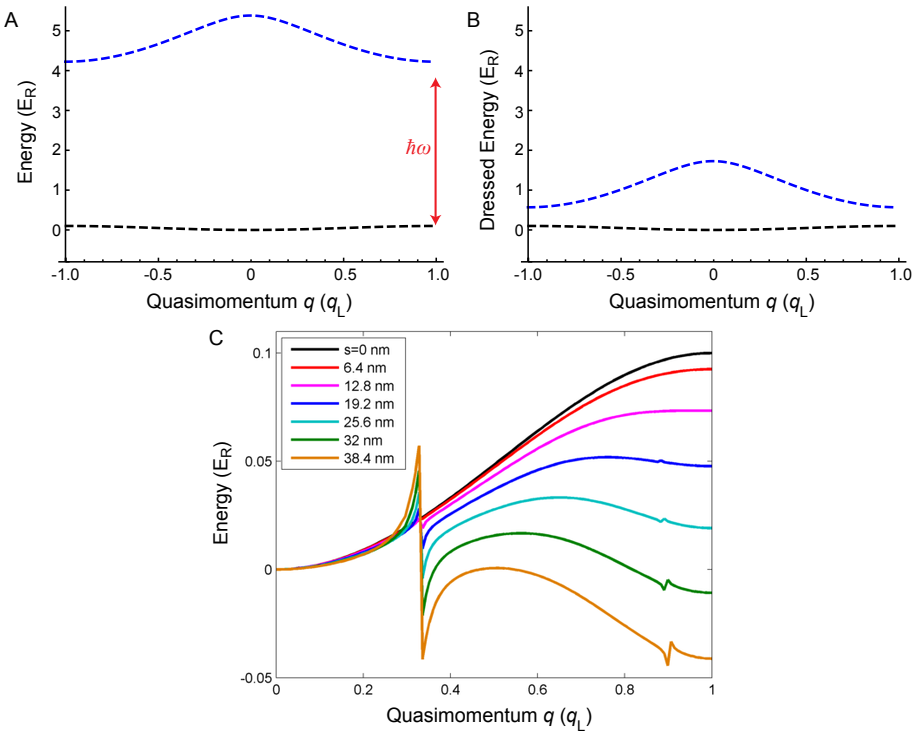

Figure 7.5: Illustration of the effects of red-detuned shaking on the band structure. (a) For red-detuned shaking experiments we shake the optical lattice at angular frequency ω slightly smaller than the band gap at the edge, $\hbar\omega < E_2(q_L) - E_1(q_L)$. (b) A dressed picture in which the second band is shifted by the shaking frequency $E_2(q_L) \to E_2(q_L) - \hbar\omega$. The gap between the bands is very small near the edge, leading to a significant admixture of the bands, but much the much larger gap near $q = 0$ prevents significant admixture. (c) The Floquet quasi-energy spectrum for the band adiabatically connected to the ground band $E_1(q)$, as a function of the shaking amplitude. The spectrum is determined by numerically solving for the Floquet steady states with lattice spacing $d = 532$ nm, depth 8.87 E_R, and shaking frequency $f = 5.2$ kHz.

transition occurs in which atoms are transferred from the band center to the band edge. Both phases have only a single minimum in the band, unlike the blue-detuned case. The interplay between micromotion and interactions is essential in the red-detuned case, and the system can be driven across the phase transition just by increasing the scattering length. In fact, we see that sufficiently strong interactions can drive the system to Bose condense in a single particle excited state. Moreover, we find that under certain conditions both inequivalent phases can still coexist simultaneously.

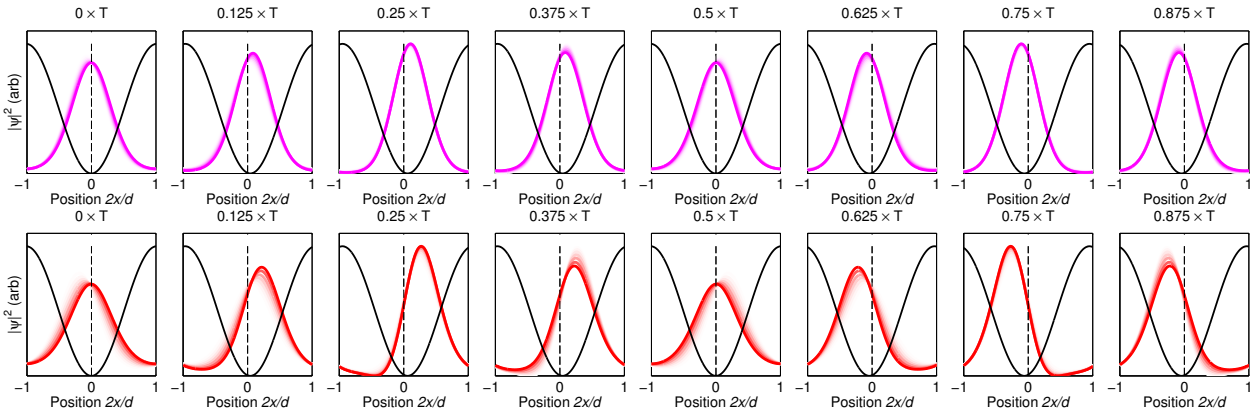

Figure 7.6: Micromotion in the two possible superfluid states with red-detuned shaking. Plots of the density in the Floquet steady state with $q = 0$ (top row) and $q = q_{\mathrm{L}}$ (bottom row) over one shaking period. The fading curves indicate the density profiles at previous times within the $T/8$ step between each plot, making the motion more apparent. Calculated with lattice spacing $d = 532$ nm, depth 8.87 E_{R}, shaking frequency $f = 5.2$ kHz, and shaking amplitude $s = 32$ nm.

We can understand the effect of red-detuned shaking on the band structure using the two-band approximation, see Fig. 7.5A. Here, the shaking frequency is slightly red-detuned from the gap at the edge of the band, $\hbar\omega < E_1(q_L) - E_0(q_L)$. In some ways, this leads to the "opposite" effect from blue detuned shaking; instead of increasing the ground band energy near the center, level repulsion in the dressed picture (Fig. 7.5B) causes the energy to *decrease* near the band *edge*. Note that, when the shaking frequency is resonant with any transition from the ground band to the first excited band, we observe much more rapid heating.

The effective ground band in the red-detuned shaken lattice based on the full Floquet calculation is shown in Fig. 7.5C. Note that only half of the Brillouin zone is shown, since it is symmetric. The main feature is that shaking decreases the energy at the band edge $\epsilon_1(q_L)$, as expected from the two-band approximation. At a critical shaking amplitude s_c it becomes degenerate with the normal ground state, $\epsilon_1(q_L; s_c) = \epsilon_1(0; s_c)$, and for larger shaking amplitudes $s > s_c$ we find that the condensate undergoes a phase transition to occupy the new ground state $q = q_L$. Note that, in the lattice, the quasimomentum states

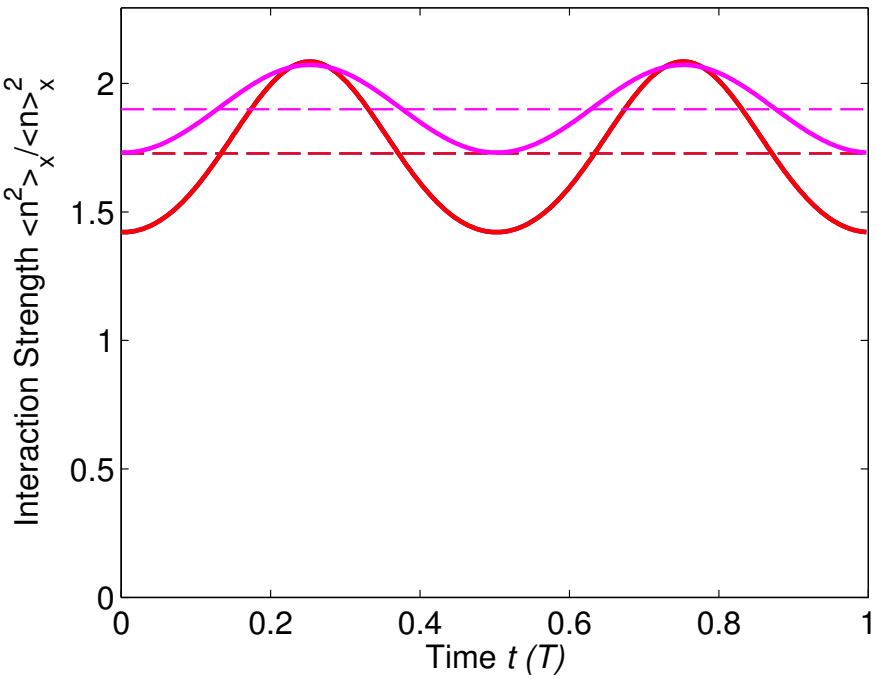

Figure 7.7: Interaction energy during micromotion with red-detuned shaking. A plot of the ratio $\eta = \langle n^2 \rangle_x / \langle n \rangle_x^2$ of the average interaction energy in the $q = 0$ (magenta) and $q = q_{\mathrm{L}}$ (red) Floquet states to the interaction energy of state with flat microscopic density. The horizontal dashed lines indicate the respective averages over the full Floquet period. Calculated with lattice spacing $d = 532$ nm, depth 8.87 E_{R}, shaking frequency $f = 5.2$ kHz, and shaking amplitude $s = 32$ nm.

$q = -q_L$ and $+q_L$ are the same; therefore, pairs of atoms can collide and both transfer to the band edge while conserving total quasimomentum.

There are also two clear avoided crossings with other Floquet bands, near $q \approx 0.33\ q_L$ and $q \approx 0.9\ q_L$. The first crossing is particularly strong, but we have seen no evidence that it qualitatively changes the expected behavior, though it is likely responsible for some heating. Therefore, we will ignore the presence of this crossing for the remainder of the discussion, focusing on the local minima at $q = 0$ and q_L with a barrier in between.

The interplay of micromotion and interactions has very interesting effects in the red-detuned shaken lattice (recall Sec. 3.3). The micromotion of the states at the band center and edge is shown in Fig. 7.6. Both states oscillate in phase with the motion of the lattice, reaching peak density at their greatest displacement and minimum density when moving

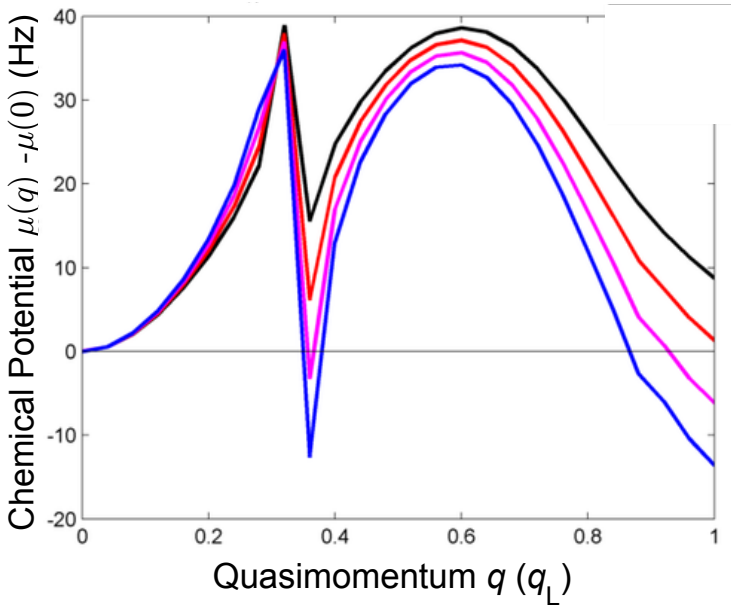

Figure 7.8: A plot of the relative chemical potentials of condensates at different quasi-momenta with red-detuned shaking and coarse-grained interaction energy scales $gn_{\text{flat}} = 0$ (black), 50 (red), 100 (magenta), and 150 Hz (blue). Calculated with lattice spacing $d = 532$ nm, depth 8.87 E_{R}, shaking frequency $f = 5.2$ kHz, and shaking amplitude $s = 29$ nm.

through zero displacement. However, the micromotion of $|q_L\rangle$ is much more extreme than that of $|0\rangle$ because shaking is much closer detuned at the band edge. Put another way, $|q_L\rangle$ includes a much greater admixture of the state in the unshaken excited band, which is more spread out than the state of the ground band. As a result, the effective interaction strength at the band edge is much lower, see Fig. 7.7. Compared to the result for blue-detuned shaking (Fig. 3.7), the effect of micromotion on interactions in the red-detuned case is enhanced because the difference in detuning between the relevant states is much greater.

As a result of the micromotion, interaction effects can determine the preferred phase. Indeed, the micromotion causes the chemical potential $\mu = g'_q n_{\text{flat}}$ to decrease at the band edge relative to the band center as the density increases, see Fig. 7.8. Here, g'_q is the effective interaction strength of the quasimomentum state $|q\rangle$ (see Sec. 3.3) and n_{flat} is the coarse-grained density. Therefore, while sufficient shaking amplitude can always drive the system across the phase transition on its own, interactions can also drive the system across the phase

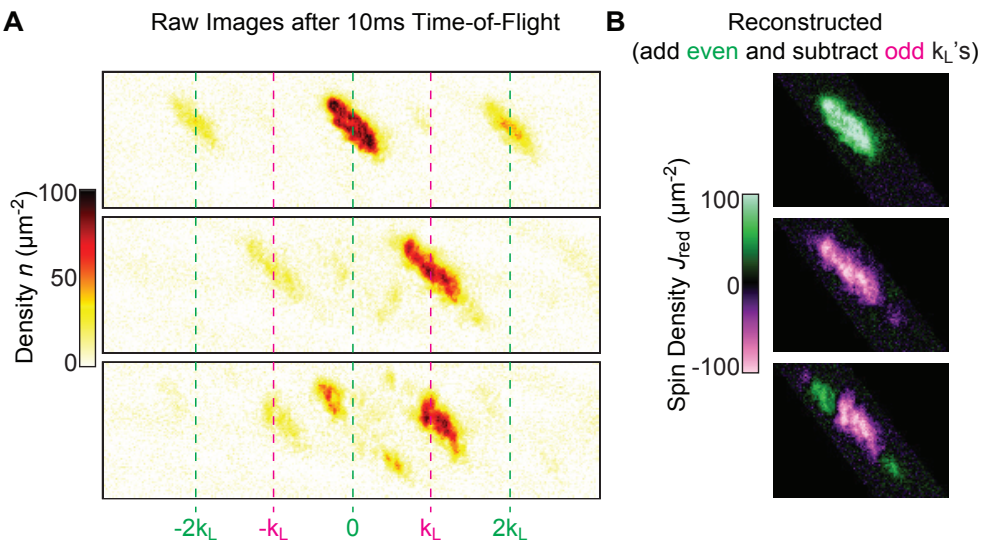

Figure 7.9: Examples of red-detuned shaking reconstruction. (A) Density profiles of the superfluid with red-detuned shaking after performing a 10 ms ToF to separate the Bragg peaks. For superfluids entirely in the $q = 0$ state (top) atoms only occupy Bragg peaks with momenta $q_{0,j} = (2j)q_{\mathrm{L}}$, while superfluids with $q = q_{\mathrm{L}}$ (middle) occupy Bragg peaks with momenta $q_{\mathrm{L},j} = (2j + 1)q_{\mathrm{L}}$. If the superfluid is split into domains with different quasi-momenta (bottom), these domains will be reflected in the density profiles of the Bragg peaks. (B) The reconstructed spin densities $J_{\mathrm{red}}(\mathbf{r}) = n_0(\mathbf{r}) - n_{\mathrm{L}}(\mathbf{r})$ corresponding to the raw images in panel (A); see text for details.

transition as one increases the scattering length or the density.

Experimentally, we can probe the state of the system in the red-detuned shaking lattice by reconstructing the *in-situ* quasimomentum distribution, as shown in Fig. 7.9. We typically prepare the system with a lattice depth of $V = 8.86\ E_R$ and shaking frequency of $f = 5.2$ kHz. Then, after shaking the lattice for some time, we perform an ordinary TOF for 5-10 ms and collect an absorption image. Raw example images are shown in Fig. 7.9A. While an amplification pulse like those discussed in Sec. 4.3.1 could potentially enhance the signal even further, the large separation in quasimomentum between the band center and edge naturally causes the relevant momentum peaks to separate in this case. After TOF, we can identify the density profiles $n'_j(\boldsymbol{r})$ corresponding to momenta $q_j = jq_L$ for integers j. Even integers correspond to atoms at the band center, while odd integers correspond to atoms at the band edge. Therefore, we reconstruct the density profiles at the band center $n_0(\boldsymbol{r}) = \sum_j n'_{2j}(\boldsymbol{r})$

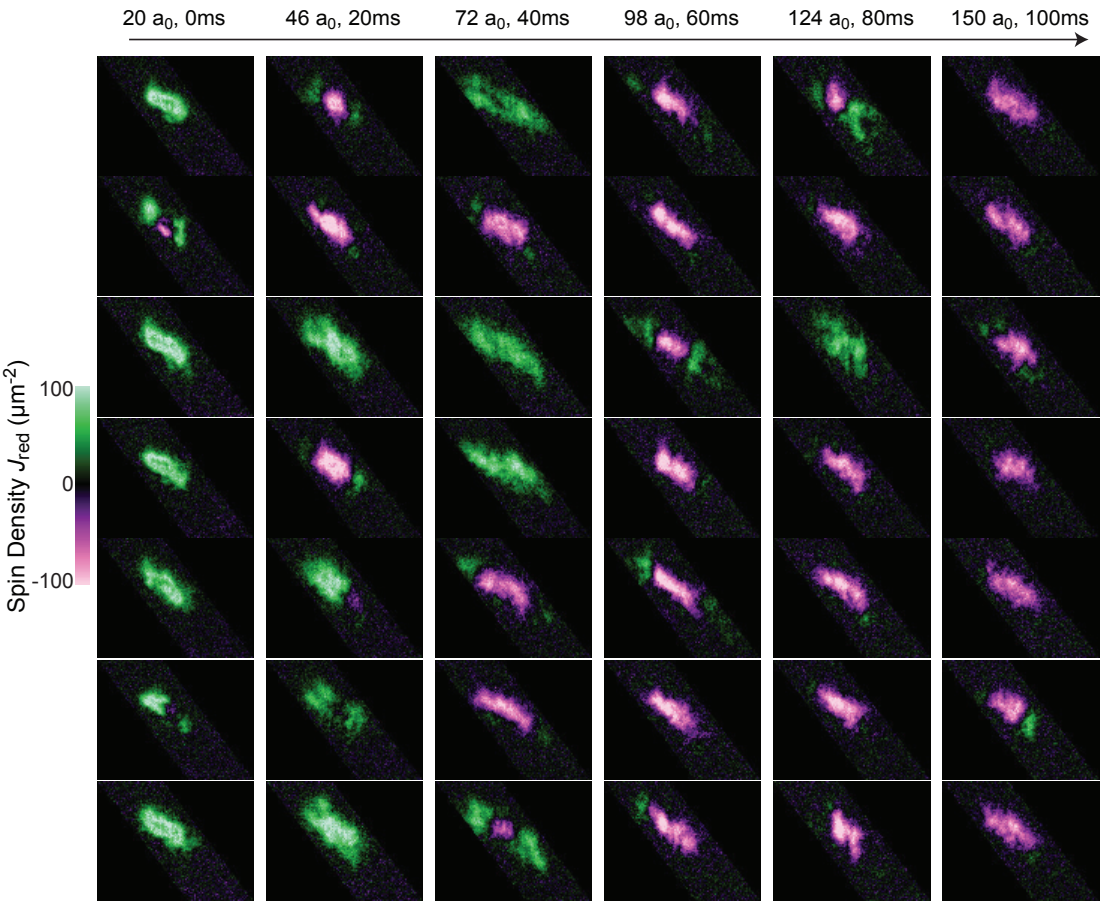

Figure 7.10: Example images of superfluids driven across the red-shaking phase transition by increasing interaction strength. BECs initially prepared in the $q = 0$ state at a shaking amplitude $s = 29$ nm near the phase boundary undergo a 100 ms ramp of the scattering length from $a_i = 20\ a_0$ to $a_f = 150\ a_0$. Each column corresponds to images taken at a different time and instantaneous scattering length, indicated at the top.

and at the band edge $n_L(\boldsymbol{r}) = \sum_j n'_{2j+1}(\boldsymbol{r})$, from which be calculate the pseudo-spin density $J_{\rm red}(\boldsymbol{r}) = n_0(\boldsymbol{r}) - n_{\rm L}(\boldsymbol{r})$. Examples of reconstructed pseudo-spin density profiles are shown in Fig. 7.9B.

Before moving on to our main results, it is worth emphasizing the difference between the interpretation of "domain" structures in the red-detuned and blue-detuned shaken lattices. We have extensively discussed the blue-detuned case, where we see domains of atoms in the two degenerate ground states of the Ferromagnetic phase. There, for any shaking amplitude

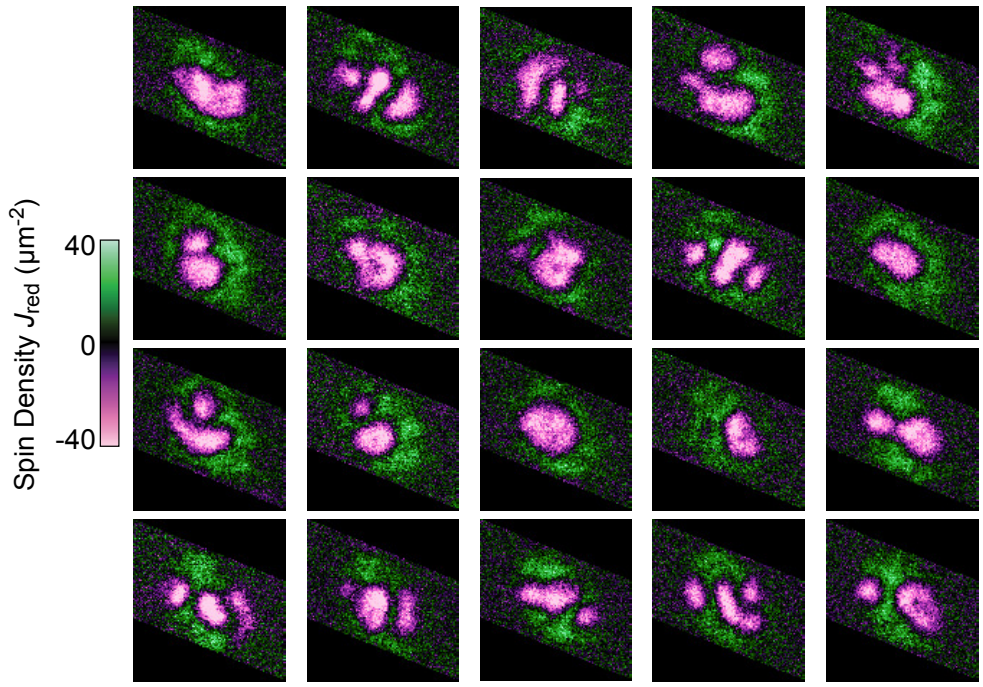

Figure 7.11: Example images with red shaking in a wide trap. Reconstructed images of circular superfluids with scattering length $a = 110\, a_0$ undergoing red-shaking with amplitude $s = 26$ nm. The circular trap has horizontal trap frequencies of $\omega_r = 2\pi \times 6$ Hz and vertical trap frequency $\omega_z = 2\pi \times 260$ Hz. Near the center of the trap the interaction energy scale is approximately $gn_{\text{flat}}/h \approx 150$ Hz.

or interaction strength these two states are equivalent, because of the inversion symmetry of the system, and their coexistence is not an enormous surprise. At first glance we observe similar "domain" structures in the red-detuned shaken lattice; for example, see the bottom image of Fig. 7.9B where there are four domains: two clear regions with $q = 0$, a large domain in the center with $q = q_L$, and a very small domain with $q = q_L$ near the top left corner. However, in this case the two states only degenerate at the phase boundary, which depends on the shaking amplitude, scattering length, and density. In practice the two states are never truly degenerate, and they correspond to different phases. Therefore, on the surface their coexistence is more reminiscent of simultaneous appearance of two phases at the coexistence line of a first order phase transition, such as the coexistence of water and ice as an ice cube is melting. In the blue-detuned shaken lattice, the $q = 0$ state only coexists with $q = \pm q^*$

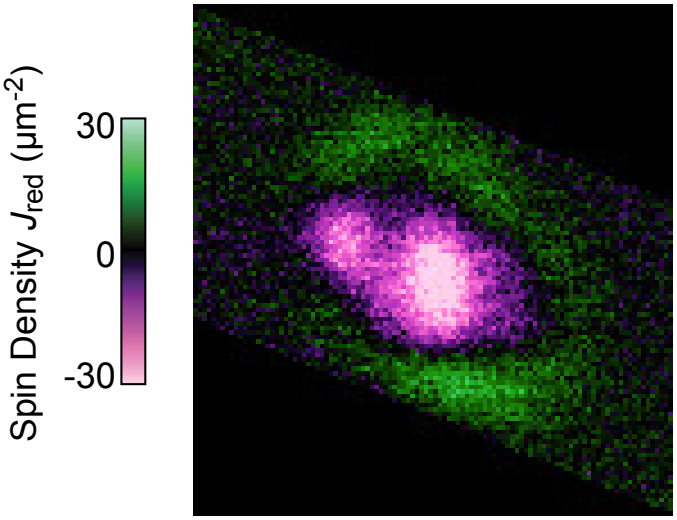

Figure 7.12: Average red-shaking "donut": The average spin density of the images shown in Fig. 7.11.

for a brief time during the unfreezing dynamics, and even then it does not exist as separate domains but as a small and rapidly shrinking amplitude across the whole gas. In short, it is worth emphasizing that in many ways the physics of the red-detuned shaken lattice should be quite different from that of the blue-detuned case.

We find that the system can be driven across the phase transition simply by increasing the scattering length. For these experiments we start with a very small scattering length of $a = 20\ a_0$, and ramp the shaking amplitude slowly up to $s = 29$ nm where the system is close to the phase transition but the single particle ground state is still at $q = 0$. Then, over 100 ms we linearly increase the scattering length to $a = 150\ a_0$. We reconstructed example images taken at 20 ms intervals during this process, which are shown in Fig. 7.10. At the beginning of the ramp the gas is almost entirely in the $q = 0$ state. The variation in the initial state likely results from small residual drifts of the lattice depth, in spite of our best efforts to eliminate them. Because we use a smaller detuning of 270 Hz here than we used in the blue-detuned case (~ 860 Hz), the band structure is even more sensitive to changes in the lattice depth. We suspect that these experiments would benefit from further

improvement of the lattice depth stability, or from the use of a different set of parameters at which the physics is lest sensitive to drifts. Regardless, as the scattering length increases the atoms are increasingly likely to be found at the band edge, and at the highest scattering length $a = 150\ a_0$ almost the entire gas has crossed the phase transition to $q = q_L$. Thus we demonstrate that interactions play a fundamental role in determining the preferred phase of this phase transition. In fact, sufficiently strong interactions have effectively caused the bosons to condense in a single particle excited state; the condensate appears at the band edge even though the single particle energy is minimized at the band center [164].

In order to further explore interaction effects in the red-detuned shaken lattice, we performed experiments in a round trap with weaker vertical confinement. By turning off ZDT and using the vertical lattice and magnetic field gradient to provide vertical confinement, we create a trap with approximately symmetric horizontal trapping frequencies of $\omega_{\mathrm{r}} = 2\pi \times 6$ Hz and vertical trap frequency $\omega_{\mathrm{z}} = 2\pi \times 260$ Hz. The larger gas in this trap allows for more space in which the superfluid can create regions in opposite phases. By tuning just below the non-interacting critical shaking amplitude and using a large scattering length $a = 110\ a_0$ we observe a large number of samples with coexisting phases, shown in Fig. 7.11. The patterns show an intriguing variety from shot to shot, and present an intriguing topic for future studies.

One consistent feature is the preferential transfer to the $q = q_L$ state near the center of the gas. This preference can be easily seen in the average spin density, shown in Fig. 7.12, which has a large region at $q = q_L$ near the center surrounded by $q = 0$ at the edges. This imbalance is driven by the higher density at the center of the harmonic trap, which makes the band edge more favorable than the center as a result of the same micromotion effects described above.

In addition to continuing the lines of investigation described above, it would be interesting to test the behavior of the gas after a quench across the red-detuned shaking phase transition.

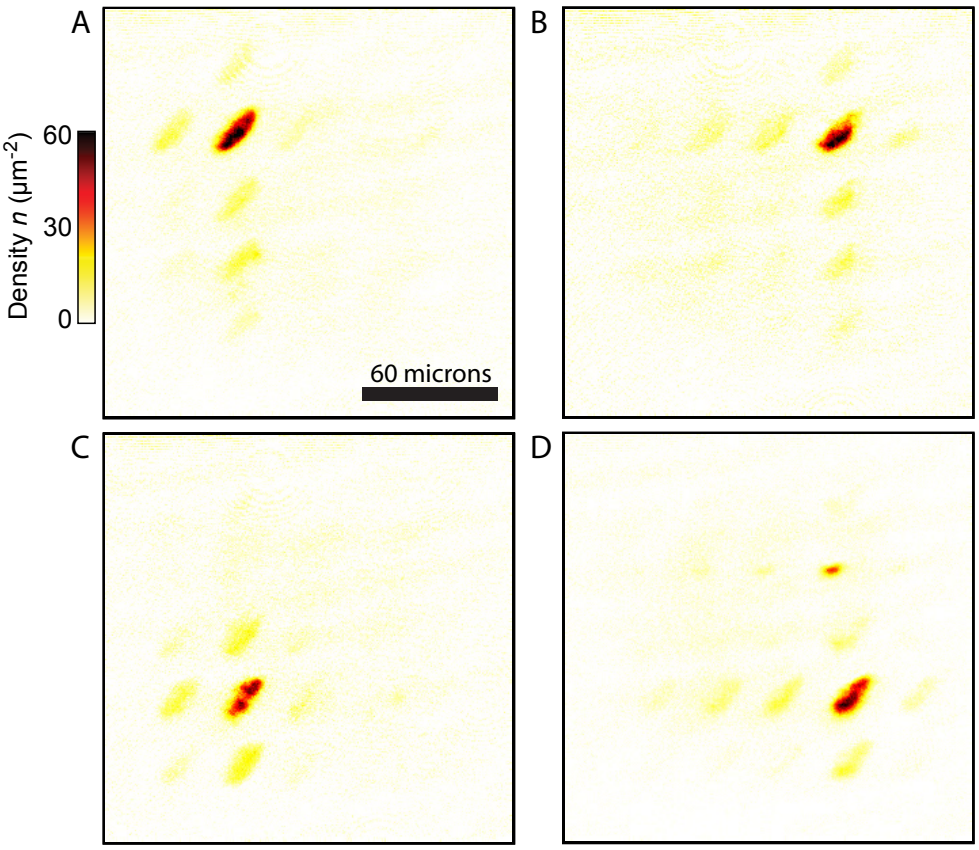

Figure 7.13: Basis states for pseudo-spin reconstruction in the 2D shaken lattice. Example images after an amplification pulse and a 10 ms TOF with condensates initialized with quasi-momentum (A) $|k_x, k_y\rangle = |-k^*, +k^*\rangle$, (B) $|+k^*, +k^*\rangle$, (C) $|-k^*, -k^*\rangle$, and (D) $|+k^*, -k^*\rangle$. A small error in the initialization procedure leads to the small fraction of atoms at $|+k^*, +k^*\rangle$ which appear as an isolated spot in the upper-right quadrant of panel (D). Compare to Fig. 4.7A.

In the blue-detuned cases, we observed behavior at early times consistent with the prediction for dynamical instability, while at later times we saw coherent oscillations of the population between different momentum states [62]. While it seems likely that the system just after a quench should also exhibit dynamical instability, it is not clear what to expect at later stages, especially in light of the coexistence of the two phases observed above.

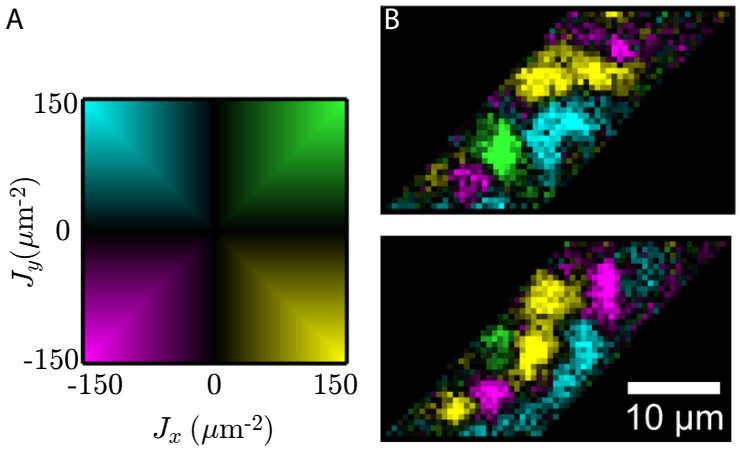

Figure 7.14: Example reconstructed pseudo-spin densities in the 2D shaken lattice. (A) Atoms in the 2D shake lattice have two pseudo-spin degrees of freedom, based on their quasimomentum along the x/y-axes ($J_{x/y}$). This panel shows the mapping from the reconstructed pseudo-spin densities to false color. (B) Two example reconstructed images of pseudo-spin domains in the 2D shaken lattice.

7.1.3 2D shaking

We have performed preliminary experiments testing the behavior of condensates in a 2D, blue detuned shaken lattice. We use a 2D shaken square lattice with equal lattice depths, shaking frequencies, and amplitudes along the x- and y-axes; each lattice has conditions equivalent to those used in Ch. 4. In the Ferromagnetic phase, the second shaking lattice splits each of the original degenerate minima into two minima, resulting in a total of four degenerate single particle minima at $|k_x, k_y\rangle = |\pm k^*, \pm k^*\rangle$.

Experimentally, the higher density of samples confined in lattices along both axes as well as the simple presence of two driving forces tends to lead to much faster heating. It is even more imperative in this case to ensure that the vertical trap depth is low, so that evaporation continues as the system is shaken and the temperature of the gas can remain low. Under that condition, we are able to obtain sample lifetimes on the order of those observed in the 1D shaken lattice.

At this point, it will probably not come as a surprise that we use a short TOF in order

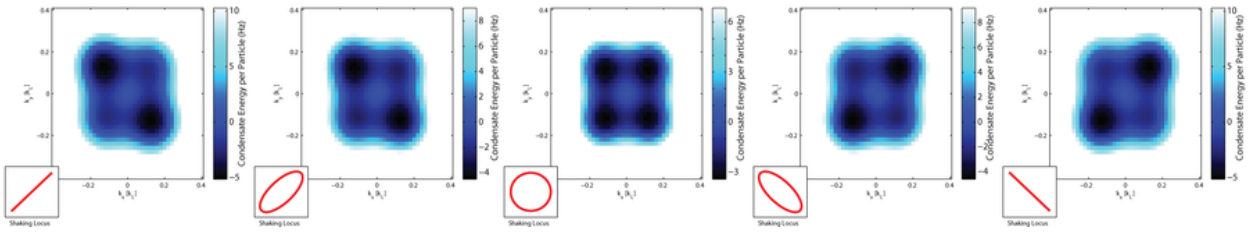

Figure 7.15: The energy of repulsively interacting condensates with uniform quasimomentum in the ferromagnetic phase with 2D shaking, calculated based on the numerical calculation described in Sec. 3.1.2 while accounting for the micromotion effects described in Sec. 3.3. Five examples for different relative phases between the x- and y-axis shaking are shown, with the phase indicated by the shaking locus at the bottom left corner of each energy landscape.

to reconstruct the in-situ quasimomentum distribution. In the case of 2D shaking, we use a procedure identical to that described in Sec. 4.3.1, but performed simultaneously on both lattices. To test the reconstruction procedure, we bias the gas with an initial velocity toward one of the minima, then cross the phase transition in order to produce pure samples in a single quasimomentum state in the ferromagnetic phase. For each ground state, the density distributions after the amplification pulse and a 10 ms TOF are shown in Fig. 7.13. From these images we calculate 2D basis "vectors" analogous to those shown in Fig. 4.7B, which we can use to reconstruct the in situ pseudo-spin density distribution as shown in Fig. 7.14.

As a result of the micromotion, the energy of a repulsively interacting condensate with uniform quasimomentum in the 2D shaken lattice depends on the relative phase between the x- and y-axis shaking lattices, see Fig. 7.15. Since the single particle Floquet calculation is separable, the wavefunction describing 2D micromotion $u_{k_x,k_y}(x,y,t) = u_{k_x}(x,t)u_{k_y}(y,t)$ can be considered the product of 1D shaken lattice wavefunctions $u_k(x,t)$ along each axis. Recall Fig. 3.6, which showed that the 1D states in the ferromagnetic phase at $q = \pm q^*$ are "circulating": they oscillate out of phase with the lattice shaking, with a minimum density when passing through zero displacement in one direction and a maximum density when passing through in the opposite direction. In 1D, the density oscillations of q^* and $-q^*$ have opposite phase, but when averaged over a full Floquet period the effective interaction

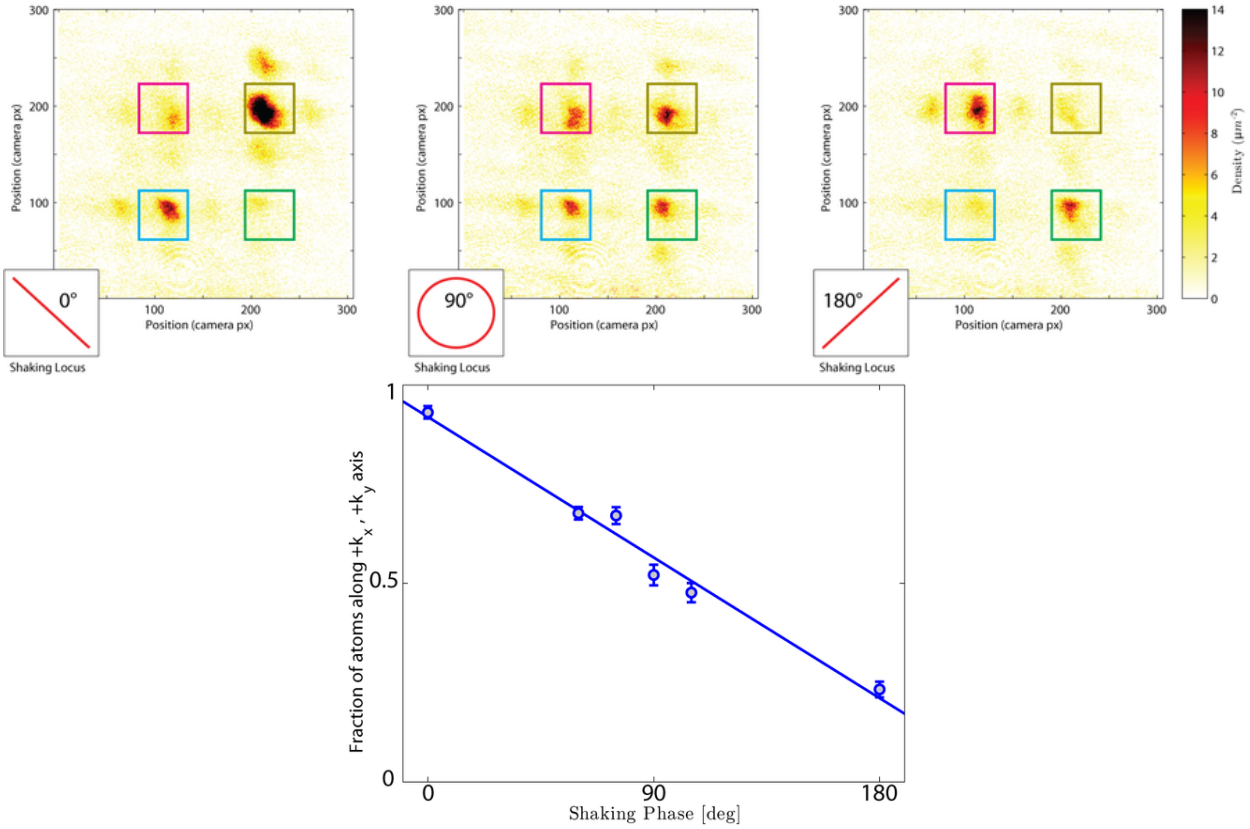

Figure 7.16: Observation of interaction effects in the 2D shaken lattice. (top row) The averages of 10 TOF images for gases in the ferromagnetic phase of the 2D shaken lattice with relative phases of 0° (linear shaking, left), 90° (circular shaking, center), and 180° (linear shaking, right) between the x- and y-axis shaken lattices are shown. Colored boxes indicate the regions containing atoms from each of the four wells (see Fig. 7.13). (bottom) The fraction of atoms in quasimomentum states along the main diagonal $(N_{++} + N_{--})/N$ depends strongly on the relative shaking phase.

strengths are the same. In a linearly-shaken 2D lattice, where the phase $\theta_{xy} = 0°$ is zero between the x- and y-axis shaking, there are now two possibilities. For states along the main diagonal ($|q^*, q^*\rangle$ or $|-q^*, -q^*\rangle$) the two factors $u_{k_x}(x,t)$ and $u_{k_y}(y,t)$ of the wavefunction oscillate in phase and reach their peak density at the same time, leading to an extremely high interaction energy at that peak. For the off-diagonal states ($|-q^*, q^*\rangle$ or $|q^*, -q^*\rangle$), the two factors reach peak density at opposite phases of the shaking, moderating the overall interaction energy. After averaging over the whole shaking period, the total interaction energy is higher for the on-diagonal states than the off-diagonal states, as seen in the leftmost

and rightmost panels in Fig. 7.15. Therefore, instead of four degenerate many-body ground states, in the presence of linear shaking the system has only two ground states. Shaking the system with a circular waveform with $\theta_{xy} = 90^\circ$ restores the symmetry between the four minima even in the presence of interactions, as seen in the middle panel of Fig. 7.15.

We have performed preliminary experiments in the 2D shaken lattice to test this prediction. Both lattices along the x- and y-axes have a depth of 8.86 E_R and shaking frequency 8 kHz. After adiabatically loading the gas into the lattice, we slowly increase the shaking amplitude at a rate of 0.2 nm/ms up to an amplitude of $s = 20$ nm. The asymmetry between the wells is most significant when the system unfreezes close to the critical point, where the interaction energy is a large compared to the kinetic energy of the wells. We then quickly ramp the shaking amplitude to $s = 32$ nm where we allow a coarsening period of 100 ms, which we expect to enhance the original imbalance between the populations in each well (see Fig. 7.3). Finally we perform a 5 ms TOF and measure the number of atoms in each quasimomentum well.

The average density distribution after TOF for three different relative phases of the shaken lattices are shown in the top row of Fig. 7.16. As predicted, for linear shaking, we see a much greater population in the off-diagonal states, while for circular shaking we see relatively even population in each of the four wells. We present the imbalance for many shaking phases by plotting the fraction of atoms in the main diagonal $(N_{++} + N_{--})/N$, where $N_{\pm\pm}$ is the total number of atoms in $|\pm q^*, \pm q^*\rangle$ in the bottom panel of Fig. 7.16.

These results demonstrate some of the interesting behaviors which arise from the interplay of interactions and micromotion in the shaken lattice. Moreover, these results lay the foundation for future investigations into the nature of the effectively ferromagnetic phase transition in the 2D shaken lattice. In order to study the behavior of a BEC in a dispersion with four degenerate wells, one must use a circular shaking waveform.

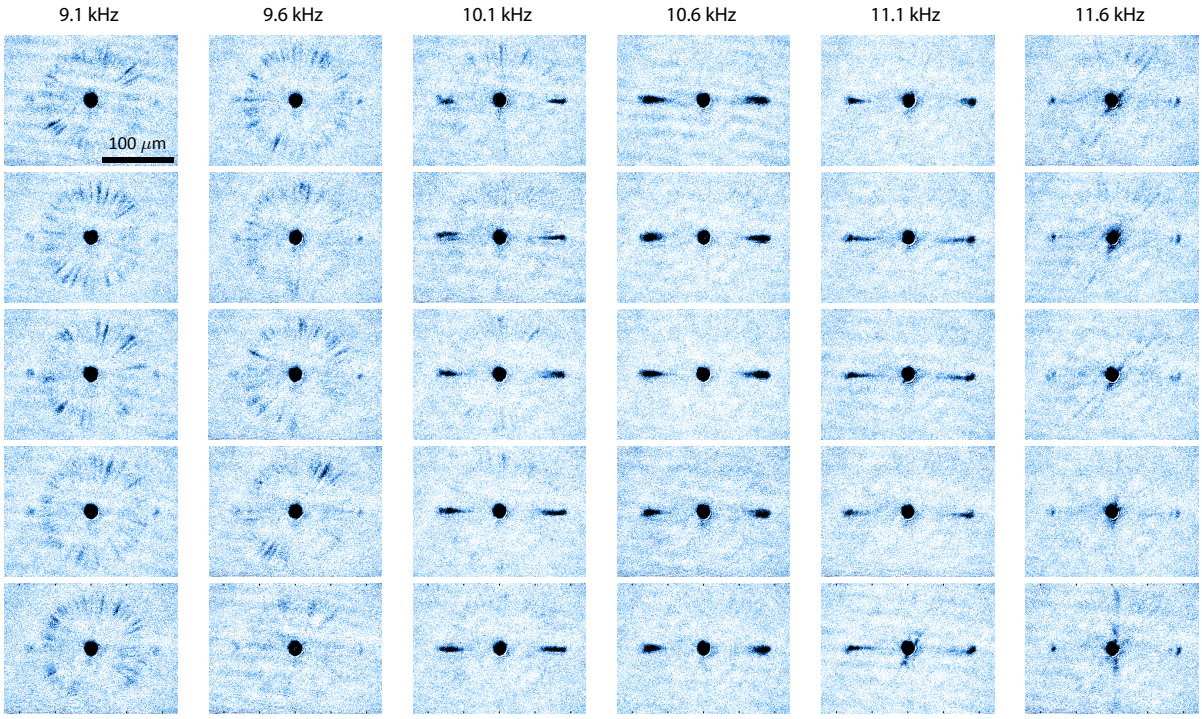

Figure 7.17: Fireworks from a gas with a seeded excited-state population. Example images of the jets which result from wiggling at various frequencies (indicated above each column) and fixed amplitude $a_{\rm ac} = 110\ a_0$. Before wiggling a 200 μs pulse of the 1D, $d = 532$ nm lattice along the x-axis seeded a small population of excited state atoms with a kinetic energy of 5.3 kHz per atom.

7.2 Bose Fireworks

7.2.1 Fireworks as an Amplifier

The Bose Fireworks effect can be used as a versatile amplifier for a small populations in excited states outside a condensate. Simply modulating the scattering length with sufficient amplitude will cause the initial population N_0 in an excited mode to be amplified exponentially. Of course, it will also create a background of spontaneous jets (the amplified quantum fluctuations studied above), but the average final population in the originally occupied mode should remain a factor of order N_0 above the average background level. The amplifier can have a narrow bandwidth limited by the power broadening or the decay rate of atoms from

the condensate, and and it operates simultaneously for any direction of the initially excited mode(s).

As a preliminary demonstration of this amplifier, we have used the fireworks effect to amplify a small excited state population which we seed by pulsing on an optical lattice. First, we applied a 200 μs pulse of the optical lattice along the x-axis. The brief pulse of the lattice achieves a small phase imprinting, effectively seeding populations of 700(100) atoms each in the +2 k_L and -2 k_L momentum states along the lattice axis. The excited modes seeded by the lattice have an energy of $4E_R = h \times 5.3$ kHz per atom.

We then modulated the scattering length with a fixed amplitude $a_{\rm ac} = 110\ a_0$ and various frequencies around the resonance. During this amplification phase, the lattice remains off. We image the density distribution once the jets have traveled far enough from the condensate to be easily identified. Example images across a range of frequencies are shown in Fig. 7.17. Away from the resonance at low frequencies, we observe the normal fireworks effect. Since the jet momentum is smaller than the seeded momentum, we observe an inner ring of normal jets as well as the initial population seeded into the higher momentum modes. Away from the resonance at high frequencies we see similar behavior, but the inner ring of fireworks is very weak. The asymmetry of the off-resonant behavior is likely a result of the threshold amplitude, which rises with frequency and suppresses the jet emission for high frequency modulation. For a sufficiently large modulation amplitude, this asymmetry would likely disappear.

When modulating on resonance at $f = 10.6$ kHz we observe strong amplification of the seeded mode with minimal population of the other, originally empty modes. We measure a final population of 4900(300) atoms each in the initially seeded modes, corresponding to amplification by a factor of seven. The background modes with the same momentum but different angles, which are initially empty, contain a total of 4600(1100) atoms after amplification. If we approximate the number of unique modes as $2\pi/w$ where w is the

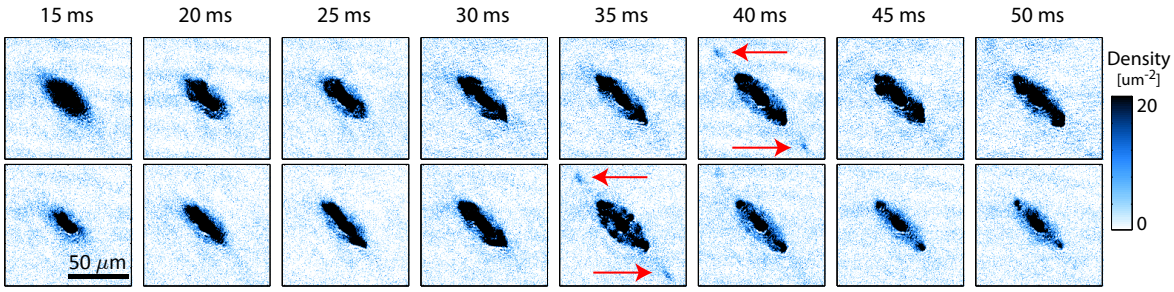

Figure 7.18: Example images taken after modulating the scattering length with amplitude $a_{\mathrm{ac}} = 40\ a_0$ at low frequency $f = 1$ kHz for various durations (indicated above each column). In some images we clearly see groups of atoms, indicated by red arrows, which have traveled twice as far from the condensate as the main fireworks.

FWHM of a mode, then there are approximately 160 modes under these conditions and this background level corresponds to 31(7) atoms per mode.

It is also noteworthy that the amplified modes do not appear as narrow jets as in the spontaneous case, but rather have an envelope approximately the size of the original condensate. This behavior is actually precisely what we predict (see Sec. 5.2); it is the spontaneous case in which the jets are narrow even in the near-field that we do not fully understand.

7.2.2 Secondary Collisions

When the population of atoms in the primary ring of momentum states with magnitude k_f becomes comparable to the population of atoms remaining in the condensate, new collision processes can become relevant. In Ch. 5 we focused on the effects of collisions which excite two atoms out of the condensate into pairs of counter-propagating modes at k_f, which we call primary collisions. Under the right conditions one can also observe collisions between outgoing atoms at k_f and the remaining condensate atoms or even between pairs of outgoing atoms; we call these secondary collisions. If the modulation amplitude is not too far above threshold, then secondary collisions will still tend to be rare, because even when the number of atoms in the primary jets is large, many of them will have escaped the condensate already and they will be spread out. Instead, modulating the scattering length at large amplitude

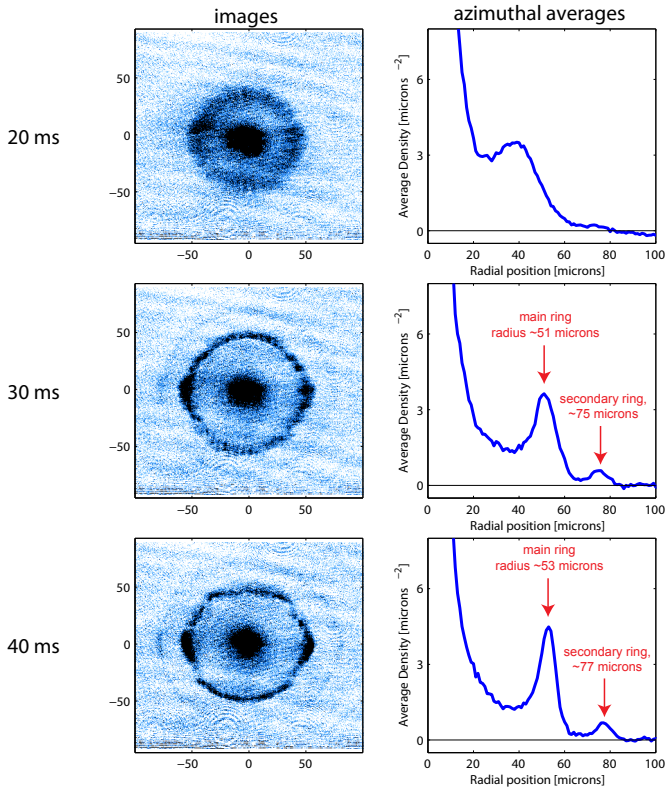

Figure 7.19: (left column) The average of images taken at various times (indicated at the left) after beginning to modulate the scattering length with amplitude $a_{\rm ac} = 125\ a_0$ at frequency $f = 2$ kHz. In the lower two images the duration is close to one quarter of the trap period, and the outgoing jets have been roughly focused into rings. (right column) Azimuthal averages for each condition shown at the left. Especially in the latter two times, there are clearly two rings of atoms, with the second ring having traveled approximately a factor of $\sqrt{2}$ farther from the original condensate center.

and low frequency allows the system to build up a large density of excited modes which all have significant overlap with each other inside the original condensate. Under those conditions, a significant number of secondary collisions can occur.

During our early investigations, two noteworthy examples of secondary collisions appeared. It is worth emphasizing that both examples occurred in a *harmonic trap*, unlike all of the other fireworks experiments reported in this chapter. While the harmonic trap does not contribute much to the rate of secondary collisions, it does help to focus the outgoing atoms so that small populations in secondary jets become dense spots or rings which are

more easily detected.

Our first observation of secondary collisions occurred in the elliptical harmonic trap formed by XDT, YDT and ZDT. We modulated the scattering length at low frequency $f = 1$ kHz and moderate amplitude $a_{\rm ac} = 40\ a_0$. A timeseries of example images after different durations of modulation is shown in Fig. 7.18. Note that the colorscale is saturated for the condensate itself and the primary jets, making them a bit hard to identify. However, this choice also reveals the secondary spots which are visible in the images at 35 and 40 ms, which correspond to roughly one quarter period of the long axis trap.

Interestingly, these secondary spots are ejected approximately twice as far as the primary jets, which suggests that they have roughly four times as much energy as atoms in the primary jets. Such energetic atoms are almost certainly the result of collisions between pairs of atoms in the primary jets, in which one atom is returned to the condensate mode at $k = 0$ and the other atom is excited to a mode with momentum $2k_f$. In this way, after undergoing two collisions, a single atom ends up with all of the energy $2hf$ available in those collisions (compared to the $hf/2$ carried by each atom after a single, primary collision).

Our second observation of secondary collision products occurred in the round harmonic trap formed by XDT, YDT and the vertical lattice. We modulated the scattering length at moderate frequency $f = 2$ kHz but very high amplitude $a_{\rm ac} = 125\ a_0$. A timeseries shows the average of 46 images at each of three different times, as well as the corresponding azimuthally averaged radial density, in Fig. 7.19. In this case, when the jets are approximately focused radially, a clear secondary ring can be seen.

Surprisingly, the secondary ring is not at twice the radius of the primary ring in this case, but is only a factor of roughly $\sqrt{2}$ farther away from the remnant condensate. In this case, it is natural to suspect that these atoms result from secondary collisions between atoms in counter-propagating, primary modes. The input and output modes of such collisions still have a net momentum of zero, meaning that any such collision between primary modes can

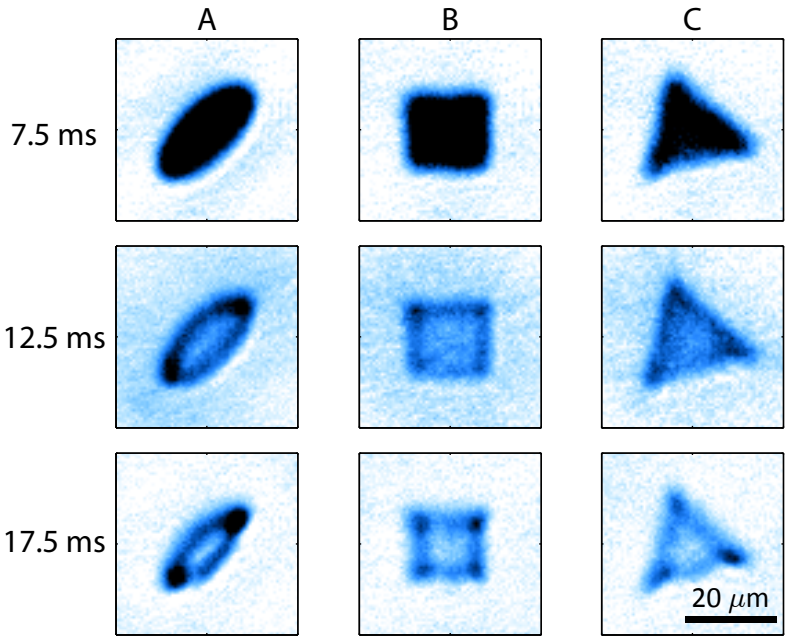

Figure 7.20: Remnant condensates after jet emission. Each panel shows the average of seven images taken after modulating the scattering length at $f = 5$ kHz and $a_{\rm ac} = 125\ a_0$ for the durations shown at the left side of each row. The columns correspond to initially (A) elliptical, (B) square, and (C) triangular condensates.

populate this secondary ring; each outgoing atom has momentum $\sqrt{2}k_f$ and energy hf.

A detailed investigation of these observations and other fascinating properties of secondary collision processes is currently ongoing in the lab.

7.2.3 Remnant Condensates

Another very interesting feature of the fireworks that merits a detailed exploration is the structure of the remnant condensate which is left behind after the jets are ejected. Even in our very early experiments (Fig. 5.1, for example) it is clear that the remnant condensate has a very interesting structure, with large fluctuations in density that fluctuate from shot to shot. It seems likely that the structure of the remnant reflects the pattern of the jets, and one could test for correlations between the remnant density fluctuation and the azimuthal density profile of the jets. Unfortunately, for the experiments discussed in Ch. 5, we used a lower

imaging beam intensity to improve the signal to noise ratio in the regions with fireworks. This choice made the beam intensity too weak to faithfully image the high density remnant. Therefore, further experiments into this very interesting area are required. Moreover, the theory described in Sec. 5.2 is inadequate for describing the remnant, since it neglects the population of condensate modes by making the Bogoliubov approximation. Even worse, that treatment neglects the propagation of outgoing wavepackets due to the kinetic energy term, which is likely to have a huge impact on the remnant structure.

As a starting point, we have made some interesting observations regarding the average structure of remnants imaged with sufficient imaging beam intensity. We measured the remnant density profiles of condensates with initial elliptical, triangular, and square shapes undergoing scattering length modulation at frequency $f = 5$ kHz and large amplitude $a_{\rm ac} = 125\ a_0$. The average remnant density profiles are shown in Fig. 7.20. At the earliest time shown, 7.5 ms, the jets are mostly still inside the condensate. After 12.5 ms most of the atoms in jets are visible just outside the condensate, and after 17.5 ms the jets have propagated away and the density profile primarily reflects the structure of the remnant.

For all three shapes, the remnant condensate has a low-density "hole" near its center. In the square and triangular samples, it appears that the highest density of atoms remains at the vertics, while the edges have moderate density. It is possible that these features result from the interplay between the propagation of outgoing jets and their continuing amplification. That is, the greatest depletion of condensate atoms should occur where there is the greatest density of outgoing atoms being amplified. Since all of the outgoing modes pass through the center, the density of the condensate in the center would be depleted the most. One might expect this behavior to be modified for modulation amplitudes closer to threshold, where the dependence of the threshold amplitude on the propagation direction should have a significant influence on the dynamics. Our understanding of the remnant structure would benefit greatly from a more complete model which does not rely on the

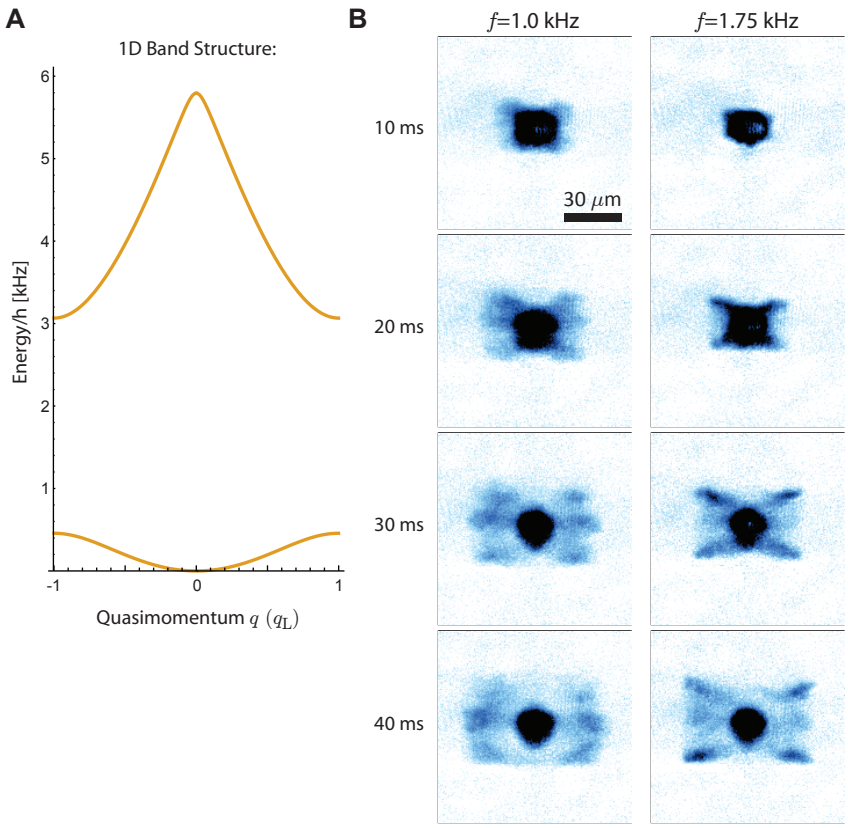

Figure 7.21: Jet emission at low modulation frequencies in a 2D, 4 E_R lattice with amplitude $a_{ac} = 50\ a_0$. (**A**) The band structure for atoms in a 1D lattice of depth 4 E_R. Keep in mind that the atoms are in a 2D lattice, and therefore have this band structure along both the x- and y-axes. (**B**) Each panel shows an average of 3 images corresponding to the wiggling frequency indicated at the top of the column and the duration at the left of the row.

Bogoliubov approximation and includes the motion of the outgoing atoms.

7.2.4 Fireworks in an Optical Lattice

Ordinarily, we perform fireworks experiments in homogeneous samples, which are in free space except for the boundary from the DMD. In this situation, the excitation spectrum of the gas in 2D (neglecting the average scattering length a_{dc}) is the familiar $E(k_x, k_y) = \hbar^2(k_x^2+k_y^2)/2m$ for free particles, such that the density of states is independent of the energy. The constant density of states results in the relatively simple form of the scaling of the jet emission with modulation frequency, discussed in Ch. 5.

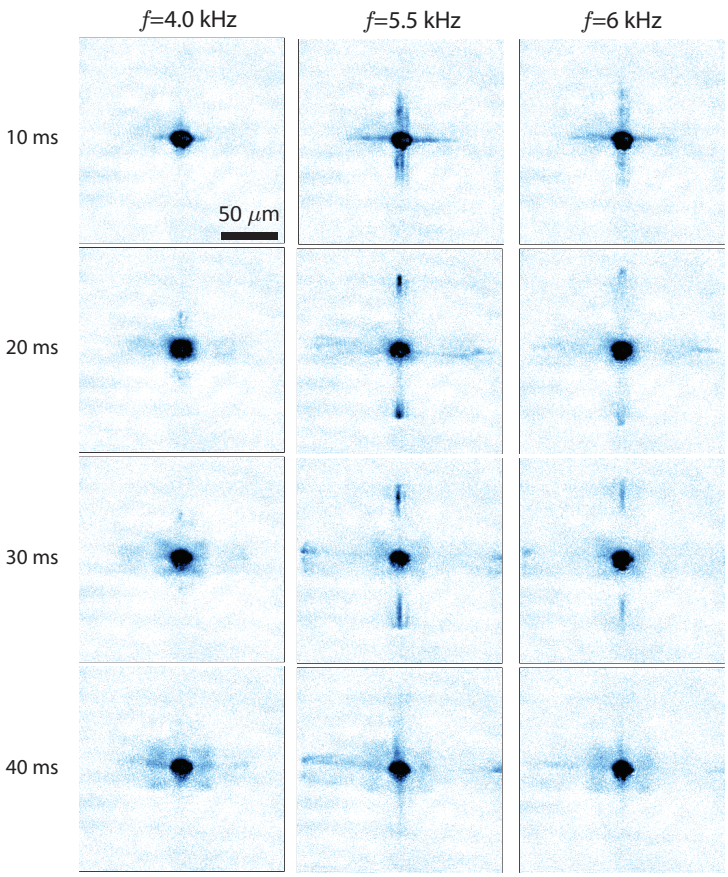

Figure 7.22: Jet emission at low modulation frequencies in a 2D, 4 E_R lattice with amplitude $a_{\rm ac} = 50\ a_0$. Each panel shows an average of 3 images corresponding to the wiggling frequency indicated at the top of the column and the duration at the left of the row.

The situation is dramatically modified in the presence of an optical lattice. For simplicity, first consider the case of a 1D system in an optical lattice. The excitation spectrum takes the form of a band structure, as shown in Fig. 7.21A. It is natural to make two predictions. First, if the energy per outgoing atom $hf/2$ approaches the edge of a band, the collision rate should be enhanced due to the greater density of outgoing resonant states. Second, if the energy per atom $hf/2$ lies in the gap where there are no possible outgoing modes, the collision rate should be close to zero. For this section we work in lattice(s) with depth 4 E_R. In 1D the ground band width is $E_1(k_{\rm L}) - E_1(0) = 0.46kHz$ and the first excited band starts at $E_2(0) - E_1(0) = 3.07$ kHz, as shown in Fig. 7.21A.

Similar predictions apply in a 2D square optical lattice, with the addition of additional

effects which cause spontaneous directionality of the outgoing jets. In the 2D lattice, the excitation spectrum takes the form of a band structure along *both* axes. I will denote the (separable) band energies as $E_{ij}(k_x, k_y)$ for the i'th band in the x direction and the j'th band in the y direction (with index $i = 1$ corresponding to the ground band). First, when the energy per atom $hf/2 < E_{11}(k_L, 0)$ is sufficiently low (near the bottom of the lowest band), there should be outgoing modes in every direction which are resonant with the modulation. Since these modes have slightly different total momenta, they may have slightly different thresholds and thus the emission could have a small anisotropy, but the effect should be relatively small. However, once the modulation frequency exceeds the energy at the band edge for excitations along just one axis, $hf/2 > E_{11}(k_L, 0)$, there are no longer outgoing modes available in every direction. The only available resonant modes are off the axes. In particular, as the energy per atom approaches the gap $hf/2 \approx E_{11}(k_\mathrm{L}, k_\mathrm{L})$, the only states available propagate diagonally.

We observe this spontaneous directionality experimentally, see Fig. 7.21B. Note that the need to have the XDT and YDT dipole traps on in order to create the optical lattice leads to a somewhat anisotropic trap which is wider along the x-axis, causing a spurious preference for x-axis emission even without the presence of any lattice. Even so, we can see the stark contrast between the typical jet patterns emitted at $f = 1$ kHz, where outgoing modes are available in all directions, and $f = 1.75$ kHz where the only available states are along the diagonal and thus there is a much higher density of atoms emitted diagonally.

If we further increase the modulation frequency such that $hf/2$ lies in the gap, we see far less emission as shown for $f = 4$ kHz in the first column of Fig. 7.22. Even so, there is clearly some emission. Two types of processes might allow collisions to occur even when $hf/2$ lies in a gap. First, by stating that $hf/2$ lies in the gap we are assuming that both atoms should be emitted into the same band, and thus have the same energy. In the lattice, it is possible to have processes which conserve quasimomentum but not total momentum,

such that one atom could go to the excited band and the other to the ground band, but still with opposite quasimomenta. In this case processes which conserve energy and momentum are still possible at $f = 4$ kHz. Second, but probably less important, is the role of the third axis. As always, the vertical axis is tightly confined to suppress jet emission away from the horizontal plane. However, it still has $p^2/2m$ dispersion which can in principle provide some states to fill in the gap, especially in the absence of strong horizontal emission.

Further increasing the modulation frequency, we eventually see the return of strong emission, which is primarily directed along the horizontal and vertical axes, as shown in the right two columns of Fig. 7.22. We expect the observed on-axis jets, since the only states available when $hf/2 \approx E_{12}(0, k_L)$ are in the ground band with small quasimomentum along one axis and in the excited band with large quasimomentum along the other axis. Off-axis states are not available, or at least have a much lower density of states. Note that the strong emission at $f = 5.5$ kHz is appearing at a slightly lower frequency than our treatment would predict; it is possible that the lattice depth was slightly lower than we thought, or that some other unexpected effect is playing a role here. Note also that the some of the anisotropy in the distance that the jets travel from the gas likely results from the anisotropy of the harmonic trap.

7.2.5 Fireworks in the presence of collective excitations

Last but not least, we have seen intriguing examples of jets which do not propagate radially even from a circular condensate. Specifically, under certain conditions we observe a small fraction of trials ($\sim 5\%$) in which the jets are "twisted" counterclockwise or clockwise, see the examples in Fig. 7.23. We ordinarily observe jets which appear to propagate purely radially, and here we present images with a significant twist, but we do not seem to observe trials with intermediate twisting. Based on these preliminary observations, we attribute the twisting of the jets to the presence of a single vortex present in the condensate before modulation [8]. In

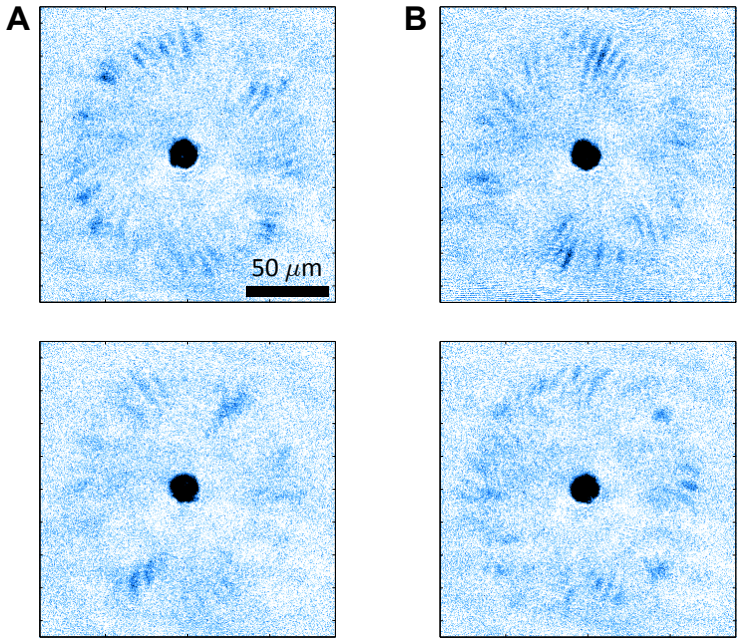

Figure 7.23: Example images of condensates with twisted jets, which appear randomly in some datasets. The jets can twist either counterclockwise (A) or clockwise (B). These images were obtained with $f = 3$ kHz and $a_{\mathrm{ac}} = 65\ a_0$.

the future it would be very interesting to study the jet patterns from condensates prepared deterministically to have a known collective excitation, such as a vortex or a soliton.

APPENDIX A

LIST OF PUBLICATIONS

(1) **Logan W. Clark**, Anita Gaj, Lei Feng, and Cheng Chin. Collective emission of matter-wave jets from driven bose-einstein condensates. *Nature*, doi:10.1038/nature24272, 2017.

(2) Lei Feng, **Logan W. Clark**, Anita Gaj, and Cheng Chin. Coherent inflationary dynamics for bose-einstein condensates crossing a quantum critical point. *arXiv:1706.01440*, 2017. (accepted in *Nature Physics*)

(3) Brandon M. Anderson, **Logan W. Clark**, Jennifer Crawford, Andreas Glatz, Igor S Aranson, Peter Scherpelz, Lei Feng, Cheng Chin, and K Levin. Direct lattice shaking of bose condensates: Finite momentum superfluids. *Physical Review Letters*, 118(22):220401, 2017.

(4) Klaus Hueck, Niclas Luick, Lennart Sobirey, Jonas Siegl, Thomas Lompe, Henning Moritz, **Logan W. Clark**, and Cheng Chin. Calibrating high intensity absorption imaging of ultracold atoms. *Optics Express*, 25(8):8670–8679, 2017.

(5) **Logan W. Clark**, Lei Feng, and Cheng Chin. Universal space-time scaling symmetry in the dynamics of bosons across a quantum phase transition. *Science*, 354(6312):606–610, 2016.

(6) Tongtong Liu, **Logan W. Clark**, and Cheng Chin. Exotic domain walls in Bose-Einstein condensates with double-well dispersion. *Physical Review A*, 94(6):063646, 2016.

(7) **Logan W. Clark**, Li-Chung Ha, Chen-Yu Xu, and Cheng Chin. Quantum dynamics with spatiotemporal control of interactions in a stable bose-einstein condensate. *Physical Review Letters*, 115(15):155301, 2015.

(8) Li-Chung Ha, **Logan W. Clark**, Colin V Parker, Brandon M. Anderson, and Cheng Chin. Roton-maxon excitation spectrum of bose condensates in a shaken optical lattice. *Physical Review Letters*, 114(5):055301, 2015.

REFERENCES

[1] F. Kh. Abdullaev, Jean Guy Caputo, Robert A. Kraenkel, and Boris A. Malomed. Controlling collapse in bose-einstein condensates by temporal modulation of the scattering length. *Phys. Rev. A*, 67(1):013605, Jan 2003.

[2] F. Kh. Abdullaev, P. G. Kevrekidis, and M. Salerno. Compactons in nonlinear schrödinger lattices with strong nonlinearity management. *Phys. Rev. Lett.*, 105(11):113901, Sep 2010.

[3] Monika Aidelsburger, Marcos Atala, Michael Lohse, Julio T Barreiro, B Paredes, and Immanuel Bloch. Realization of the hofstadter hamiltonian with ultracold atoms in optical lattices. *Physical review letters*, 111(18):185301, 2013.

[4] Monika Aidelsburger, Marcos Atala, Sylvain Nascimbène, Stefan Trotzky, Y-A Chen, and Immanuel Bloch. Experimental realization of strong effective magnetic fields in an optical lattice. *Physical review letters*, 107(25):255301, 2011.

[5] K. Aikawa, A. Frisch, M. Mark, S. Baier, A. Rietzler, R. Grimm, and F. Ferlaino. Bose-einstein condensation of erbium. *Phys. Rev. Lett.*, 108(21):210401, May 2012.

[6] B. P. Anderson and M. A. Kasevich. Macroscopic Quantum Interference from Atomic Tunnel Arrays. *Science*, 282:1686, 1998.

[7] Brandon M Anderson, Logan W Clark, Jennifer Crawford, Andreas Glatz, Igor S Aranson, Peter Scherpelz, Lei Feng, Cheng Chin, and K Levin. Direct lattice shaking of bose condensates: Finite momentum superfluids. *Physical Review Letters*, 118(22):220401, 2017.

[8] Brian P. Anderson. Resource article: Experiments with vortices insuperfluid atomic gases. *Journal of Low Temperature Physics*, 161(5):574–602, 2010.

[9] M. H. Anderson, J. R. Ensher, M. R. Matthews, C. E. Wieman, and E. A. Cornell. Observation of bose-einstein condensation in a dilute atomic vapor. *Science*, 269(5221):198–201, 1995.

[10] M. R. Andrews, C. G. Townsend, H.-J. Miesner, D. S. Durfee, D. M. Kurn, and W. Ketterle. Observation of Interference Between Two Bose Condensates. *Science*, 275:637, 1997.

[11] M. Anquez, B. A. Robbins, H. M. Bharath, M. J. Boguslawski, T. M. Hoang, and M. S. Chapman. Quantum Kibble-Zurek Mechanism in a Spin-1 Bose-Einstein Condensate. *Phys. Rev. Lett.*, 116(15):155301, 2016.

[12] P. Ao and S. T. Chui. Binary bose-einstein condensate mixtures in weakly and strongly segregated phases. *Phys. Rev. A*, 58(6):4836–4840, Dec 1998.

[13] N.W. Ashcroft and N.D. Mermin. *Solid State Physics*. HRW international editions. Holt, Rinehart and Winston, 1976.

[14] Radka Bach, Marek Trippenbach, and Kazimierz Rzążewski. Spontaneous emission of atoms via collisions of Bose-Einstein condensates. *Phys. Rev. A*, 65(6):636051–636055, 2002.

[15] Roberto Balbinot, Alessandro Fabbri, Serena Fagnocchi, Alessio Recati, and Iacopo Carusotto. Nonlocal density correlations as a signature of hawking radiation from acoustic black holes. *Phys. Rev. A*, 78(2):021603, Aug 2008.

[16] M. Bartenstein, a. Altmeyer, S. Riedl, S. Jochim, C. Chin, J. Hecker Denschlag, and R. Grimm. Crossover from a molecular Bose-Einstein condensate to a degenerate Fermi gas. *Phys. Rev. Lett.*, 92(12):120401, 2004.

[17] Dominik M. Bauer, Matthias Lettner, Christoph Vo, Gerhard Rempe, and Stephan Dürr. Combination of a magnetic feshbach resonance and an optical bound-to-bound transition. *Phys. Rev. A*, 79(6):062713, Jun 2009.

[18] Dominik M. Bauer, Matthias Lettner, Christoph Vo, Gerhard Rempe, and Stephan Durr. Control of a magnetic feshbach resonance with laser light. *Nat Phys*, 5(5):339–342, May 2009.

[19] K. Baumann, Nathaniel Q. Burdick, Mingwu Lu, and Benjamin L. Lev. Observation of low-field fano-feshbach resonances in ultracold gases of dysprosium. *Phys. Rev. A*, 89(2):020701, Feb 2014.

[20] K. Baumann, R. Mottl, F. Brennecke, and T. Esslinger. Exploring Symmetry Breaking at the Dicke Quantum Phase Transition. *Phys. Rev. Lett.*, 107(14):140402, 2011.

[21] Juan Belmonte-Beitia, Víctor M. Pérez-García, Vadym Vekslerchik, and Pedro J. Torres. Lie symmetries and solitons in nonlinear systems with spatially inhomogeneous nonlinearities. *Phys. Rev. Lett.*, 98(6):064102, Feb 2007.

[22] Martin Berninger, Alessandro Zenesini, Bo Huang, Walter Harm, Hanns-Christoph Nägerl, Francesca Ferlaino, Rudolf Grimm, Paul S. Julienne, and Jeremy M. Hutson. Feshbach resonances, weakly bound molecular states, and coupled-channel potentials for cesium at high magnetic fields. *Phys. Rev. A*, 87(3):032517, Mar 2013.

[23] S. Blatt, T. L. Nicholson, B. J. Bloom, J. R. Williams, J. W. Thomsen, P. S. Julienne, and J. Ye. Measurement of optical feshbach resonances in an ideal gas. *Phys. Rev. Lett.*, 107(7):073202, Aug 2011.

[24] Immanuel Bloch, Jean Dalibard, and Wilhelm Zwerger. Many-body physics with ultracold gases. *Rev. Mod. Phys.*, 80(3):885, 2008.

[25] John L. Bohn and P. S. Julienne. Prospects for influencing scattering lengths with far-off-resonant light. *Phys. Rev. A*, 56(2):1486–1491, Aug 1997.

[26] Massimo Boninsegni and Nikolay V Prokofev. Colloquium: Supersolids: What and where are they? *Reviews of Modern Physics*, 84(2):759, 2012.

[27] Eva M. Bookjans, Christopher D. Hamley, and Michael S. Chapman. Strong quantum spin correlations observed in atomic spin mixing. *Phys. Rev. Lett.*, 107(21):210406, 2011.

[28] Simon Braun, Mathis Friesdorf, Sean S. Hodgman, Michael Schreiber, Jens Philipp Ronzheimer, Arnau Riera, Marco del Rey, Immanuel Bloch, Jens Eisert, and Ulrich Schneider. Emergence of coherence and the dynamics of quantum phase transitions. *Proc. Natl. Acad. Sci.*, 112(12):3641, 2015.

[29] A. J. Bray. Theory of phase-ordering kinetics. *Advances in Physics*, 51(2):481–587, 2002.

[30] C. Buggle, J. Léonard, W. Von Klitzing, and J. T M Walraven. Interferometric determination of the s and d-wave scattering amplitudes in 87Rb. *Phys. Rev. Lett.*, 93(17):173202, 2004.

[31] Y. Castin and R. Dum. Bose-einstein condensates in time dependent traps. *Phys. Rev. Lett.*, 77(27):5315–5319, Dec 1996.

[32] Marko Cetina, Michael Jag, Rianne S. Lous, Jook T. M. Walraven, Rudolf Grimm, Rasmus S. Christensen, and Georg M. Bruun. Decoherence of impurities in a fermi sea of ultracold atoms. *Phys. Rev. Lett.*, 115(13):135302, Sep 2015.

[33] Anushya Chandran, Amir Erez, Steven S. Gubser, and S. L. Sondhi. Kibble-Zurek problem: Universality and the scaling limit. *Phys. Rev. B*, 86(6):064304, 2012.

[34] David Chen, Matthew White, Cecilia Borries, and Brian DeMarco. Quantum quench of an atomic mott insulator. *Phys. Rev. Lett.*, 106(23):235304, 2011.

[35] A. P. Chikkatur, A. Görlitz, D. M. Stamper-Kurn, S. Inouye, S. Gupta, and W. Ketterle. Suppression and enhancement of impurity scattering in a Bose-Einstein condensate. *Phys. Rev. Lett.*, 85(3):483–486, 2000.

[36] Cheng Chin, Rudolf Grimm, Paul Julienne, and Eite Tiesinga. Feshbach resonances in ultracold gases. *Rev. Mod. Phys.*, 82(2):1225–1286, Apr 2010.

[37] Cheng Chin, Andrew J Kerman, Vladan Vuletić, and Steven Chu. Sensitive detection of cold cesium molecules formed on Feshbach resonances. *Phys. Rev. Lett.*, 90(3):033201, 2003.

[38] Sayan Choudhury and Erich J Mueller. Stability of a floquet bose-einstein condensate in a one-dimensional optical lattice. *Physical Review A*, 90(1):013621, 2014.

[39] Sayan Choudhury and Erich J Mueller. Stability of a bose-einstein condensate in a driven optical lattice: Crossover between weak and tight transverse confinement. *Physical Review A*, 92(6):063639, 2015.

[40] Sayan Choudhury and Erich J Mueller. Transverse collisional instabilities of a bose-einstein condensate in a driven one-dimensional lattice. *Physical Review A*, 91(2):023624, 2015.

[41] Isaac Chuang, Ruth Durrer, Neil Turok, and Bernard Yurke. Cosmology in the laboratory: Defect dynamics in liquid crystals. *Science*, 251(4999):1336–1342, 1991.

[42] Logan W Clark, Lei Feng, and Cheng Chin. Universal space-time scaling symmetry in the dynamics of bosons across a quantum phase transition. *Science*, 354(6312):606–610, 2016.

[43] Logan W. Clark, Anita Gaj, Lei Feng, and Cheng Chin. Collective emission of matter-wave jets from driven bose-einstein condensates. *Nature*, doi:10.1038/nature24272, 2017.

[44] Logan W Clark, Li-Chung Ha, Chen-Yu Xu, and Cheng Chin. Quantum dynamics with spatiotemporal control of interactions in a stable bose-einstein condensate. *Physical review letters*, 115(15):155301, 2015.

[45] L. Corman, L. Chomaz, T. Bienaimé, R. Desbuquois, C. Weitenberg, S. Nascimbène, J. Dalibard, and J. Beugnon. Quench-Induced Supercurrents in an Annular Bose Gas. *Phys. Rev. Lett.*, 113(13):135302, 2014.

[46] Simon L. Cornish, Sarah T. Thompson, and Carl E. Wieman. Formation of bright matter-wave solitons during the collapse of attractive bose-einstein condensates. *Phys. Rev. Lett.*, 96(17):170401, May 2006.

[47] Luca D'Alessio and Marcos Rigol. Long-time behavior of isolated periodically driven interacting lattice systems. *Phys. Rev. X*, 4(4):041048, Dec 2014.

[48] Bogdan Damski. The simplest quantum model supporting the kibble-zurek mechanism of topological defect production: Landau-zener transitions from a new perspective. *Phys. Rev. Lett.*, 95(3):035701, 2005.

[49] Kendall B Davis, M-O Mewes, Michael R Andrews, NJ Van Druten, DS Durfee, DM Kurn, and Wolfgang Ketterle. Bose-einstein condensation in a gas of sodium atoms. *Physical review letters*, 75(22):3969, 1995.

[50] Adolfo del Campo and Wojciech H. Zurek. Universality of phase transition dynamics: Topological defects from symmetry breaking. *Int. J. Mod. Phys. A*, 29(08):1430018, 2014.

[51] L. Deng, E. W. Hagley, J. Wen, M. Trippenbach, Y. Band, P. S. Julienne, J. E. Simsarian, K. Helmerson, S. L. Rolston, and W. D. Phillips. Four-wave mixing with matter waves. *Nature*, 398(6724):218–220, 1999.

[52] P. Deuar, J. C. Jaskula, M. Bonneau, V. Krachmalnicoff, D. Boiron, C. I. Westbrook, and K. V. Kheruntsyan. Anisotropy in s-wave Bose-Einstein condensate collisions and its relationship to superradiance. *Phys. Rev. A*, 90(3):033613, 2014.

[53] Simone Donadello, Simone Serafini, Tom Bienaimé, Franco Dalfovo, Giacomo Lamporesi, and Gabriele Ferrari. Creation and counting of defects in a temperature-quenched bose-einstein condensate. *Physical Review A*, 94(2):023628, 2016.

[54] Elizabeth A. Donley, Neil R. Claussen, Simon L. Cornish, Jacob L. Roberts, Eric A. Cornell, and Carl E. Wieman. Dynamics of collapsing and exploding Bose-Einstein condensates. *Nature*, 412:295–299, 2001.

[55] L. M. Duan, A. Sørensen, J. I. Cirac, and P. Zoller. Squeezing and entanglement of atomic beams. *Phys. Rev. Lett.*, 85(19):3991–3994, 2000.

[56] Jacek Dziarmaga. Dynamics of a quantum phase transition: Exact solution of the quantum ising model. *Phys. Rev. Lett.*, 95(24):245701, 2005.

[57] Jacek Dziarmaga. Dynamics of a quantum phase transition and relaxation to a steady state. *Advances in Physics*, 59(6):1063–1189, 2010.

[58] André Eckardt. Colloquium: Atomic quantum gases in periodically driven optical lattices. *Rev. Mod. Phys.*, 89(1):011004, Mar 2017.

[59] K. Enomoto, K. Kasa, M. Kitagawa, and Y. Takahashi. Optical feshbach resonance using the intercombination transition. *Phys. Rev. Lett.*, 101(20):203201, Nov 2008.

[60] F. K. Fatemi, K. M. Jones, and P. D. Lett. Observation of optically induced feshbach resonances in collisions of cold atoms. *Phys. Rev. Lett.*, 85(21):4462–4465, Nov 2000.

[61] P. O. Fedichev, Yu. Kagan, G. V. Shlyapnikov, and J. T. M. Walraven. Influence of nearly resonant light on the scattering length in low-temperature atomic gases. *Phys. Rev. Lett.*, 77(14):2913–2916, Sep 1996.

[62] Lei Feng, Logan W Clark, Anita Gaj, and Cheng Chin. Coherent inflationary dynamics for bose-einstein condensates crossing a quantum critical point. *arXiv:1706.01440*, 2017.

[63] Richard P Feynman. Simulating physics with computers. *International journal of theoretical physics*, 21(6):467–488, 1982.

[64] Anna Francuz, Jacek Dziarmaga, Bartlomiej Gardas, and Wojciech Hubert Zurek. Space and time renormalization in phase transition dynamics. *Phys. Rev. B*, 93(7):075134, 2016.

[65] Albert Frisch, Michael Mark, Kiyotaka Aikawa, Francesca Ferlaino, John L. Bohn, Constantinos Makrides, Alexander Petrov, and Svetlana Kotochigova. Quantum chaos in ultracold collisions of gas-phase erbium atoms. *Nature*, 507(7493):475–479, Mar 2014.

[66] Zhengkun Fu, Pengjun Wang, Lianghui Huang, Zengming Meng, Hui Hu, and Jing Zhang. Optical control of a magnetic Feshbach resonance in an ultracold Fermi gas. *Phys. Rev. A*, 88:041601, 2013.

[67] G Gauthier, I Lenton, N McKay Parry, M Baker, MJ Davis, H Rubinsztein-Dunlop, and TW Neely. Direct imaging of a digital-micromirror device for configurable microscopic optical potentials. *Optica*, 3(10):1136–1143, 2016.

[68] N. Gemelke, E. Sarajlic, Y. Bidel, S. Hong, and S. Chu. Parametric amplification of matter waves in periodically translated optical lattices. *Phys. Rev. Lett.*, 95(17):170404, 2005.

[69] Jiangbin Gong, Luis Morales-Molina, and Peter Hänggi. Many-body coherent destruction of tunneling. *Phys. Rev. Lett.*, 103(13):133002, Sep 2009.

[70] Joseph W Goodman. *Introduction to Fourier optics*. Roberts and Company Publishers, 2005.

[71] Chris H Greene, P Giannakeas, and J Perez-Rios. Universal few-body physics and cluster formation. *arXiv:1704.02029*, 2017.

[72] Markus Greiner, Cindy A Regal, and Deborah S Jin. Emergence of a molecular Bose-Einstein condensate from a Fermi gas. *Nature*, 426(6966):537–40, 2003.

[73] S. Greschner, G. Sun, D. Poletti, and L. Santos. Density-dependent synthetic gauge fields using periodically modulated interactions. *Phys. Rev. Lett.*, 113(21):215303, Nov 2014.

[74] C. Gross, H. Strobel, E. Nicklas, T. Zibold, Nir Bar-Gill, G. Kurizki, and Markus K. Oberthaler. Atomic homodyne detection of continuous-variable entangled twin-atom states. *Nature*, 480:219–223, 2011.

[75] Li-Chung Ha. *Bose-Einstein condensates in a shaken optical lattice*. The University of Chicago, 2016.

[76] Li-Chung Ha, Logan W Clark, Colin V Parker, Brandon M Anderson, and Cheng Chin. Roton-maxon excitation spectrum of bose condensates in a shaken optical lattice. *Physical review letters*, 114(5):055301, 2015.

[77] D. S. Hall, M. R. Matthews, J. R. Ensher, C. E. Wieman, and E. A. Cornell. Dynamics of component separation in a binary mixture of bose-einstein condensates. *Phys. Rev. Lett.*, 81(8):1539–1542, Aug 1998.

[78] Michael J. Hartmann and Martin B. Plenio. Migration of bosonic particles across a mott insulator to a superfluid phase interface. *Phys. Rev. Lett.*, 100(7):070602, Feb 2008.

[79] Martin Holthaus. Floquet engineering with quasienergy bands of periodically driven optical lattices. *Journal of Physics B: Atomic, Molecular and Optical Physics*, 49(1):013001, 2016.

[80] Klaus Hueck, Anton Mazurenko, Niclas Luick, Thomas Lompe, and Henning Moritz. Note: Suppression of khz-frequency switching noise in digital micro-mirror devices. *Review of Scientific Instruments*, 88(1):016103, 2017.

[81] Chen-Lung Hung. *In situ probing of two-dimensional quantum gases*. The University of Chicago, 2011.

[82] Chen-Lung Hung, Xibo Zhang, Nathan Gemelke, and Cheng Chin. Accelerating evaporative cooling of atoms into Bose-Einstein condensation in optical traps. *Phys. Rev. A*, 78(1):011604, 2008.

[83] Chen-Lung Hung, Xibo Zhang, Li-Chung Ha, Shih-Kuang Tung, Nathan Gemelke, and Cheng Chin. Extracting density-density correlations from in situ images of atomic quantum gases. *New J. Phys.*, 13(7):075019, 2011.

[84] S. Inouye, M. R. Andrews, J. Stenger, H.-J. Miesner, D. M. Stamper-Kurn, and W. Ketterle. Observation of feshbach resonances in a bose-einstein condensate. *Nature*, 392(6672):151–154, Mar 1998.

[85] S. Inouye, A. P. Chikkatur, D. M. Stamper-Kurn, J. Stenger, D. E. Pritchard, and W. Ketterle. Superradiant Rayleigh Scattering from a Bose-Einstein Condensate. *Science*, 285(5427):571–574, 1999.

[86] Heinrich M Jaeger and Andrea J Liu. Far-from-equilibrium physics: An overview. *arXiv:1009.4874*, 2010.

[87] J. C. Jaskula, M. Bonneau, G. B. Partridge, V. Krachmalnicoff, P. Deuar, K. V. Kheruntsyan, A. Aspect, D. Boiron, and C. I. Westbrook. Sub-poissonian number differences in four-wave mixing of matter waves. *Phys. Rev. Lett.*, 105(19):190402, 2010.

[88] S Jochim, M Bartenstein, A Altmeyer, G Hendl, S Riedl, C Chin, J Hecker Denschlag, and R Grimm. Bose-Einstein Condensation of Molecules. *Science*, 302(5653):2101–2103, 2003.

[89] Gregor Jotzu, Michael Messer, Rémi Desbuquois, Martin Lebrat, Thomas Uehlinger, Daniel Greif, and Tilman Esslinger. Experimental realization of the topological haldane model with ultracold fermions. *Nature*, 515(7526):237–240, 2014.

[90] L Khaykovich, F Schreck, G Ferrari, T Bourdel, J Cubizolles, L D Carr, Y Castin, and C Salomon. Formation of a matter-wave bright soliton. *Science*, 296(5571):1290–1293, 2002.

[91] T W B Kibble. Topology of cosmic domains and strings. *J. Phys. A-Math. Gen.*, 9(8):1387–1398, 1976.

[92] Michael Kolodrubetz, Bryan K. Clark, and David A. Huse. Nonequilibrium dynamic critical scaling of the quantum ising chain. *Phys. Rev. Lett.*, 109(1):1–5, 2012.

[93] T Kraemer, M Mark, P Waldburger, J G Danzl, C Chin, B Engeser, a D Lange, K Pilch, a Jaakkola, H-C Nägerl, and R Grimm. Evidence for Efimov quantum states in an ultracold gas of caesium atoms. *Nature*, 440(7082):315–8, 2006.

[94] Jochen Kronjäger. *Coherent Dynamics of Spinor Bose-Einstein Condensates*. The University of Hamburg, 2007.

[95] Avinash Kumar, Neil Anderson, William D Phillips, S Eckel, Gretchen K Campbell, and Sandro Stringari. Minimally destructive, doppler measurement of a quantized flow in a ring-shaped bose–einstein condensate. *New Journal of Physics*, 18(2):025001, 2016.

[96] Giacomo Lamporesi, Simone Donadello, Simone Serafini, Franco Dalfovo, and Gabriele Ferrari. Spontaneous creation of KibbleZurek solitons in a BoseEinstein condensate. *Nat. Phys.*, 9(10):656–660, 2013.

[97] A. D. Lange, K. Pilch, A. Prantner, F. Ferlaino, B. Engeser, H.-C. Nägerl, R. Grimm, and C. Chin. Determination of atomic scattering lengths from measurements of molecular binding energies near feshbach resonances. *Phys. Rev. A*, 79(1):013622, Jan 2009.

[98] Tim Langen, Thomas Gasenzer, and Jrg Schmiedmayer. Prethermalization and universal dynamics in near-integrable quantum systems. *Journal of Statistical Mechanics: Theory and Experiment*, 2016(6):064009, 2016.

[99] Achilleas Lazarides, Arnab Das, and Roderich Moessner. Equilibrium states of generic quantum systems subject to periodic driving. *Phys. Rev. E*, 90(1):012110, Jul 2014.

[100] Fam Le Kien, Philipp Schneeweiss, and Arno Rauschenbeutel. Dynamical polarizability of atoms in arbitrary light fields: general theory and application to cesium. *The European Physical Journal D*, 67(5), 2013.

[101] L. J. Leblanc and J. H. Thywissen. Species-specific optical lattices. *Phys. Rev. A*, 75(5):053612, 2007.

[102] Julian Léonard, Andrea Morales, Philip Zupancic, Tilman Esslinger, and Tobias Donner. Supersolid formation in a quantum gas breaking a continuous translational symmetry. *Nature*, 543(7643):87–90, 2017.

[103] Jun-Ru Li, Jeongwon Lee, Wujie Huang, Sean Burchesky, Boris Shteynas, Furkan Çağrı Top, Alan O Jamison, and Wolfgang Ketterle. A stripe phase with supersolid properties in spin–orbit-coupled bose–einstein condensates. *Nature*, 543(7643):91–94, 2017.

[104] Jinyang Liang, Rudolph N Kohn Jr, Michael F Becker, and Daniel J Heinzen. 1.5% root-mean-square flat-intensity laser beam formed using a binary-amplitude spatial light modulator. *Applied optics*, 48(10):1955–1962, 2009.

[105] H. Lignier, C. Sias, D. Ciampini, Y. Singh, A. Zenesini, O. Morsch, and E. Arimondo. Dynamical control of matter-wave tunneling in periodic potentials. *Phys. Rev. Lett.*, 99(22):220403, 2007.

[106] Tongtong Liu, Logan W Clark, and Cheng Chin. Exotic domain walls in bose-einstein condensates with double-well dispersion. *Physical Review A*, 94(6):063646, 2016.

[107] Mingwu Lu, Nathaniel Q. Burdick, Seo Ho Youn, and Benjamin L. Lev. Strongly dipolar bose-einstein condensate of dysprosium. *Phys. Rev. Lett.*, 107(19):190401, Oct 2011.

[108] B. Lucke, M. Scherer, J. Kruse, L. Pezze, F. Deuretzbacher, P. Hyllus, O. Topic, J. Peise, W. Ertmer, J. Arlt, L. Santos, a. Smerzi, and C. Klempt. Twin Matter Waves for Interferometry Beyond the Classical Limit. *Science*, 334(6057):773–776, 2011.

[109] Florian Meinert, Manfred J. Mark, Katharina Lauber, Andrew J. Daley, and Hanns-Christoph Nägerl. Floquet engineering of correlated tunneling in the Bose-Hubbard model with ultracold atoms. *Phys. Rev. Lett.*, 116:205301, 2016.

[110] Carolyn Meldgin, Ushnish Ray, Philip Russ, David Chen, David M. Ceperley, and Brian DeMarco. Probing the Bose glass–superfluid transition using quantum quenches of disorder. *Nat. Phys.*, doi:10.1038/nphys3695, 2016.

[111] Harold J Metcalf and Peter Van der Straten. *Laser cooling and trapping*. Springer Science & Business Media, 2012.

[112] Hirokazu Miyake, Georgios A. Siviloglou, Colin J. Kennedy, William Cody Burton, and Wolfgang Ketterle. Realizing the harper hamiltonian with laser-assisted tunneling in optical lattices. *Phys. Rev. Lett.*, 111(18):185302, Oct 2013.

[113] M G Moore and P Meystre. Theory of Superradiant Scattering of Laser Light from Bose-Einstein Condensates. *Phys. Rev. Lett.*, 83:5202, 1999.

[114] Nir Navon, Alexander L. Gaunt, Robert P. Smith, and Z. Hadzibabic. Critical dynamics of spontaneous symmetry breaking in a homogeneous Bose gas. *Science*, 347(6218):167, 2015.

[115] Eike Nicklas, Markus Karl, Moritz Höfer, Aisling Johnson, Wolfgang Muessel, Helmut Strobel, Jií Tomkovič, Thomas Gasenzer, and Markus Oberthaler. Observation of scaling in the dynamics of a strongly quenched quantum gas. *Phys. Rev. Lett.*, 115(24):245301, 2015.

[116] A. A. Norrie, R. J. Ballagh, and C. W. Gardiner. Quantum turbulence in condensate collisions: An application of the classical field method. *Physical Review Letters*, 94(4):040401, 2005.

[117] Magnus Ögren and K. V. Kheruntsyan. Atom-atom correlations in colliding Bose-Einstein condensates. *Phys. Rev. A*, 79(2):021606, 2009.

[118] R. Ozeri, N. Katz, J. Steinhauer, and N. Davidson. Colloquium. *Rev. Mod. Phys.*, 77(1):187–205, Apr 2005.

[119] Colin V. Parker, Li-Chung Ha, and Cheng Chin. Direct observation of effective ferromagnetic domains of cold atoms in a shaken optical lattice. *Nat. Phys.*, 9(12):769–774, oct 2013.

[120] A. Perrin, H. Chang, V. Krachmalnicoff, M. Schellekens, D. Boiron, A. Aspect, and C. I. Westbrook. Observation of atom pairs in spontaneous four-wave mixing of two colliding Bose-Einstein condensates. *Phys. Rev. Lett.*, 99(15):150405, 2007.

[121] A. Perrin, C. M. Savage, D. Boiron, V. Krachmalnicoff, C. I. Westbrook, and K. V. Kheruntsyan. Atomic four-wave mixing via condensate collisions. *New J. Phys.*, 10:045021, 2008.

[122] Christopher J Pethick and Henrik Smith. *Bose-Einstein condensation in dilute gases*. Cambridge university press, 2002.

[123] Anatoli Polkovnikov. Universal adiabatic dynamics in the vicinity of a quantum critical point. *Phys. Rev. B*, 72(16):161201, 2005.

[124] Anatoli Polkovnikov, Krishnendu Sengupta, Alessandro Silva, and Mukund Vengalattore. Colloquium: Nonequilibrium dynamics of closed interacting quantum systems. *Rev. Mod. Phys.*, 83(3):863–883, 2011.

[125] S. E. Pollack, D. Dries, R. G. Hulet, K. M. F. Magalhães, E. A. L. Henn, E. R. F. Ramos, M. A. Caracanhas, and V. S. Bagnato. Collective excitation of a bose-einstein condensate by modulation of the atomic scattering length. *Phys. Rev. A*, 81(5):053627, May 2010.

[126] H. Pu and P. Meystre. Creating macroscopic atomic Einstein-Podolsky-Rosen states from Bose-Einstein condensates. *Phys. Rev. Lett.*, 85(19):3987–3990, 2000.

[127] E. R. F. Ramos, E. A. L. Henn, J. A. Seman, M. A. Caracanhas, K. M. F. Magalhães, K. Helmerson, V. I. Yukalov, and V. S. Bagnato. Generation of nonground-state bose-einstein condensates by modulating atomic interactions. *Phys. Rev. A*, 78(6):063412, Dec 2008.

[128] Ákos Rapp, Xiaolong Deng, and Luis Santos. Ultracold lattice gases with periodically modulated interactions. *Phys. Rev. Lett.*, 109(20):203005, Nov 2012.

[129] C A Regal, M Greiner, and D S Jin. Observation of resonance condensation of fermionic atom pairs. *Phys. Rev. Lett.*, 92(4):040403, 2004.

[130] G Reinaudi, T Lahaye, Z Wang, and D Guéry-Odelin. Strong saturation absorption imaging of dense clouds of ultracold atoms. *Optics letters*, 32(21):3143–3145, 2007.

[131] María I. Rodas-Verde, Humberto Michinel, and Víctor M. Pérez-García. Controllable soliton emission from a bose-einstein condensate. *Phys. Rev. Lett.*, 95(15):153903, Oct 2005.

[132] Wu RuGway, S. S. Hodgman, R. G. Dall, M. T. Johnsson, and A. G. Truscott. Correlations in amplified four-wave mixing of matter waves. *Phys. Rev. Lett.*, 107(7):075301, 2011.

[133] Angelo Russomanno and Emanuele G. Dalla Torre. Kibble-zurek scaling in periodically driven quantum systems. *Europhysics Letters*, 115(3):30006, 2016.

[134] Subir Sachdev. *Quantum phase transitions*. Cambridge University Press, 2011.

[135] L. E. Sadler, J. M. Higbie, S. R. Leslie, M. Vengalattore, and D. M. Stamper-Kurn. Spontaneous symmetry breaking in a quenched ferromagnetic spinor BoseEinstein condensate. *Nature*, 443(7109):312–315, 2006.

[136] Hiroki Saito and Masahito Ueda. Bose-einstein droplet in free space. *Phys. Rev. A*, 70(5):053610, Nov 2004.

[137] M. Salerno, V. V. Konotop, and Yu. V. Bludov. Long-living bloch oscillations of matter waves in periodic potentials. *Phys. Rev. Lett.*, 101(3):030405, Jul 2008.

[138] Dominik Schneble, Yoshio Torii, Micah Boyd, Erik W. Streed, David E. Pritchard, and Wolfgang Ketterle. The Onset of Matter-Wave Amplification in a Superradiant Bose-Einstein Condensate. *Science*, 300(5618):475–478, 2003.

[139] Kestutis Staliunas, Stefano Longhi, and Germán J. de Valcárcel. Faraday patterns in bose-einstein condensates. *Phys. Rev. Lett.*, 89(21):210406, Nov 2002.

[140] J Stenger, S Inouye, DM Stamper-Kurn, H-J Miesner, AP Chikkatur, and W Ketterle. Spin domains in ground-state bose–einstein condensates. *Nature*, 396(6709):345–348, 1998.

[141] Kevin E Strecker, Guthrie B Partridge, Andrew G Truscott, and Randall G Hulet. Formation and propagation of matter-wave soliton trains. *Nature*, 417(6885):150–153, 2002.

[142] J. Struck, C. Ölschläger, R. Le Targat, P. Soltan-Panahi, A. Eckardt, M. Lewenstein, P. Windpassinger, and K. Sengstock. Quantum Simulation of Frustrated Classical Magnetism in Triangular Optical Lattices. *Science*, 333(6045):996—-999, 2011.

[143] J. Struck, C. Ölschläger, M. Weinberg, P. Hauke, J. Simonet, A. Eckardt, M. Lewenstein, K. Sengstock, and P. Windpassinger. Tunable gauge potential for neutral and spinless particles in driven optical lattices. *Phys. Rev. Lett.*, 108(22):225304, 2012.

[144] M. Theis, G. Thalhammer, K. Winkler, M. Hellwig, G. Ruff, R. Grimm, and J. Hecker Denschlag. Tuning the scattering length with an optically induced feshbach resonance. *Phys. Rev. Lett.*, 93(12):123001, Sep 2004.

[145] S. T. Thompson, E. Hodby, and C. E. Wieman. Ultracold molecule production via a resonant oscillating magnetic field. *Phys. Rev. Lett.*, 95(19):190404, Nov 2005.

[146] E. Timmermans. Phase separation of bose-einstein condensates. *Phys. Rev. Lett.*, 81(26):5718–5721, Dec 1998.

[147] A Vardi and M G Moore. Directional "Superradiant" Collisions: Bosonic Amplification of Atom Pairs Emitted from an Elongated Bose-Einstein Condensate. *Phys. Rev. Lett.*, 89(9):090403, 2002.

[148] Sarah L. Veatch, Olivier Soubias, Sarah L. Keller, and Klaus Gawrisch. Critical fluctuations in domain-forming lipid mixtures. *Proc. Natl. Acad. Sci.*, 104(45):17650–17655, 2007.

[149] J. M. Vogels, K. Xu, and W. Ketterle. Generation of macroscopic pair-correlated atomic beams by four-wave mixing in Bose-Einstein condensates. *Phys. Rev. Lett.*, 89(2):204011, 2002.

[150] Thomas Volz, Stephan Dürr, Sebastian Ernst, Andreas Marte, and Gerhard Rempe. Characterization of elastic scattering near a feshbach resonance in ^{87}Rb. *Phys. Rev. A*, 68(1):010702, Jul 2003.

[151] T. Wasak, P. Szańkowski, R. Bücker, J. Chwedeńczuk, and M. Trippenbach. Bogoliubov theory for atom scattering into separate regions. *New Journal of Physics*, 16:013041, 2014.

[152] Tino Weber, Jens Herbig, Michael Mark, Hanns-Christoph Nägerl, and Rudolf Grimm. Bose-Einstein condensation of cesium. *Science*, 299(5604):232, 2003.

[153] Chad N. Weiler, Tyler W. Neely, David R. Scherer, Ashton S. Bradley, Matthew J. Davis, and Brian P. Anderson. Spontaneous vortices in the formation of BoseEinstein condensates. *Nature*, 455(7215):948–951, 2008.

[154] Christof Weitenberg, Manuel Endres, Jacob F. Sherson, Marc Cheneau, Peter Schausz, Takeshi Fukuhara, Immanuel Bloch, and Stefan Kuhr. Single-spin addressing in an atomic mott insulator. *Nature*, 471(7338):319–324, Mar 2011.

[155] Artur Widera, Olaf Mandel, Markus Greiner, Susanne Kreim, Theodor W. Hänsch, and Immanuel Bloch. Entanglement interferometry for precision measurement of atomic scattering properties. *Phys. Rev. Lett.*, 92(16):160406, Apr 2004.

[156] R. A. Williams, M. C. Beeler, L. J. LeBlanc, K. Jiménez-García, and I. B. Spielman. Raman-induced interactions in a single-component fermi gas near an s-wave feshbach resonance. *Phys. Rev. Lett.*, 111(9):095301, Aug 2013.

[157] Jun Xu, Shuyuan Wu, Xizhou Qin, Jiahao Huang, Yongguan Ke, Honghua Zhong, and Chaohong Lee. Kibble-Zurek dynamics in an array of coupled binary Bose condensates. *Europhysics Lett.*, 113(5):50003, 2016.

[158] Rekishu Yamazaki, Shintaro Taie, Seiji Sugawa, and Yoshiro Takahashi. Submicron spatial modulation of an interatomic interaction in a bose-einstein condensate. *Phys. Rev. Lett.*, 105(5):050405, Jul 2010.

[159] Mi Yan, B. J. DeSalvo, B. Ramachandhran, H. Pu, and T. C. Killian. Controlling condensate collapse and expansion with an optical feshbach resonance. *Phys. Rev. Lett.*, 110(12):123201, Mar 2013.

[160] T. Zelevinsky, M. M. Boyd, A. D. Ludlow, T. Ido, J. Ye, R. Ciuryło, P. Naidon, and P. S. Julienne. Narrow line photoassociation in an optical lattice. *Phys. Rev. Lett.*, 96(20):203201, May 2006.

[161] Alessandro Zenesini, Hans Lignier, Donatella Ciampini, Oliver Morsch, and Ennio Arimondo. Coherent control of dressed matter waves. *Phys. Rev. Lett.*, 102(10):100403, Mar 2009.

[162] Xibo Zhang. *Observation of quantum criticality with ultracold atoms in optical lattices*. The University of Chicago, 2012.

[163] Xibo Zhang, Chen-Lung Hung, Shih-Kuang Tung, and Cheng Chin. Observation of quantum criticality with ultracold atoms in optical lattices. *Science*, 335(6072):1070–1072, 2012.

[164] Wei Zheng, Boyang Liu, Jiao Miao, Cheng Chin, and Hui Zhai. Strong Interaction Effects and Criticality of Bosons in Shaken Optical Lattices. *Phys. Rev. Lett.*, 113(15):155303, 2014.

[165] Qi Zhou and Tin Lun Ho. Signature of quantum criticality in the density profiles of cold atom systems. *Phys. Rev. Lett.*, 105(24):245702, 2010.

[166] P. Ziń, J. Chwedeńczuk, A. Veitia, K. Rzążewski, and M. Trippenbach. Quantum multimode model of elastic scattering from Bose-Einstein condensates. *Phys. Rev. Lett.*, 94(20):200401, 2005.

[167] Philip Zupancic, Philipp M. Preiss, Ruichao Ma, Alexander Lukin, M. Eric Tai, Matthew Rispoli, Rajibul Islam, and Markus Greiner. Ultra-precise holographic beam shaping for microscopic quantum control. *Opt. Express*, 24(13):13881–13893, Jun 2016.

[168] Wojciech H. Zurek. Cosmological experiments in superfluid helium? *Nature*, 317(6037):505–508, 1985.

[169] Wojciech H Zurek. Causality in condensates: gray solitons as relics of bec formation. *Physical review letters*, 102(10):105702, 2009.

[170] Wojciech H. Zurek, Uwe Dorner, and Peter Zoller. Dynamics of a quantum phase transition. *Phys. Rev. Lett.*, 95(10):105701, 2005.

[171] M. W. Zwierlein, C. A. Stan, C. H. Schunck, S. M F Raupach, A. J. Kerman, and W. Ketterle. Condensation of pairs of fermionic atoms near a Feshbach resonance. *Phys. Rev. Lett.*, 92(12):120403, 2004.